Ph.D. THESIS

Study on neutron anisotropic emission from photonuclear reaction in giant dipole resonance energy region

Supervisors

Prof. SANAMI, Toshiya

Prof. YAMAZAKI, Hirohito

The Graduate University for Advanced Studies, SOKENDAI

School of High Energy Accelerator Science

Department of Accelerator Science

Tran Kim Tuyet

Tsukuba - June, 2021

Examination Committee

1. Prof. NAMITO, Yoshihito
2. Prof. MATSUMURA, Hiroshi
3. Asst. Prof. IWASE, Hiroshi
4. Prof. NAKASHIMA, Hiroshi
5. Assoc. Prof. YAMAZAKI, Hirohito
6. Prof. SANAMI, Toshiya

Date of Final Defense: July 26$^{\text{th}}$, 2021

Acknowledgment

The study in this dissertation was conducted with a lot of assistance and support from many people. I would like to express my sincere appreciation to them.

The first words of gratitude must go to my supervisor, Prof. Toshiya Sanami. He has extensively guided me since I started this research. I gratefully appreciate his precious and invaluable support, time, and patience in guidance, discussion, and feedback.

I am incredibly grateful to Prof. Hirohito Yamazaki, my co-supervisor. During my Ph.D. study, he always provided his time for discussion and valuable feedback through research meetings.

Both supervisors convincingly guided and encouraged me to be professional and do the right things. Without their persistent help and troubleshooting, the objective of this research would not have been achieved.

I would like to thank Prof. Yoshihito Namito, the chair of the dissertation committee. His advice and discussions have enabled me to complete this research. In addition, I am grateful to Prof. Hiroshi Matsumura and Prof. Hiroshi Iwase for their helpful comments and discussions, which helped enhance the quality of my thesis.

I would like to express my gratitude to Prof. Yoshihiro Asano, who gave me much support during this research. He spent his valuable time in performing the experiments with me.

Additionally, I would like to thank Dr. Toshiro Itoga of Japan Synchrotron Radiation Research Institute, who helped arrange and set up the experiments at New-

SUBARU and also contributed to a simulation code.

I am grateful to Dr. Yoichi Kirihara at the Japan Atomic Energy Agency, who contributed to developing the data acquisition system for the experiment.

I would like to thank Prof. Yasuhito Sakaki at the Japan High Energy Accelerator Research Organization (KEK). He performed an experiment with me and developed Python-based code for reading the evaluated nuclear data used in this research.

I would also like to express my appreciation to Prof. Shuji Miyamoto and the staff at NewSUBARU, BL-01 facility, for supporting me when I performed the experiments.

I would also like to acknowledge the support from Prof. Hiroshi Nakashima of Hokkaido University. He not only attended my experiment and gave me valuable comments but also reviewed my dissertation as a member of the dissertation committee.

I would like to thank Dr. Toshihiko Kawano at Los Alamos National Laboratory, who provided the CoH_3 code and discussed it through e-mail. I also thank Dr. Osamu Iwamoto and Dr. Nobuyuki Iwamoto at Japan Atomic Energy Agency, who spent their time in providing comments on the calculation results.

I wish to thank the KEK Scholarship for International Students Foundation for the financial support during my Ph.D. course. In addition, I would like to thank the staff of SOKEDNAI and User Office at KEK; they have supported me personally during my Ph.D. study in Japan.

Finally, I wish to express my deepest gratitude to my family members for their encouragement during my years of studying in Japan. I am grateful to my parents for always respecting my choices irrespective of the circumstances. I would like to thank Dr. Bui Tuan Khai who has encouraged and supported me. I am also grateful to my friends who have helped and encouraged me so far.

Abstract

The nucleus absorbs photons with an energy ranging from 10 to 30 MeV, resulting in the relative displacement of neutrons and protons included in the nucleus and leading to nucleon emission. Data of photon-induced nucleon emission, called photonuclear reaction, are important for developing nuclear reaction models, designing radiation shielding, analyzing radiation transport, and evaluating the dosimetry of radiotherapy in various applications of electron accelerators. Thus far, data of photonuclear reactions were obtained for calculating the (γ,xn) reaction cross section through numerous experiments with different photon sources. Recently, the energy spectrum of neutrons and its angular distribution are obtained for an Au target at a photon energy of 17 MeV. The data show a large amount of low-energy isotropic neutron emission and a small amount of high-energy anisotropic neutron emission.

The energy and angular distributions of photoneutrons should be taken into account in the shielding design of electron accelerators. Experimental data of the photonuclear reaction for describing the cross section with the emitted particle energy and angular distribution, called the double differential cross-section (DDX), are scarce. DDX enables not only the evaluation of the nuclear data library used in radiation transport but also the development of its physics model. Thus, the DDXs of photoneutrons should be measured for various target materials and incident photon energies. The objective of this thesis is to establish a methodology for measuring the DDXs of photoneutrons, conduct systematic data acquisition of the DDXs, and study the impact of the data on the shielding design of electron accelerators.

In this research, beams of linearly polarized monoenergetic photons were prepared at the BL-01, NewSUBARU facility (Spring-8, Japan) by using the laser Compton scattering (LCS) technique. The photons were generated by the collisions of the laser photons with a wavelength of 1.064 μm and a beam of high-energy electrons, the energy of which was adjusted to produce back-scattered photons with maximum energies of 14, 17, and 20 MeV. The photons were collimated by lead blocks before reaching a cylindrical target at its circular center. Targets were made of $^{\mathrm{nat}}$Pb, ^{197}Au, $^{\mathrm{nat}}$Sn, $^{\mathrm{nat}}$Cu, $^{\mathrm{nat}}$Fe, and $^{\mathrm{nat}}$Ti. Each target was separately placed on the pathway of the collimated photons. Owing to the photonuclear reactions, neutrons were generated in the target. Surrounding the target, neutron detectors filled with an organic liquid scintillator were placed to detect neutrons. An event-by-event data acquisition (DAQ) system was assembled with the time-of-flight (ToF) function to determine the neutron energy, and the pulse shape discrimination (PSD) function was applied to distinguish neutrons and background photons. The raw data were stored in a Linux computer and interpreted using C++ and the ROOT framework.

The DDXs of photoneutrons were determined by normalizing neutron yield with the number of incident photons on the target, attenuations of photons and neutrons in the target, neutron detection efficiency, number of target atoms, and solid angle. Neutron events were selected using the PSD parameter, which was the ratio of the tail integral to the total integral. Neutron energy was determined by the ToF that was obtained as a sum of the photon flight time from the target to the detector and the time difference between the neutron data and the target scattered photon peak. To evaluate the number of incident photons, the number of counts in the plastic scintillator placed upstream of the target was used with the consideration of its photon detection efficiency. Using Monte Carlo calculations, the attenuation of incident photons in each target was determined by taking the ratio of the average track length of the photons to the target thickness. The photoneutrons were attenuated when they penetrated through the target, and the neutron attenuation

was calculated. The neutron detection efficiency was determined by combining the results of a ^{252}Cf neutron measurement and SCINFUL-QMD code.

The calculation results of DDXs for Pb, Au, Sn, Cu, Fe, and Ti targets were obtained using Monte Carlo code, Particle and Heavy Ion Transport code System (PHITS), the nuclear data library, and the cascade exiton model. All the results did not express the angular distribution of the photoneutron. All three DDX results were taken into account for the abundances of isotopes in the targets, the width of the incident photon energy within 14 MeV - 17 MeV, and the neutron energy resolution of the experiment. In general, the DDX spectra produced by these calculations of Pb, Au, or Sn were comparable below 4 MeV and different above 4 MeV because of the consideration of the pre-equilibrium process in JENDL and CoH_3 but not PHITS; the calculated DDXs of Cu, Fe, and Ti were comparable.

The experimental results of DDXs of photoneutrons were obtained for Pb, Au, Sn, Cu, Fe, and Ti targets at polar angles of 30°, 60°, 90°, 120°, and 150° and an azimuthal angle of 90° for 14, 17, and 20 MeV linearly polarized photons. Two components were observed in all the DDXs: one component had a Maxwellian tail shape and mainly occupied the energy range of 2 – 4 MeV, while the other component had a non-Maxwellian shape and mainly occupied the energy range above 4 MeV. To determine the energy to separate these two components, the Maxwellian tail-shaped component was fitted with a Maxwellian distribution, which can be explained by the evaporation process of low energy neutrons. To discuss the angular distribution of the photoneutrons, the angular differential cross sections (ADXs) were obtained for each component as a function of the angles of the incident photons and the emitted neutrons. The angular dependence of the neutrons in the Maxwellian-shaped and non-Maxwellian-shaped components could be well expressed by the fitting function $ADX(\Theta)=a+b\cos(2\Theta)$. The anisotropy parameter in the Legendre polynomial expansion, a_2, had been used to compare the angular distribution. I calculated the a_2 parameter using a and b and compared it with other experiments. The numerical

values of a_2 in Ti and Sn targets were obtained for the first time in the present study. The a_2 values in Cu and Fe were consistent with the results obtained in previous studies, while the a_2 values of Pb and Au were smaller than the previous results.

The target mass dependence of the photoneutron spectrum indicated that the magnitude of the photoneutron spectrum decreases with decreasing target mass number. The obtained cross sections for the (γ, xn) reaction were calculated for each component corresponding to $\sigma_{\mathrm{Max.}}$ (Maxwellian-shaped component) and $\sigma_{\mathrm{non-Max}}$ (non-Maxwellian-shaped component) and fitted as a function of $A^{1/3}$. The ratio of $\sigma_{\mathrm{Max.}}$ to σ_{sum} (sum of two components) and that of $\sigma_{\mathrm{non-Max.}}$ to σ_{sum} were calculated to discuss the contribution of each component to the photoneutron spectrum. For Ti, Fe, and Cu, the contribution of the Maxwell-shaped component was larger than that of the non Maxwellian-shaped component according to the values of σ. On the order hand, for Sn, Au, and Pb, the contributions of the two components were comparable, at approximately 50% of the photoneutron spectrum.

The dependence of the photoneutron spectrum on the photon energy was discussed based on data of the DDXs of ^{197}Au(γ,xn), $^{\mathrm{nat}}$Cu(γ,xn), and $^{\mathrm{nat}}$Ti(γ,xn) for 14 MeV, 17 MeV, and 20 MeV incident photons. Typically, a magnitude of the photoneutron spectrum increase with a higher photon energy. The Maxwellian-shaped and non-Maxwellian-shaped components were observed for all three photon energies. The separation energy to distinguish the two components for the three photon energies was 4.2 MeV, which was determined by fitting the Maxwellian distribution for the DDX data. For the data of Ti obtained with 20 MeV photons, the maximum DDX value was at H90 and the minimum at V90, which is opposite to the trend obtained with 17 MeV photons. Angular differential cross sections (ADXs) were obtained for the components. The ADX of Au for both the components decreases with increasing photon energy. For Cu, the ADX of both the components increases with increasing photon energy, while the total cross section of the (γ,xn) reaction decreases. For Ti, the ADX values sharply increase with increasing photon energy,

especially for the non-Maxwellian-shaped component. The ratio of the ADXs obtained with different photon energies was calculated to discuss the change in each component with increasing photon energy.

The effect of the photoneutron spectrum shape on the shielding calculation was studied by considering the leakage dose rate using PHITS code for Pb(γ,xn) with 17 MeV incident photons. The geometry for this concrete shielding calculation was a simple sphere. The thickness of shielding concrete was varied from 0 cm to 180 cm. Two neutron spectra that is a Maxwellian-shaped spectrum and an experimental-based spectrum consisting of Maxwellian and non-Maxwellian components, were applied for the shielding calculations. After penetrating the shield, the neutrons of the non-Maxwellian-shaped component lose their energy and cause differences in the lower energy range with increasing shielding thickness. The result shows that the dose could be underestimated by a factor of almost 2.5 with increasing shielding thickness if we use only the Maxwellian-shaped spectrum for shielding calculation. The underestimation will be mitigated in an actual shielding design that was performed for bremsstrahlung unpolarized photons because the result was obtained for horizontally polarized photons, which yield the maximum non-Maxwellian-shaped component.

Publication list

• Academic journal

1. Tran Kim Tuyet, Toshiya Sanami, Hirohito Yamazaki, Toshiro Itoga, Akihiro Takeuchi, Yoshihito Namito, Shuji Miyamoto, Yoshihiro Asano, Energy and angular distribution of photo-neutrons for 16.6 MeV polarized photon on medium–heavy targets, Nuclear Inst. and Methods in Physics, A 989 (2021) 164965. Access Link

• International Conference

2. T.K. Tuyet, T. Sanami, H. Yamazaki, Impact of photo-neutron spectrum shape for Pb(γ,xn) on shielding design, ICRS14/RPSD 2020 at Seattle. This presentation was accepted but this conference was postponed to 2022 due to COVID-19.

• Conference proceedings

3. T.K. Tuyet, Y. Sakaki, T. Sanami, H. Yamazaki, T. Itoga, A. Takeuchi, S. Miyamoto, Y. Asano, Comparison of double-differential cross section between JENDL/PD-2016.1 and experimental data for photo-neutron production of medium-heavy nuclei at 16.6 MeV, Symposium on Nuclear Data, RIKEN, Wako, Japan, 26^{th} - 27^{th} November, 2020. (accepted)

4. T.K. Tuyet, T. Sanami, H. Yamazaki, T. Itoga, A. Takeuchi, S. Miyamoto, Y. Asano, Comparison between experimental and calculation neutron spectra

of the ^{197}Au(γ,sn) reaction for 17 MeV polarized photon, Symposium on Nuclear Data, Kyushu University, Fukuoka, Japan, 28th - 30th November, 2019. Access Link

5. T.K. Tuyet, T. Sanami, H. Yamazaki, Experimental approach to determine detection efficiency of organic liquid scintillators with different volumes, 33th Symposium on radiation detectors and their uses KEK, Tsukuba, Japan, January, 2020. Access Link

• Oral Presentation

6. Tran Kim Tuyet, Toshiya Sanami, Hirohito Yamazaki, Toshiro Itoga, Yasuhito Sakaki, Linh Thi Truc Nguyen, Yoichi Kirihara, Hiroshi Nakashima, Shuji Miyamoto, Yoshihiro Asano, Photon energy dependence of photo-neutron production from the ^{197}Au(γ,xn) reaction, 2021 Annual Meeting of AESJ, Online meeting, 19th March. Access Link

7. T.K. Tuyet, T. Sanami, H. Yamazaki, T. Itoga, Y. Sakaki, H. Nakashima, Y. Kirihara, S. Miyamoto, Y. Asano, Measurement of photoneutron energy spectrum with Laser Compton back scattering photon at NewSUBARU BL-01, 35th Symposium on Radiation Detector and Their Uses, KEK, 2021 20th-22th January. Access Link

8. T.K. Tuyet, T. Sanami, H. Yamazaki, T. Itoga, A. Takeuchi, S. Miyamoto, H. Nakashima, Y. Asano, Double differential cross-section measurement of the medium-heavy nuclei (γ,xn) reaction for 16.6 MeV polarized photons, 2020 Fall meeting of AESJ, Online meeting, 16th September. Access Link

9. T.K. Tuyet, T. Sanami, H. Yamazaki, T. Itoga, Y. Asano, S. Miyamoto, A. Takeuchi, Double differential cross-section measurement of the ^{197}Au(γ,n) reaction for 13 MeV and 17 MeV linearly polarized photon, 2020 Annual meeting of AESJ, 16th March. This presentation was accepted but this meeting was

canceled due to COVID-19. Access Link

10. T.K. Tuyet, T. Sanami, H. Yamazaki, Experimental approach to determine detection efficiency of organic liquid scintillators with different volumes, 34th Symposium on Radiation Detector and Their Uses, KEK, 2020 January .

11. T.K. Tuyet, T. Sanami, H. Yamazaki, T. Itoga, A. Takeuchi, Y. Asano, S. Miyamoto, Target mass dependence of photo-neutron production with 17 MeV linearly polarized photons, 2019 Fall Meeting of AESJ, University of Toyama, 12th September. Access Link

• Poster Presentation

12. T.K. Tuyet, Y. Sakaki, T. Sanami, H. Yamazaki, T. Itoga, A. Takeuchi, S. Miyamoto, Y. Asano, Comparison of double-differential cross section between JENDL/PD-2016.1 and experimental data for photo-neutron production of medium-heavy nuclei at 16.6 MeV, Symposium on Nuclear Data, Riken, 26th - 27th November, 2020. Access Link

13. T.K. Tuyet, T. Sanami, H. Yamazaki, S. Miyamoto, T. Itoga, Y. Asano, A. Takeuchi, Comparison between experimental and calculation neutron spectra of the ^{197}Au(γ,sn) reaction for 17 MeV polarized photon, Symposium on Nuclear Data, Kyushu University, 28th - 30th November, 2019. Access Link

Table of Contents

List of Figures

List of Tables

Chapter 1

Introduction

1.1 Photonuclear reactions and their importance

A photonuclear reaction consists of two main processes: the absorption of an incident photon in a nucleus and the emission of one or more secondary particles from the nucleus. There are several theoretical mechanisms to describe each process. For photon absorption in a nucleus, this section focuses mainly on the energy range up to 150 MeV. For energy less than 150 MeV, the photon absorption is mainly described by giant dipole resonance (GDR) and quasi-deuteron (QD) nuclear modelings, which are described in the following paragraphs. For photon energy above 150 MeV, which is the energy threshold for the production of pions, more complicated nuclear modeling is required.

Among the processes used to describe photoabsorption, GDR is the most intense. In GDR modeling, the photon, as an electro-magnetic wave, interacts with the whole dipole moment of the nucleus. The probability of photon absorption by GDR corresponds to the wavelength of the photon (or its energy). The probability peaks when the wavelength of the incident photon is approximately equal to the size of the nucleus. The width of this resonance peak is a few MeV. Outside of this region, the probability of GDR is negligible. This process was described in detail by Bohr

and Mottelson [1].

The energy threshold to enhance the resonance depends on the nucleon's binding energy, which corresponds to the atomic mass number (A) of the nucleus: with a photon energy of approximately 20 MeV, the GDR occurs in light nuclei ($A \leq 30$), and in the photon energy range of 14–18 MeV, the GDR occurs in medium and heavy nuclei ($30 < A \leq 100$). In heavy nuclei, the GDR mainly leads to the (γ, n) reactions and the (γ, 2n) reactions with higher photon energy. In these heavy nuclei, the Coulomb force barrier ($B \simeq Z^2 A^{-1/3}$ MeV) is higher than the GDR energy; hence, the cross-section for the (γ, p) reactions is very low. On the other hand, in light nuclei, in which the Coulomb barrier is lower, the probabilities of (γ, n) and (γ, p) reactions are almost equal to each other [2, 3].

The QD modeling can be described as the interaction of an electro-magnetic wave with the dipole moment of a QD, which is a neutron-proton pair in the nucleus. The probability of photon absorption by a QD is less intense compared to one by GDR; however, QDs still contribute at in all energies of incident photons. The model has been described in Reference [4].

After photon absorption, secondary particles (e.g., proton, neutron, deuteron, tritium, ^{3}He, alpha, or a combination of these) are emitted from the nucleus. The nucleus also emits γ-rays if it is not in the ground state after the emission of secondary particles. The emission of secondary particles can be conceptualized by the pre-equilibrium and equilibrium processes.

In the equilibrium process, the energy of incident photons is absorbed and distributed to the particles. The particles are "boiled" and tend to escape from the nucleus after penetrating the nuclear potential barrier, as in evaporation. This potential barrier includes the Coulomb potential; thus, for heavy elements, neutrons are preferentially evaporated because they are not affected by the Coulomb barrier. In a classical sense, the particles evaporated from this process have an isotropic angular distribution [5].

For the pre-equilibrium process, a particle receives a large amount of energy originating from the photoabsorbtion and escapes from the nucleus. The particles emitted this process should be characterized by a higher energy distribution. Equilibrium and pre-equilibrium processes have been studied with detailed theoretical calculations and comparisons with experimental data [6, 7, 8].

Photonuclear reactions play important roles in a wide range of applications, such as (i) radiation shielding, radiation transport analyses, and the calculation of dose rate; (ii) activation analysis based on high-energy photons; (iii) nuclear waste transmutation to convert long-lived fission products to short-lived nuclei [9]. A database of photonuclear reactions is required in these applications. In this thesis, I will mainly focus on the effect of photonuclear reactions on the radiation shielding of electron accelerators.

According to Reference [10], in 2016, there were about 900 electron linear accelerators operated in hospitals in Japan, and electron acceleration energies ranging from 6 to 15 MeV were used in cancer therapy. These accelerated electrons induce highly energetic bremsstrahlung photons when the electron beam strikes surrounding objects in the accelerator such as shielding walls and magnets. These photons are harmful to the human body; thus, radiation shielding is important when constructing an accelerator. However, via photonuclear reactions, secondary particles can be produced when these photons penetrate and interact with the materials used in the components of accelerators and shielding.

These photons with energy above 8 MeV interact with human tissues and produce secondary particles (α, n, p, d, t, and ^{3}He) through photonuclear reactions. The list of reactions was reported in Table 1 of Reference [11], and the contributions to absorbed dose were presented in Figure 1 of Reference [12].

In particular, it is much more difficult to shield neutrons than to shield other particles, and neutrons can activate the surrounding material. As shown in Figure 1.1a, the increase in the bremsstrahlung yield depends on the atomic number of the

material and the electron energy [13]. Figure 1.1b indicates that the neutron yield increases with increasing electron energy and target mass number [13].

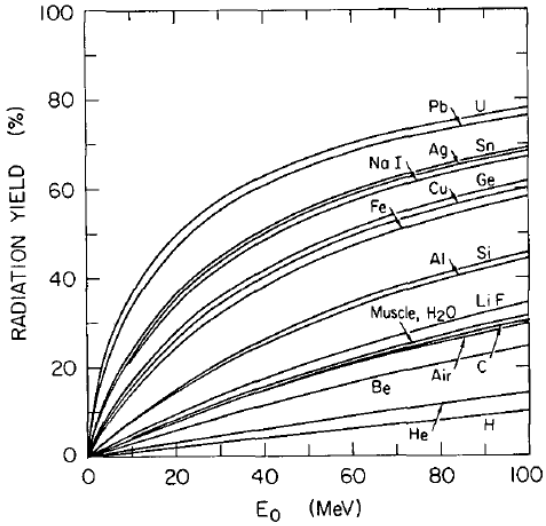

(a) Bremsstrahlung yield

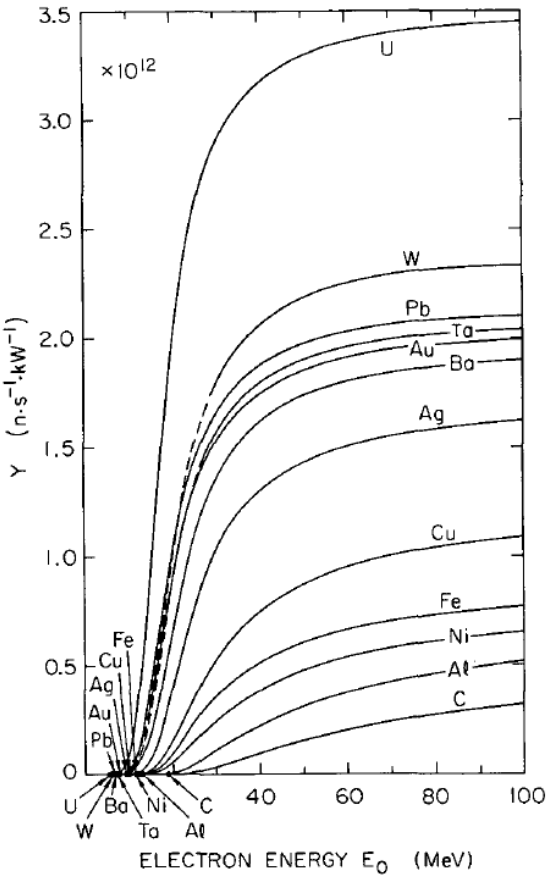

(b) Neutron yields from infinitely thick targets, per kW of electron beam power

Figure 1.1: Bremsstrahlung yield and neutron yield produced by electron beams on various targets [13].

1.2 Simulation of photonuclear reaction

In accelerator and shielding design, particle transport is simulated using the Monte Carlo method. The Monte Carlo simulation code can be used to estimate the shielding ability of the material and the thickness required for reducing the hazards of radiation particles such as protons, neutrons, alpha particles, and gamma-rays. Photonuclear reactions are described in the simulation code based on theoretical models and photonuclear reaction data libraries. The succeeding sections present the simulation of a photonuclear reaction in Monte Carlo codes, the evaluated nuclear library, and nuclear models of photonuclear reactions.

1.2.1 Monte Carlo code

In this section, two Monte Carlo simulation codes are described, the Particle and Heavy Ion Transport code System (PHITS) and Monte Carlo N-Particle Transport Code (MCNP6), which are widely used in many applications.

Nuclear reactions are simulated in PHITS using theoretical models and nuclear data libraries. The theoretical models used for the calculation of nuclear reactions are the Liège Intranuclear Cascade model (INCL 4.6) [14] followed by the generalized evaporation model (GEM) [15] implemented in PHITS. The interaction of neutrons is calculated using the nuclear data library for energy below 20 MeV. In cases where data are not available in the library, it is calculated based on the physics models.

The total cross-sections of photonuclear reactions, which are implemented in the PHITS, are obtained from JENDL/PD-2004 [16]. However, JENDL/PD-2004 was released with only 68 nuclides for energies from threshold to 140 MeV. If the data is not available in JENDL/PD-2004, the cross-section is estimated using Lorentzian equation in PHITS [17].

The photonuclear processes are implemented in MCNPX. Previous studies have reported the cross section, spectra, and implementation of photonuclear processes

[18, 19]. For transport applications in MCNPX, the nuclear data of photonuclear reactions were evaluated using the GNASH code system, and the GDR and QD models for photoabsorption were taken into account in the calculations. The emission of secondary particles and gamma rays from the nucleus were calculated using the pre-equilibrium theory and Hauser-Feshbach theory [20].

1.2.2 Evaluated photonuclear data library

An evaluated photonuclear data library is a digital file containing cross-section data as well as the production cross-section, energy, and angular distributions of the emitted particles. The library is created based on experimental data, nuclear reaction theory, and reaction models.

Users often rely on raw photonuclear data, primarily reaction cross sections from different measurements. The evaluation of nuclear reaction data consists of several systematic steps. These include a bibliographic compilation, and a compilation of experimental data, followed by a critical analysis of the measurement techniques used, together with evaluation based on theoretical nuclear reaction modeling. In the past, several laboratories, mainly LLNL Livermore (USA), CEA Saclay (France), and MSU Moscow (Rusia), have reported a large body of experimental data. These data were partly compiled into the internationally available computerized library EXFOR. Evaluation methods are required for photonuclear data because it is difficult to develop a complete photonuclear data file on the basis of measured cross section alone. These data were often from different kinds of photon sources, causing significant systematic discrepancies, and there is a lack of data in a number of important cases. Nevertheless, recent developments both in methods to resolve experimental discrepancies and in nuclear reaction theory are promising for us in the generation of evaluated photonuclear data.

The evaluation of nuclear data for photonuclear reactions was carried out by Japan Atomic Energy Agency. JENDL photonuclear data file 2004, called JENDL/PD-

2004, was released in March 2004 and contained the photonuclear data for 68 nuclides with an incident photon energy of up to 140 MeV [16]. The nuclear data were evaluated using theoretical calculation based on statistical nuclear reaction models. Thus far, the file has been updated to JENDL/PD-2016.1, which includes 2681 nuclei and an incident photon energy of up to 140 MeV [21]. The updated version provided reaction cross section, cross sections for secondary particle production, and double-differential cross sections (DDXs) of particles emitted by photonuclear reactions and emitted γ-rays.

In addition to JENDL/PD, the IAEA-2019 photonuclear data library is the latest library addressing the reaction cross section, energy, and angular distribution of secondary particles. The latest version of IAEA-2019 introduced improvements with new evaluation using new experimental data from the EXPOR database (up to the cut-off date of April 2019) [9].

1.2.3 Nuclear reaction models

Nuclear reaction models play a significant role in producing an evaluated nuclear data library. In particular, it is necessary for reproducing the energy and angular distributions of particles emitted through nuclear interactions because of the lack of experimental data. CCONE [22], EMPIRE [23], and CoH_3 [24] are example of codes used in computing nuclear interactions. Here, CCONE and CoH_3 codes are introduced because they are used in JENDL/PD-2016.1 and IAEA.2019.

The computer code system CCONE was developed by JAEA for generating the JENDL/PD, which is a part of the JENDL project. The CCONE code can provide not only the cross section of a nucleon-induced reaction but also particle emission spectra, angular distributions, and so on by taking into account the emission of multiple particles such as photoneutron, photoproton, deuteron, triton, helium-3, alpha particle, and photon in addition to fission. high-energy photons excite the target nucleus through the GDR and QD disintergration mechanisms. Subsequently,

the secondary particle emissions were reproduced through a pre-equilibrium exciton model and the Hauser-Feshbach model for pre-equilirium and equilibrium processes [21].

CoH_3 is used to compute nuclear reactions at relatively low energies. The CoH_3 code was designed based on a development of the Hauser-Feshbach code and a new optical model. The CoH_3 code is not used to produce an evaluated nuclear data library owing to the limited energy for nucleon-induced reactions, 100 MeV [9, 24]. The pre-equilibrium exciton model employed in the various reaction models (CCONE and CoH3) is different; thus, the pre-equilibrium components of the secondary particles reproduced in different codes are different [9]. In this work, I study the photoneutron as a secondary particle emitted via a photonuclear reaction; thus, the status of experimental data on photoneutrons is reviewed in the next subsection.

Typically, reaction cross sections were successfully reproduced by evaluated photonuclear data libraries. These data libraries were benchmarked with the experimental data set obtained with various photon sources including bremsstrahlung, quasi-monoegenetic photons and polarized photons (laser Compton scattering photon). Figure 1.2 shows a sample comparison of photoneutron cross sections of JENDL/PD-2016 and IAEA-2019 with experimental data. Here, the data at NewSUBARU were obtained with polarized photons. The IAEA-2019 data are comparable with the NewSUBARU data. The JENDL/PD-2016 data are lower than the IAEA-2019 data and the experimental data obtained at NewSUBARU.

The energy spectrum of the photoneutron produced via photonuclear interaction was mainly generated using nuclear reaction codes. These codes employed the exciton model and the Hauser-Feshbach statistical model to calculate the energy spectrum. Here, a difference in the exciton models occurred because the exciton codes were implemented in different nuclear reaction codes; thus, the energy spectrum cannot be compared. The energy range was close to the GDR range in which the compound nucleus decay dominates, yielding an isotropic evaporation spectrum,

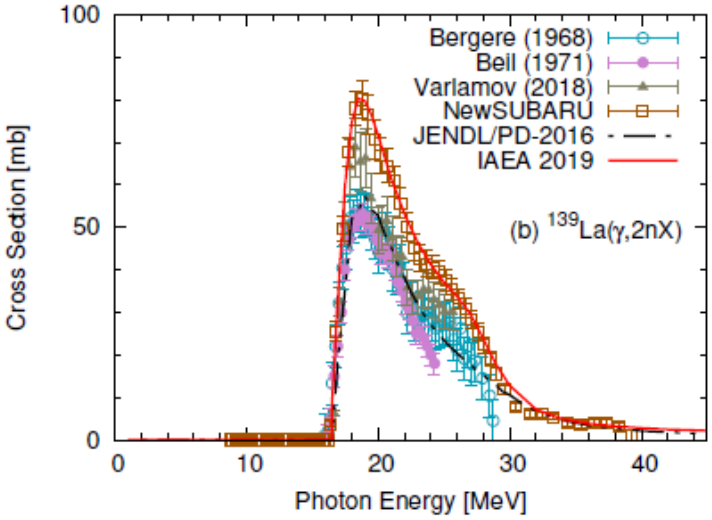

Figure 1.2: Comparison of photoneutron cross sections between the evaluated (JENDL/PD-2016) and experimental data for ^{139}La(γ,2nX) [9].

and all the codes expressed this part similarly [9].

The angular distribution of photoneutrons emitted via the pre-equilibrium process with a high incident photon energy has not been generated in an evaluated photonuclear data library [9].

Today, with the development of electron accelerators and laser techniques, polarized photons can be generated. Only the EMPIRE code used in IAEA-2019 evaluated the new data obtained with polarized photons. The evaluation was performed on data of the photoneutron reaction cross section for ^{59}Co, ^{89}Y, ^{103}Rh, ^{159}Tb, ^{165}Ho, ^{169}Tm, and ^{181}Ta. These reaction cross sections were measured with polarized photons in the GDR region [9].

1.3 Status of experimental data on photoneutrons

In the 1950s, photoneutrons were measured in many experiments using various photon sources [25, 26, 27, 28, 29, 30, 31, 32]. These experiments yielded not only reaction cross sections, but also the energy spectrum and angular distribution of photoneutrons. From previous studies, the energy distribution of photoneutrons emitted in the evaporation process was predicted following the Maxwell distribution [30]. However, high-energy neutrons generated by pre-equilibrium processes are still being studied. Figure 1.3 shows the photoneutron spectrum of the pre-equilibrium process on ^{208}Pb. In Reference [25], Mutchler measured the neutron spectrum using 15 MeV and 14 MeV bremsstrahlung photons and the time-of-flight (ToF) technique. A difference spectrum was determined by subtracting the spectrum obtained at 14 MeV from that at 15 MeV. He determined the high-energy photoneutron spectrum for ^{208}Pb by subtracting the Maxwellian fitting shape from the difference spectrum.

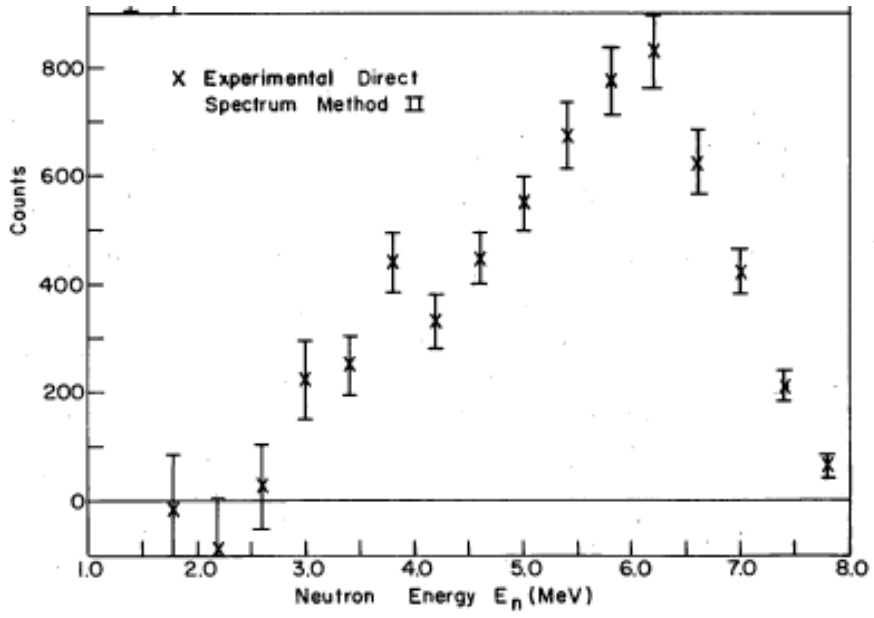

Figure 1.3: High-energy photoneutron spectrum for ^{208}Pb [25].

The angular distribution of photoneutrons was studied by previous studies previously [25, 26, 27, 28, 29, 30] using bremsstrahlung and quasi-monoenergetic photons.

The angular distribution of evaporation photoneutrons was isotropic, while that of photoneutrons emitted in a pre-equilibrium process was anisotropic [33]. The ToF technique and the activation detectors ^{28}Si(n,p) and ^{27}Al(n,p) were employed to detect photonneutrons. Using the activation detectors with detection thresholds of 6 MeV and 4 MeV, the anisotropic photoneutrons emission was obtained. The angular distribution of the anisotropic photoneutron was expressed by $A + Bsin^2(\theta)$ with the polar angle, θ, between directions of the incident photon and detector. The anisotropy parameter B/A was reported for medium-heavy nuclei, for instance, as shown in Figure 1.4 [27]. These experiments were performed with bremsstrahlung and quasi-monoenergetic photons. However, these photon sources contained disadvantages such as a huge background, continuous spectrum, and low intensity. The anisotropy parameter was obtained as an averaged value over the resonance.

With modern laser and accelerator technology, the laser Compton scattering (LCS) technique provides a highly monoenergetic and fully polarized photon source, which can be used for studying photonuclear reactions [34, 35].

By using LCS photons, Horikawa et al. conducted a study [36] to experimentally verify the azimuthal angle (ϕ) anisotropy of neutron emission, predicted by Agodi [33], in three nuclei. The anisotropy of the photoneutron angular distribution of ^{197}Au as a function of $a + bcos(2\phi)$ is shown in Figure 1.5 [36]. Despite interesting results, Horikawa did not obtain the energy spectra at different azimuthal angles.

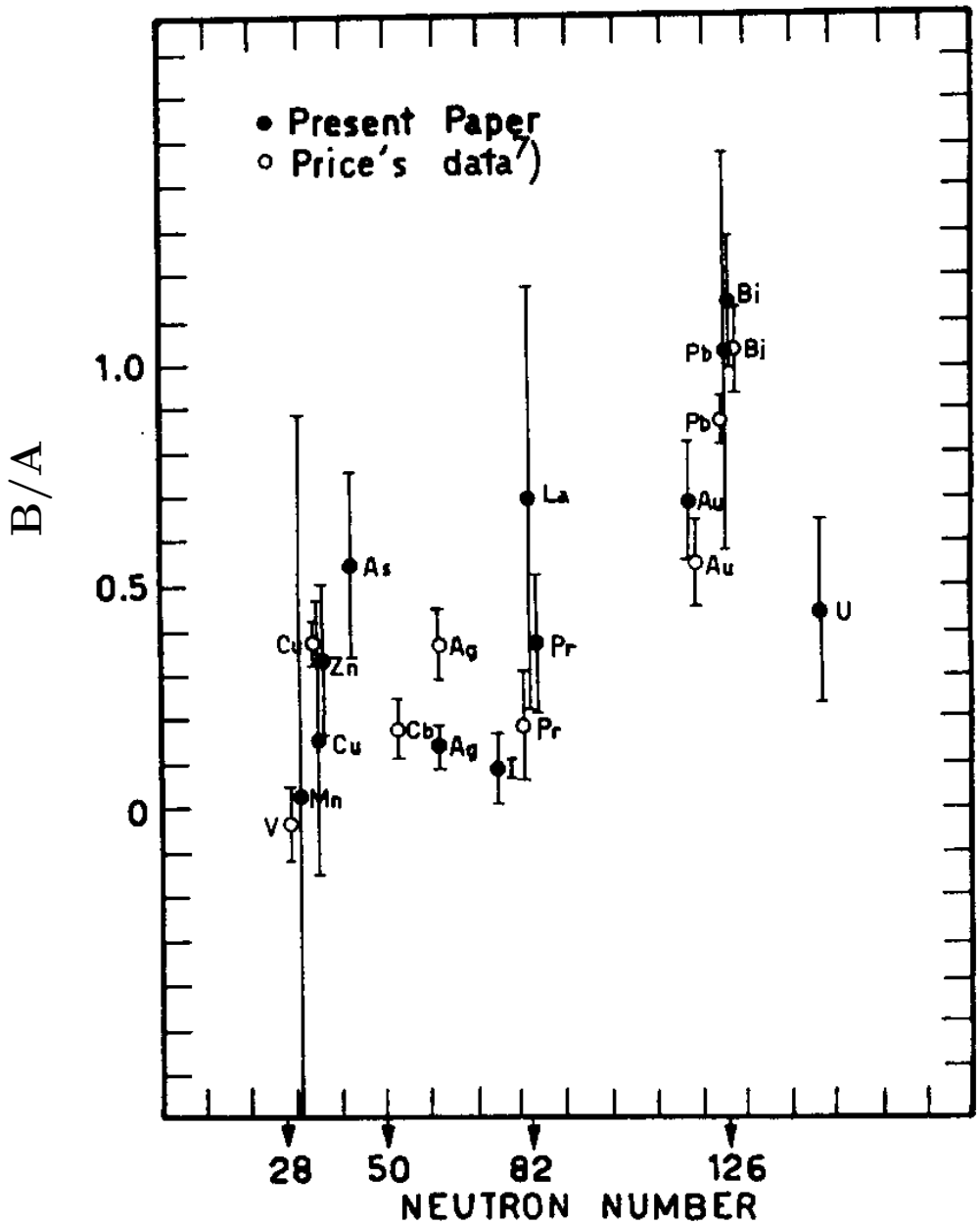

Figure 1.4: Experimental anisotropy, B/A, of fast photoneutrons obtained using a ^{28}Si(n,p) detector; the angular distribution was fitted by A+Bsin$^2(\theta)$ [27].

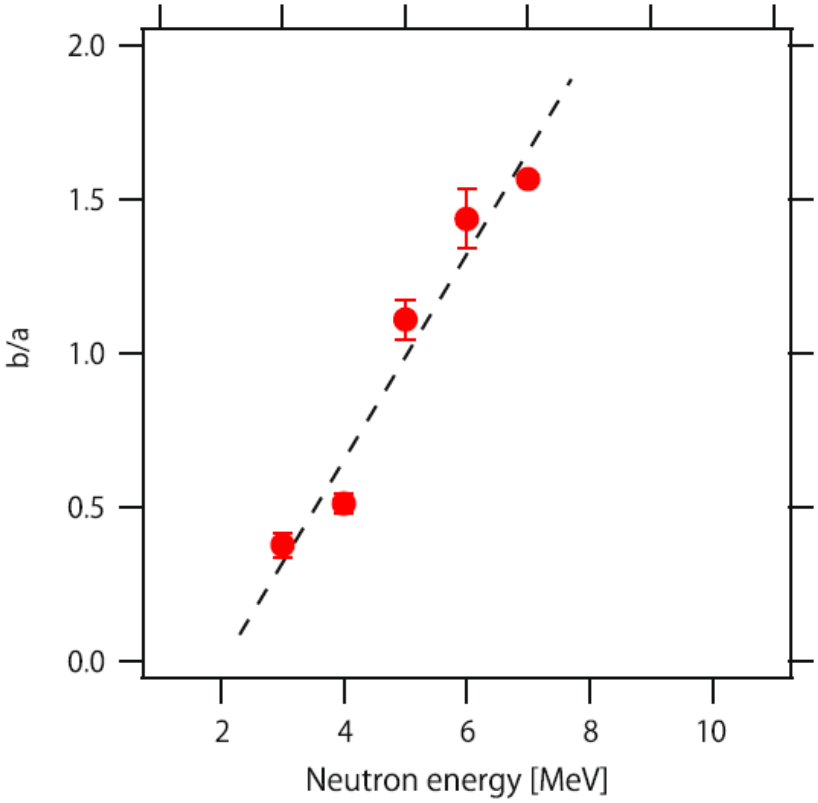

Figure 1.5: Anisotropy, b/a, of the neutron angular distribution as a function of neutron energy for ^{197}Au [36].

In 2019, Kirihara et al. [37] studied the photonuclear reaction on a gold target using 16.6 MeV linearly polarized LCS photons, and reported the energy spectra of photoneutrons as well as their dependence on the polar and azimuthal angles, as shown in Figure 1.6. This result was the first to show the energy distribution of photoneutrons as a function of azimuthal and polar angles. The neutron spectrum as reported in Reference [37] consists of two components: one is the evaporation component, which is distributed in the low-energy range, and the other is the direct component in the high-energy range [37]. Moreover, his work elucidated the dependence of the direct component on the polarization of the LCS photons.

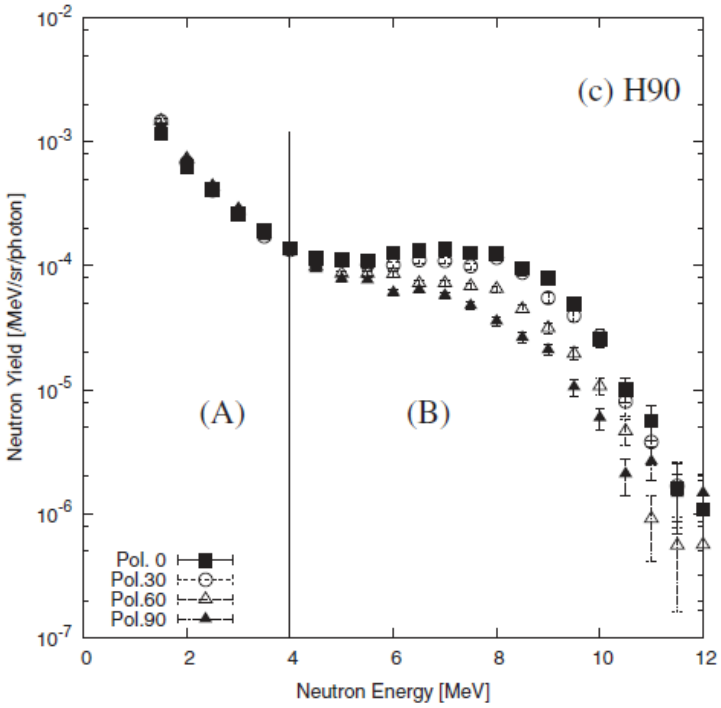

Figure 1.6: Neutron energy spectrum of ^{197}Au(γ,xn) with various polarizations of the LCS photons [37].

1.4 Motivation for this study

As discussed in section 1.3 in relation to the current status of experimental data on photoneutrons, interesting results have been obtained with polarized monoenergetic photons [36, 37]. The findings in Reference [37] indicated that a polarization of photons causes anisotropic photoneutron emission, as shown in Figure 1.6. However, the current nuclear reaction models do not take into account the polarization of photons when reproducing photoneutrons.

For the design of electron accelerators, information on the energy and angular distributions is highly important in radiation shielding calculation. Thus, the current Monte Carlo code, evaluated nuclear data, and nuclear reaction models should be tested for the distributions. The systematic measurement DDX data is quite necessary for this purpose. However, no data are available on DDX at present.

1.5 Objective of this study

This thesis aims to measure the DDX of photoneutrons of the (γ,xn) reaction to (i) reveal the nature of the reaction, (ii) establish the systematic data acquisition of the DDX, and (iii) study its impact on applications.

Recently, monoenergetic polarized photon beams have been identified to have the following advantages: (i) a high intensity of approximately 2×10^6 photons/s, (ii) a narrow energy width of a few percent of the full width at half maximum [9], and (iii) the polarization of the photons. Thus, monoenergetic polarized photons are employed in this research as a potential photon source to provide new experimental data.

For the experiment, I used the monoenergetic linearly polarized photon beam at NewSUBARU BL-01 and the ToF technique. The photoneutrons were obtained using NE213 neutron detectors placed at six laboratory angles.

The experiment aimed to measure the DDX of the (γ,xn) reaction on several targets including common shielding material such as Pb, Au, Sn, Cu, Fe, and Ti. The target mass dependence of photoneutron was discussed though the DDX data obtained using 17 MeV polarized photon. In addition to the target mass dependence, a measurement was performed to discuss the photon energy dependence of the photoneutrons through the DDX data. The photon energies were used 14, 17, and 20 MeV. Moreover, through the DDX data, the following interesting issues related to the photoneutron were addressed: (i) The angular distributions of photoneutrons are parameterized to compare with the previous data for checking consistency. (ii) In order to understand the current status of photoneutron production in particle transport simulation, the DDXs were compared with that from Monte Carlo code, evaluated nuclear data files, and a nuclear reaction model. (iii) The impact of anisotropic high-energy neutrons observed in the experimental neutron spectrum in shielding calculation was demonstrated through the calculation of the leakage dose for a simple shielding structure.

Chapter 2

Experiment

To experimentally study the neutrons produced by photonuclear reactions, experiments were conducted at the NewSUBARU facility in Hyogo, Japan to measure the DDX of photoneutron production. In this chapter, I will introduce the experimental setup, together with explanations of the LCS technique, neutron detectors, targets, electronic system for the measurement of neutron energy as well as background subtraction, and calibration experiment. This chapter supports the analysis method presented in chapter 3 of this thesis.

2.1 NewSUBARU experiment

2.1.1 Laser Compton scattering photons

The LCS technique was employed to generate linearly polarized monoenergetic photon beams. In the LCS technique, high-energy photons are produced from the collisions of high-energy electrons and low-energy laser photons. Figure 2.1 illustrates the LCS technique. The laser photons from the oscillator are guided to the electron ring by mirrors to cause collisions. The linear polarization of the LCS is determined by the polarized laser photons.

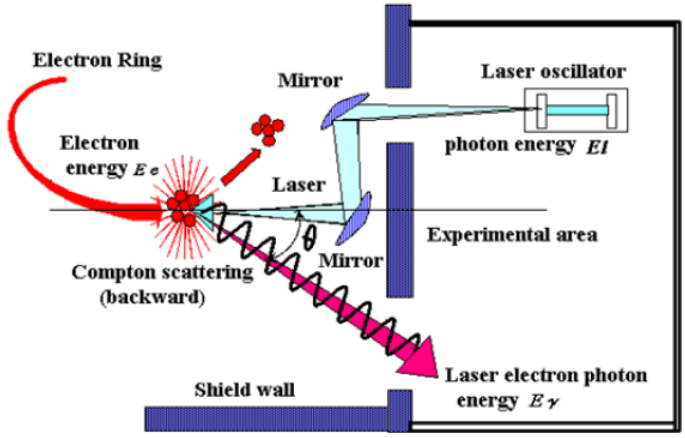

Figure 2.1: Production of laser electron photons at NewSUBARU, Hyogo, Japan [35].

The maximum photon energy is observed at a scattering angle of 180°, which is the angle between the laser photons and backscattered photons, as expressed below [38]:

$$E_{\gamma,max} \approx 4\gamma^2 E_p, \tag{2.1}$$

where

$E_{\gamma,max}$: is the maximum energy of backscatterd photons;

γ : is the Lorentz factor, which is calculated as $\gamma = (1 - v^2/c^2)^{-1/2}$ with the electron velocity v; and

E_p : is the energy of laser photons.

The energy of the LCS photons is determined by the energies of the laser photons and electrons. The intensity of the LCS photons is proportional to both the laser photon intensity and electron beam current.

Table 2.1 lists the parameters of the laser system, electron energy, and maximum (Max.) LCS energy at NewSUBARU. The maximum LCS energy produced using the $NdYVO_4$ system is 39.1 MeV.

Table 2.1: Parameters for the generation of LCS photons.

Electron energy [GeV]	1.0 - 1.5	
Laser wavelength [μm]	CO_2 10.59	$NdYVO_4$ 1.064
Max. LCS energy [MeV]	4.02	39.1

In this study, a 982.4 MeV electron beam was injected in the storage ring. The electrons were circulated at energies of 892.6 MeV, 982.4 MeV, and 1068.8 MeV in the storage ring, which was operated in the single bunch mode. Incident photons with a wavelength of 1.064 μm were generated by a 20 W $NdYVO_4$ laser system and guided to the electron storage ring's straight section. In order to generate the 14 MeV and 20 MeV LCS photons, the electron beam was operated in the decay mode. For producing the 17 MeV LCS photons, the electron beam was operated in the top-up mode. The laser system was synchronized with the bunch of electrons to optimize the collision rate. The laser photons were backscattered and accelerated upon collision with the electrons in the storage ring.

The factor $4\gamma^2$ in Equation 2.1 is the amplification factor, which depends on the energy of the electron beam. In this experiment, electrons were separately circulated at different energies, resulting in different amplification factors and different maximum energies of LCS photons ($E_{\gamma,\mathrm{max}}$) to be used for investigating the dependence of photoneutron production on LCS energy (section 5.4).

2.1.2 Experimental setup

In this study, I performed two experiments at the BL-01 NewSUBARU facility. In the first experiment, the photoneutrons from the (γ,xn) reactions with 17 MeV photons on Pb, Au, Sn, Cu, Fe, and Ti targets were measured at six angles. In the second experiment, the photoneutrons from the reaction on Au, Cu, and Ti targets were measured with 14 MeV, 17 MeV, and 20 MeV photons.

A schematic of the experimental setup is shown in Figure 2.3. A $\lambda/2$ wave plate was placed after the laser generator's output to make the LCS photons horizontally polarized, with respect to the floor. The collision point of the $NdYVO_4$ laser with the electrons was where the LCS photons were produced. The photons scattered at 180° were guided to optics Hutch 2 via optics Hutch 1 of BL-01 NewSUBARU. The width of the high-energy photon beam was controlled by two sets of collimators placed before optics Hutch 1 and Hutch 2, and the inner collimators' diameters were 3 mm and 2 mm, corresponding to C1 and C2 in Figure 2.3, respectively. Through numerical simulation, the energy width of the photon beam was evaluated as ± 0.2 MeV ($\pm 1\sigma$), as shown in Figure 2.2. In Hutch 2, the detectors were set

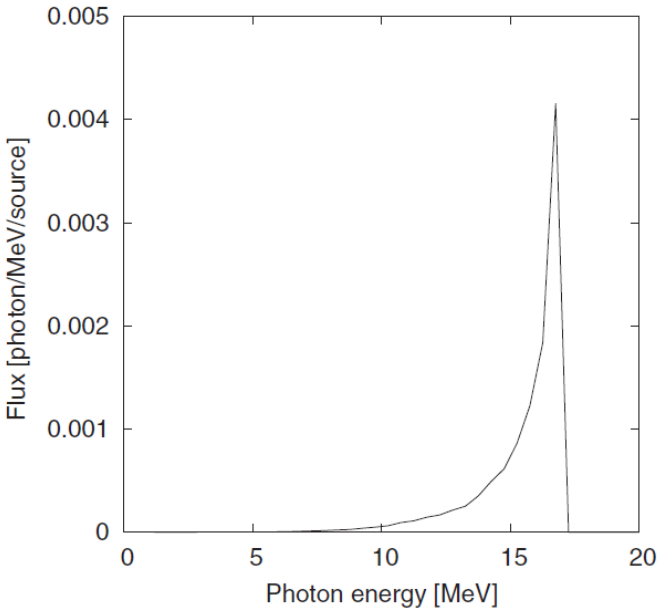

Figure 2.2: LCS photon spectrum obtained from simulation [37].

up to evaluate the rate of LCS photons and measure the neutrons produced from photonuclear reactions.

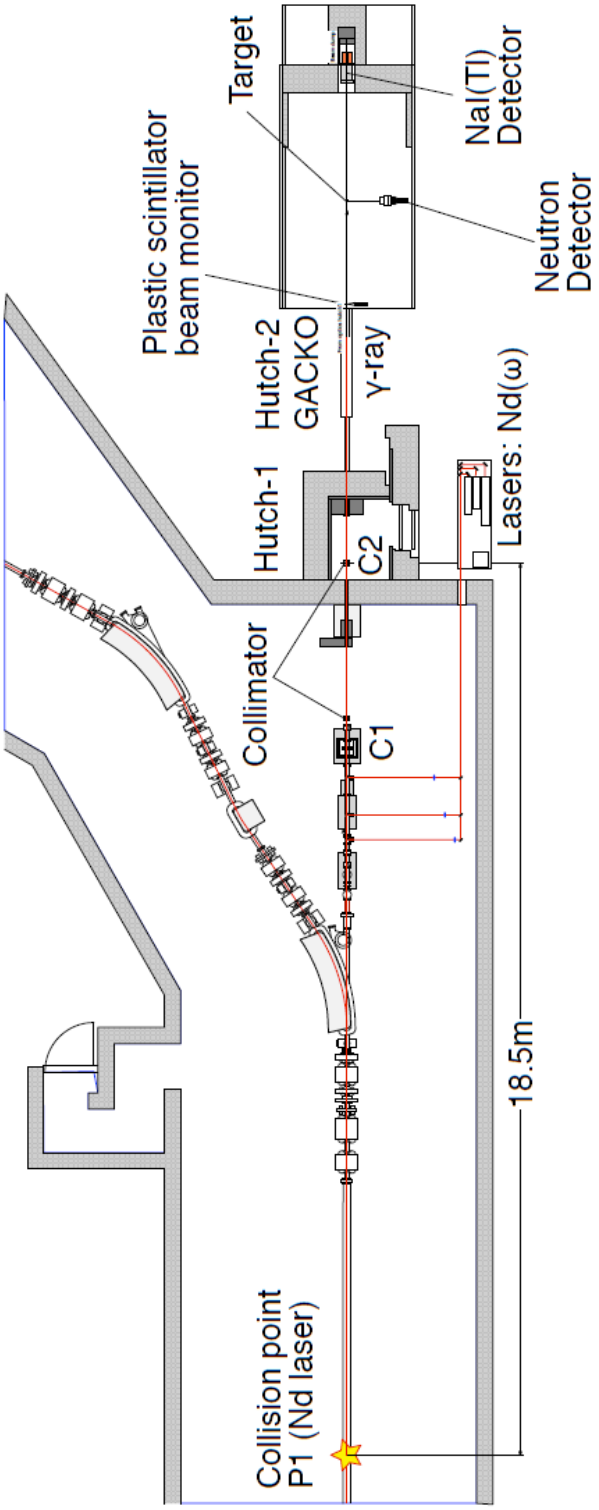

Figure 2.3: Overview of the BL-01 NewSUBARU facility.

Figures 2.4 and 2.5 show the setup of a target and detectors in Hutch 2 for the first experiment. In addition, Figure 2.6 shows the setup for the second experiment. The difference between the two experimental setups was in the number of neutron detectors employed to detect photoneutrons. Small neutron detectors were added in the second experiment; however, the photoneutrons detected by the small neutron detectors are not reported in this thesis.

When the LCS photons entered Hutch 2, they were transmitted through a plastic scintillator, the thickness and surface area of which were, respectively, 0.5 cm and 5×5 cm^2 functioning as a monitor of LCS intensity before the photons approached the target. Prior to data acquisition, a silicon pixel imager was placed at the target position to confirm the alignment and spot size of the LCS beam. LCS photons passing through the target were dumped on a cylindrical $15.04^{\phi}\times12.5^{t}$ cm NaI(Tl) detector placed 211 cm downstream of the target. This NaI(Tl) detector was used as an LCS beam absorber as well as a beam intensity monitor for beam preparation.

Only a fraction of the LCS photons interacted with the nuclei inside the target via photonuclear reactions. The irradiation of the target produced secondary particles. The secondary particles were charged particles (electron, positron, proton, or alpha particles) and neutral particles (neutron or photon). The neutrons induced by photonuclear reactions in different targets were the main object in this study. These neutrons approached the cylindrical detectors filled with the organic liquid scintillator NE213 (a product of Nuclear Enterprises Ltd., U.K., or equivalent). These neutron detectors were prepared with both a diameter and thickness of 12.7 cm and placed in positions surrounding the target. The NE213 scintillator was filled in a cylindrical aluminum container with 1-mm thickness at the side and bottom surface and a 13-mm-thick Pyrex glass window at the other bottom surface allowing the transmission of scintillation photons from the NE213 scintillator to the photomultiplier tube (PMT). To study the angular dependence of neutron production, these detectors were placed at 150°, 120°, 90°, 60°, 30° (horizontally),

and 90° (vertically) with respect to the direction of the incident LCS photon beam. The six detectors were mounted on a mechanical support made from aluminum, as shown in Figure 2.5. Table 2.2 presents the labels, angles, and distances of 6 neutron detectors from the target for two experiments. The distances between the centers of the target and each neutron detector were determined so that the ToF method could be applied to determine the neutron energy. The θ in Table 2.2 represents the angle between the directions of the incident LCS photons and the emitted neutrons.

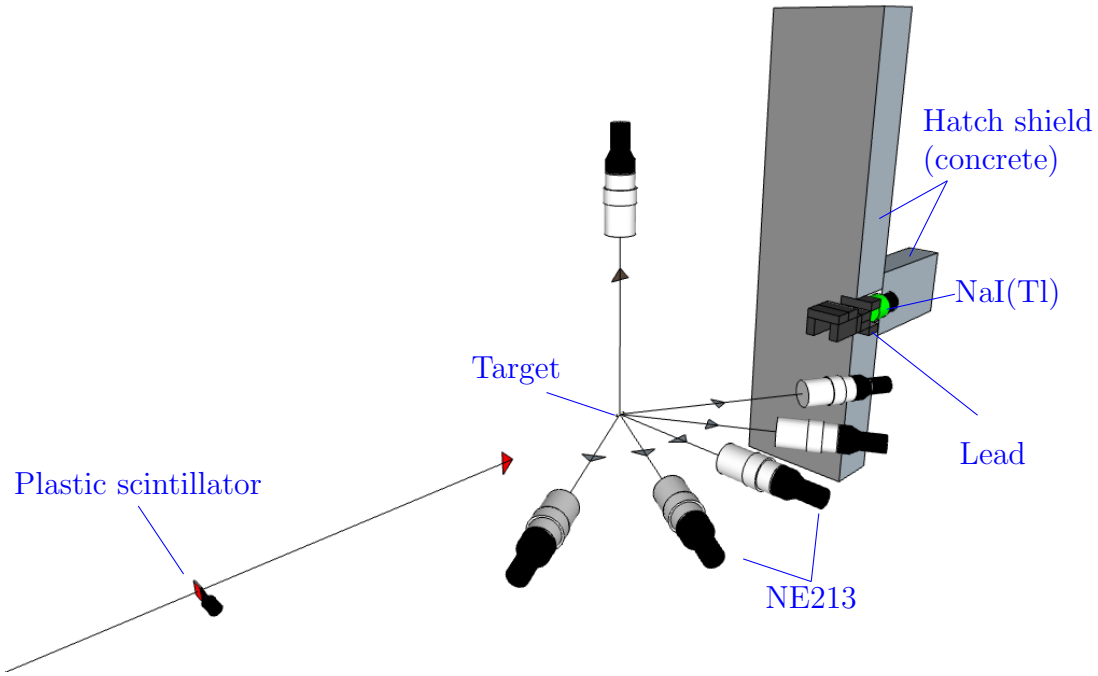

Figure 2.4: Experimental setup. The LCS photon beam passed through a plastic scintillator (drawn in red), approached the target, and produced photoneutrons detected by six NE213 detectors (drawn in white color) surrounding the target. One NaI(Tl) detector (drawn in green) was used as a photon absorber and beam intensity monitor in beam preparation.

Figure 2.5: Photograph of the first experimental setup in Hutch 2, NewSUBARU, BL-01 facility.

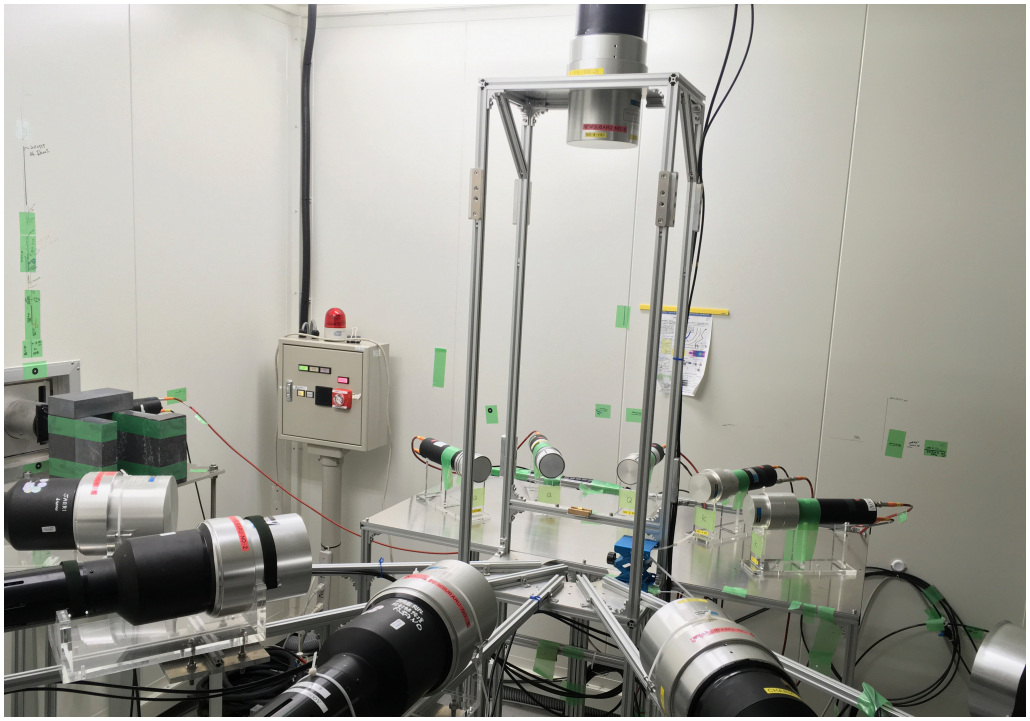

Figure 2.6: Photograph of the second experimental setup in Hutch 2, NewSUBARU, BL-01 facility.

Table 2.2: Labels, angles, and distances from the target to the centers of 6 neutron detectors.

Detector label	θ[°]	Flight path [cm]	
		1st experiment	2nd experiment
H150	150 (horizontal)	86.35	93.65
H120	120 (horizontal)	75.85	72.75
H90	90 (horizontal)	65.35	68.15
H60	60 (horizontal)	74.35	75.25
H30	30 (horizontal)	93.85	97.65
V90	90 (vertical)	86.85	86.25

The target was made of different materials, including ^{nat}Pb, Au, ^{nat}Sn, ^{nat}Cu, ^{nat}Fe, and ^{nat}Ti, and each material was separately placed on the pathway of the LCS beam for measurement. The targets mainly include the materials used in radiation shielding (^{nat}Pb, ^{nat}Sn, ^{nat}Cu, ^{nat}Fe, and ^{nat}Ti), and the measurement with the Au target is included because it consists of a single isotope. The target's thicknesses ranged from 1 to 4 cm depending on the attenuation of LCS photons and the yield of neutrons. The calculation of the LCS photon attenuation will be presented in section 3.5. A diameter of 1 cm was chosen considering the accuracy of the target alignment and the LCS beam spot size. Table 2.3 presents the materials, diameters, thicknesses, photon attenuation factors and purities of the targets used in this study.

Table 2.3: Materials, diameters, and thicknesses of targets.

Target	Diameter [cm]	Thickness [cm]	Photon attenuation factor			Purity [%]
			14 MeV	17 MeV	20 MeV	
^{nat}Pb	1.0	1.0		0.73		99.99
^{197}Au	1.0	1.0	0.51	0.60	0.62	99.99
^{nat}Sn	1.0	2.0		0.69		99.99
^{nat}Cu	1.0	2.0		0.75	0.71	99.99
^{nat}Fe	1.0	2.0		0.80		99.50
^{nat}Ti	1.0	4.0		0.78	0.79	99.90

2.1.3 Data acquisition system

The photonuclear reactions on the targets produced different types of secondary particles, including neutrons, γ-rays, and charged particles. The charged particles could not reach the NE213 neutron detectors because of their short ranges. Therefore, each NE213 neutron detector detected not only neutrons but also γ-rays produced in the target. Those γ-rays were the background. An event-by-event data acquisition (DAQ) system was assembled with the ToF function to measure the neutron energy and with the pulse shape discrimination (PSD) function to distinguish neutrons and γ-rays. The neutrons at higher energy traveled the same distance for a shorter time, and the ToF technique enabled the measurement of traveling time from the target to the neutron detector, which was then used to determine the neutron energy. The difference in interactions of neutrons and γ-rays on the NE213 scintillator resulted in the different pulse shapes, corresponding to neutron and γ-ray events, output from the PMTs. The PSD technique allowed the separation of neutrons and γ-rays. The difference between the pulses of neutrons and γ-rays was in the tail parts. Figure 2.7 shows an example taken from Reference [32].

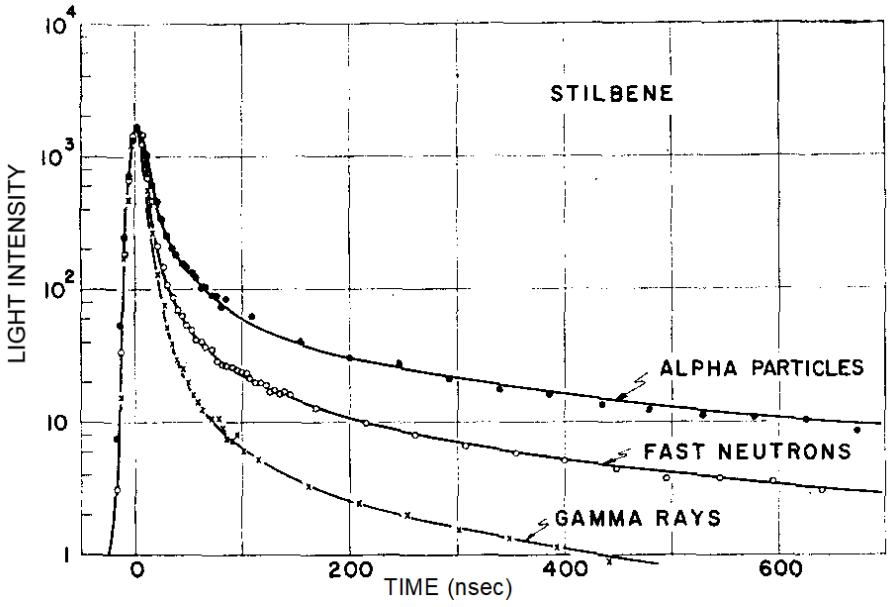

Figure 2.7: Pulses of different radiations obtained upon interaction with an organic scintillator [32].

A schematic diagram of the DAQ system for each neutron detector is shown in Figure 2.8. There were two main parts: the upper part was set up to measure the pulse height distribution as well as PSD, and the lower part was used for the ToF measurement. Each signal formed at the PMT anode of the NE213 detector was divided into three small signals using signal dividers (Div): two signals were, respectively, utilized for total-charge and tail-charge integration by using a charge-to-digital convertor (QDC: Nikiglass A3200), and the remaining signal was used to create a trigger. The remaining signal was fed into a constant-fraction discriminator (CFD: ORTEC 935), which generated a timing signal. The timing signal was fed into a four-fold-one-veto module (4F1V: Technoland N-TM 103), together with the demultiplied radio-frequency (RF) signal, to create a coincidence trigger. This coincidence trigger was fed to a gate generator (GG: Kaizu works 1500) to output a gate signal with a pulse width of 400 ns.

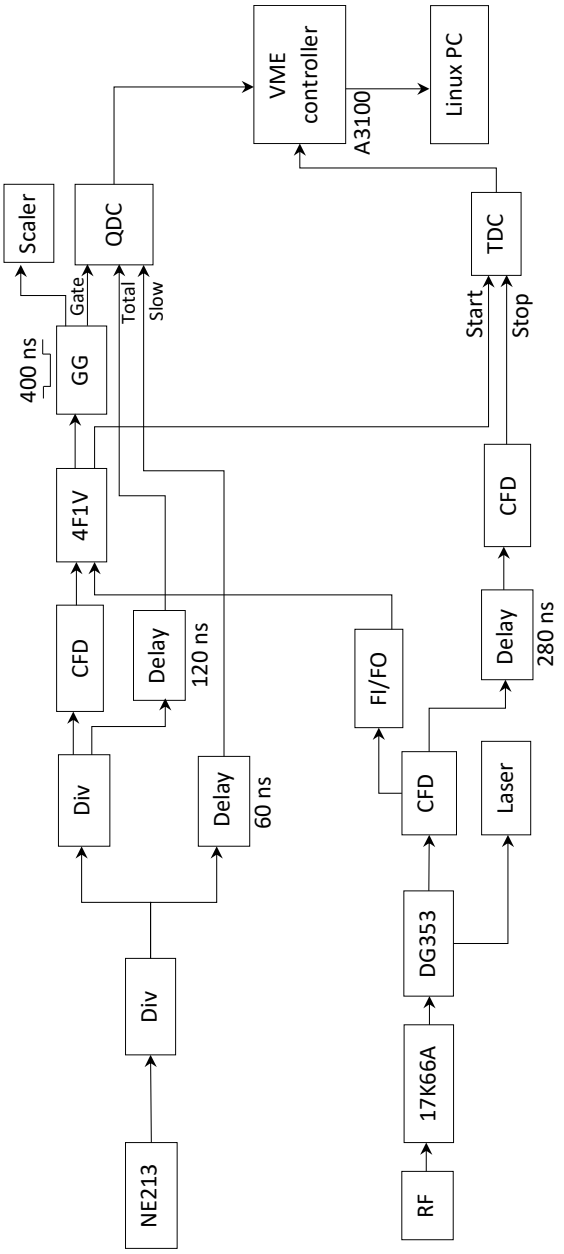

Figure 2.8: Schematic diagram of the data acquisition system.

Figure 2.9 shows the pulse processing for PSD using the DAQ system. The QDC integrated the total and tail charges from two divided signals, which were, respectively, delayed by 120 ns and 60 ns by using cable delay modules (Delay: Repic with fixed delay) within 400 ns.

The DG353 output signal was used for enabling the laser emission, and coincidence trigger, together with the signal from each NE213 detector, for ToF measurement. The signal was prepared from the RF signal used for controlling electron bunches in the storage ring, with the frequency reduced by 1/19800 times with a demultiplier (17K66A) to match the operating frequency of the laser generator and a delay applied for the coincidence trigger at the 4F1V module using DG353 (Stanford Electronics). The coincidence signal from the 4F1V module and the delayed beam signal were, respectively, fed as start and stop signals to the time-to-digital converter (TDC: Nikiglass A3300).

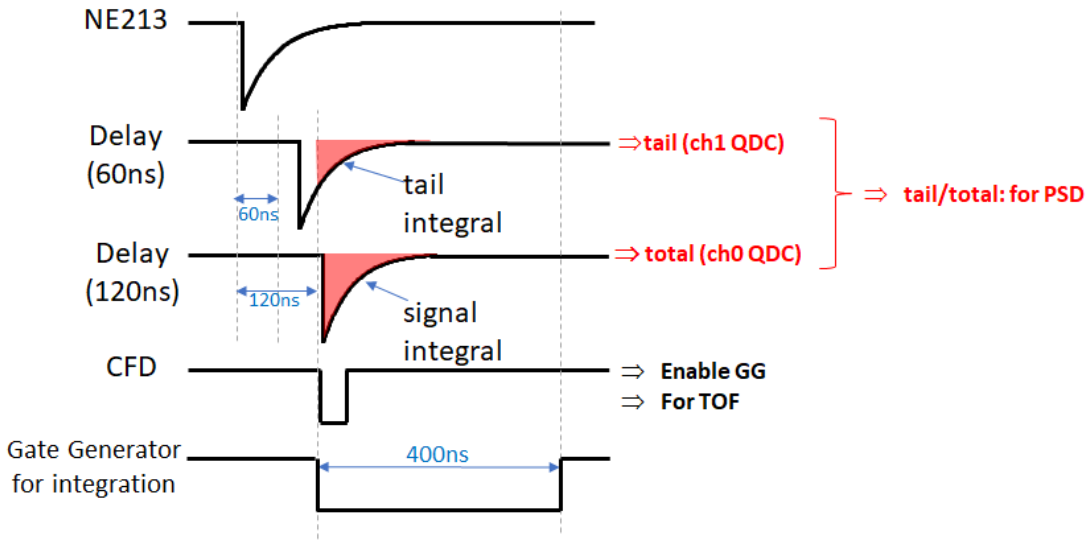

Figure 2.9: Pulse processing for PSD.

Figure 2.10 shows the pulse processing for the ToF method. After a laser photon was generated, it traveled a distance of L_1 in time L_1/c to reach the collision point. After the laser photon is backscattered at the collision point, the LCS photon traveled a distance of L_2 before approaching the target. After interaction at the target, the neutron was slower than the photon, and the traveling time of the photon from

the target (t_γ) to the neutron detector can be obtained from the flight path. To determine the traveling time of the neutron from the target to the neutron detector, I computed the time difference between the photon and neutron $t_{n-\gamma} = T_\gamma$ - T_n by using a delayed RF signal. The traveling time of the neutron is $t_n = t_\gamma + t_{n-\gamma}$.

The QDC and TDC modules were based on the Versa Module Europa (VME) standard. They could be accessed from a VME controller connected to a computer running in Linux (Linux PC).

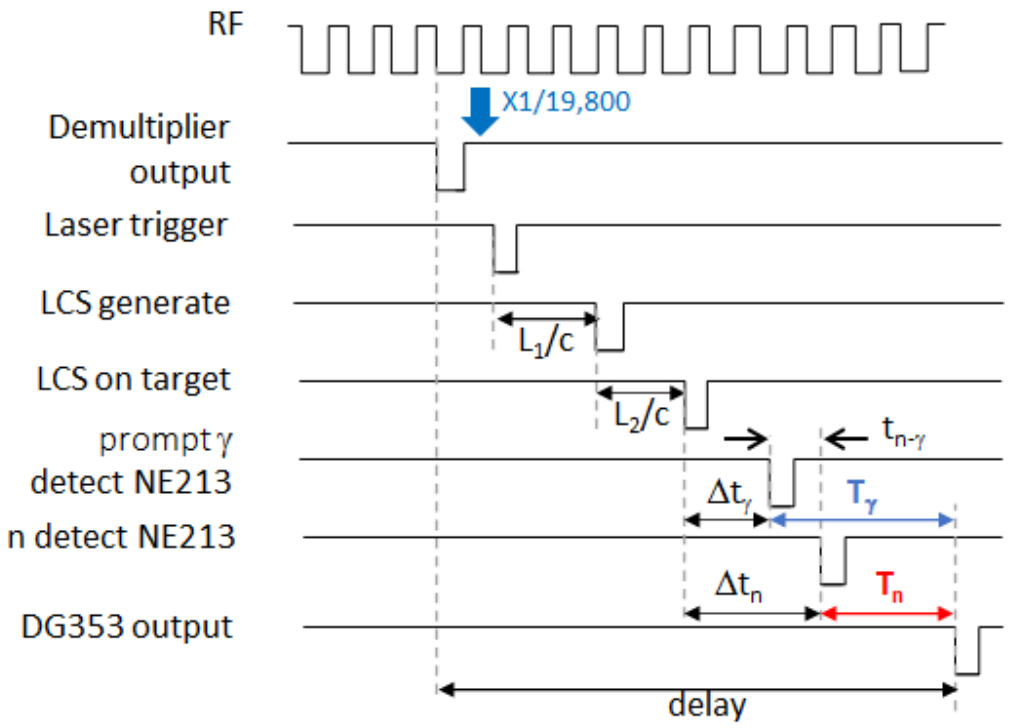

Figure 2.10: Pulse processing for the ToF method. L_1 is the distance from laser to the the collision point in Figure 2.5. L_2 is the distance from the collision point to the target. Δt_γ and Δt_n are the traveling times of γ-rays and neutrons, respectively, from the target to the NE213 detector.

2.2 Detection efficiency determination

2.2.1 ^{252}Cf fission neutron measurement

Before measuring the photoneutrons with the LCS photons, the neutron detection efficiency was determined using a ^{252}Cf neutron source. The experimental setup shown in Figure 2.11 was used to measure fission neutrons from the ^{252}Cf source, the radioactivity of which was 3.7 MBq. The source was placed at the target position, and six neutron detectors were placed at the same positions as in the photonuclear measurements mentioned in section 2.5. The spontaneous fission of ^{252}Cf emits prompt γ-rays and neutrons. A plastic scintillator was placed on the ^{252}Cf source to detect the γ-rays as a trigger, and the six neutron detectors detected neutrons. In the ToF measurement, the stop signal was the trigger signal generated by the plastic scintillator detector.

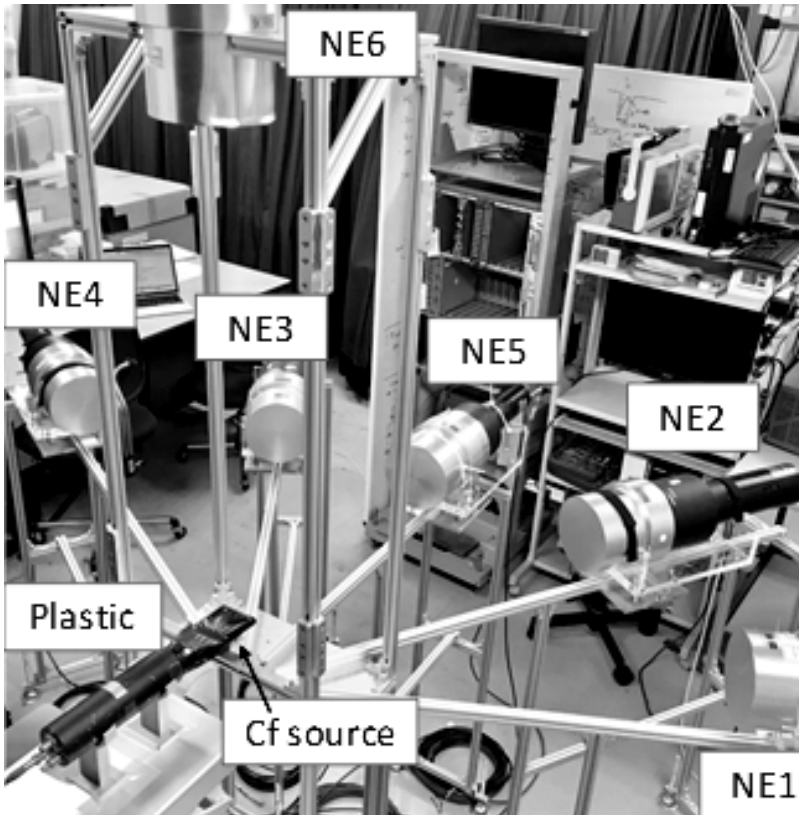

Figure 2.11: Experimental setup for ^{252}Cf measurement.

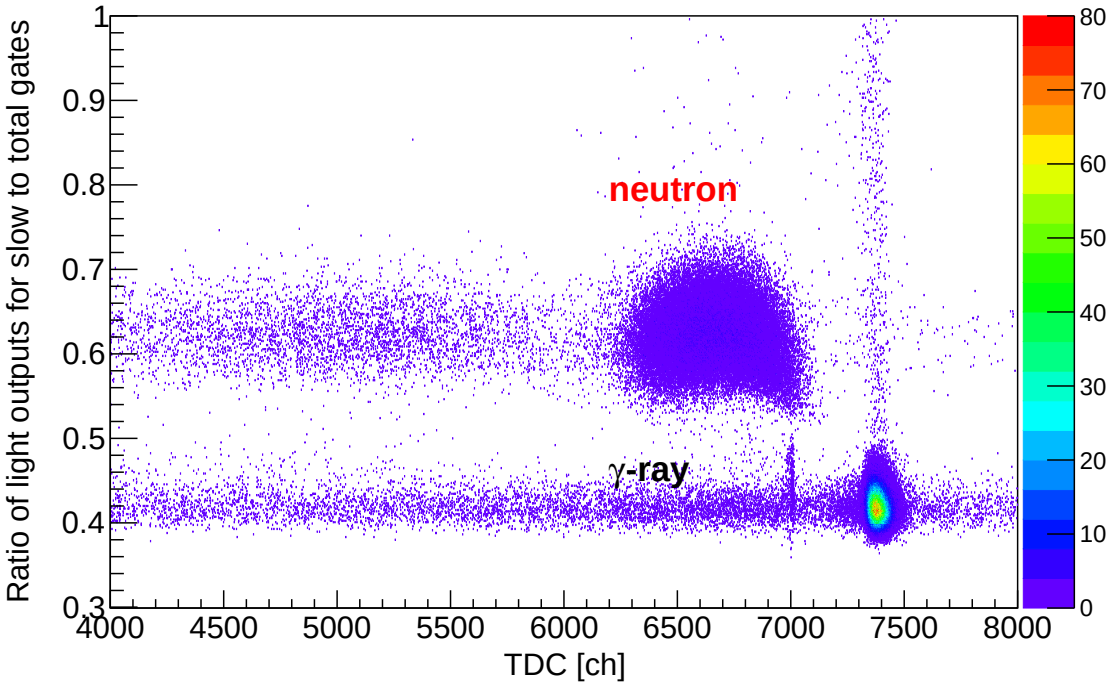

(a) Neutron-gamma separation

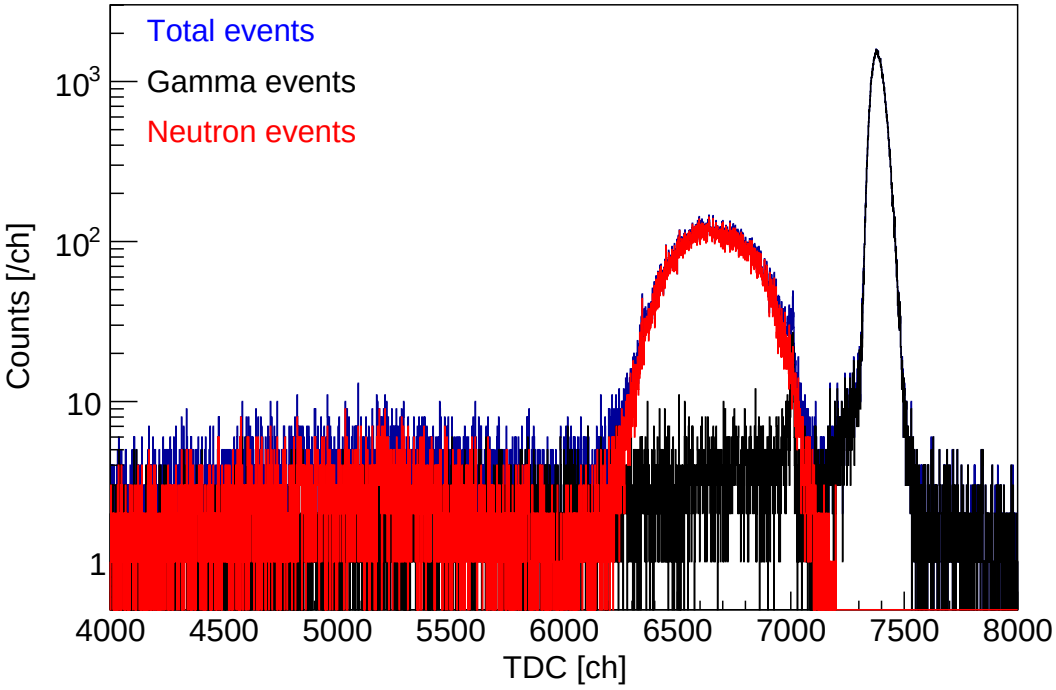

(b) ToF of neutrons and γ-rays from ^{252}Cf

Figure 2.12: Neutron and gamma events measured from ^{252}Cf.

Using the PSD technique, neutron events were distinguished from gamma events, as shown in Figure 2.12a. This separation was realized by determining the ratio of light outputs for slow and total gates, which will be explained in section 3.3.1.

Figure 2.12b shows the neutron and gamma time spectra obtained using the PSD and the ToF techniques. Neutron events in the range of 6000 ch – 7100 ch are fission neutrons from the Cf source. Neutron events observed in the range below 6000 ch could be scattering neutrons. Finally, using the PSD and ToF techniques, the fission neutron spectrum was obtained without considering the neutron detection efficiency, as shown in Figure 2.13. This demonstrates that the DAQ and detector system can be employed to measure the photoneutrons. Moreover, these spectra will be used in section 3.7 to determine the neutron detection efficiency.

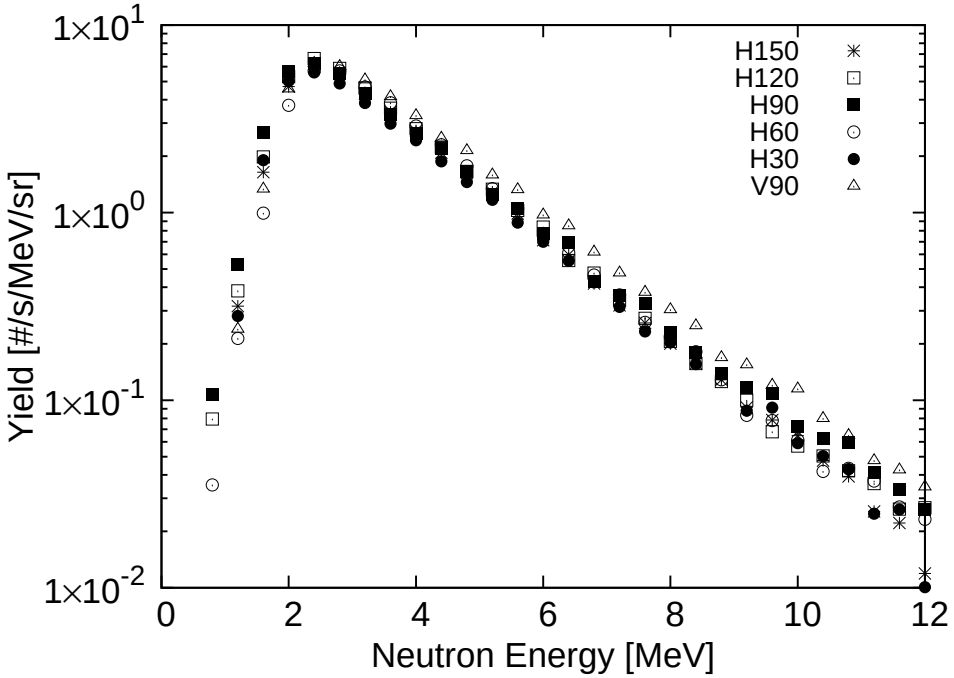

Figure 2.13: Neutron spectra obtained by the six detectors for the ^{252}Cf neutron source.

2.2.2 Measurement of gamma sources

The γ-rays of ^{137}Cs, ^{60}Co, and ^{22}Na standard sources were used to determine biases for analyzing data. Table 2.4 lists the values of high voltages that were applied to the NE213 detectors and Compton edge channels for ^{137}Cs, ^{22}Na, and ^{60}Co. Figure 2.14 displays the Compton edges and Compton peaks obtained on the H150 detector as blue and red dotted lines, respectively. The Compton edges were determined by multiplying the value of the channel corresponding to the Compton peak and the f-factor, as indicated in Table 2.5 [39, 40]. The Compton edge was located through the following procedures: (i) determine the maximum counts at the Compton peak; (ii) multiply this count value with the f-factor, where the result was the count at the Compton edge channel; and (iii) locate the channel where the count is equal to the count obtained in step (ii); this channel was determined as the Compton edge.

Table 2.4: Values of high voltages applied to NE213 detectors and Compton edges (in ADC channel) of ^{137}Cs, ^{60}Co, and ^{22}Na.

Detector label	High voltage [V]	Compton edge [ch]		
		^{137}Cs	^{22} Na	^{60}Co
H150	- 1700	316	596	660
H120	- 1800	341	654	726
H90	- 2790	202	315	337
H60	- 2250	175	323	354
H30	- 1900	291	507	554
V90	- 2800	283	482	525

Table 2.5: Values of Compton edges (in MeVee) and f-factors of ^{137}Cs, ^{60}Co, and ^{22}Na.

Gamma source	Compton peak [MeVee]	f-factor
^{137}Cs	0.5	0.449
^{60}Co	1.06	0.303
^{22}Na	1.15	0.768

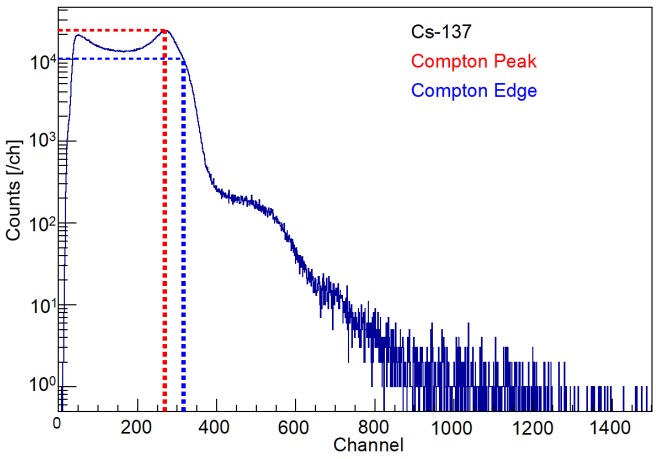

(a) ^{137}Cs

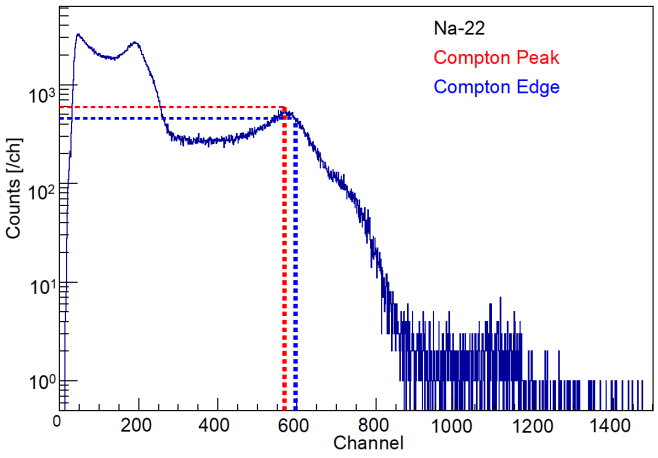

(b) ^{22}Na

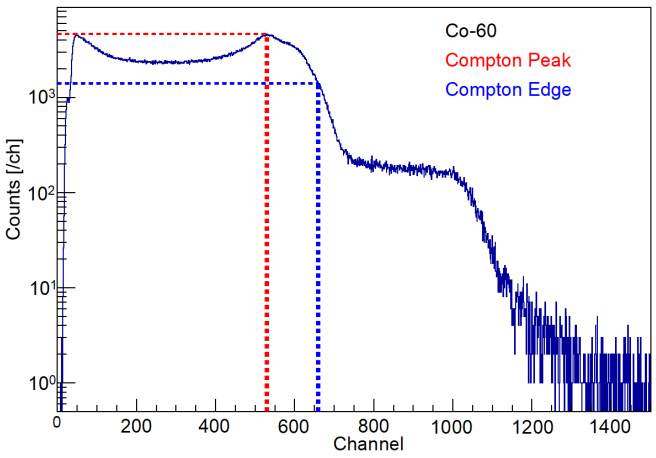

(c) ^{60}Co

Figure 2.14: ^{137}Cs, ^{22}Na, and ^{60}Co spectra used for determining Compton edges.

2.3 Preparation of data acquisition runs

2.3.1 Collimator alignment

To collimate the photon beam at the center of the target, collimators C1 and C2, as shown in Figure 2.3, were set at positions with values of X and Z for two experimentss which are reported in Table 2.6. The positions of C1 and C2 were selected to maximize the number of LCS photons obtained on the NaI(Tl) detector. This was to verify that the intensity of the LCS photons was the highest. A silicon pixel imager, MiniPIX (AVACAM, model MNXTXS-XPx181116), was placed behind the target to confirm the spot of the LCS photon beam. The setup for measuring the spot is displayed in Figure 2.15.

Table 2.6: Positions of collimators C1 and C2.

	X [mm]	Z [mm]
	1st experiment	
C1	-11765	-14200
C2	-1741	-14005
	2nd experiment	
C1	4055	-31416
C2	-3186	-13877

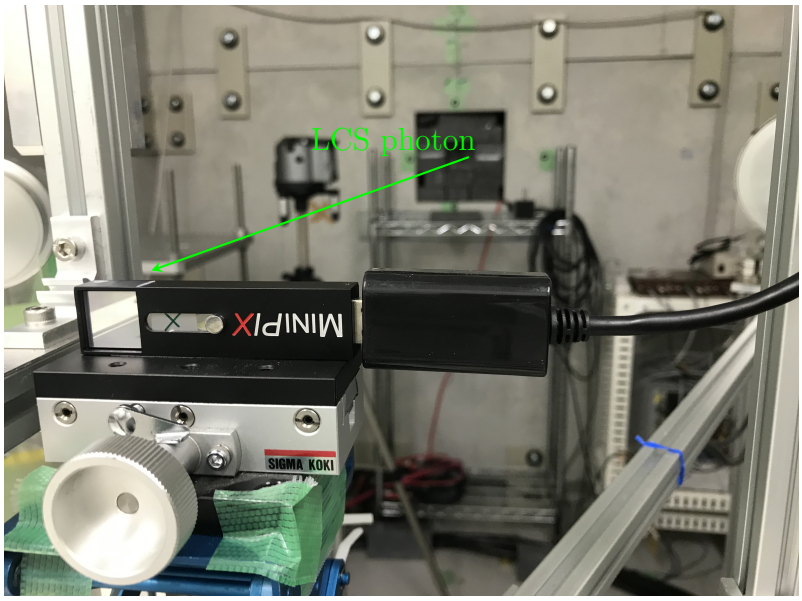

Figure 2.15: Setup for measuring the spot of the LCS photon beam.

Figure 2.16 shows the spot of the LCS beam without a target, where the gray color indicates the profile of the beam. Figure 2.17 illustrates the spot of the LCS beam obtained after placing a target, 1 cm in diameter, on the holder. The shadow region was a scan of the target. The two spots were scanned by the MiNiPIX imager as mentioned above.

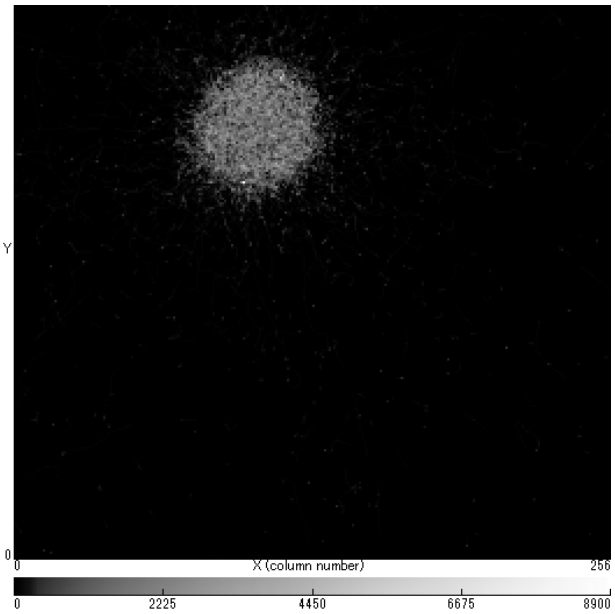

Figure 2.16: Profile of the LCS beam without a target.

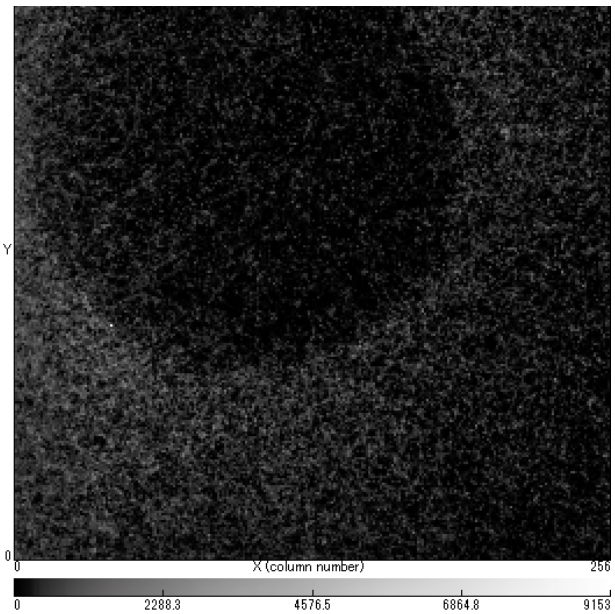

Figure 2.17: Profile of the LCS beam with a target.

2.3.2 Timing adjustment

To adjust the timing for the DAQ, an RF signal (508 MHz) was reduced by using the 17K66A module. The reduced signal (25 kHz) was guided to the DG535 module to be delayed for triggering the DAQ and laser system. The DG535 module provides four delay output channels, A, B, C, and and D. Timing adjustment is expressed in Figure 2.18, and value of T, 85 ns, was set in the DG535 module. Numerical values of the delay time, Δt_A, Δt_B, Δt_C, and Δt_D, are reported in Table 2.7. Signals from the B and D channels were used to trigger the laser system and create a stop signal for ToF measurement, respectively.

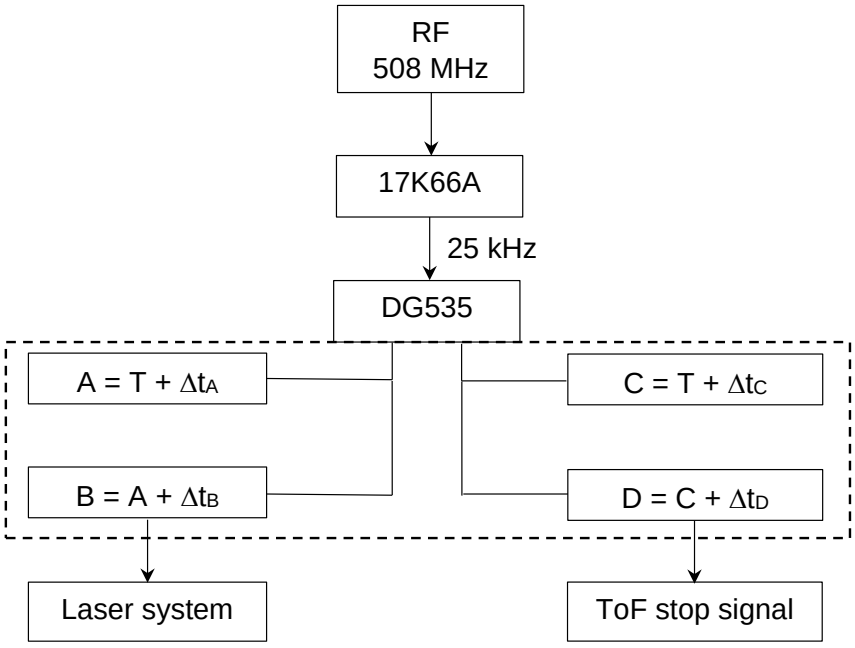

Figure 2.18: Timing adjustment for the laser system and ToF measurement.

Table 2.7: Values of delay time in ns unit.

Delay time [ns]	Δt_A	Δt_B	Δt_C	Δt_D
1st experiment	367	700	2420	100
2nd experiment				
14 MeV	3420	0	5020	0
17 MeV	3460	0	5020	0
20 MeV	3420	0	5020	0

2.3.3 Calibration of NaI(Tl) and the PLS detectors

The LCS photons were counted using NaI(Tl) and plastic scintillator (PLS) detectors. Figure 2.19 shows spectra obtained using the NaI(Tl) and the PLS detectors. Measurements were performed with different powers and different currents, (0.9 W; 2.85 mA) and (23.8 W; 30 mA). To reduce the intensity of the LCS photons approaching the NaI(Tl) detector, a lead block 10 cm in thickness was placed behind the PLS. Red spectra indicate the pulse height spectra containing the sum of events from the LCS photons, bremsstrahlung photons (Brem), and background (BG). Events from bremsstrahlung photons and background are displayed in magenta, and those from background only are displayed in black. The red spectra were obtained under the operation of the laser system and storage ring. To observe the magenta spectrum, the laser system was turned off. The red spectra obtained with (30 mA; 23.8 W) indicate that the number of LCS photons was significantly higher than that obtained with (2.85 mA and 0.9 W). These statistics were sufficient for photoneutron measurement.

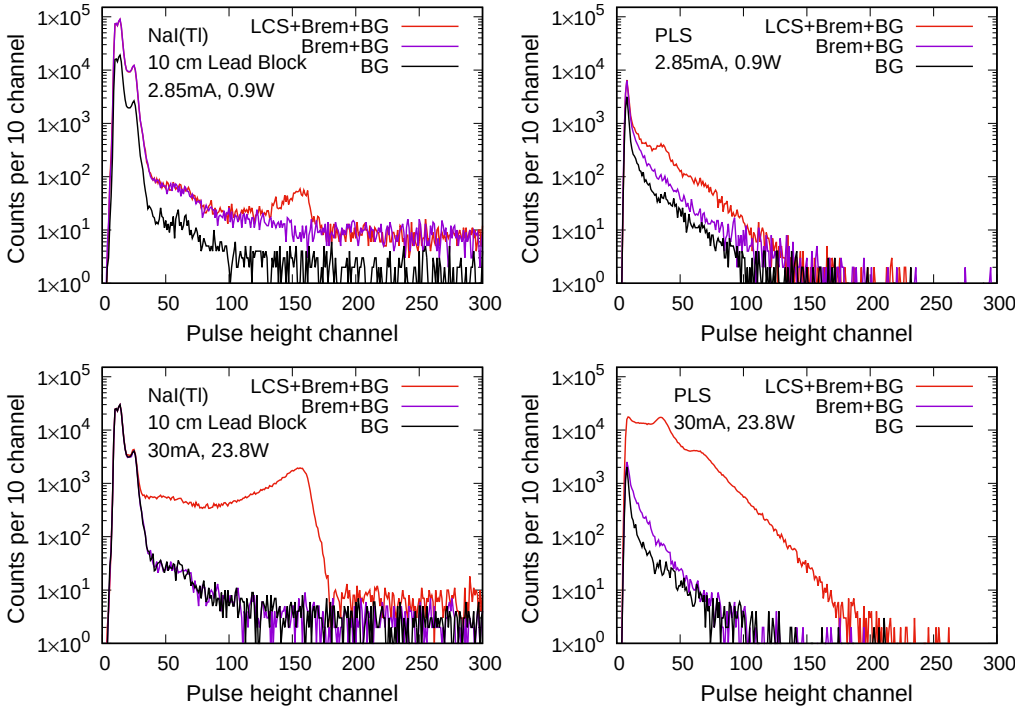

Figure 2.19: Spectra measured using the NaI(Tl) and PLS detectors.

2.3.4 Data acquisition runs

Table 2.8 and Table 2.9 present information on the beam current, laser power, and measurement time for each data acquisition run in two experiments. Data acquisition for each target using 17 MeV photons was performed for the time periods reported in Table 2.8 and Table 2.9. For 14 MeV and 20 MeV, data acquisition was performed 2 or 3 times to obtain sufficient statistics because the beam current was not stable under the operation of the storage ring in decay mode.

Table 2.8: Laser power, beam current, and measurement time for the first experiment using 17 MeV photons under operation in the top-up mode.

Target	Current [mA]	Power [W]	Time [min]
Pb	30.0	23.5	125.30
Au	30.0	23.5	120.74
Sn	30.0	23.5	119.71
Cu	30.0	23.5	119.51
Fe	30.0	23.5	119.52
Ti	30.0	23.5	120.21

Table 2.9: Laser power, beam current, and measurement time for the second experiment.

Target	Current [mA]	Power [W]	Time [min]
	E_γ=14 MeV, decay mode		
Au	23.21	24.27	59.97
	23.10	25.00	60.00
	E_γ=17 MeV, top-up mode		
Au	25.16	23.50	113.19
Cu	25.10	23.50	53.49
Ti	25.26	23.50	90.01
	E_γ=20 MeV, decay mode		
Au	22.91	23.7	18.52
	22.71	23.7	89.30
	22.71	24.0	74.35
Cu	23.40	24.5	59.05
	22.74	24.0	60.00
	23.03	23.9	60.00
Ti	23.04	24.0	60.00
	23.01	24.0	60.00
	22.67	23.5	60.00

Chapter 3

Data analysis

After the data acquisition runs described in Chapter 2, the data set was stored in a Linux PC with the file format of the A3x00 system. In this format, the data set includes both neutron and gamma events which were stored in the QDC and TDC modules. Each module consists of 16 channels. This data set was analyzed event by event.

In this chapter, the analysis of the experimental data set is presented in the following sections:

3.1 Overview of data analysis

The DDXs of photo-neutrons were obtained from the following equation:

$$\frac{\mathrm{d}^2\sigma}{\mathrm{dEd}\Omega} = \frac{\mathrm{Y(E)}/\eta(\mathrm{E})}{\mathrm{N}\cdot(\tau\cdot\phi)\cdot\Omega\cdot\varepsilon(\mathrm{E})\cdot\Delta\mathrm{E}}, \tag{3.1}$$

$$\mathrm{N} = \frac{\frac{\mathrm{mN_A}}{\mathrm{A}}}{\pi \mathrm{r}^2}, \tag{3.2}$$

$$\Omega = \frac{\pi(\frac{\mathrm{a}}{2})^2}{\mathrm{l}^2} \tag{3.3}$$

where

Y(E) is the neutron counting spectrum, E is the neutron energy [MeV],

A is the atomic mass number of the target [g/mol],

r is the radius of the target [cm] and equal to 0.5 cm,

m is the weight of the target [g],

N_A is Avogadro number 6.023×10^{23} [mol^{-1}],

τ is the factor of the attenuation of the LCS photon in the target,

ϕ is the number of LCS photons,

a is the diameter of the front surface of the neutron detector [cm] and equal to 12.7cm,

l is the distance between the target and the center of the detector [cm] as presented in Table 2.2,

$\varepsilon(E)$ is the neutron detection efficiency,

ΔE is the energy bin width [MeV] (It was 0.4 MeV in the analysis of the 14 MeV and 17 MeV data and 0.8 MeV in the analysis of the 20 MeV data), and

$\eta(E)$ is the neutron attenuation factor.

Table 3.1 lists the parameters of A and m used in this study.

The methods used to determine the neutron energy E, the neutron spectrum

Y(E), the attenuation factor of LCS photons in the target τ, the number of LCS photons φ, the neutron detection efficiency $\varepsilon(E)$, and the attenuation factor of neutrons inside the target $\eta(E)$ are discussed in the following sections.

Table 3.1: Values of A and m for Pb, Au, Sn, Cu, Fe, and Ti targets.

Target	A [g/mol]	m [g]
^{nat}Pb	207.2	9.0
^{197}Au	196.96	15.19
^{nat}Sn	118.71	11.47
^{nat}Cu	63.54	14.17
^{nat}Fe	55.84	12.49
^{nat}Ti	48.86	14.08

3.2 Correction of walk effect

In the present study, timing information is very important to determine the ToF of neutrons as well as their energy. Discriminators are usually employed in accelerator-based experiments to provide timing information. When discriminators receive an input signal, a logic signal is generated from the discriminators. In the case of leading-edge discriminators, the logic signal is output when the amplitude exceeds a threshold. The timing of the logic signal depends on the amplitude of the input signal, and the timing variation is referred as the walk effect. To improve the timing resolution of the system, the walk effect should be corrected. In References [41, 42], the walk of a leading-edge discriminator was measured as a function of pulse height, and it was found that walk corresponds to the square root of pulse height.

In this experiment, I used a constant fraction discriminator (CFD), which can minimize the walk effect to 100 ps for an input-signal dynamic range of 100:1; however, the walk effect is worse for a higher dynamic range [43, 44]. Heilbronn et al. [45] applied a correction method in offline analysis, which is similar to References [41, 42], to minimize the walk effect in CFD in a neutron time-of-flight spectroscopy. Heilbronn corrected time-of-flight of photons by using the following function:

$$\mathrm{T_{peak}} = \mathrm{a_1} - \mathrm{a_2 exp}\left(\frac{\mathrm{a_3}}{\mathrm{Q}}\right) \tag{3.4}$$

where $\mathrm{a_1}$, $\mathrm{a_2}$, and $\mathrm{a_3}$ are fitting parameters; Q is equivalent to the pulse charge measured by the QDC; and T_{peak} is the value measured by the TDC. The corrected function is used to correct data from neutron events. In this thesis, I followed a procedure similar to Heilbronn et al.'s method. Figure 3.1 shows the fitting for QDC data and TDC data obtained using Equation 3.4 for the detector at V90. The data for the other detectors were also fitted as the V90 data. The data of the gamma peak were used for fitting.

Figure 3.2a illustrates the walk effect on the data of TDC channels obtained

in this experiment. Some events at 6530 ch were shifted. Figure 3.2b illustrates the data of TDC channels after applying correction using the fitting parameters in Table 3.2.

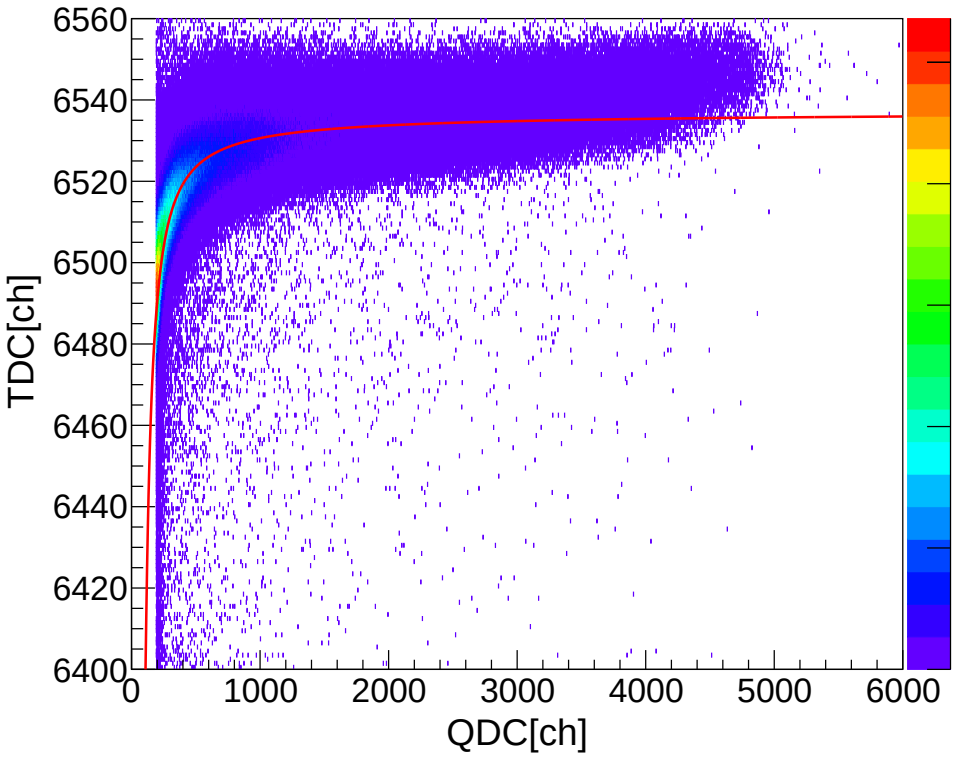

Figure 3.1: Fitting of the experimental data for correcting the walk effect. The red line is the fitting curve obtained using Equation 3.4.

Table 3.2: Fitting parameters for the correction of the walk effect for six detectors in the two experiments.

	1^{st} experiment			2^{nd} experiment		
Detector	a_1	a_2	a_3	a_1	a_2	a_3
H150	6708.757	24.785	12.505	6577.235	57.251	7.500
H120	7495.828	717.450	0.904	14798.385	8096.661	0.114
H90	6676.564	3.424	32.146	9621.562	3029.906	0.111
H60	6735.408	54.002	3.299	6336.705	1.877	40.043
H30	6542.247	4.468	35.251	6209.892	6.594	31.346
V90	6556.295	14.099	22.167	8010.763	1686.416	0.187

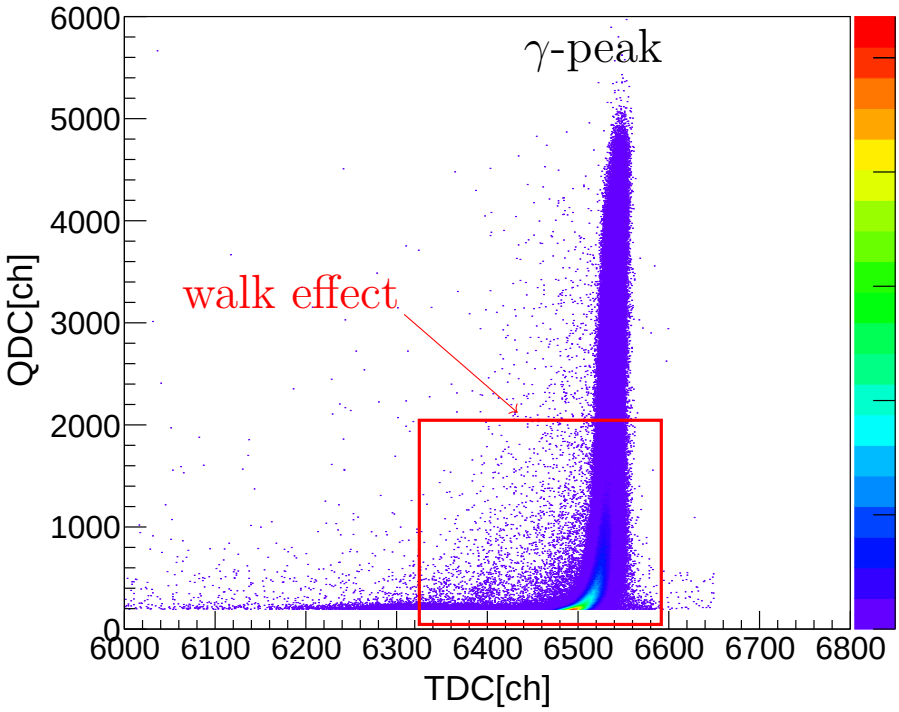

(a) Before correction of the walk effect

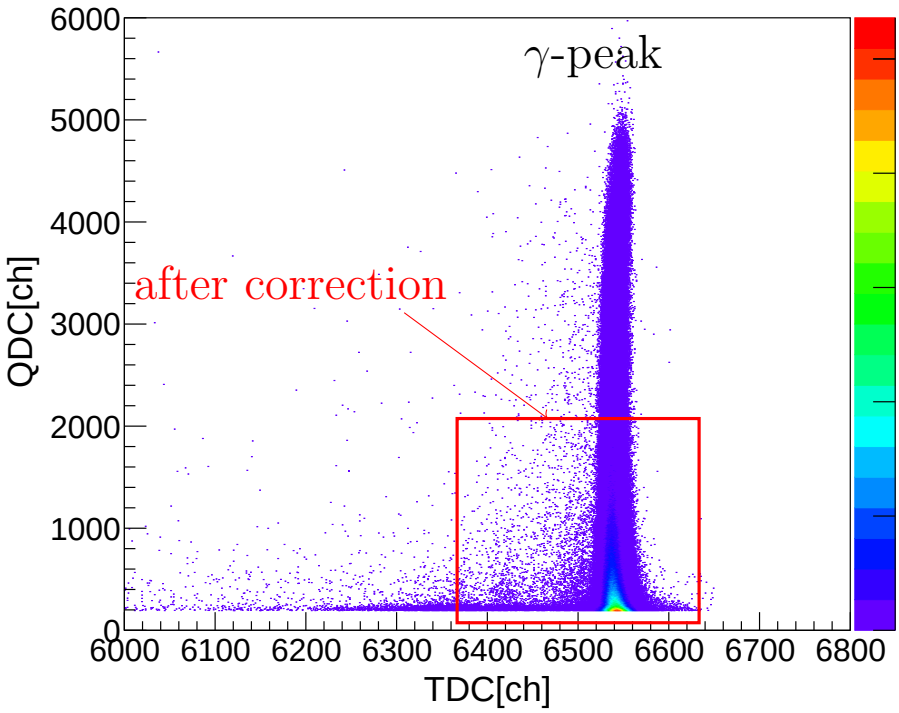

(b) After correction of the walk effect

Figure 3.2: Data at H30 before and after correction of walk effect.

3.3 Neutron energy spectrum and its resolution

3.3.1 Neutron-gamma separation using PSD

As mentioned in section 2.1.3, the PSD method was employed to separate neutron and gamma events. With the DAQ system setup described in section 2.1.3, both the charge integrals in the tail part and the whole signal were measured. In order to distinguish neutron and gamma events, data of light outputs of slow and total gates and TDC channels were used in this analysis. The PSD parameter was the ratio of the tail integral to the total integral. Table 3.3 lists the numerical values of PSD parameter and range of TDC which were used to analyze the data obtained on the six detectors in the two experiments.

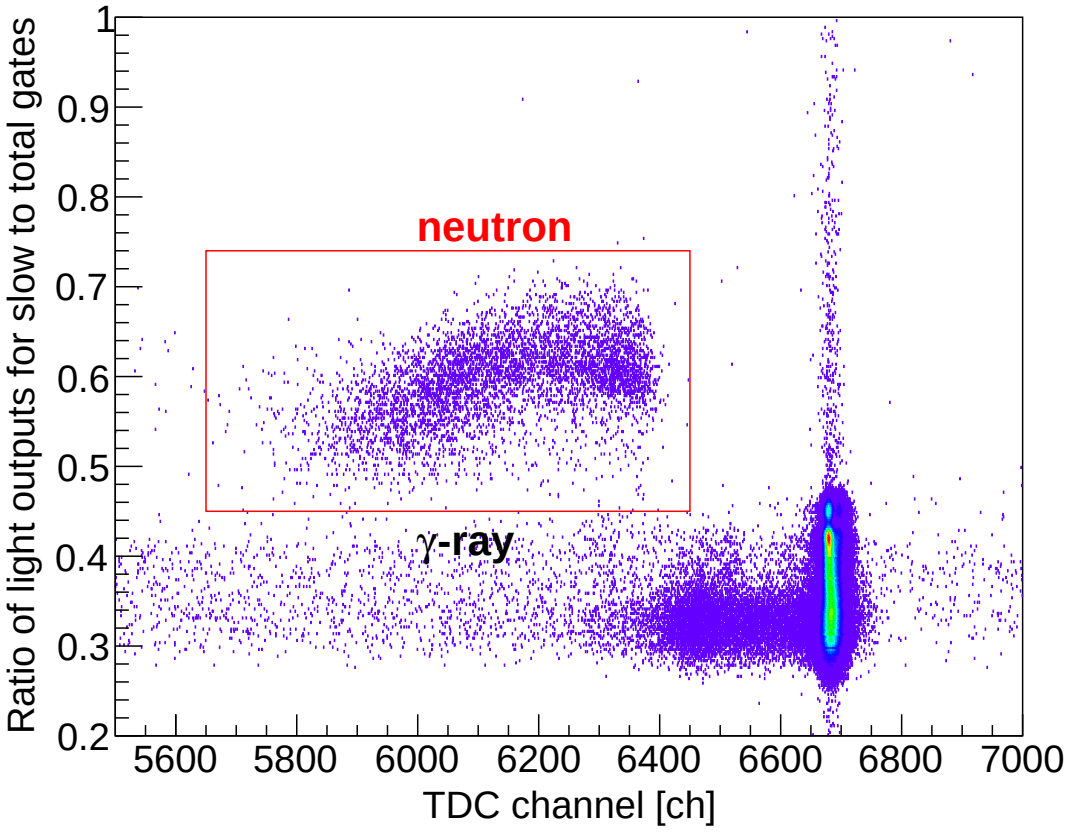

Figure 3.3: Neutron-gamma separation for the Pb target. The neutron and gamma events were detected in the H60 detector, and the energy bias was 0.25 MeVee.

Table 3.3: The numerical values of PSD parameter and TDC channel used to separate neutron-gamma for the 6 detectors.

	1^{st} experiment		2^{nd} experiment	
Detector label	PSD parameter	TDC [ch]	PSD parameter	TDC [ch]
H150	0.5 – 0.75	5500 < ch < 6500	0.5 – 0.75	4300 < ch < 6000
H120	0.5 – 0.75	5700 < ch < 6500	0.34 – 0.75	4700 < ch < 6500
H90	0.5 – 0.75	5800 < ch < 6500	0.4 – 0.75	4700 < ch < 6200
H60	0.46 – 0.75	5500 < ch < 6500	0.44 – 0.75	4400 < ch < 6000
H30	0.5 – 0.75	5300 < ch < 6400	0.5 – 0.75	3700 < ch < 6000
V90	0.5 – 0.75	5400 < ch < 6400	0.5 – 0.75	4150 < ch < 6000

Figure 3.3 shows a two-dimensional plot of the PSD parameters as a function of TDC channel for the H60 detector. The vertical axis is the PSD parameter. Owing to the difference in the tail region, the neutron and gamma events were separated well. On the horizontal axis, the TDC channel corresponds to the traveling time of neutrons or γ-rays from the target to one NE213 detector. A similar explanation for the difference between neutron and gamma events in TDC channels can be found in the description of Figure 3.4 in section 3.3.2. Using the three parameters i.e., the light outputs of slow and total gates and TDC channel, the separation of neutron and gamma events was performed well. The gamma events in the PSD range of neutron events were completely removed using the TDC data.

3.3.2 Neutron energy by ToF method

The TDC spectra of neutron and gamma events detected by the H60 detector are shown, respectively, by red and blue lines in Figure 3.4. By using the PSD

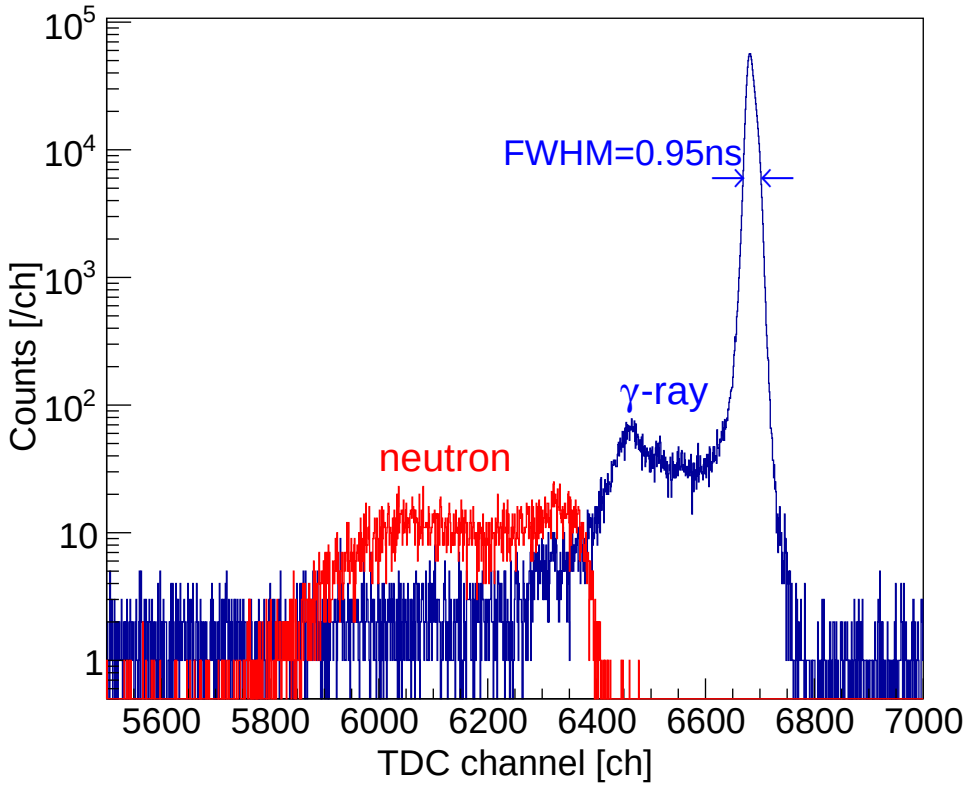

Figure 3.4: ToF spectra of neutrons and gamma rays for the Pb target. The ToF spectra for neutron and gamma events were measured with the H60 detector at an energy bias of 0.25 MeVee.

parameter defined in the previous section, I could construct individual time spectra for neutrons and γ-rays. The different speeds of γ-rays and neutrons in air lead to the different maximum TDC positions of the gamma and neutron ToF spectra.

The time resolution of the ToF system, which was determined by measuring the full-width at half-maximum (FWHM) of the prompt-gamma peak, ranged from 0.82 ns to 0.95 ns, and from 0.72 ns to 0.82 ns for the six detectors in the first and second experiment, respectively. The difference between the FWHM values was due to the time resolution of the electronic circuit, time fluctuation of neutron

emission from target. For the H60 detector, the peak rising up at TDC channel 6450 of these gamma events was attributed to the backscattered photons at the NaI(Tl) scintillator. Similar peaks at approximately TDC channel 6450 were found in other detectors. From the ToF and flight path, which is presented in Table 2.2, the spectrum of the neutron energy, E_n, can be obtained by converting time of flight spectrum as follows:

$$E_n(x) = M_o c^2 \left(\frac{1}{\sqrt{1-\beta^2}} - 1\right), \tag{3.5}$$

$$\beta = \frac{V_n(x)}{c} = \frac{L}{c.T_n(x)}, \tag{3.6}$$

$$M_o c^2 = 939.573 \text{ [MeV]}, \tag{3.7}$$

where,

L is the flight path length (m),

$V_n(x)$ is the neutron speed (m/ns),

c is the speed of light or 0.29978 (m/ns), and

$T_n(x)$ is the ToF of neutrons (ns).

Energy resolution was determined through the partial differentiation of Equation 3.5, which yielded Equation 3.8 [46, 47]:

$$\frac{\Delta E}{E} = \frac{1}{E}.\sqrt{\left(\frac{\partial E}{\partial L}\right)^2.\Delta L^2 + \left(\frac{\partial E}{\partial T}\right)^2.\Delta T^2}, \tag{3.8}$$

$$\frac{\Delta E}{E} = \frac{E + M_o c^2}{E}.\frac{\beta^2}{1-\beta^2}.\sqrt{\left(\frac{\Delta L}{L}\right)^2 + \left(\frac{\Delta T}{T}\right)^2}. \tag{3.9}$$

The ΔT originates from (a) the LCS beam pulse width, (b) time fluctuation of neutron emission from the target, and (c) time resolution of the electronic circuit. The ΔL originates from (d) the target thickness and (e) detector thickness. The

width of the γ-peak in Figure 3.4 includes (a), (b), (c), and (d). To include (e) for neutrons, the time difference between neutrons and γ-rays for half of the detector thickness, 0.127/2 m, is included.

$$\sqrt{(\frac{\Delta L}{L})^2 + (\frac{\Delta T}{T})^2} \approx \sqrt{(\frac{\Delta T_\gamma}{T})^2 + (\frac{\Delta T_d}{T})^2} = \frac{1}{T} \cdot \sqrt{\Delta T_\gamma^2 + \Delta T_d^2}, \tag{3.10}$$

$$\Delta T_d = \frac{R}{c} \cdot \left(\frac{c}{V_n(E_n)} - 1 \right), \tag{3.11}$$

where

ΔT_d: flight time of neutron for half thickness of detector.

T: time of flight of neutron [nsec], was obtained as a sum of the gamma flight time and the time difference between the neutron data and the prompt γ peak.

ΔT_γ : FWHM of gamma peak. It was been determined by fitting Gaussian [nsec].

R: half of detector thickness 0.127/2 [m]

Figure 3.5 shows the neutron energy resolution, which was calculated using Equation 3.8.

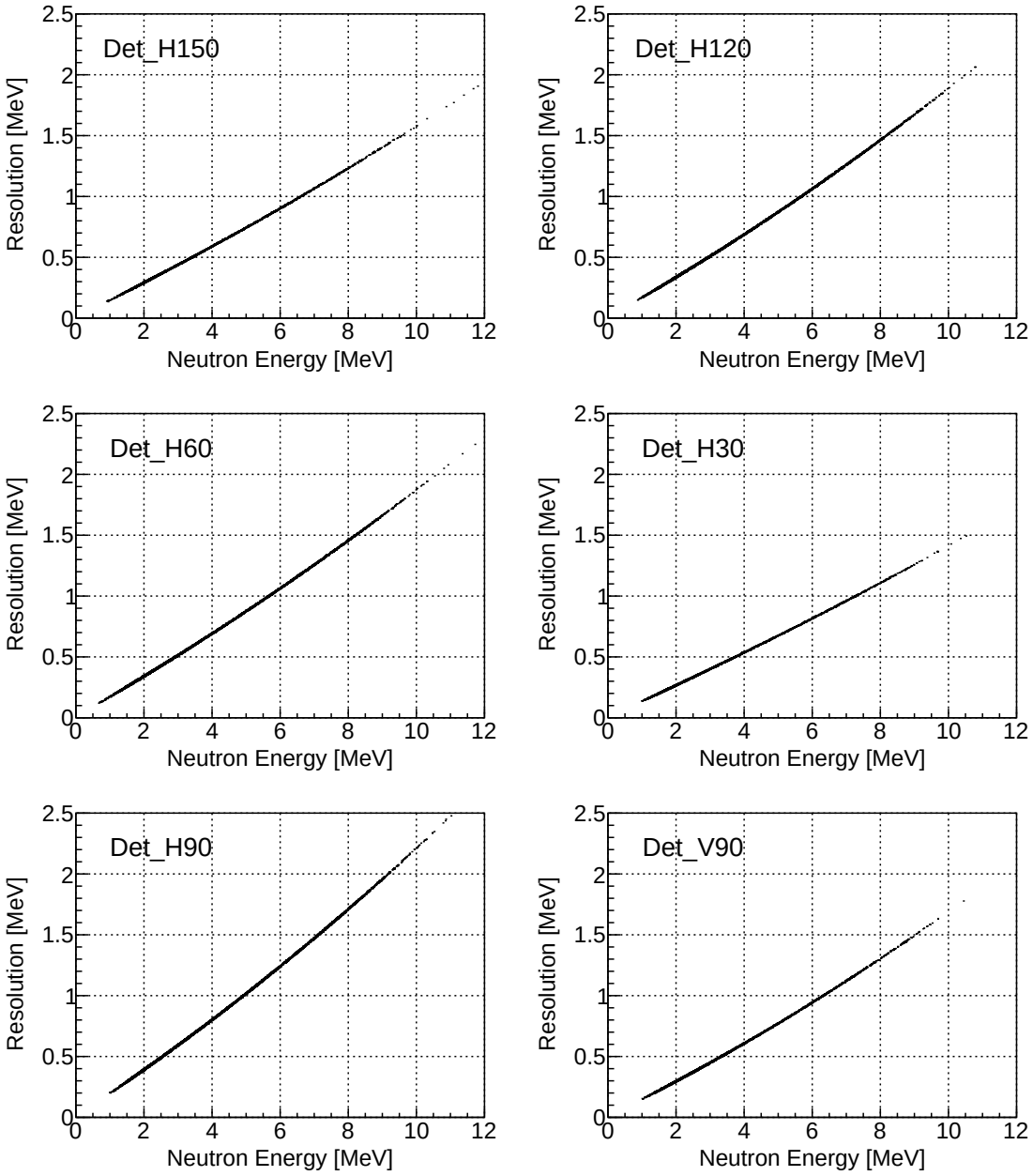

Figure 3.5: Energy resolution for the six detectors in the first experiment.

3.4 Number of LCS photons

The number of LCS photons on the target was obtained with the consideration of the detection efficiency of the PLS (ϕ). The PLS's detection efficiency was obtained using the Electron-Gamma Shower (EGS5) code, which is a Monte Carlo simulation tool [48]. In this simulation, a monoenergetic photon source was incident on the PLS, and the PLS was sandwiched by two aluminum foils with thicknesses of 48 μm, on the upstream and downstream surfaces. The distance from the LCS generation point to the PLS was 23.5 m. The calculation was conducted with and without air between the LCS generation point and PLS.

Figure 3.6 displays the energy deposition on the PLS calculated using EGS5. The lines in Figure 3.6 are results of the calculation for 14 MeV, 17 MeV, and 20 MeV photons with geometry including air, and the circle-lines are those of the calculation without air. During the propagation of the photon beam to the PLS, the photon beam interacts with the air and produces electrons and positrons; thus, the lines show two peaks in the spectra.

The number of LCS photons, ϕ, was determined using a PLS, the detection efficiency of which was obtained from the simulation result obtained with the following procedure. Figure 3.7 and Figure 3.8 display the calculated energy deposition compared with the experimental data for 14 MeV and 17 MeV photons in the acquisition run for Au and Ti targets, respectively. The pulse-height channels of the experimental data were calibrated using a peak at 0.9 MeV and a slope above 2 MeV. The red lines are energy spectra obtained using the EGS5 calculation, which accounted for the energy resolution values and are compared with the experimental data. The energy resolution, 8 %, was applied to each energy bin of the calculation spectra.

The photon counting efficiency was determined to be (0.68 $\pm$ 5)% from the integration of photons with deposition energies greater than the energy threshold of 0.5 MeV. The uncertainty of the counting efficiency was 5 % because it includes EGS5 simulation uncertainty and the experimental uncertainty. The efficiency was

used to determine the number of LCS photons for data acquisition runs of each target.

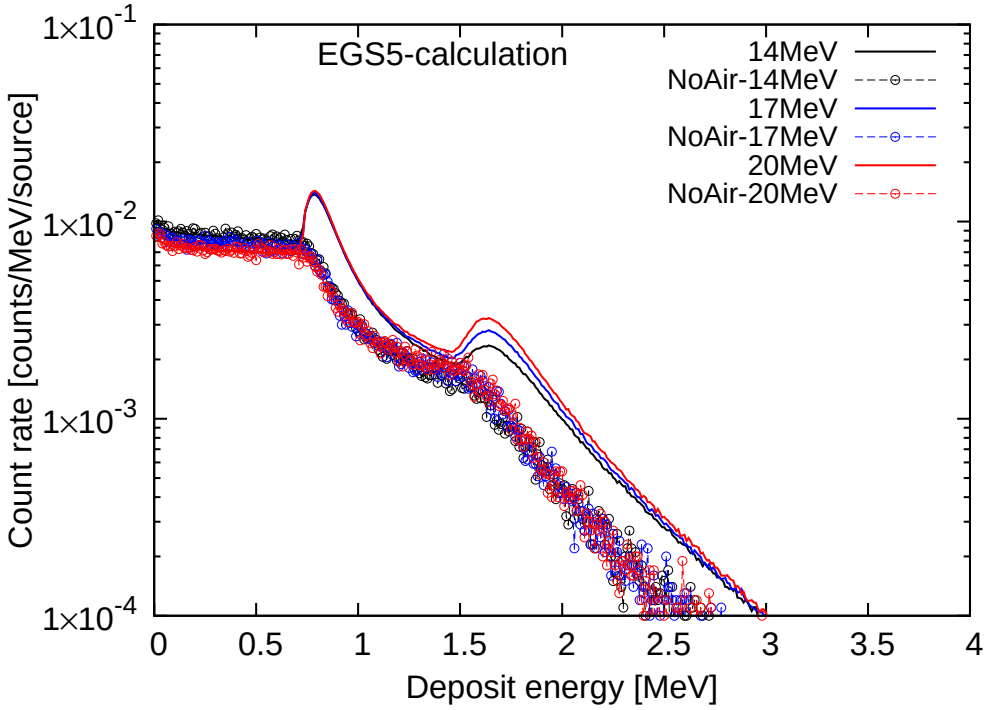

Figure 3.6: EGS5 calculation for the deposition energy of photons on PLS.

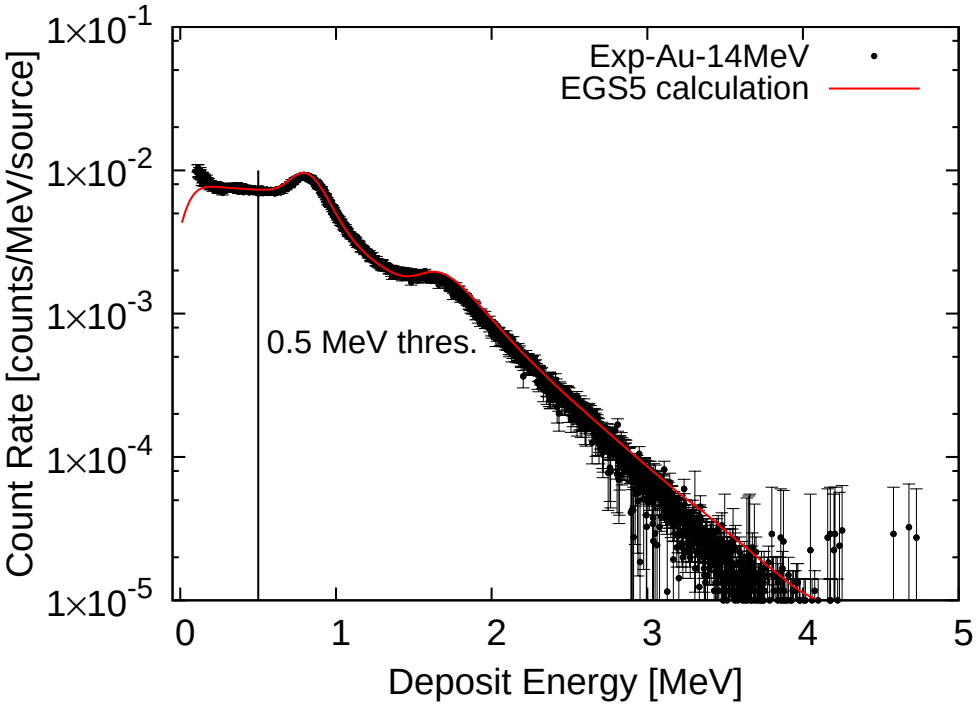

Figure 3.7: Experimental and calculated pulse height distribution for 14 MeV photons.

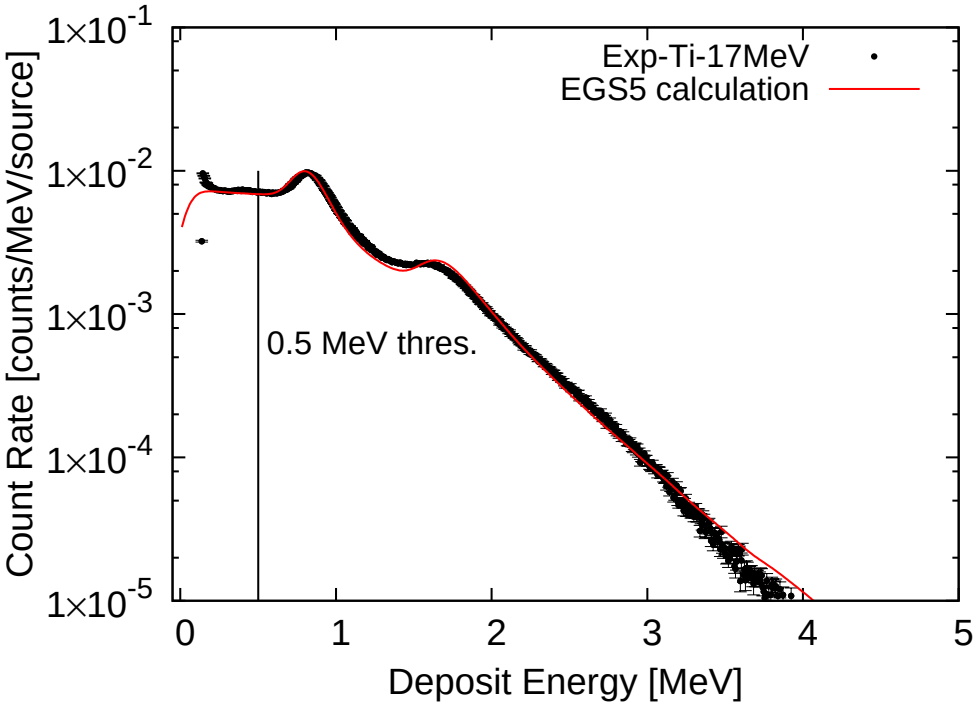

Figure 3.8: Experimental and calculated pulse height distribution for 17 MeV photons.

Table 3.4 reports values of the LCS photon intensity (ϕ) for 14 MeV, 17 MeV, and 20 MeV photons. The values for 17 MeV photons are approximately equal to 10^5, while they are about 10^4 for 14 MeV and 20 MeV photons. The difference is because the current of the electron beam operated in the top-up mode for producing the 17 MeV LCS photons was much more stable than that for producing the 14 MeV and 20 MeV LCS photons. In order to generate the 14 MeV and 20 MeV LCS photons, the electron beam was operated in the decay mode, and data acquisition runs were conducted 2 – 3 times to obtain sufficient statistics of the photoneutrons. Details on the data acquisition runs were presented in section 2.3.4 and Table 2.9.

Table 3.4: Number of LCS photons determined by the EGS5 calculation and the experiment on PLS for 14 MeV, 17 MeV, and 20 MeV photons.

	ϕ [photon/s] 1^{st} experiment	ϕ [photon/s] 2^{nd} experiment		
Target	17 MeV	14 MeV	17 MeV	20 MeV
^{nat}Pb	2.0x10^5			
^{197}Au	2.09x10^5	3.66x10^4	1.48x10^5	4.05x10^4
^{nat}Sn	1.10x10^5			
^{nat}Cu	1.99x10^5		1.37x10^5	3.97x10^4
^{nat}Fe	1.88x10^5			
^{nat}Ti	1.95x10^5		1.44x10^5	4.3x10^4

3.5 Photon attenuation

The number of LCS photons attenuated as the photons penetrated the target. To compensate for the attenuation, a compensation factor was determined by using the PHITS version 3.16 Monte Carlo simulation tool [49]. With the known material and dimensions of each target, PHITS was used to obtain the average track length of 14 MeV, 17 MeV, and 20 MeV incident photons, and the factor τ was determined by taking the ratio of the average track length of photons to the target thickness. The values are listed in Table 3.5.

In the simulation, a pencil beam of photons was shot into a cylindrical target. The beam direction was along the target thickness, and the beam was indicent on the target at its circular center. After interaction with the target material by penetrating through a certain distance inside the target, the photon energy was changed. The average track length was calculated by taking the sum of the distance divided by the total number of incident photons. The contribution of secondary particles after interaction was small because the main interaction of the photons was electron-positron pair production, and its energy was below the threshold for photonuclear reaction.

Table 3.5: Material and thickness of targets and photon attenuation factors for 14 MeV, 17 MeV, and 20 MeV photons.

		Photon attenuation factor (τ)		
Target	Thickness [cm]	14 MeV	17 MeV	20 MeV
^{nat}Pb	1.0		0.73	
Au	1.0	0.51	0.60	0.62
^{nat}Sn	2.0		0.69	
^{nat}Cu	2.0		0.75	0.71
^{nat}Fe	2.0		0.80	
^{nat}Ti	4.0		0.78	0.79

3.6 Neutron attenuation

Like the LCS photons, the photoneutrons emitted from the target attenuated as they penetrating through the target to reach the NE213 detectors. The attenuation factor of photoneutrons, η(E), depended on the neutron energy, target thickness, target material, and detection angle.

The factor η(E) was determined as follows:

$$\eta(\mathrm{E}) = \frac{\mathrm{Y_d(E)}}{\mathrm{Y_i(E)}}, \tag{3.12}$$

where $\mathrm{Y_d(E)}$ and $\mathrm{Y_i(E)}$ are, respectively, the energy spectra of neutrons after and without passing through the target. The factor η(E) was calculated by considering two geometries in the PHITS calculation. The first geometry is shown in Figure 3.9. The distances from the target to the six detectors were listed in Table 2.2. The geometry was the same as the experimental setup. NE213 detectors were simulated as cylindrical volumes without any material. The geometry contains air. The incident neutron spectrum was the experimental neutron spectrum.

As the number of photoneutrons depends on the photon attenuation in the target, the distribution of the neutron source was considered following the exponential distribution of the photon. Figure 3.10 shows the distribution of the neutron source in the calculation of the η(E) for an Au target, 1 cm in thickness with 17 MeV photons. The triangle points are values of the input data for initializing the neutron distribution. The circle points are the values of the output data obtained from calculation. This distribution was determined using the formula $\mathrm{I = I_0 e^{-\mu \cdot t}}$, where μ is the mass attenuation coefficient in $\mathrm{cm^2/g}$ and t is the thickness of the target in $\mathrm{g/cm^3}$. The value of μ depends on the energy of photons and the target material.

In the first calculation, the neutron spectrum source passed through the target and travelled to the cylinders. The neutron spectrum obtained on the cylinder was $\mathrm{Y_d(E)}$.

For the second geometry, the neutron spectrum is basically the same as in the first geometry. The only difference is the absence of any target material in the second geometry. The neutron spectrum was $Y_i(E)$.

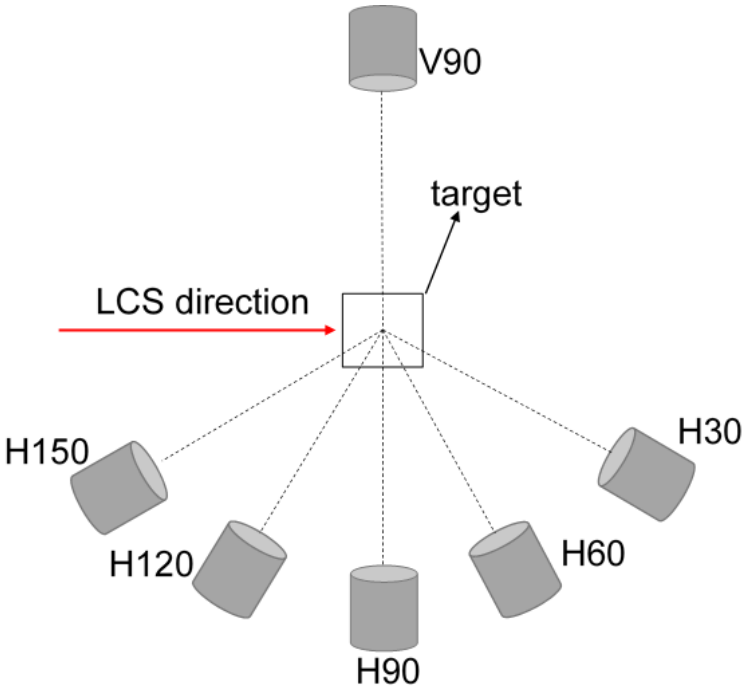

Figure 3.9: Geometry used for the calculation of $\eta(E)$.

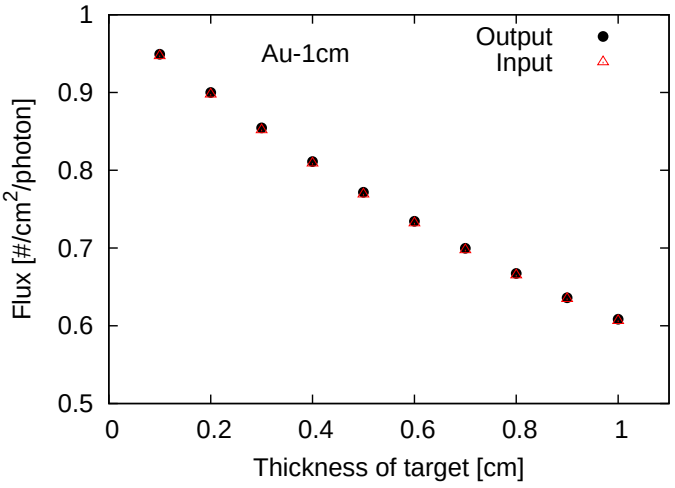

Figure 3.10: Distribution of the neutron source initialized in calculation by using the photon attenuation for 17 MeV photons in an Au target. Black points show data from the output of the calculation, and red triangles indicate input data.

Figure 3.11, Figure 3.12, and Figure 3.13 show values of η(E) for an Au target 1 cm in thickness for 14, 17, and 20 MeV photons, respectively. The values ranged from 0.9 to 0.95, and the attenuation of neutrons at H30 was the largest at approximately 0.1.

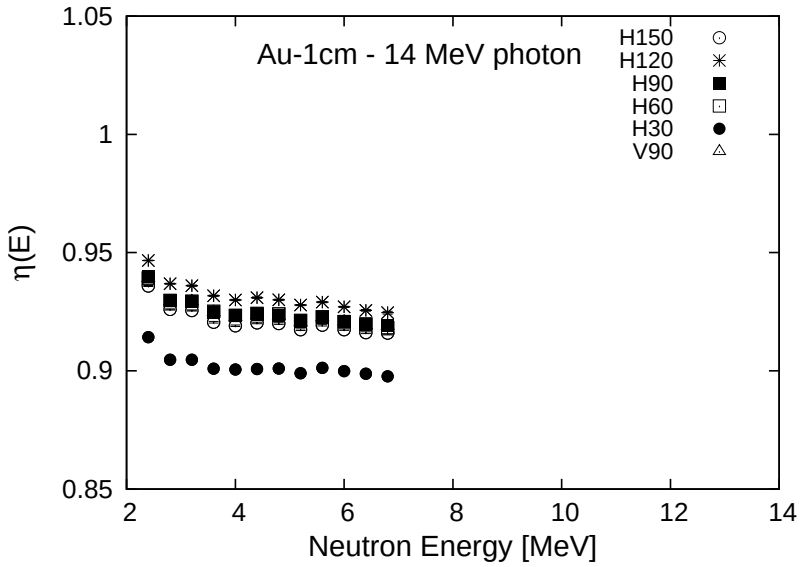

Figure 3.11: Neutron attenuation factors for Au using 14 MeV photons.

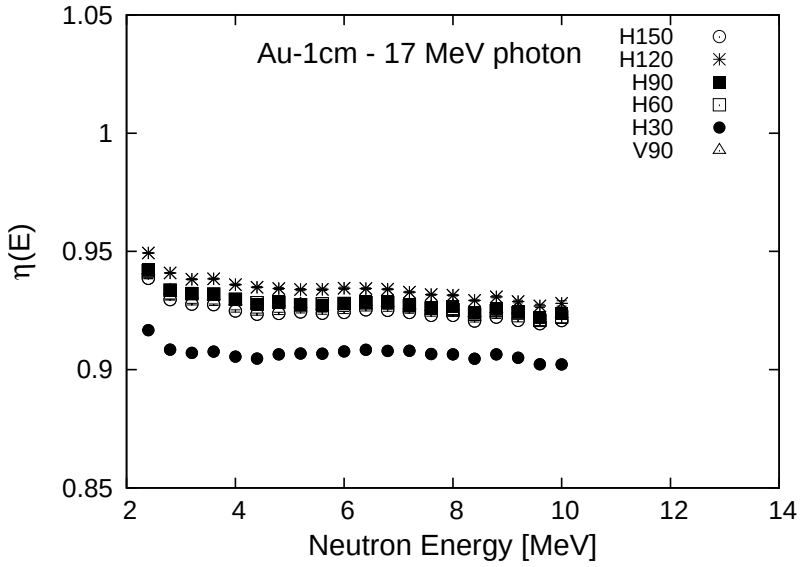

Figure 3.12: Neutron attenuation factors for Au using 17 MeV photons.

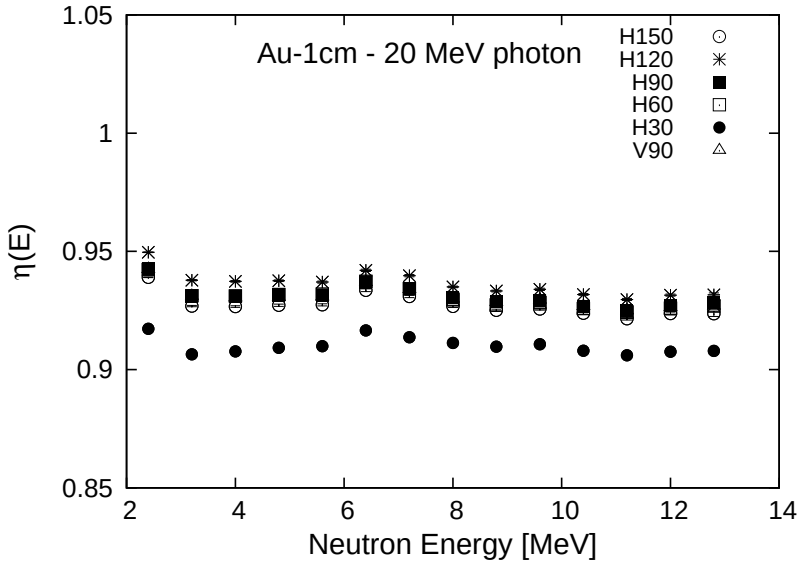

Figure 3.13: Neutron attenuation factors for Au using 20 MeV photons.

For a Pb target with 17 MeV photons, as shown in Figure 3.14, η(E) ranged from 0.95 to 1.0, and the minimum value was at H30. These η(E) values are greater than those for the Au target.

Figure 3.15 shows values of η(E) for a Sn target using 17 MeV photons. The η(E) at H30 and H150 are approximately 0.94 – 0.96, while the values at H60, H90, H120, and V90 are approximately 0.97 – 0.99.

In the case of Fe, the difference in the values is large. These values are shown in Figure 3.16. The values at H30 and H150 ranged from 0.89 to 0.95. On the order hand, the values at H60, H90, H120, and V90 ranged from 0.94 to 1.0.

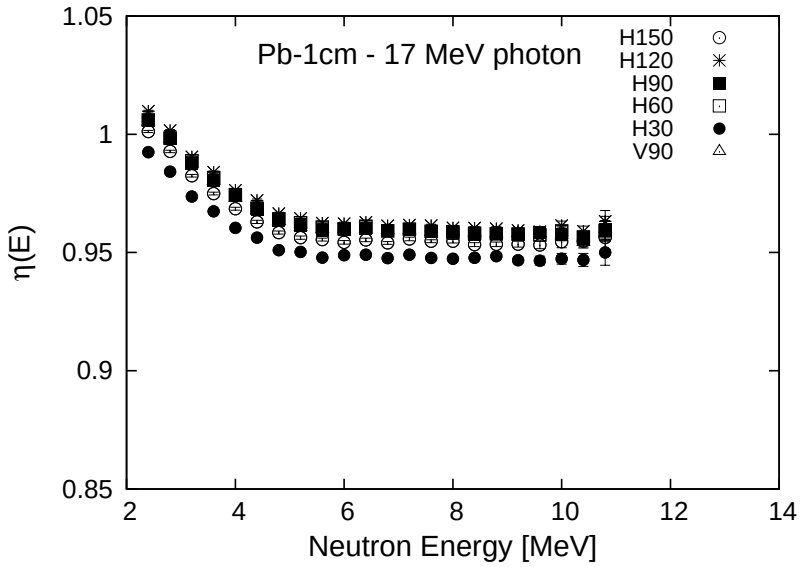

Figure 3.14: Neutron attenuation factors for Pb using 17 MeV photons.

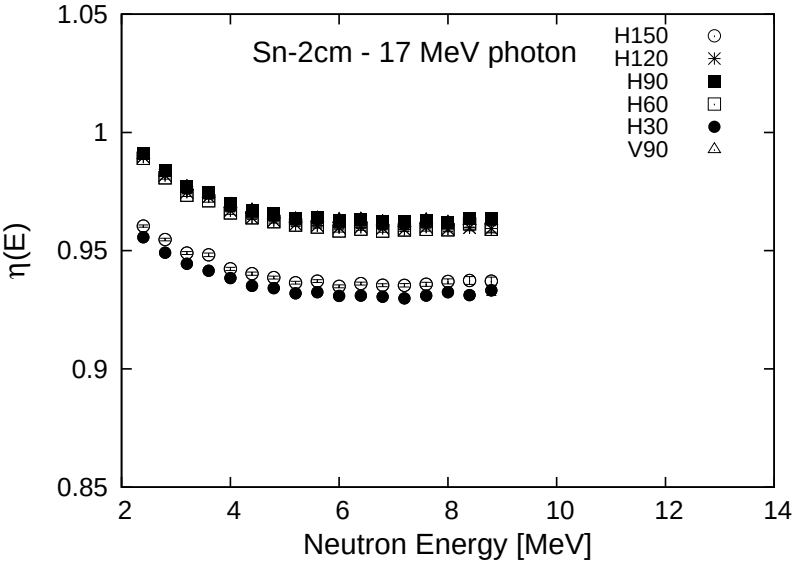

Figure 3.15: Neutron attenuation factors for Sn using 17 MeV photons.

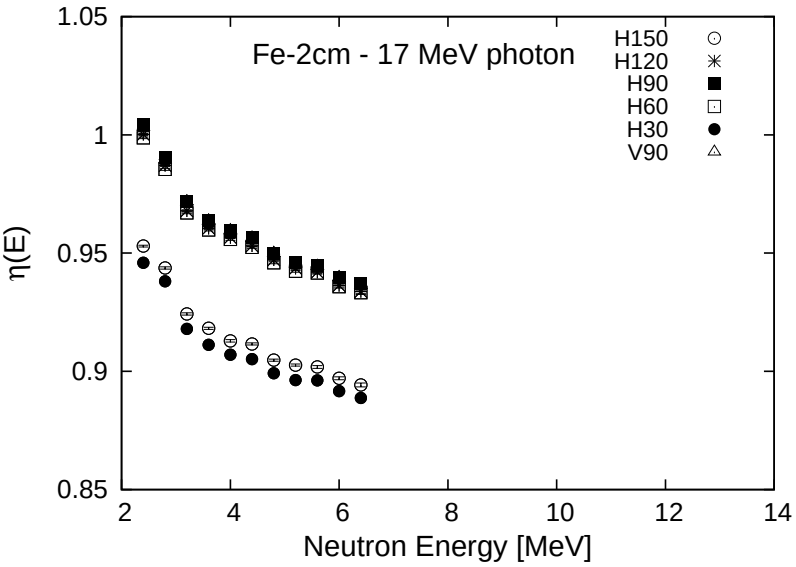

Figure 3.16: Neutron attenuation factors for Fe using 17 MeV photons.

Figure 3.17 and Figure 3.18 show the values for a Cu target using 17 MeV and 20 MeV photons. For 17 NeV photons, the η(E) values at H30 and H150 were approximately 0.87 – 0.94, while these values at H60, H90, H120, and V90 were 0.93 – 0.99. In the case of 20 MeV photons, at H30 and H150, η(E) is approximately 0.9 – 0.91, while that at other detectors is 0.94 – 0.96.

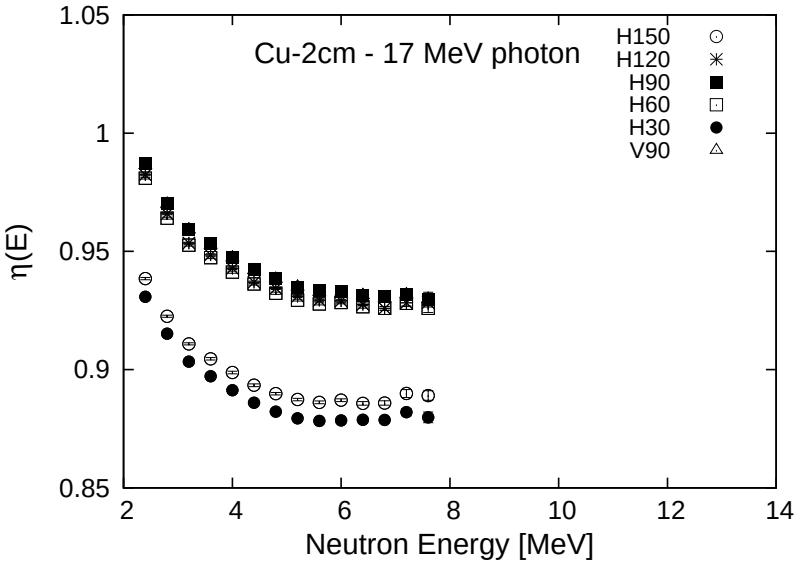

Figure 3.17: Neutron attenuation factors for Cu using 17 MeV photons.

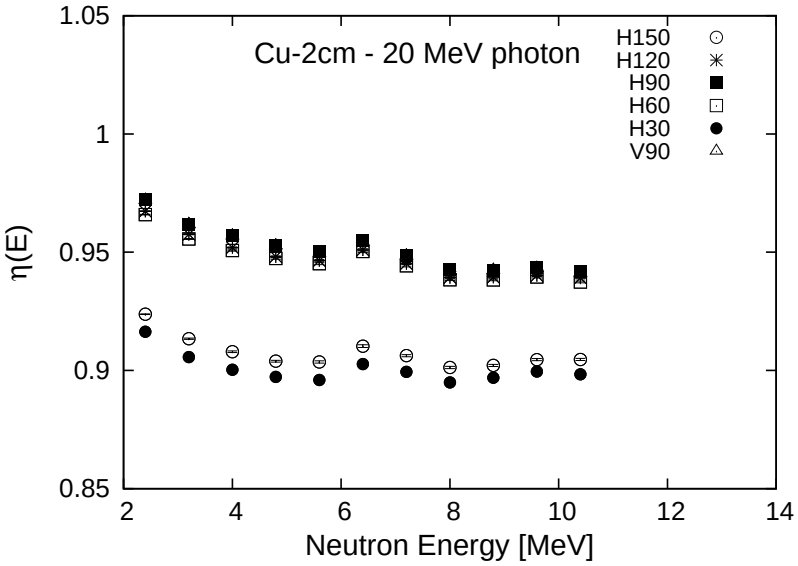

Figure 3.18: Neutron attenuation factors for Cu using 20 MeV photons.

The η(E) values for a Ti target with 17 MeV and 20 MeV photons are shown in Figure 3.19 and Figure 3.20, respectively. These values at H30 and H150 were approximately 0.93 – 0.94 for both 17 MeV and 20 MeV photons. The values at other detectors were 0.97 – 1.0. In general, the η(E) at H30 was the lowest among all the detectors for all the photon energies.

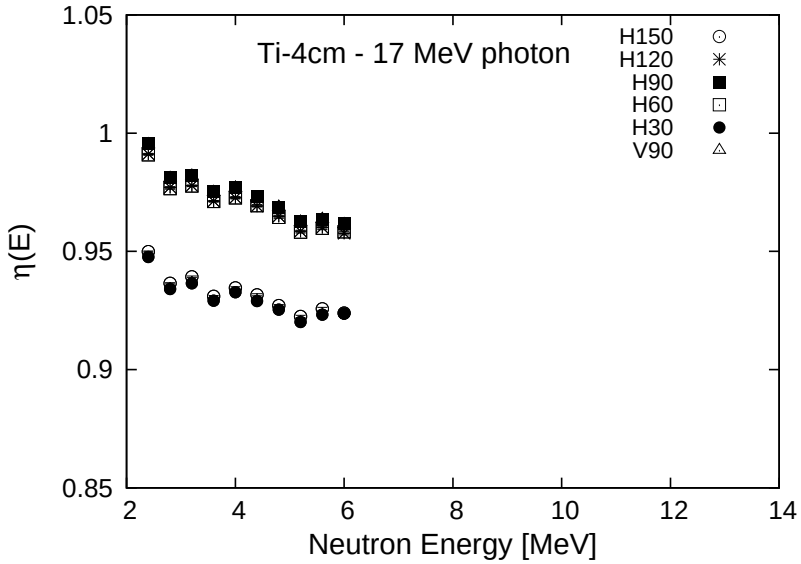

Figure 3.19: Neutron attenuation factors for Ti using 17 MeV photons.

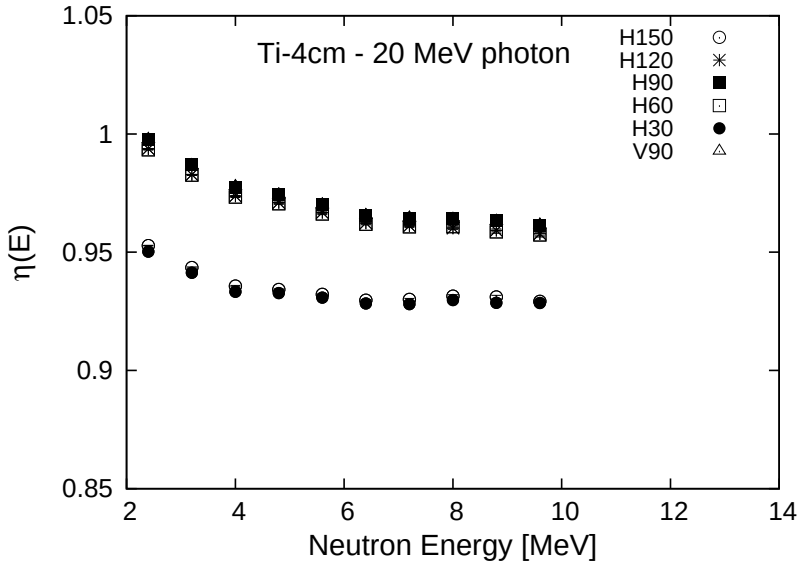

Figure 3.20: Neutron attenuation factors for Ti using 20 MeV photons.

3.7 Detection efficiency

The six organic liquid scintillation detectors have different histories. Half of them were prepared 17 years ago for the Japan Atomic Energy Research Institute (JAERI). The others were prepared 15 years ago for RIKEN and KEK. The liquid of two detectors for JAERI were refilled 5 years ago. The RIKEN and KEK detectors were opened to gauge the amount of liquid, and the filling ratio of each detector varied from 80% to 100%, as shown in Figure 3.21. The ages and filling ratios of the liquid scintillators result in different energy resolutions and detection efficiencies. Therefore, the calculation results obtained using SCINFULQMD code, the theoretical calculation code for neutron detection efficiency, are not applied directly.

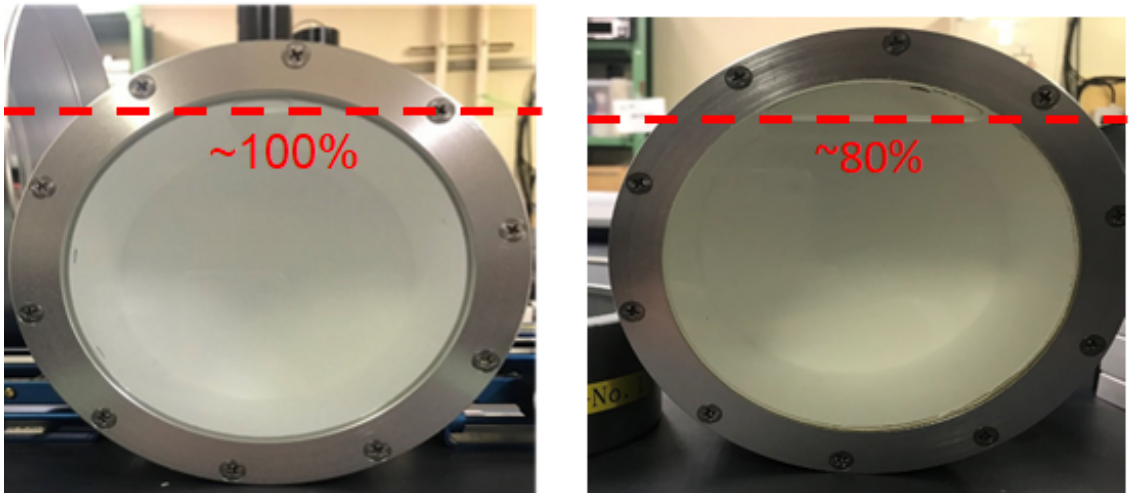

Figure 3.21: Liquid scintillator NE213 in neutron detector.

The spectrum of spontaneous fission neutrons of the ^{252}Cf source was measured using the ToF method, as described in section 2.2.1 to determine efficiency of low-energy neutrons. Figure 2.13 compares the neutron spectra of all detectors without considering detection efficiencies. Differences were observed in the magnitude (above 4 MeV) and in the shapes around their threshold. They may be attributed to the differences in filling ratio and energy resolutions and should be compensated for using

the experimentally determined detector efficiencies so that the efficiencies may be applied to the photoneutron data.

3.7.1 Efficiency for low-energy region

The neutron detection efficiency, ε(E), was calculated as the ratio of the experimental data to the theoretical data. It is difficult to determine the neutron detection efficiencies of the six detectors in the low-energy region by using the calculations alone because of the detector-dependent energy resolution in the low-energy region. Therefore, each NE213 detector's detection efficiency for energies $\leq$3 MeV was determined using a ^{252}Cf neutron spectrum measurement.

The relative detection efficiency was deduced by dividing the measured energy distribution of fission neutrons with the NBS spectrum, as expressed by the following function:

$$\varepsilon(\mathrm{E}) = \mathrm{C}\frac{\mathrm{Y(E)}}{\mathrm{N(E)}}, \tag{3.13}$$

where

N(E) is the spectrum evaluted by the members of the National Bureau of Standards (NBS spectrum),

C is a normalization factor determined by the ratio between the SCINFULQMD [50] and National Bureau of Standards (NBS) spectra,

Y(E) is the measured neutron energy distribution of ^{252}Cf, and

ε(E) is the efficiency of the detector.

The NBS spectrum was constructed based on eight differential spectrum measurements. These measurements were performed between 1965 and 1974. The NBS spectrum was expressed using Equation 3.15 based on Reference [51]:

$$\mathrm{N(E)} = \sum_{\mathrm{i=1}}^{\mathrm{i=5}} \mu_{\mathrm{i}}(\mathrm{E}) \cdot \mathrm{X_{Cf}(E)}, \tag{3.14}$$

$$X_{Cf}(E) = 0.6672\sqrt{E}e^{\frac{-E}{1.42}}, \tag{3.15}$$

where

E energy in MeV,

$X_{Cf}(E)$ in MeV^{-1},

$\mu_i(E)$ denotes five line-segment corrections given as follows,

$\mu_i(E) = 0.763 + 1.2E$, $0 \leq E \leq 0.25$ MeV,

$\mu_i(E) = 1.098 - 0.14E$, $0.25 \leq E \leq 0.08$ MeV,

$\mu_i(E) = 0.9668 + 0.024E$, $0.80 \leq E \leq 1.50$ MeV,

$\mu_i(E) = 1.0332 - 0.0006E$, $1.50 \leq E \leq 6.0$ MeV,

$\mu_i(E) = e^{-0.03(E-6.0)}$, 6.0 MeV$\leq E \leq \infty$

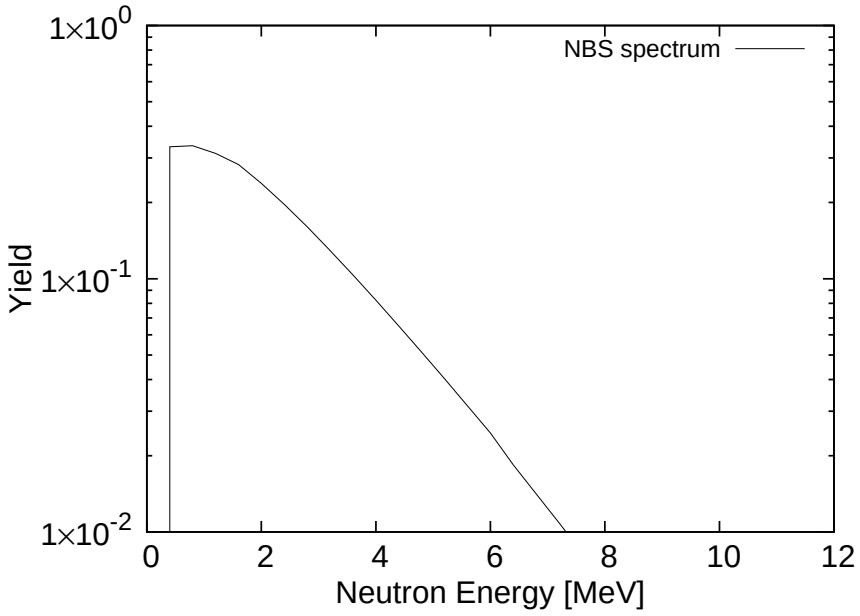

Figure 3.22: NBS spectrum was reproduced by Equation 3.15

The NBS spectrum created using Equation 3.15 is shown in Figure 3.22. In order to determine the detection efficiency by Equation 3.13, the C factor should be determined. Thus, the SCINFULQMD code was used to calculate the neutron detection efficiency for the six NE213 detectors. In the SCINFULQMD calculation,

distances from the neutron source to the NE213 detector were same as the values in Table 2.2. The efficiencies were computed with a bias of 0.25 MeVee. Figure 3.23 indicates the SCINFULQMD efficiencies for the six NE213 detectors. These values are consistent because the variation among the distances was small. However, the six NE213 detectors were not identical; thus, the SCINFULQMD efficiencies should be normalized with the experimental data before determining the C factors.

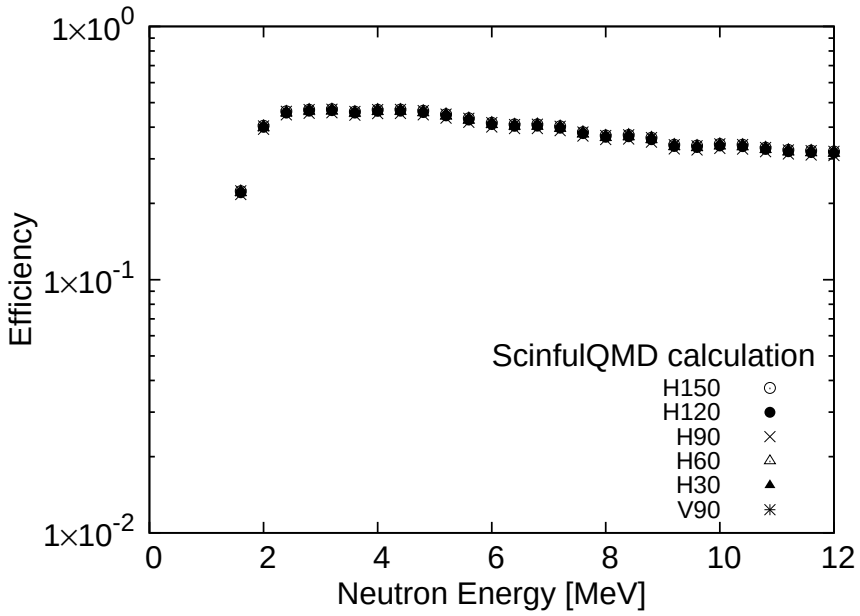

Figure 3.23: Detection efficiencies of the six NE213 detectors computed using SCINFULQMD with a bias of 0.25 MeVee.

Using the SCINFULQMD code, the corrected efficiencies for the six detectors were obtained by multiplying the calculated efficiencies by the ratio of yield of the fission neutrons. Figure 3.24 shows the SCINFULQMD efficiencies that were corrected. The ratio was determined by assuming an efficiency equal to the SCINFULQMD result for the detector labeled V90 (from KEK), which showed the highest count rate, as shown in Figure 2.13. Table 3.6 lists the C-factors of the six detectors, which were calculated by Equation 3.13. Here, ε(E) is the corrected SCINFULQMD efficiency, and Y(E) is the observed yield of the fission neutrons. These values of the C-factors were applied to Equation 3.13 to determine the detection efficiency for neutron energies lower than 3 MeV.

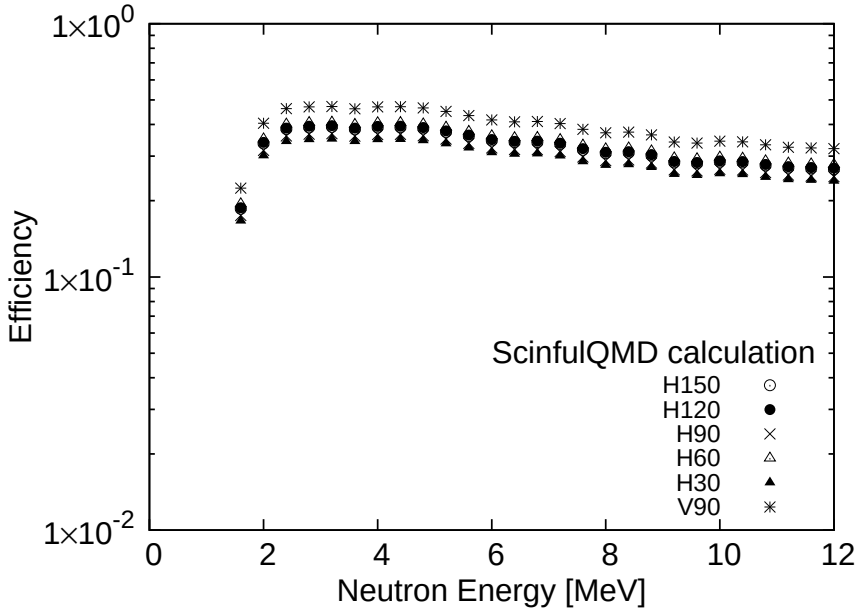

Figure 3.24: Normalized results of the SCINFULQMD calculations for the six organic liquid scintillator detectors.

Table 3.6: C-factors for determining the efficiency of the detectors.

Detectors	C-factors
H150	1.17E-02
H120	1.16E-02
H90	1.13E-02
H60	1.15E-02
H30	1.18E-02
V90	1.17E-02

A comparison of the efficiencies obtained from the ScinfulQMD calculation and the ^{252}Cf neutron spectrum measurements for the same detector show good agreement for energies ranging from 3 MeV to 7 MeV. The comparison is shown indicated in Figure 3.25. The efficiencies obtained from the ^{252}Cf neutron spectrum measurements above 7 MeV varied because of low statistics. Below 3 MeV, the shape of the efficiency curve determined from measurement was different from that obtained from ScinfulQMD because of the energy resolution, which should be taken into account properly.

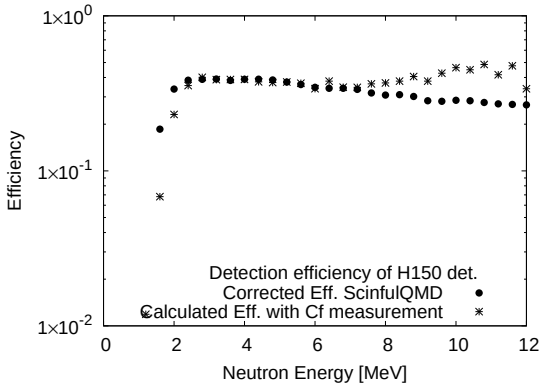

(a) Detection efficiency of the H150 detector

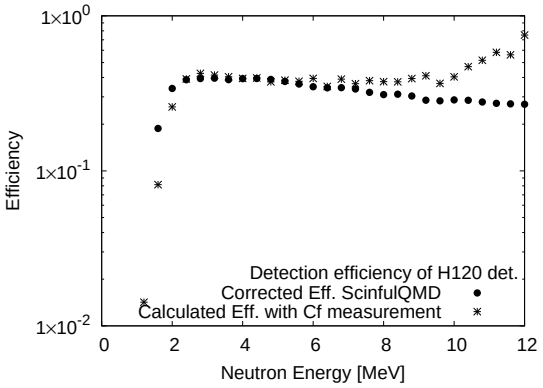

(b) Detection efficiency of the H120 detector

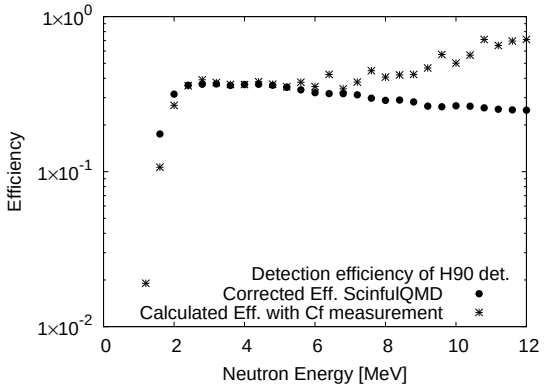

(c) Detection efficiency of the H90 detector

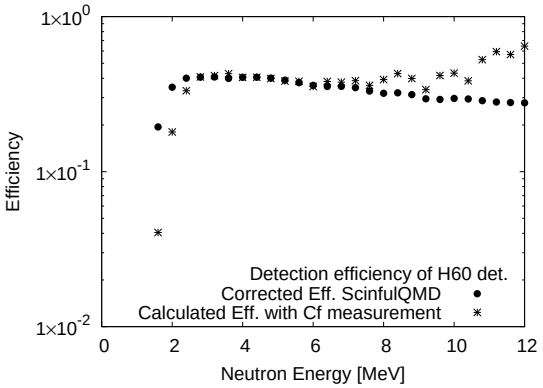

(d) Detection efficiency of the H60 detector

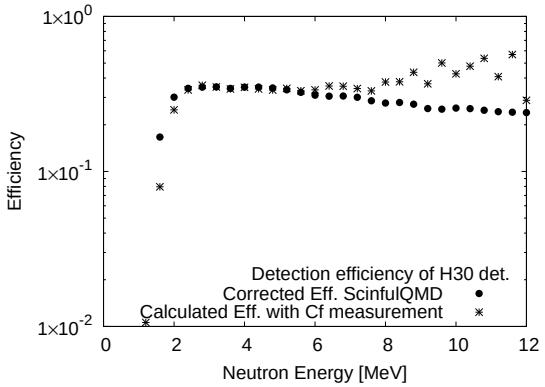

(e) Detection efficiency of the H30 detector

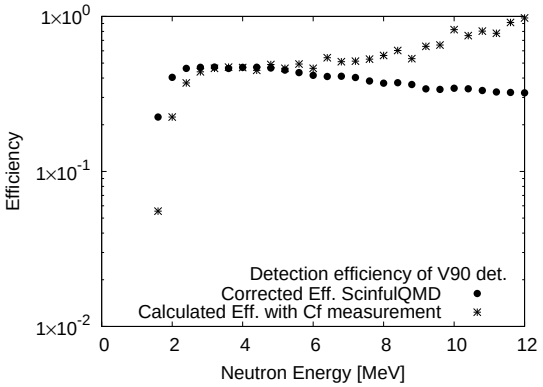

(f) Detection efficiency of the V90 detector

Figure 3.25: Efficiencies obtained from the SCINFULQMD calculation and ^{252}Cf measurement.

3.7.2 Efficiency for high-energy region

The corrected efficiency from SCINFULQMD was applied directly to the detection of neutrons in the high-energy region above 4 MeV. These corrected efficiencies are shown in Figure 3.24.

3.7.3 Efficiency results

In order to cover the entire energy region, the efficiencies obtained using the calculation code for energies above 3 MeV and those obtained using the ^{252}Cf neutron spectrum measurements for energies below 3 MeV were adopted. The above data were determined for the first experiment of the photoneutron measurement. These efficiencies were applied to the previous ^{252}Cf neutron yield spectra to confirm the variation among the spectra of the six detectors. Figure 3.26 shows the results of the ^{252}Cf neutron energy spectra; the differences were successfully compensated, and the difference between spectra was less than 10% for low energies. Additionally, these spectra were consistent with the NBS spectra with the energy ranging from 0.8 MeV to 8 MeV.

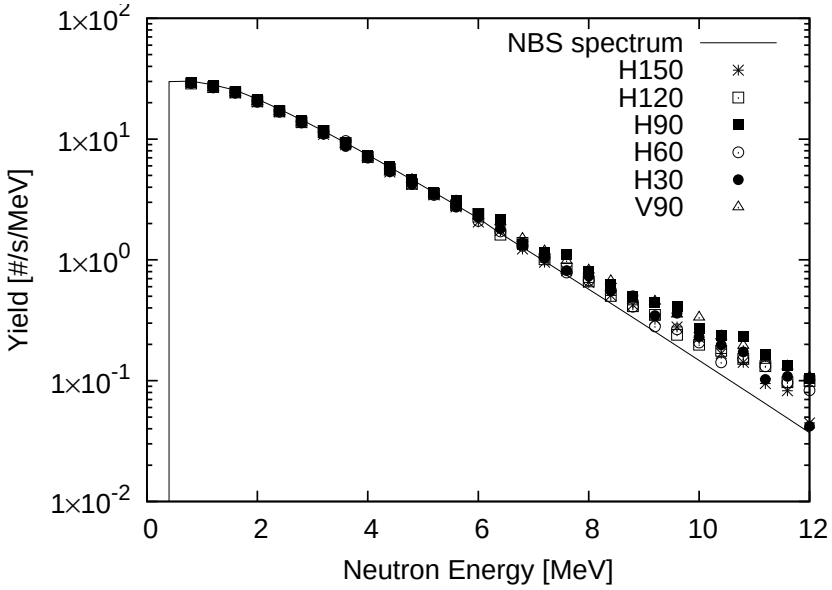

Figure 3.26: Neutron spectra of the six detectors for a ^{252}Cf neutron source after mixture correction.

The same method was applied to the second experiment. The detection efficiency $\varepsilon(E)$ of the six NE213 detectors in both the experiments are shown in Figures 3.27, 3.28, and 3.29. As the efficiency is a function of neutron energy, the energy bin was varied in the data analysis of the second experiment, and the efficiencies were calculated for $\Delta E = 0.4$ MeV and 0.8 MeV, as shown in Figures 3.28 and Figure 3.29.

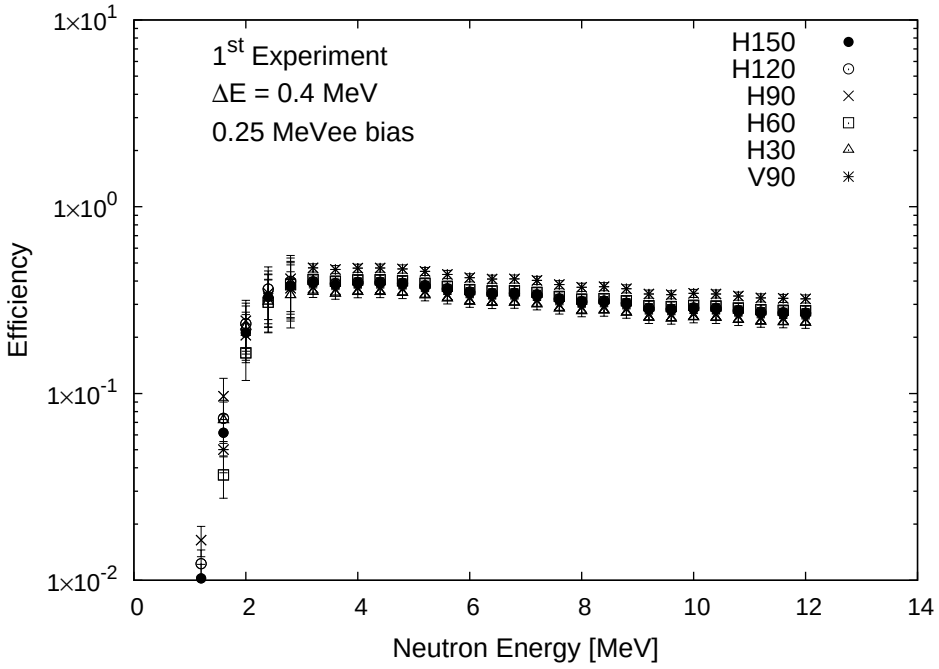

Figure 3.27: Neutron detection efficiencies used in analysis of 17 MeV photon for the fist experiment.

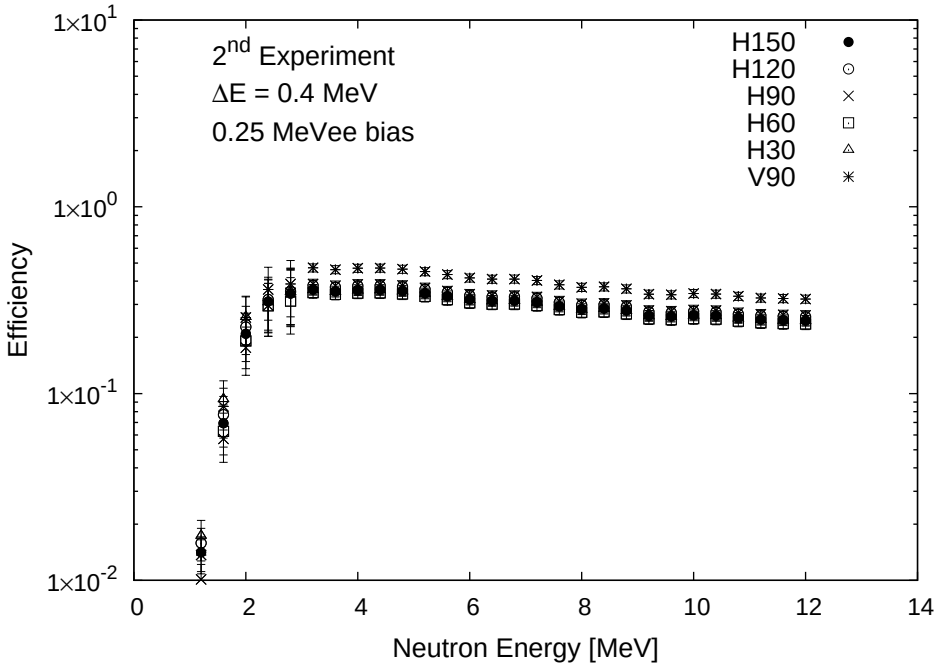

Figure 3.28: Neutron detection efficiencies used in the data analysis of 14 MeV and 17 MeV photons in the second experiment.

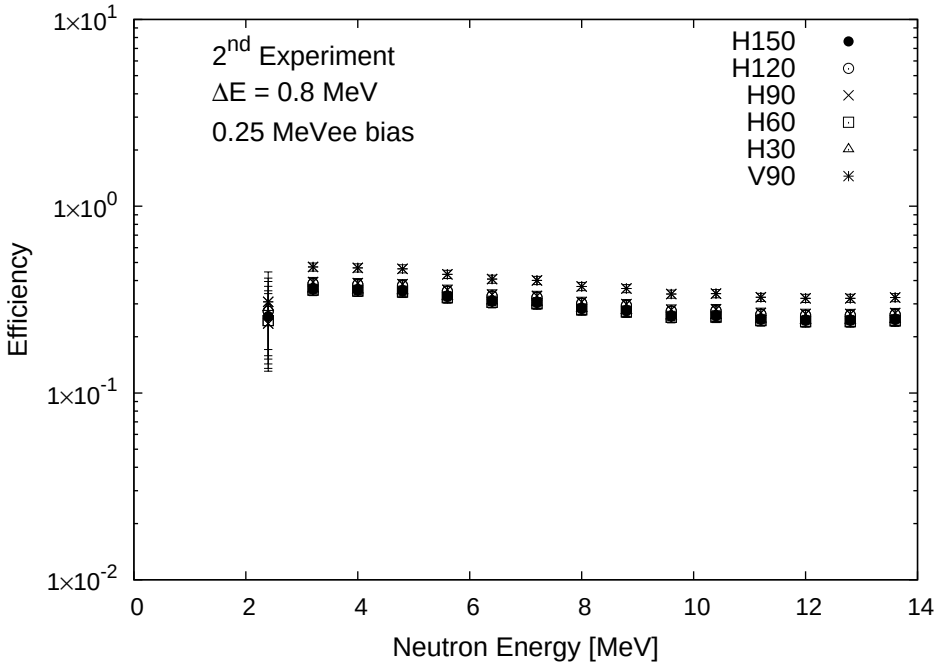

Figure 3.29: Neutron detection efficiencies used in the analysis of 20 MeV photons in the second experiment.

3.8 Uncertainties

As expressed in Equation 3.1, the uncertainty in the DDX value is affected by different components. The uncertainties considered in this study are listed in Table 3.7. They include the statistical uncertainty of neutron events detected in each NE213 detector $Y(E)$, the uncertainty in the number of LCS photons ϕ, the uncertainty in the solid angle Ω, and the uncertainty in the efficiency of neutron detection $\varepsilon(E)$. The statistical uncertainty of $Y(E)$ was calculated by taking the square root of the number of neutrons detected, and the values of each detector ranged from 4.5% to 15%. The uncertainty of ϕ was determined by calculating the statistics of the number of LCS photons while considering the energy resolution of the PLS, and this value was evaluated to be 5%. The uncertainty in Ω was affected by the detector position, and this value was 0.2%. The uncertainty in $\varepsilon(E)$ was related to the accuracy of the SCINFUL-QMD code used in the estimation of the detection efficiency, and this value was 5%.

Table 3.7: List of uncertainties and their corresponding numerical values.

Uncertainty	[%]
Statistics of neutron events (Y(E))	4.5-15
Number of photons ϕ	5
Solid angle	0.2
Detection efficiency ($\varepsilon(E)$)	5

3.9 Comparison of DDX data obtained from two experiments

The goal of this section is to check the consistency of the DDX data of the (γ,xn) reaction on the Au target using 17 MeV photons which were observed in both the experiments. The difference in the experimental setups was mentioned in section 2.1.2. The DDX data at H150, H120, H90, V90, H60, and H30 were shown in Figure 3.30 to Figure 3.35. The DDX data obtained in the second experiment are greater than those obtained in of the first experiment. Figure 3.31 indicates that the DDX data obtained in the second experiment are 1.3 times the DDX data at H120. For H90, Figure 3.32 shows a large difference data of the two experiments. This difference can be seen clearly in the neutron energy range of 7 – 10 MeV.

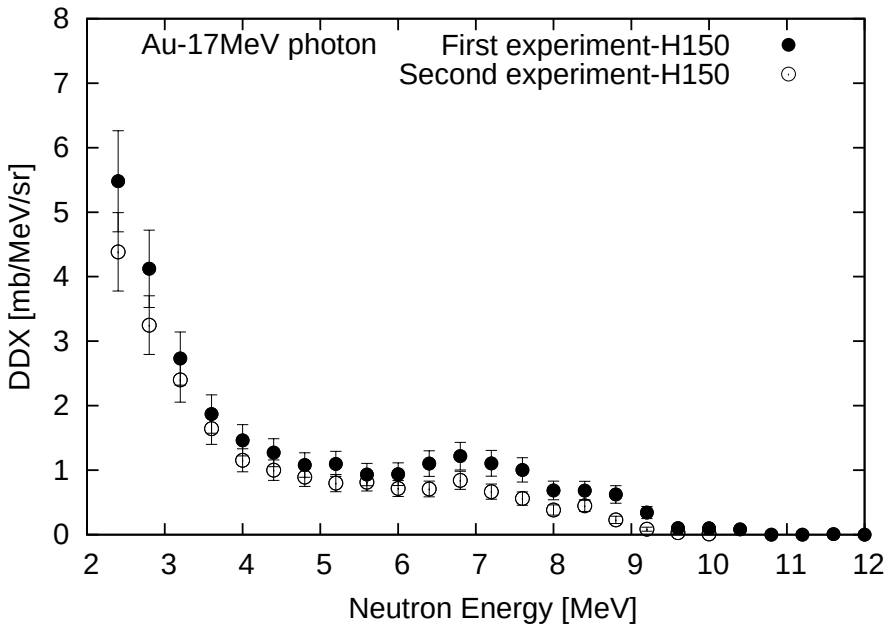

Figure 3.30: DDX results of Au at H150 obtained in both experiments.

In the second experiment, small neutron detectors and lead blocks were added to the first experimental setup. The small detectors were positioned 40 cm away from the target. The lead blocks were placed near the PLS monitor to shield the photon to neutron detectors. In addition, the positions of neutron detectors, labeled H150,

H120, and H90, were quite close the lead blocks (these can be seen in Figure 2.6). Thus, scattering neutrons from the background were able to contribute to the photoneutron data. This could be studied using Monte Carlo calculation; however, such a calculation has not yet been performed in my work and is a task for the future.

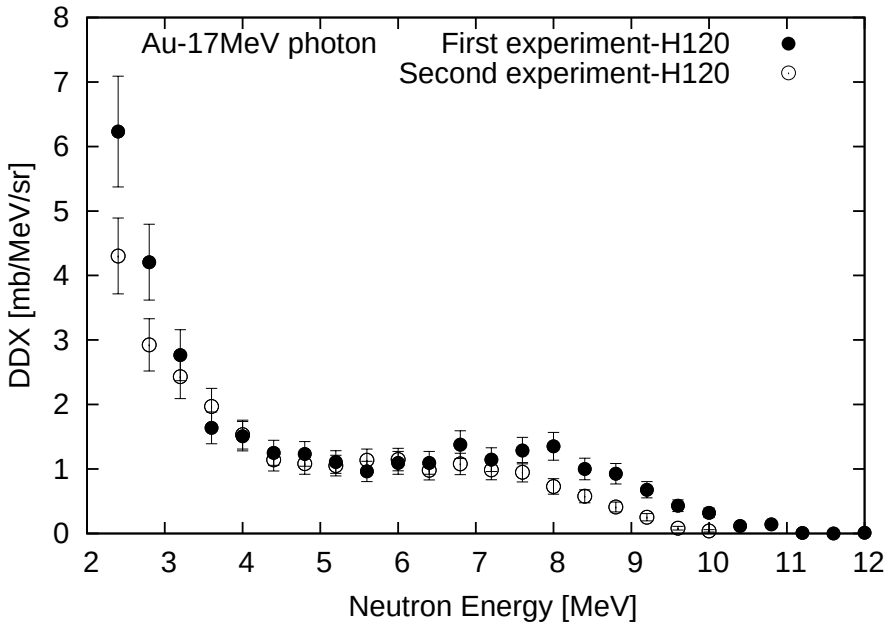

Figure 3.31: DDX results of Au at H120 obtained in both experiments.

On the order hand, for the data at V90, the DDX data in the first experiment were consistent with those in the second experiment, except for energies less than 3 MeV. Correspondingly, the data at H60 in the first experiment were also similar to the data in the second experiment, while the H30 data showed slight differences for neutron energies below 4 MeV. The DDX data for Cu and Ti are compared in Appendix A.

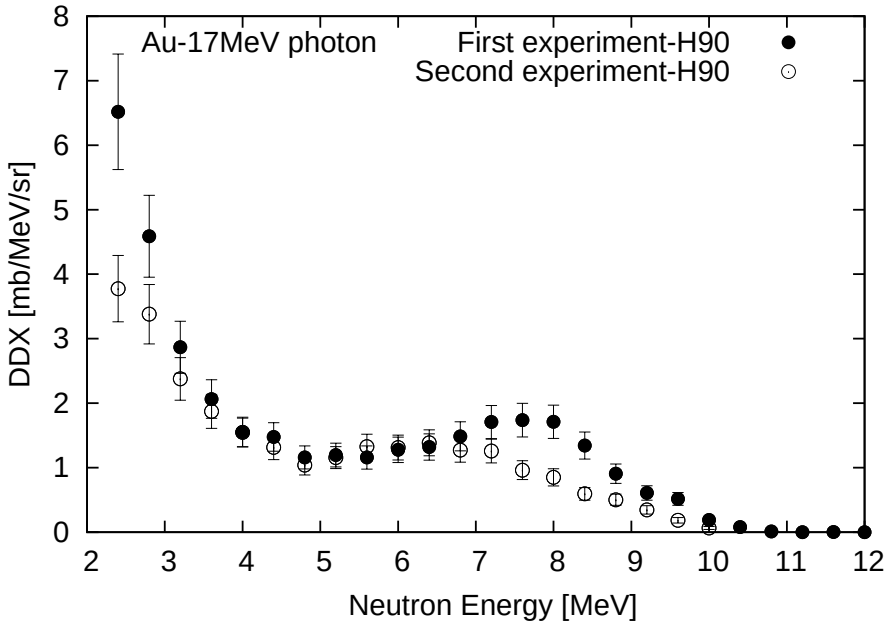

Figure 3.32: DDX results of Au at H90 obtained in both experiments.

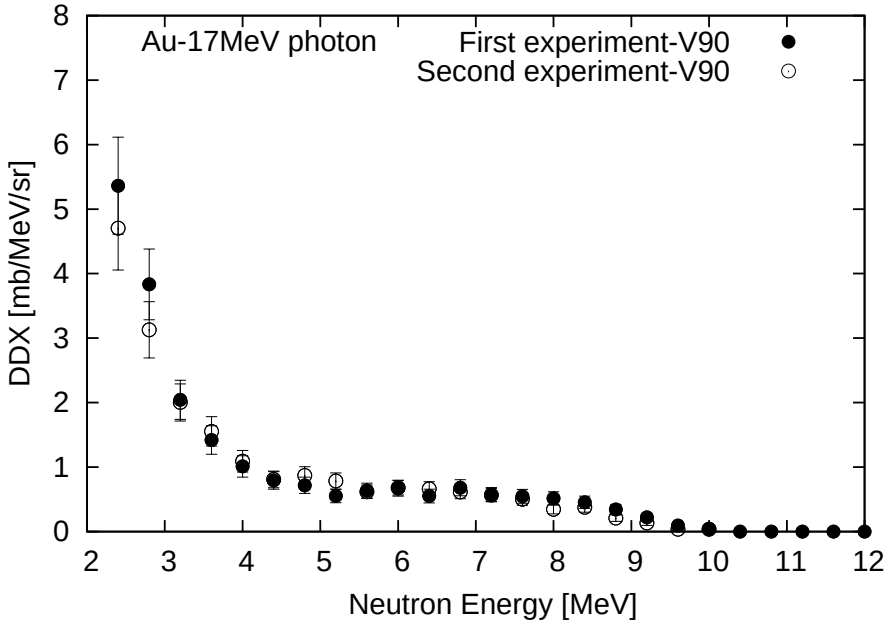

Figure 3.33: DDX results of Au at V90 obtained in both experiments.

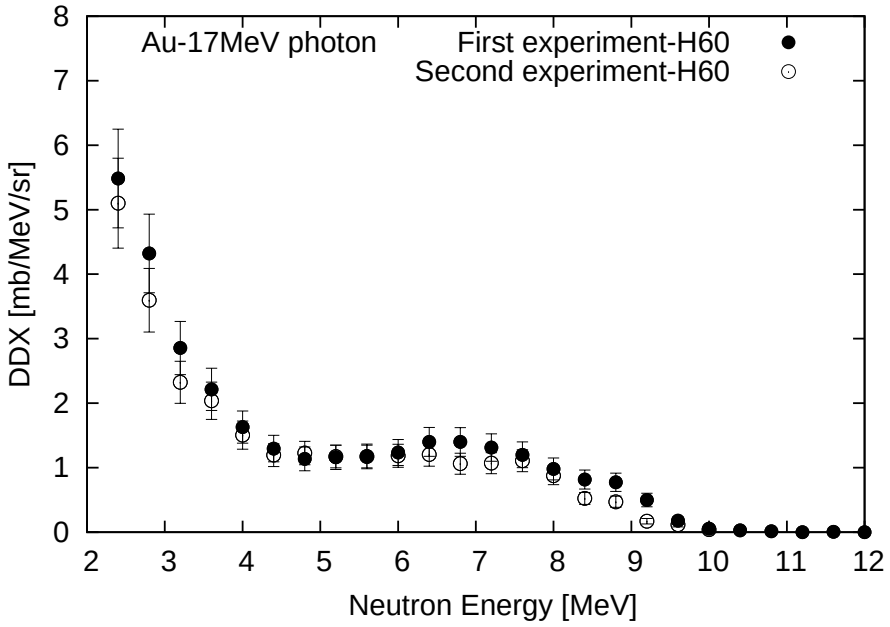

Figure 3.34: DDX results of Au at H60 obtained in both experiments.

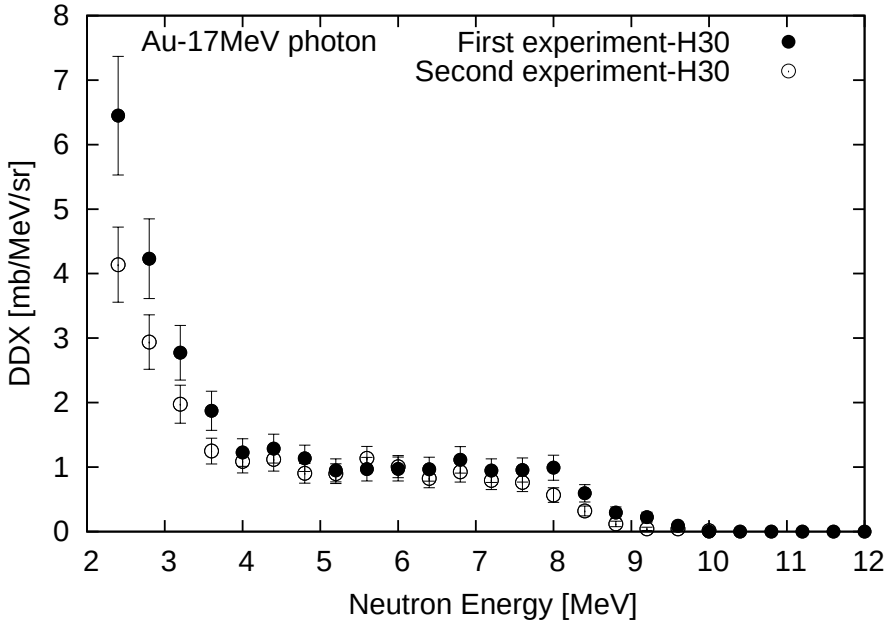

Figure 3.35: DDX results of Au at H30 obtained in both experiments.

Chapter 4

Theoretical calculations and nuclear data

In order to verify the accuracy of the theoretical model's results and nuclear data on DDXs, the photoneutrons were computed for the target materials studied in Chapter 2 through Monte Carlo calculation, the evaluated nuclear data, and the nuclear reaction model. The calculation of the DDX is presented in the following sections:

4.1 PHITS code calculation

4.2 JENDL/PD photonuclear data library

4.3 CoH_3 code

4.4 Comparison of the raw DDX data from JENDL and CoH_3

4.5 Natural abundance of isotopes

4.6 Photon energy width

4.7 Neutron energy width

4.8 Comparison of DDXs from theoretical calculation and nuclear data

Subsequently, these DDXs will be compared with the experimental data in Chapter 5.

4.1 PHITS code calculation

In addition to the measured DDXs of the photoneutrons from the (γ,xn) reaction, the DDXs are calculated by Monte Carlo transport simulation code, Particle Heavy Ion Transport code System (PHITS) [52] version 3.20. PHITS can handle the transport for neutrons, protons, electrons, and heavy ions using reaction models and data libraries. For simulating a photonuclear reaction, the reaction cross section from JENDL/PD-2004 [16] has been employed. Subsequently, a photoneutron energy spectrum has been generated using GEM [15] for GDR region. Above this region, the QD process is modeled using the intranuclear cascade (INC) model. The DDXs were calculated using PHITS for Pb, Au, Sn, Cu, Fe and Ti targets. In this section, the calculation results for Au are presented to check the target thickness effect and angular distribution of neutrons. The results for the other targets are similar to those for Au.

4.1.1 Calculation geometry

The geometry considered in the DDX calculation in PHITS was the same as that of the first experiment. The target was a thin cylindrical pill placed at the center of the geometry. The NE213 detectors were simulated as cylinders having diameter and thickness of 12.7 cm, without containing the NE213 material in their volumes defined as the detection region. The distances from the target to the detection regions were the same as those in Table 2.2. Figure 4.1 shows the geometry used in the DDX calculation, where the green cylinders are the detection regions and a yellow one is the target. The photon beam was simulated as a pencil beam traveling from the left to right of the geometry.

The DDXs were determined using T-cross tally. Neutrons produced through the (γ,xn) reaction were counted in the detection regions. Subsequently, the DDXs were calculated by normalizing the number of neutrons with the upcoming photon source, the number of target atoms, and solid angle.

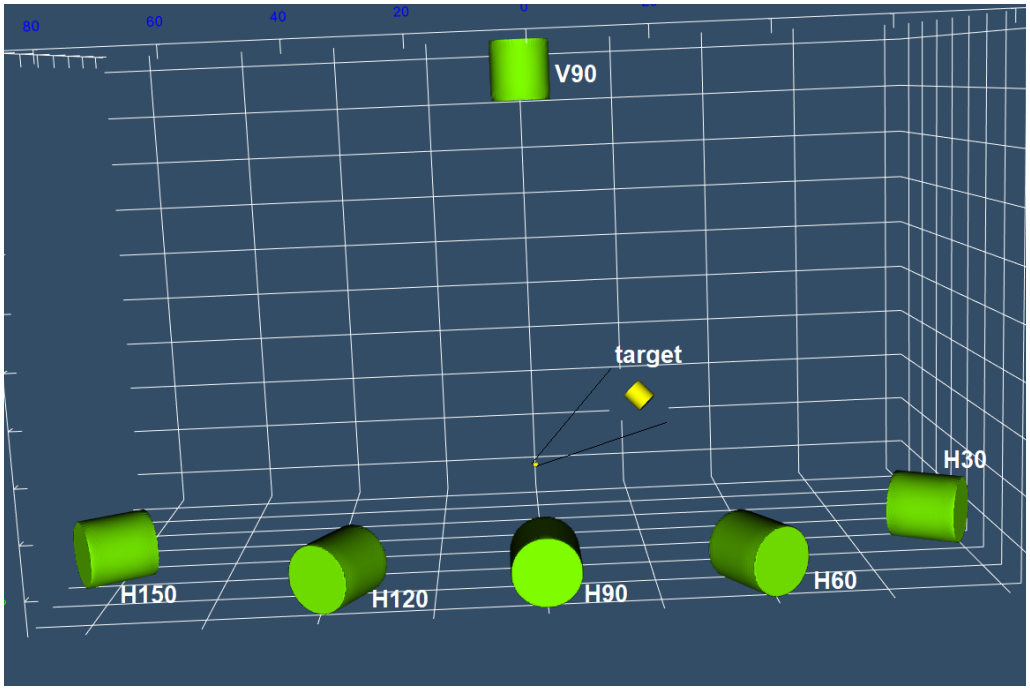

Figure 4.1: Geometry of the DDX calculation in PHITS.

4.1.2 Target thickness effect

As discussed in section 3.5 and session 3.6, the attenuation of photons and neutrons in the target affected the DDX results. Thus, to confirm the effect of attenuation in the PHITS calculation, the DDX calculation was performed with the same target diameter of 5 μm but different target thicknesses of 5 μm, 1 cm, and 4 cm.

Figure 4.2 shows the DDX results from the PHITS calculation for Au targets with the different thicknesses. The DDX for a thickness of 5 μm is 2.7 times greater than that of 1 cm and 5 times greater than that for 4 cm. These reductions are caused by photon attenuation in the target. As shown in section 3.5, the attenuation of photons was already corrected based on calculation. Therefore, a target thickness of 5 μm was chosen in the subsequent DDX calculations without considering the actual target thickness in the experiment.

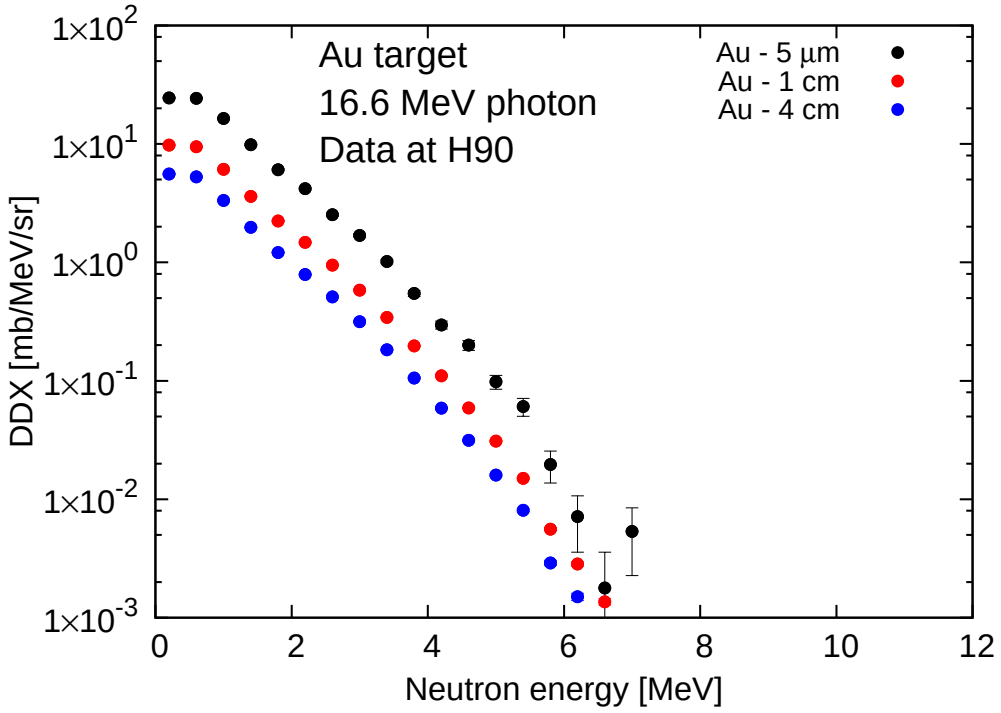

Figure 4.2: DDX data at different Au thicknesses. Black points are the DDX results for an Au thickness of 5 μm, red points are those for a thickness of 1 cm, and blue points are those for a thickness of 4 cm.

4.1.3 Angular distribution of neutrons

In the experiment, the neutron detectors were placed at different angles to measure the angular distribution of the photoneutrons. In the calculation, the green detection regions at different angles, as shown in Figure 4.1, were used to account for the angular distribution. Figure 4.3 displays the ratios of DDXs for an Au thickness of 5 μm at different angles to that at V90. The ratio ranges from 0.9 to 1.1 for all energies below 6 MeV. The neutron emission of PHITS code does not show the angular distribution of the photoneutron production.

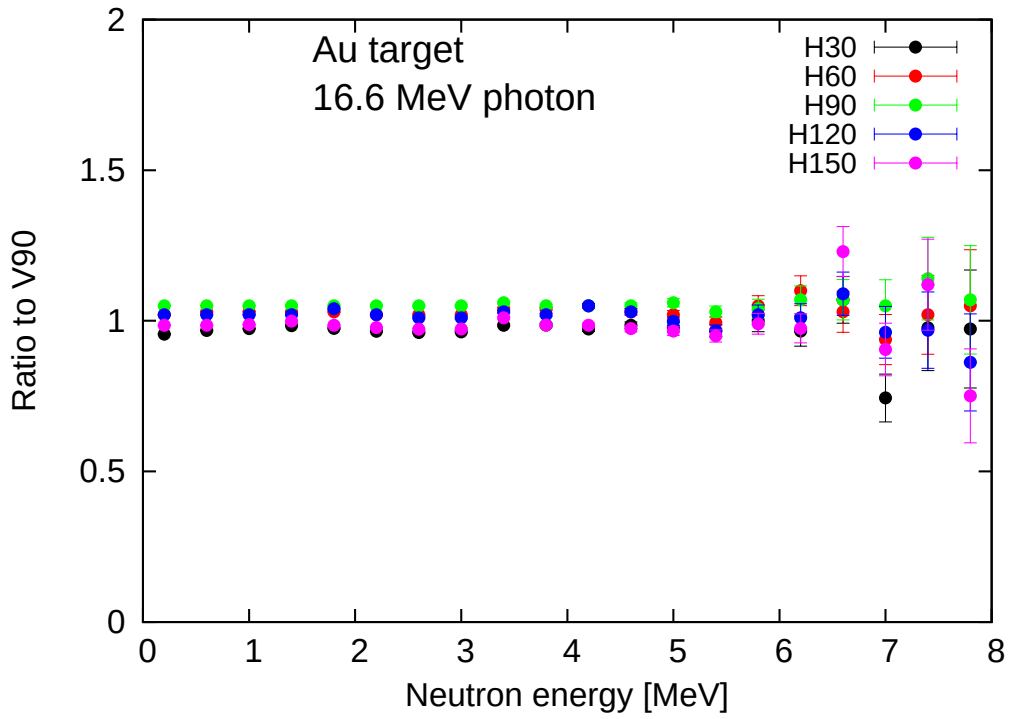

Figure 4.3: Ratios of DDX data for Au at H30, H60, H90, H120, and H150 to that at V90.

4.2 JENDL/PD photonuclear data library

The DDX data were extracted from the photonuclear data library with a Python program [53]. The DDX data of target isotopes are combined to make that of natural element with the abundance of isotope in each target. In addition, smearing was applied to account for the effect of photon width and neutron energy resolution. Subsequently, the DDXs will be compared with the experimental results in chapter 5.

Table 4.1 shows the natural abundance of isotopes in target material and the reaction Q-value for each isotope. The dominant isotopes in the targets are ^{208}Pb, ^{120}Sn, ^{63}Cu, ^{56}Fe, and ^{48}Ti. The process of two-neutron emission is possible on

Table 4.1: List of isotopes and Q-values for the calculation for natural target abundances in this study. The Q-values are quoted from Reference [56]

Isotope	Abundance [%]	Q-value [MeV]	
		(γ,n)	(γ,2n)
^{206}Pb	24.1	8.1	14.8
^{207}Pb	22.1	6.7	14.8
^{208}Pb	52.4	7.4	14.1
^{197}Au	100	8.1	14.7
^{116}Sn	14.7	9.6	17.1
^{117}Sn	7.7	6.9	16.5
^{118}Sn	24.3	9.3	16.3
^{119}Sn	8.6	6.5	15.8
^{120}Sn	32.4	9.1	15.6
^{122}Sn	4.6	8.8	14.9
^{124}Sn	5.6	8.5	14.4
^{63}Cu	69.17	10.9	19.7
^{65}Cu	30.83	9.9	17.8
^{54}Fe	5.9	13.38	24.1
^{56}Fe	91.72	11.2	20.5
^{57}Fe	2.12	7.65	18.8
^{46}Ti	8.1	13.2	22.7
^{47}Ti	7.3	8.9	22.1
^{48}Ti	73.8	11.6	20.5
^{49}Ti	5.5	8.14	19.77
^{50}Ti	5.4	10.94	19.1

Pb, Au, and Sn targets with 16.6 MeV photons because the Q-value of the (γ,2n) reaction was lower than the energy of the incident photon.

Figure 4.4 to Figure 4.9 display the raw DDX data extracted from JENDL-2004 and JENDL/PD-2016.1 for ^{208}Pb, ^{197}Au, ^{120}Sn, ^{63}Cu, ^{56}Fe, and ^{48}Ti with 16.6 MeV photons. JENDL-2004 does not contain the data of ^{120}Sn and ^{48}Ti; thus, the raw DDX data were not plotted in Figure 4.6 and Figure 4.9.

The DDX results extracted from JENDL-2004 are shown in black lines. JENDL-2004 reproduced a smoother neutron spectrum than the spectrum of JENDL/PD-2016.1. Fluctuation points exist on the spectra because JENDL/PD-2016.1 reproduces the neutron spectrum by considering discrete levels in residual nuclei, while JENDL-2004 dose not. This will be explained in section 4.3.

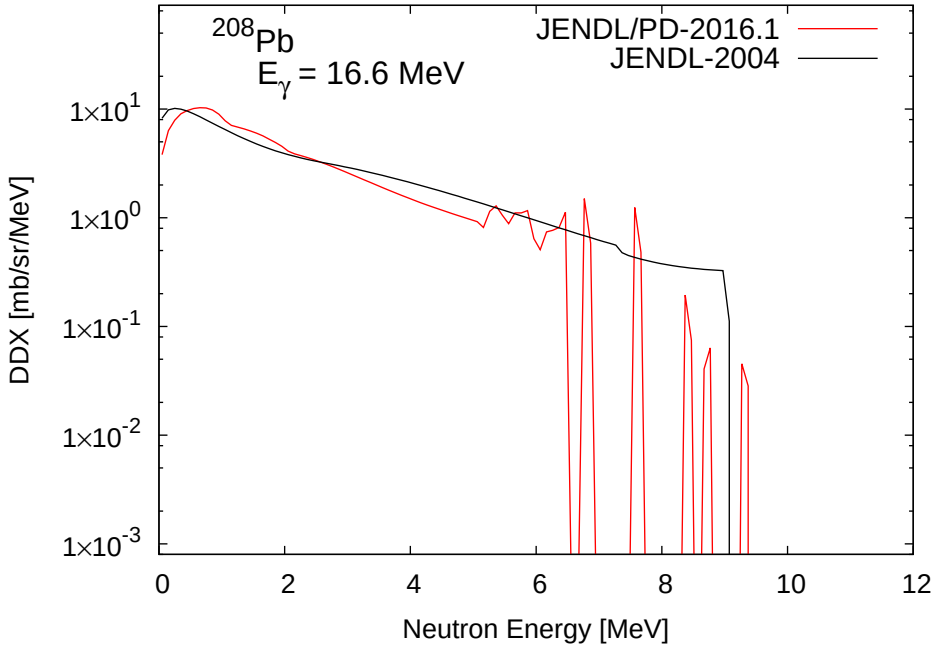

Figure 4.4: DDX results extracted from JENDL for ^{208}Pb.

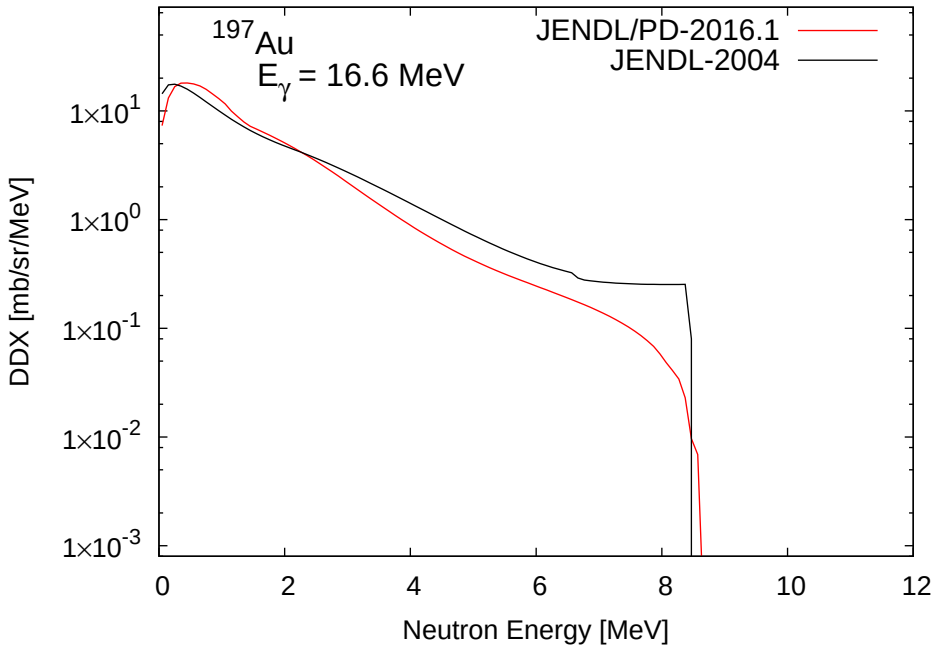

Figure 4.5: DDX results extracted from JENDL for ^{197}Au.

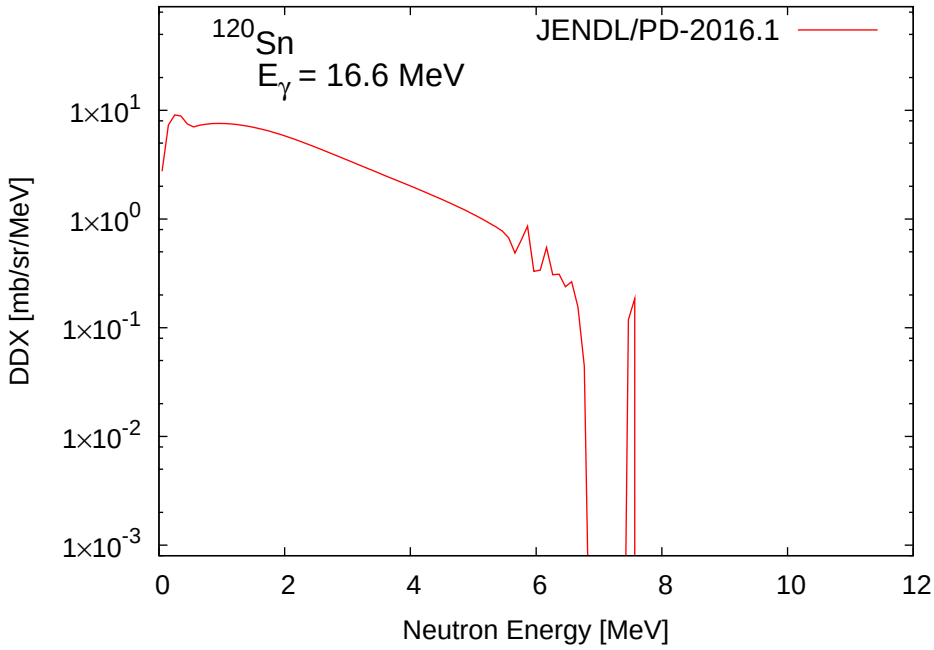

Figure 4.6: DDX results extracted from JENDL for ^{120}Sn.

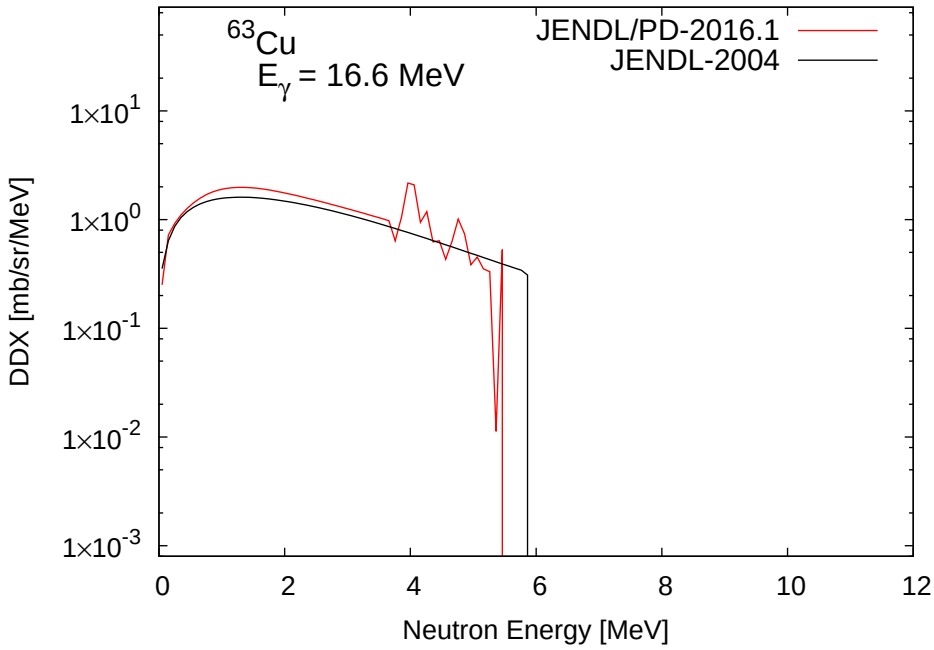

Figure 4.7: DDX results extracted from JENDL for ^{63}Cu.

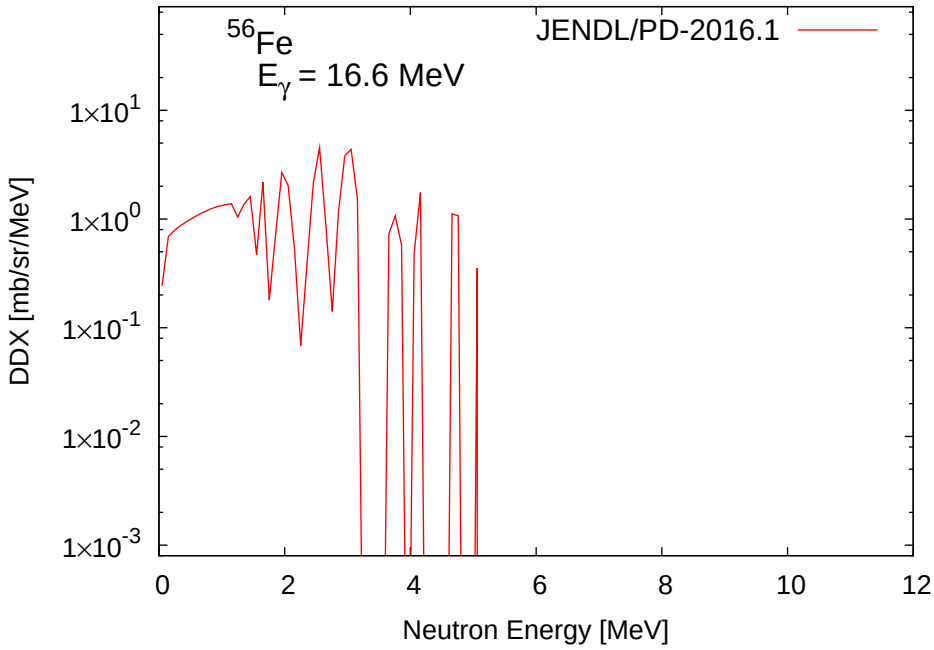

Figure 4.8: DDX results extracted from JENDL for ^{56}Fe.

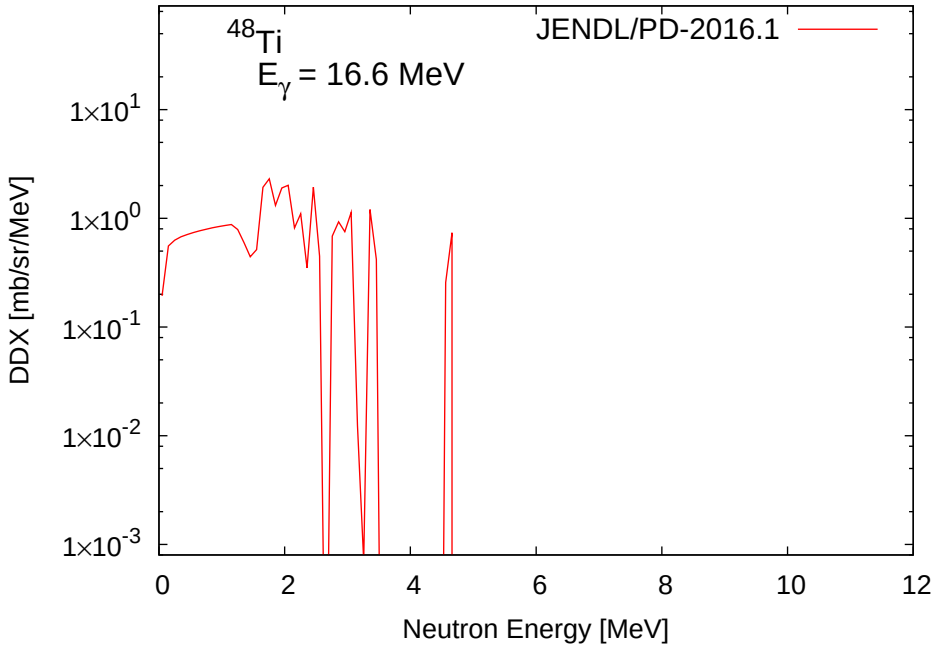

Figure 4.9: DDX results extracted from JENDL for ^{48}Ti.

4.3 CoH_3 code

The coupled-channels Hauser-Feshbach (CoH_3) code was developed by Los Alamos National Laboratory and is a main tool for calculating nuclear reactions for A > 20. The code can provide reaction cross sections as well as energy and angular distributions of the secondary particles [24] based on the Hauser-Feshbach model by considering pre-equilibrium processes.

Figures 4.10, 4.12, 4.14, 4.16, 4.18, and 4.20 show schematic diagrams of the (γ,n) reaction for ^{56}Fe, ^{208}Pb, ^{197}Au, ^{120}Sn, ^{63}Cu, and ^{48}Ti, respectively, which were excited by incident photons. These figures were plotted using data of discrete levels in CoH_3 code [24]. The left side of these figures indicates the discrete levels in MeV of the residual nuclei. The right one shows the excitation of the target nuclei by the incident photon with energy its distribution. This energy distribution of the incident photon is same with Figure 4.40.

Figures 4.11, 4.13, 4.15, 4.17, 4.19, and 4.21 show the raw DDX of the photoneutrons of the (γ,xn) reaction on ^{56}Fe, ^{208}Pb, ^{197}Au, ^{120}Sn, ^{63}Cu, and ^{48}Ti, which were calculated using the CoH_3 code with incident photon. The shape fluctuates on these figures is because CoH_3 (as well as JENDL/PD-2016.1) accounts for the discrete levels in the residual isotope for neutron emission. The energy of emitted neutrons can be calculated by Equation 4.1:

$$E_n = E_\gamma - Q_{val} - E_{level} \tag{4.1}$$

where

E_n is the neutron energy,

E_γ is the energy of the incident photons,

Q_{val} is the Q-value of the reaction, and

E_{level} is the energy at each discrete level.

High-energy neutrons were emitted with the transition from the high excited

states, as expressed by solid arrows in Figures 4.10, 4.12, 4.14, 4.16, 4.18, and 4.20, to the ground or lower-lying states on residual nuclei. On the other hand, low-energy neutron emission corresponds to the transition from higher excited states on the isotope to the lower excited states on the residual nuclei, as shown by dashed arrows in these figures.

In Figure 4.10, the excited states of ^{56}Fe decay to the ground state and excited states of ^{55}Fe through neutron emission. Thirty discrete levels of ^{55}Fe are included in this code, the energy of which is up to 3.4569 MeV, as shown in Figure 4.10. Following Equation 4.1, in Figure 4.11, fluctuation points can be explained according to the low-lying discrete levels. The neutron energy at these fluctuation points ranges is from 1.9431 MeV up to 5.4 MeV, corresponding to discrete levels from 3.4569 MeV down to 0 MeV.

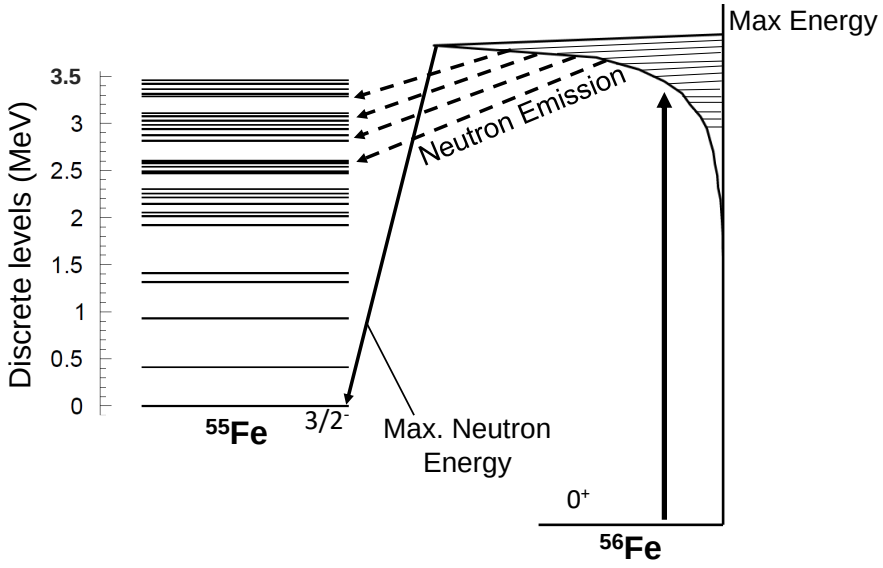

Figure 4.10: Schematic view of the (γ,n) reaction on ^{56}Fe excited by incident photons.

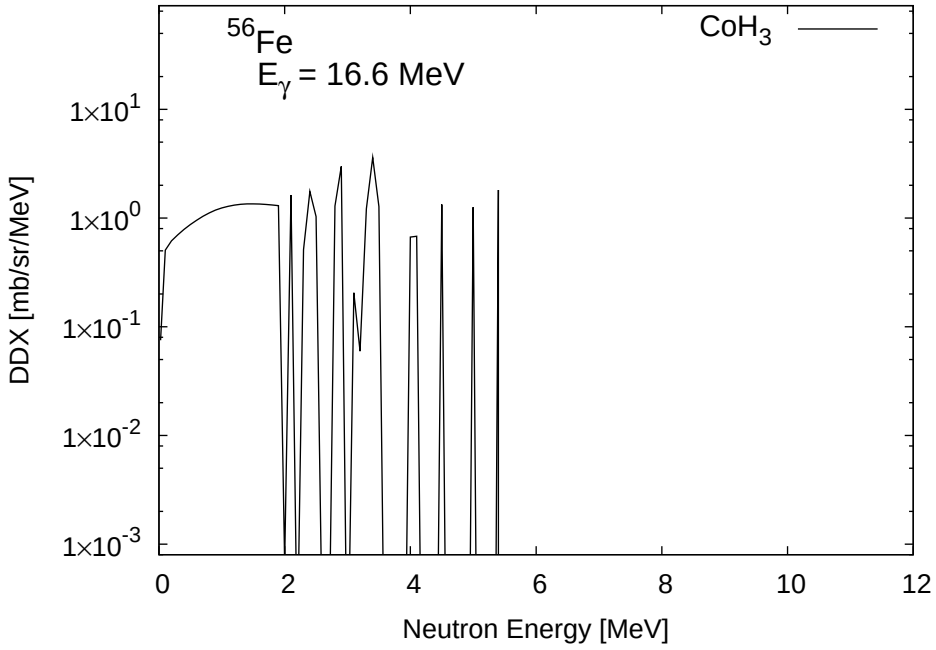

Figure 4.11: DDX results calculated using CoH_3 for ^{56}Fe

The discrete levels of the residual isotope after neutron emission, ^{207}Pb, are shown in Figure 4.12. The energy of the levels ranges from 4.25 MeV down to 0. Further calculation using Equation 4.1 with 16.6 MeV photons indicates that the fluctuating points on the neutron spectrum, as shown in Figure 4.13, ranges from 4.95 MeV to 9.2 MeV.

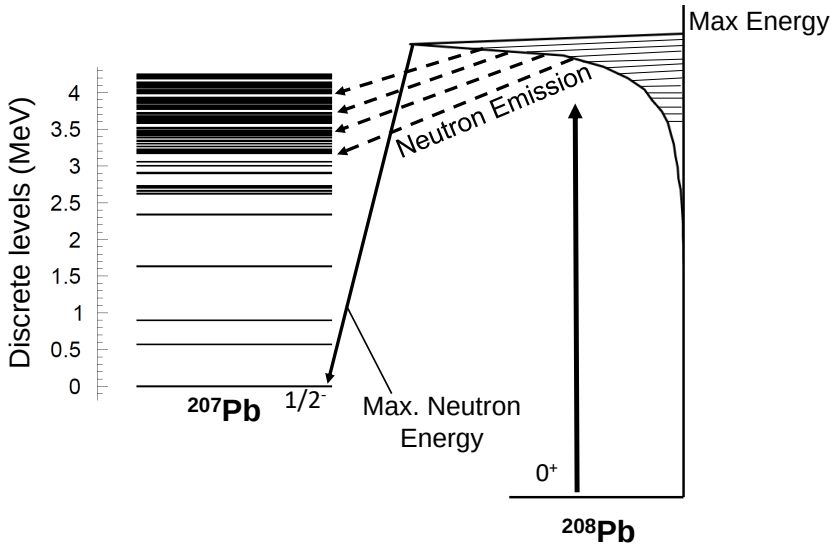

Figure 4.12: Schematic view of the (γ,n) reaction on ^{208}Pb excited by incident photons.

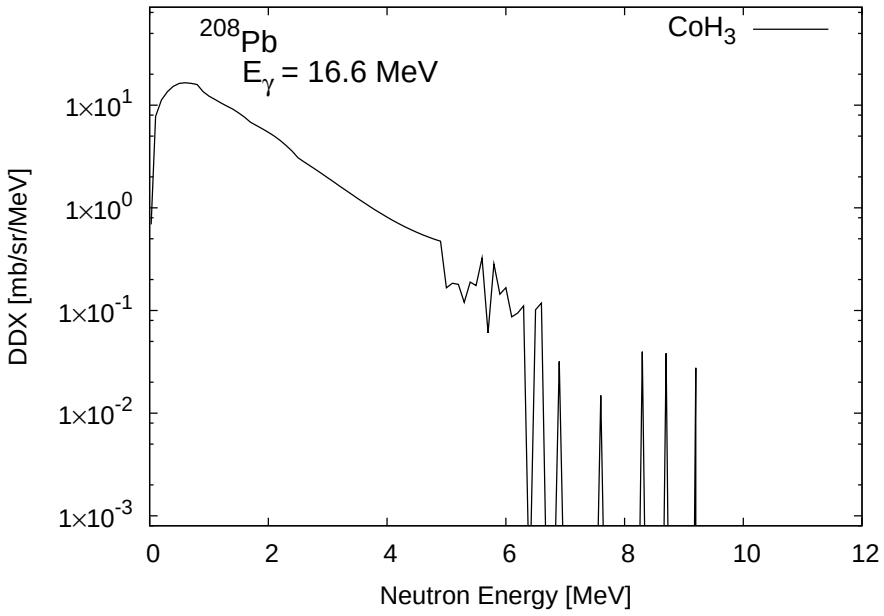

Figure 4.13: DDX results calculated using CoH_3 for ^{208}Pb.

Similarly, discrete levels of ^{196}Au are shown in Figure 4.14; the energy is up to 0.8297 MeV. Fluctuating points in the energy range of 7.67 MeV – 8.5 MeV still occur on the neutron spectrum, but they are not displayed in Figure 4.15, because their DDX values are lower than 10^{-3} mb/sr/MeV.

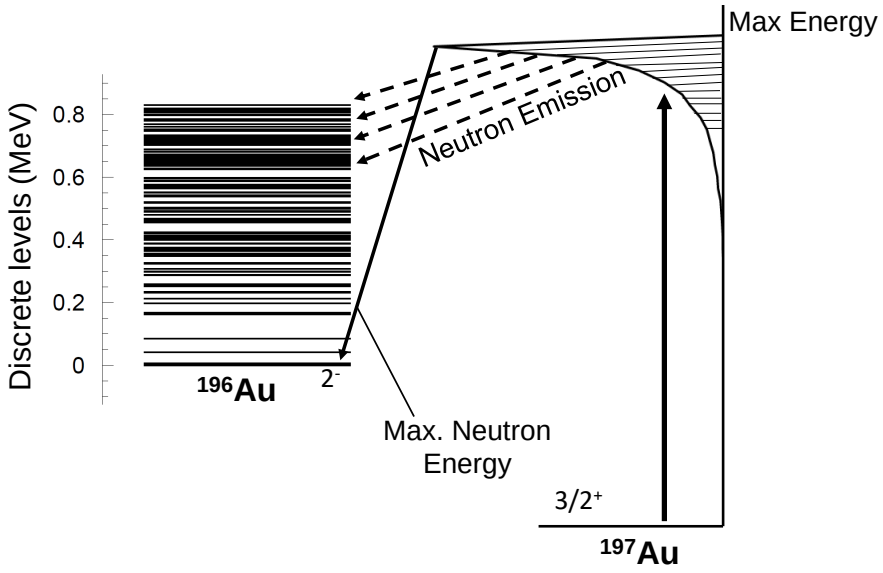

Figure 4.14: Schematic view of the (γ,n) reaction on ^{197}Au excited by incident photons.

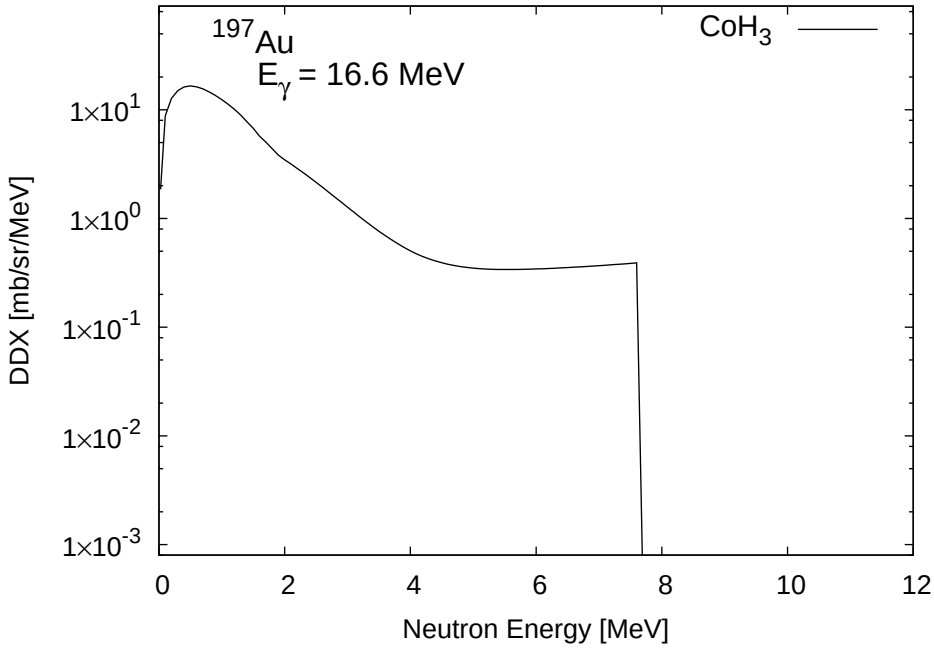

Figure 4.15: DDX results calculated using CoH_3 for ^{197}Au.

Figure 4.16 indicates discrete levels of ^{119}Sn after ^{120}Sn emits a neutron. The energy of the levels ranges from 0 to 1.6330 MeV. Thus, the neutron spectrum in Figure 4.17 shows fluctuation from 5.867 MeV to 7.5 MeV.

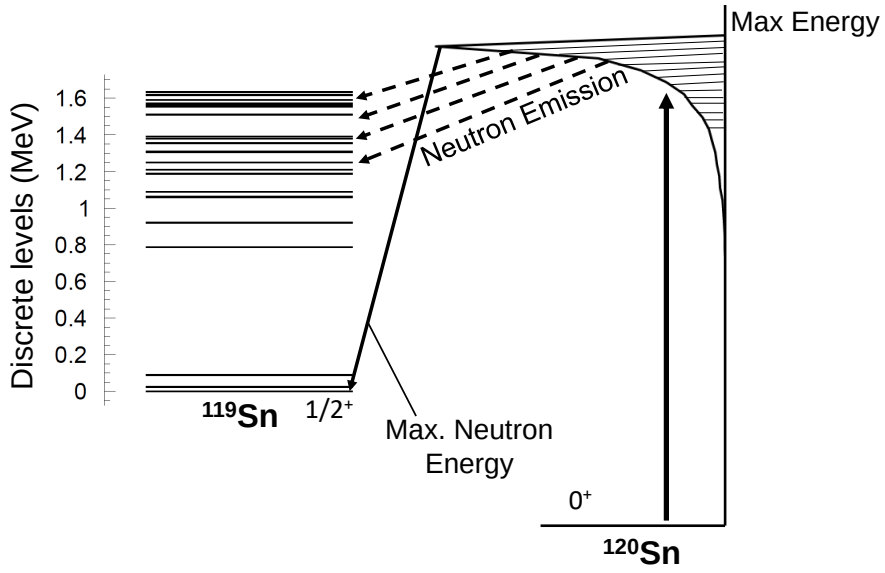

Figure 4.16: Schematic view of the (γ,n) reaction on ^{120}Sn excited by the incident photons.

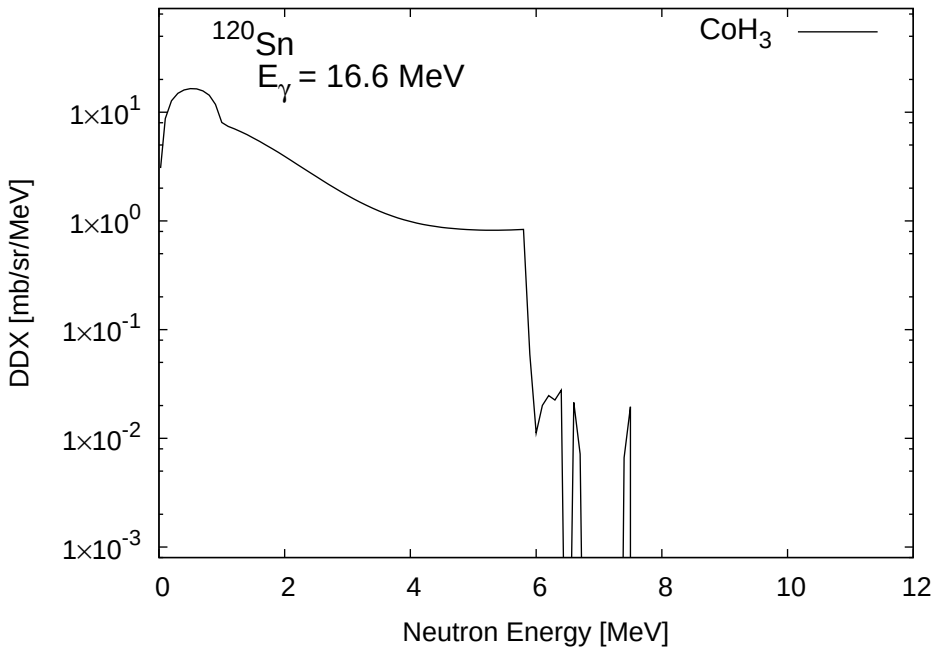

Figure 4.17: DDX results calculated using CoH_3 for ^{120}Sn.

Figure 4.18 shows the excitation of ^{63}Cu by the incident photons and the produced neutrons. The energy of the discrete levels of ^{62}Cu is up to 1.9960 MeV. Figure 4.19 shows fluctuating points in the energy range of 3.704 MeV – 5.7 MeV.

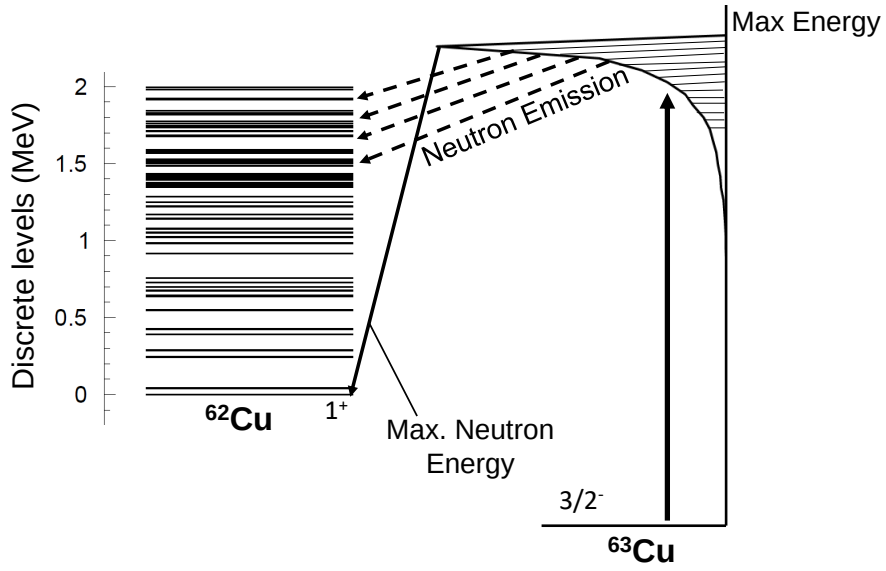

Figure 4.18: Schematic view of the (γ,n) reaction on ^{63}Cu excited by incident photons.

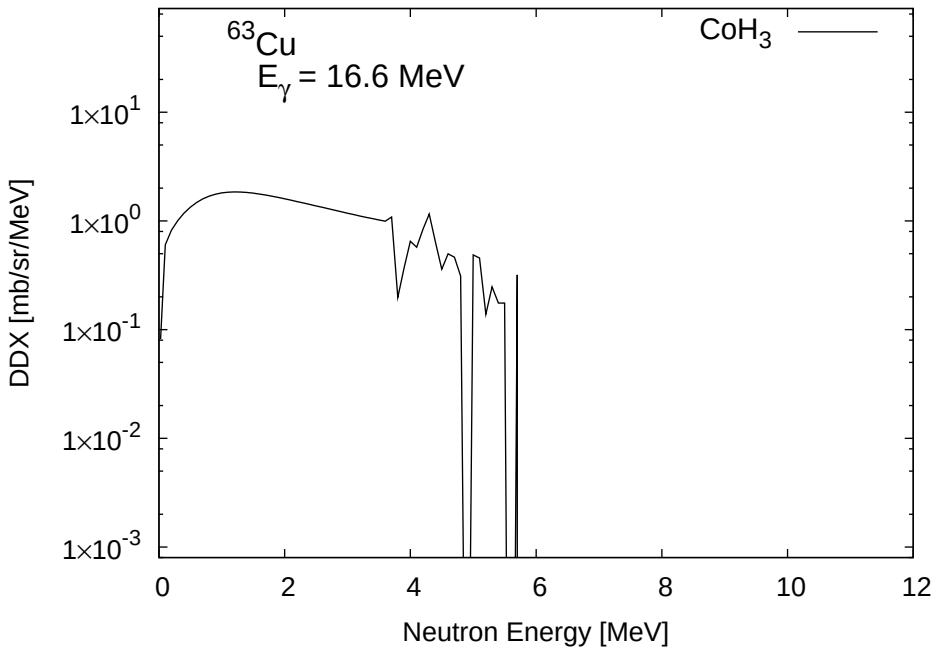

Figure 4.19: DDX results calculated using CoH_3 for ^{63}Cu.

Correspondingly, for ^{48}Ti, as shown in Figure 4.21, the neutron energy fluctuated from 1.41 MeV up to 4.84 MeV because the discrete levels of ^{47}Ti range from 3.5827 MeV down to 0 MeV, as indicated in Figure 4.20.

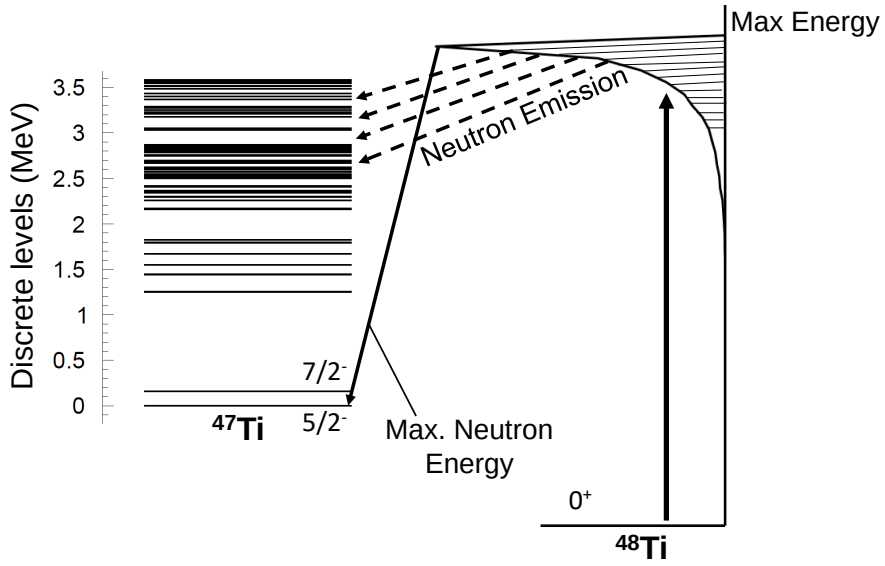

Figure 4.20: Schematic view of the (γ,n) reaction on ^{48}Ti excited by incident photons.

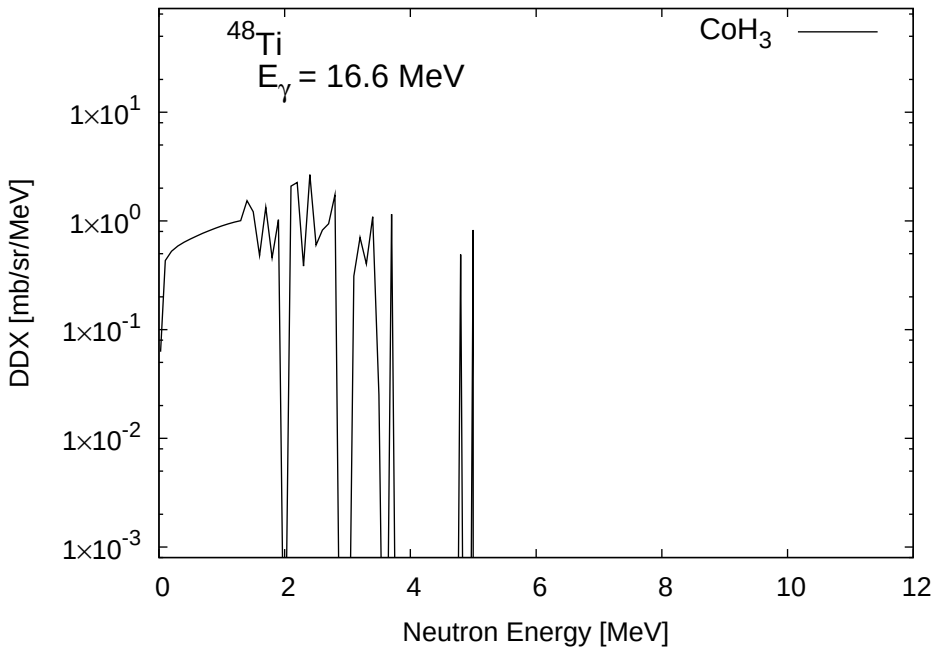

Figure 4.21: DDX results calculated using CoH_3 for ^{48}Ti

4.4 Comparison of the raw DDX data from JENDL and CoH_3

Figure 4.23 shows the DDX results for ^{197}Au. The obtained data of CoH_3 code are indicated in black, the data extracted from JENDL/PD-2016.1 are in red, and the data extracted from the JENDL-2004 data file are in blue. The shapes of neutron energy spectra are different, but the integrated cross sections are comparable. In case of ^{197}Au, the integrated cross sections are 25.3 mb, 28.9 mb, and 28.9 mb for CoH_3, JENDL/PD-2016.1, and JENDL-2004, respectively. For ^{208}Pb, these values are 27.3 mb, 23.1 mb, and 24.2 mb for CoH_3, JENDL/PD-2016.1, and JENDL-2004, respectively.

As discussed in sections 4.2 and 4.3, both CoH_3 and JENDL/PD-2016.1 took the discrete levels into account for neutron emission. However, the fluctuating shapes of these spectra are not identical.

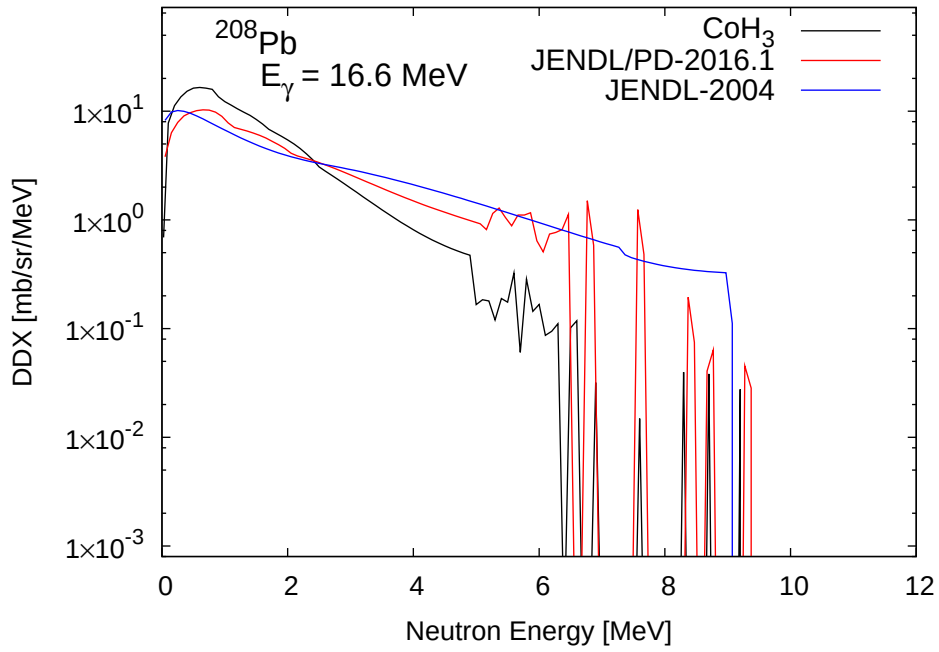

Figure 4.22: Comparison of DDX results of JENDL and CoH_3 for ^{208}Pb.

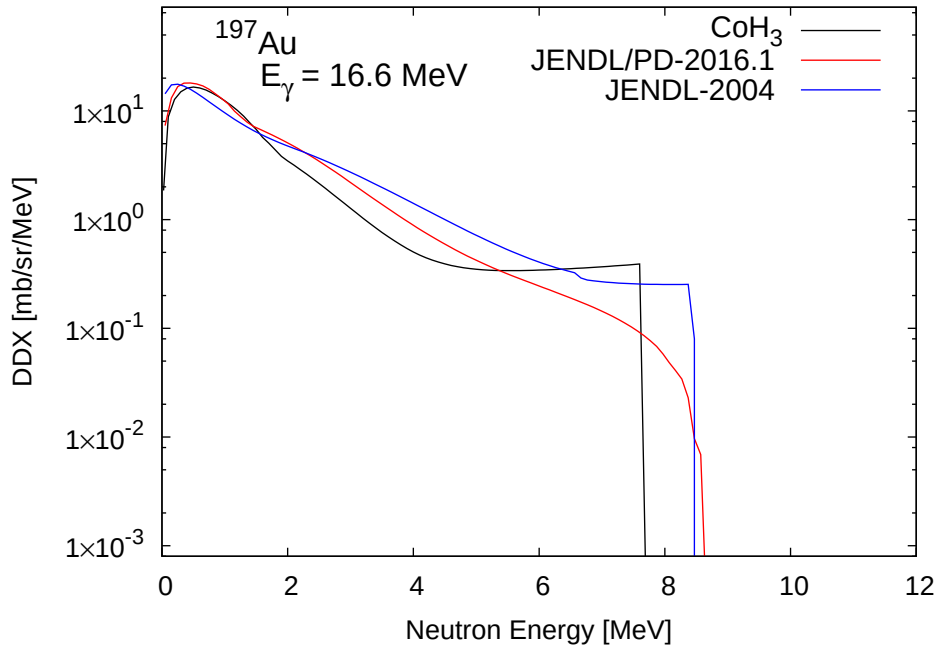

Figure 4.23: Comparison of DDX results of JENDL and CoH_3 for ^{197}Au.

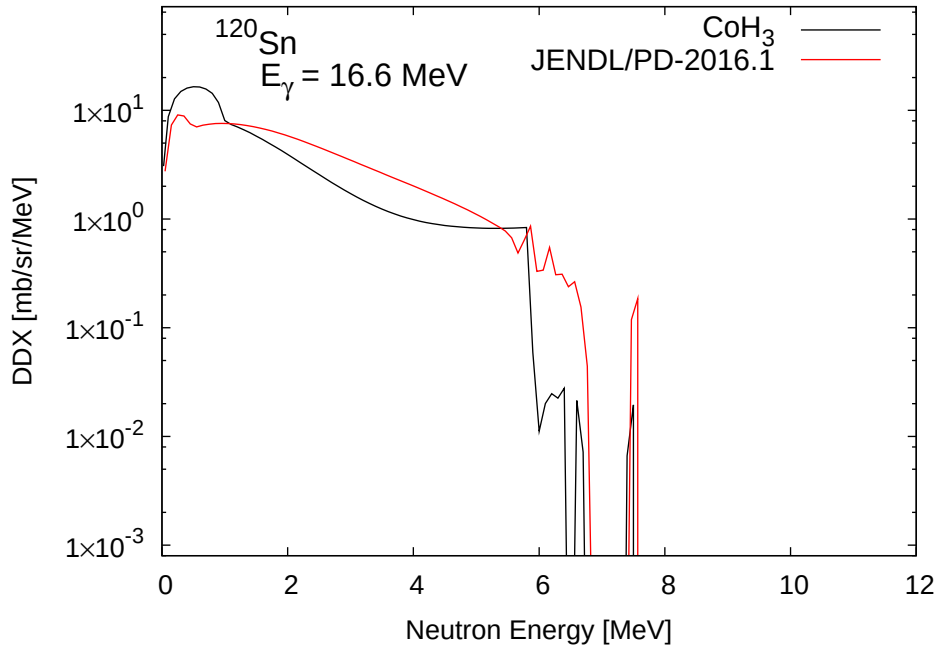

Figure 4.24: Comparison of DDX results of JENDL and CoH_3 for ^{120}Sn.

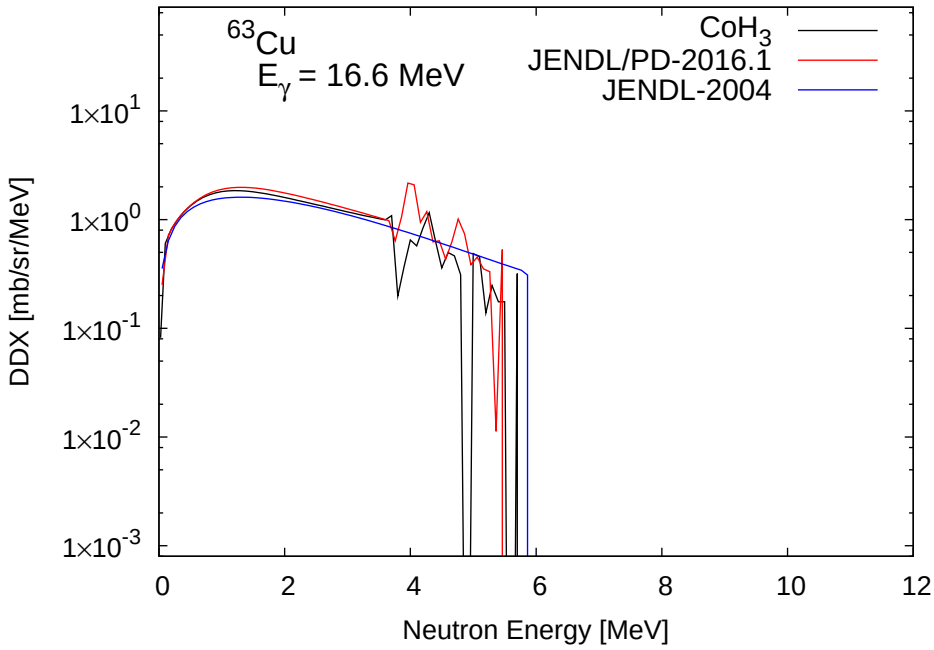

Figure 4.25: Comparison of DDX results of JENDL and CoH_3 for ^{63}Cu.

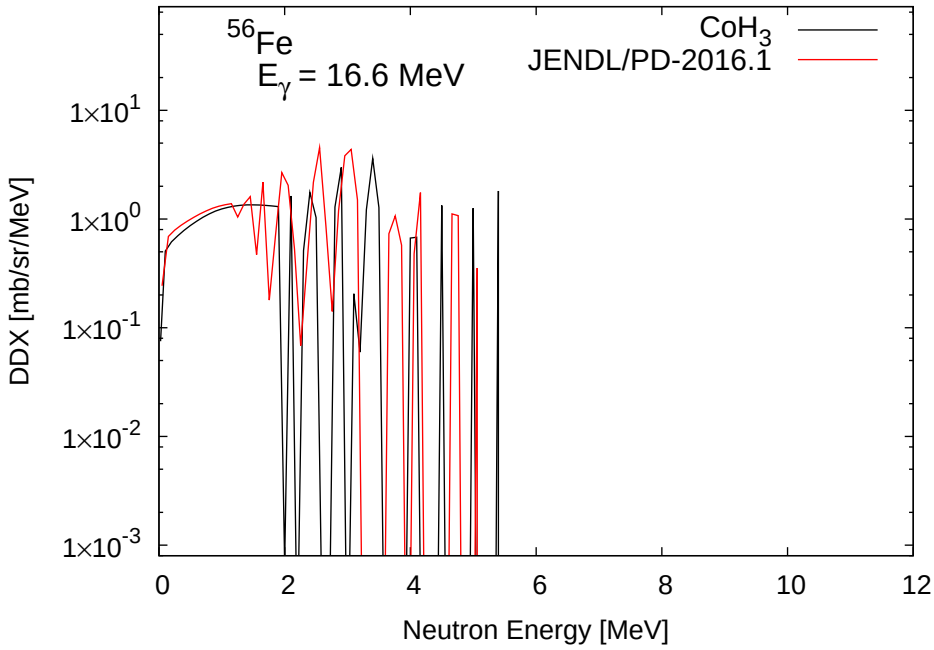

Figure 4.26: Comparison of DDX results of JENDL and CoH_3 for ^{56}Fe.

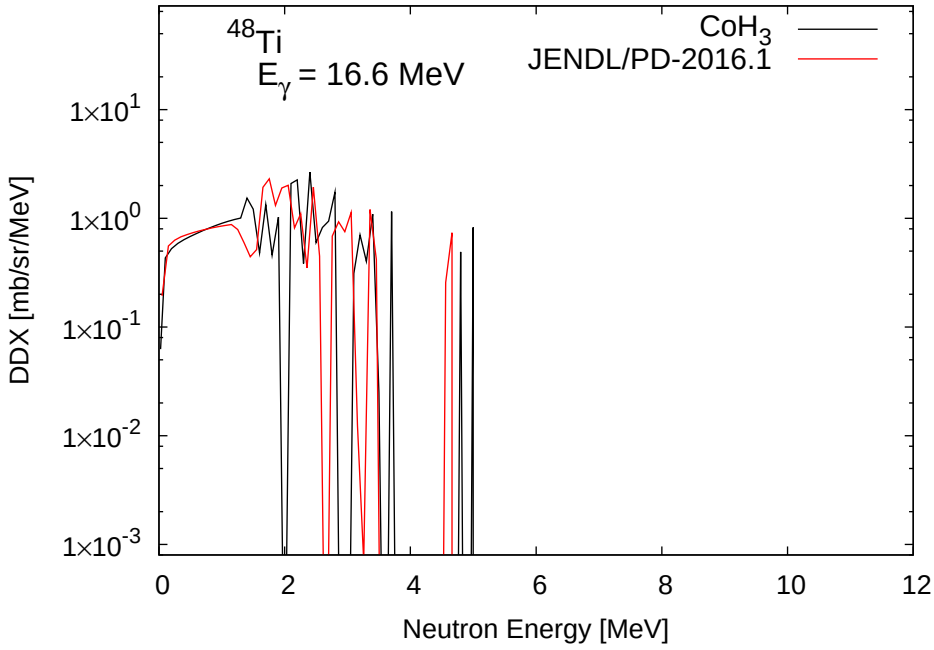

Figure 4.27: Comparison of DDX results of JENDL and CoH_3 for ^{48}Ti.

4.5 Natural abundance of isotopes

The abundances of each target's isotopes were considered in the calculation of the DDXs from the library and CoH_3 code. For the PHITS results, the abundances were automatically taken into account in the PHITS program. The abundance of an isotope was taken into account by considering the sum of the DDX data multiplied by the abundance of the isotope in the target, as reported in Table 4.1. Figure 4.28 to Figure 4.39 display the DDX data obtained by considering the abundance of isotopes in each target for Pb, Sn, Cu, Fe, and Ti targets.

For the Pb target, the dominant isotope is ^{208}Pb, but the Q-value of ^{207}Pb is the minimum at 6.7 MeV. The maximum neutron energy was determined by the Q-value. Thus, the maximum neutron energy is shown in Figures 4.28, 4.29, and 4.30 is approximately equal to 10 MeV because of the contribution of ^{207}Pb.

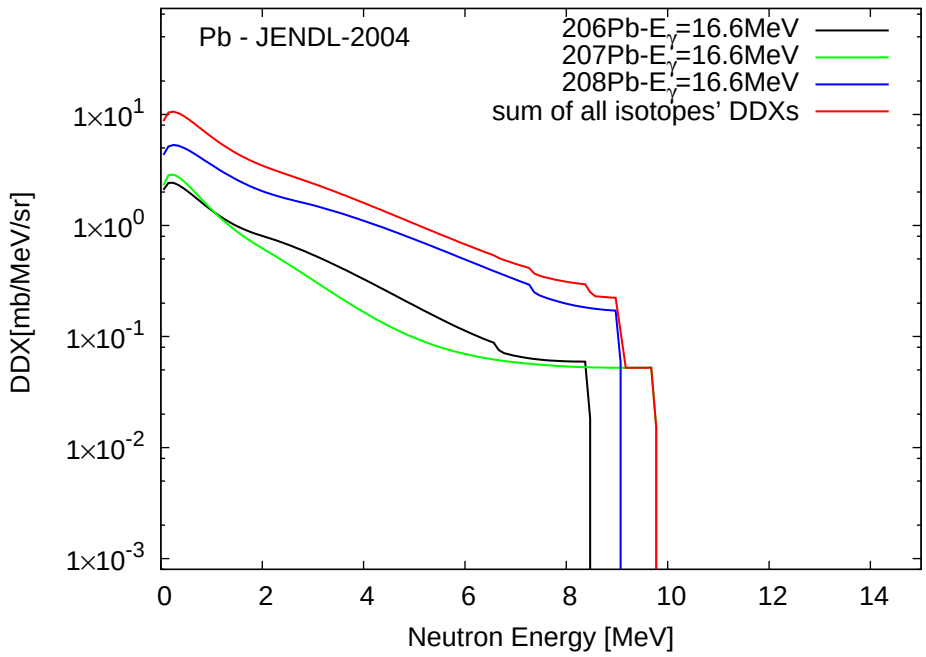

Figure 4.28: JENDL-2004 DDX data normalized with the abundance of isotopes in a Pb target using 16.6 MeV photons.

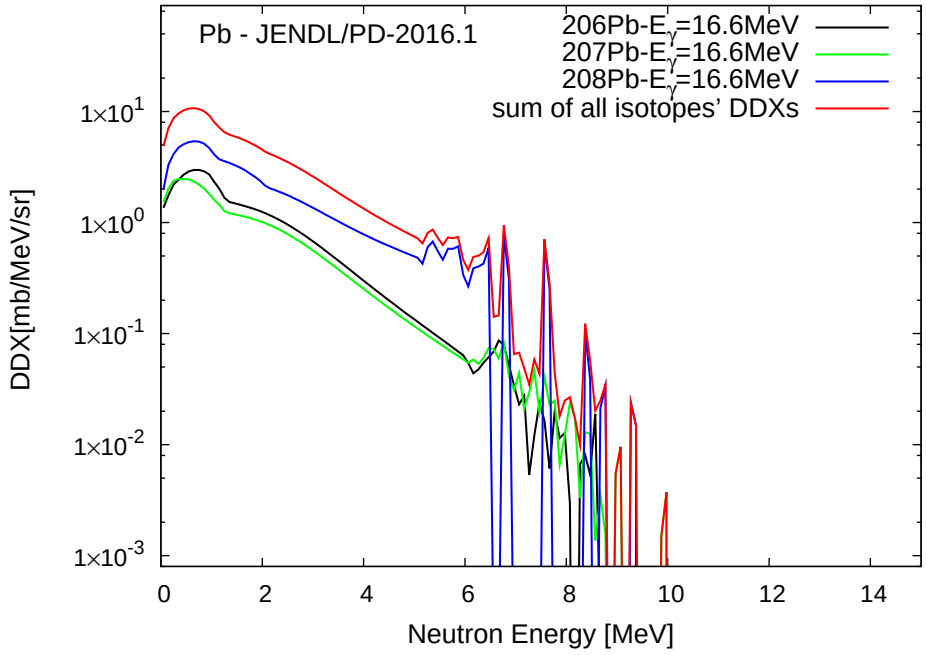

Figure 4.29: JENDL/PD-2016.1 DDX data normalized with the abundance of isotopes in a Pb target using 16.6 MeV photons.

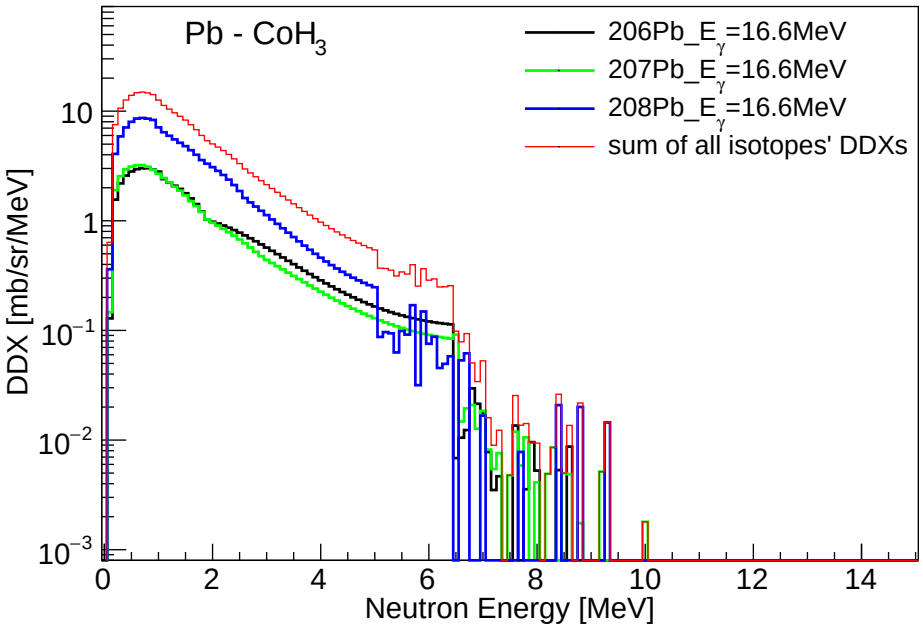

Figure 4.30: CoH_3 DDX data normalized with the abundance of isotopes in a Pb target using 16.6 MeV photons.

In case of Sn, the dominant isotope, ^{120}Sn, significantly contributes to the DDX data. Although the abundance of the ^{119}Sn isotope is low at 8.6%, its Q-value is 6.5 MeV, and the maximum neutron energy was due to the data of the ^{119}Sn isotope, as shown in Figure 4.31 and Figure 4.32.

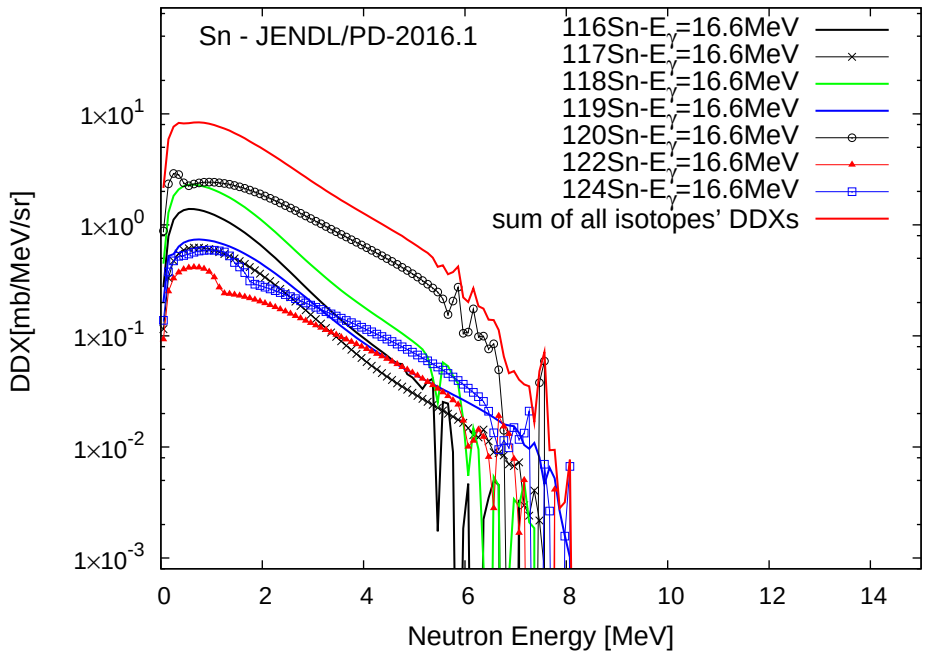

Figure 4.31: JENDL/PD-2016.1 DDX data normalized with the abundance of isotopes in a Sn target using 16.6 MeV photons.

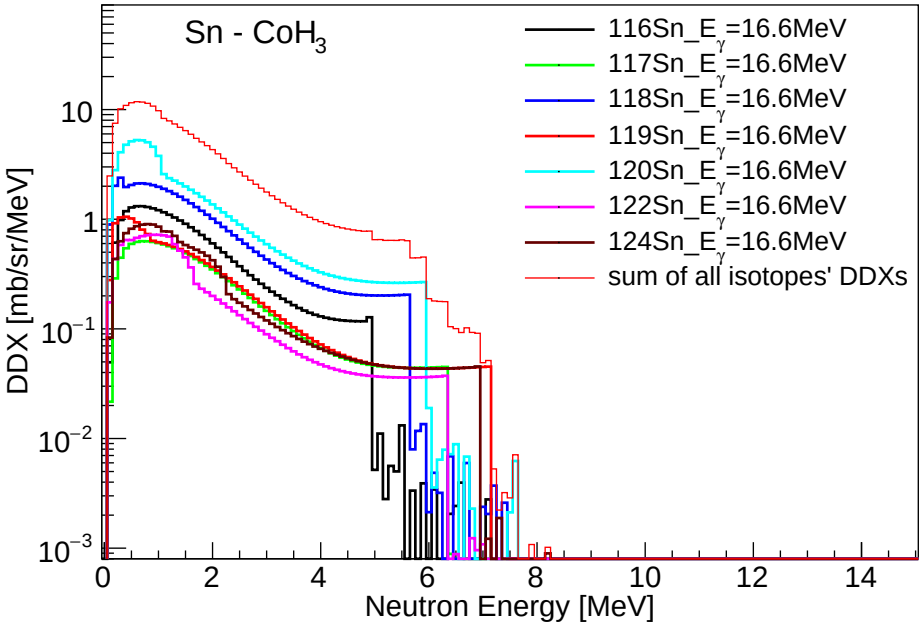

Figure 4.32: CoH_3 DDX data normalized with the abundance of isotopes in a Sn target using 16.6 MeV photons.

Figures 4.33, 4.34, and 4.35 show the DDX data for Cu from JENDL-2004, JENDL/PD-2016.1, and CoH_3, respectively, by considering its abundance. Similarly to the case of Sn, the abundance of ^{65}Cu is lower than that of ^{63}Cu at 30.83%, but the maximum energy of the neutron spectrum was due to its Q-value of 9.9 MeV.

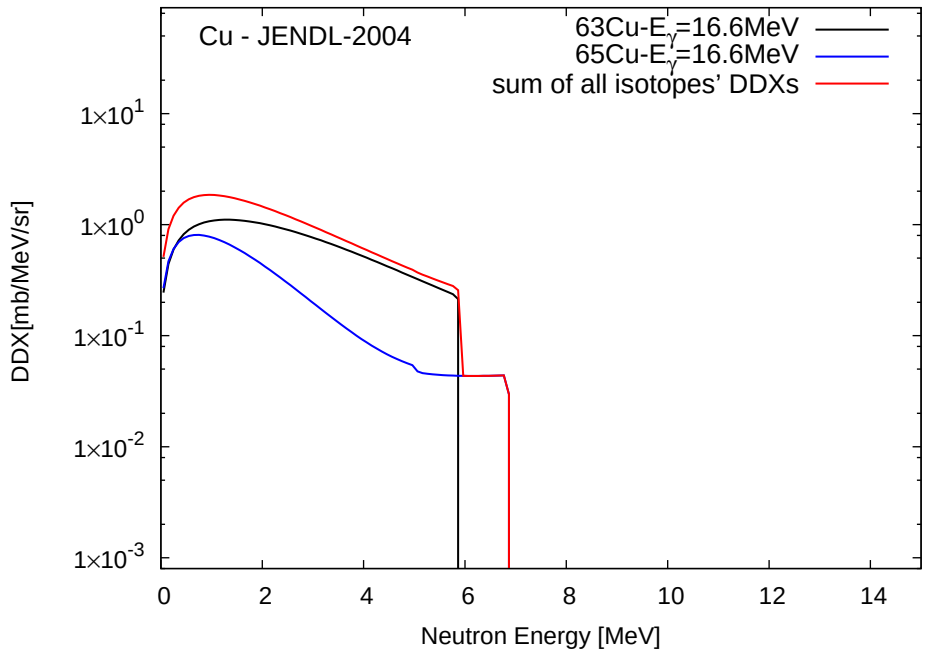

Figure 4.33: JENDL-2004 DDX data normalized with the abundance of isotopes in a Cu target using 16.6 MeV photons.

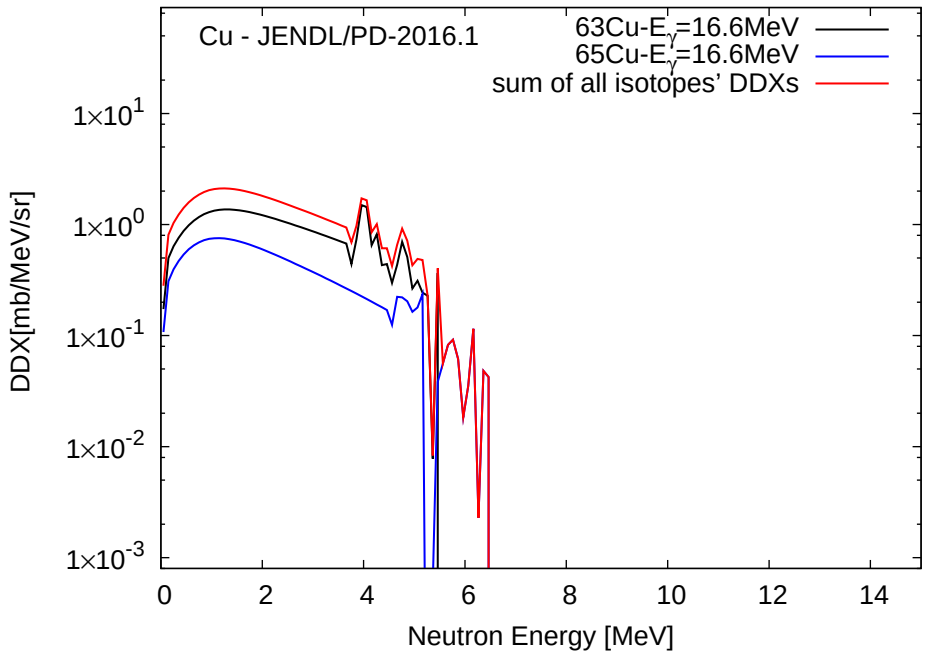

Figure 4.34: JENDL/PD-2016.1 DDX data normalized with the abundance of isotopes in a Cu target using 16.6 MeV photons.

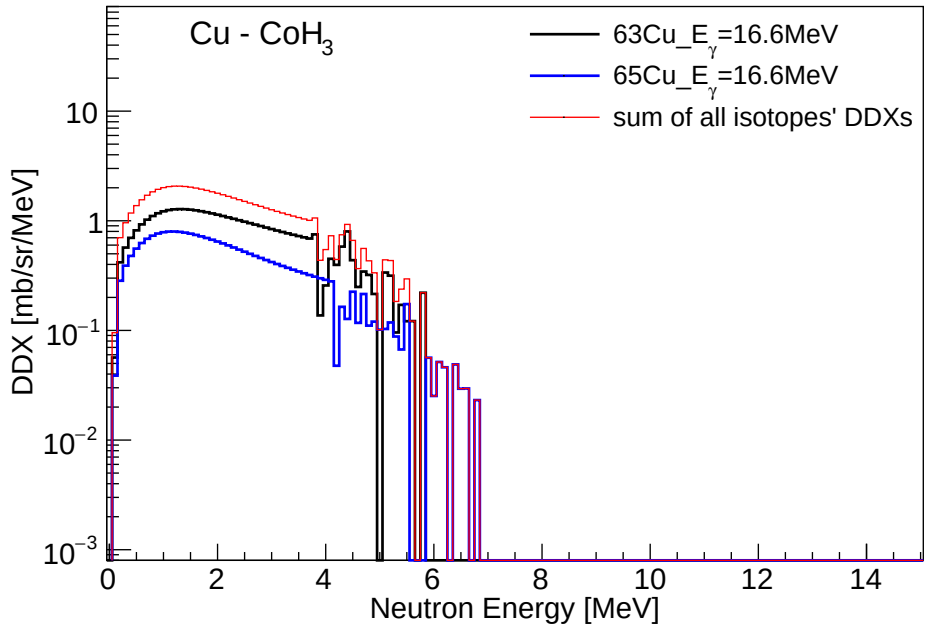

Figure 4.35: CoH_3 DDX data normalized with the abundance of isotopes in a Cu target using 16.6 MeV photons.

In Figures 4.36 and 4.37, the fluctuation of the neutron spectrum is quite significant because of the discrete levels of residual isotopes after neutron emission. Although the abundance of ^{56}Fe is the highest, the maximum energy of the neutron spectrum based on the data for ^{57}Fe is due to its Q-value. Using 16.6 MeV photons, for ^{57}Fe, the residual isotope after neutron emission is ^{56}Fe. It contains 76 discrete levels, and the excited energy ranges from 5.3078 MeV down to 0.0 MeV, which corresponds to a fluctuation point range from 3.64 MeV to 8.95 MeV because its Q-value is 7.65 MeV. Correspondingly, ^{53}Fe is the residual isotope after neutron emission from ^{54}Fe. It has 23 discrete levels, with energies ranging from 0 MeV up to 3.1759 MeV, and its Q-value is 13.38 MeV. Thus, the maximum energy is 3.22 MeV.

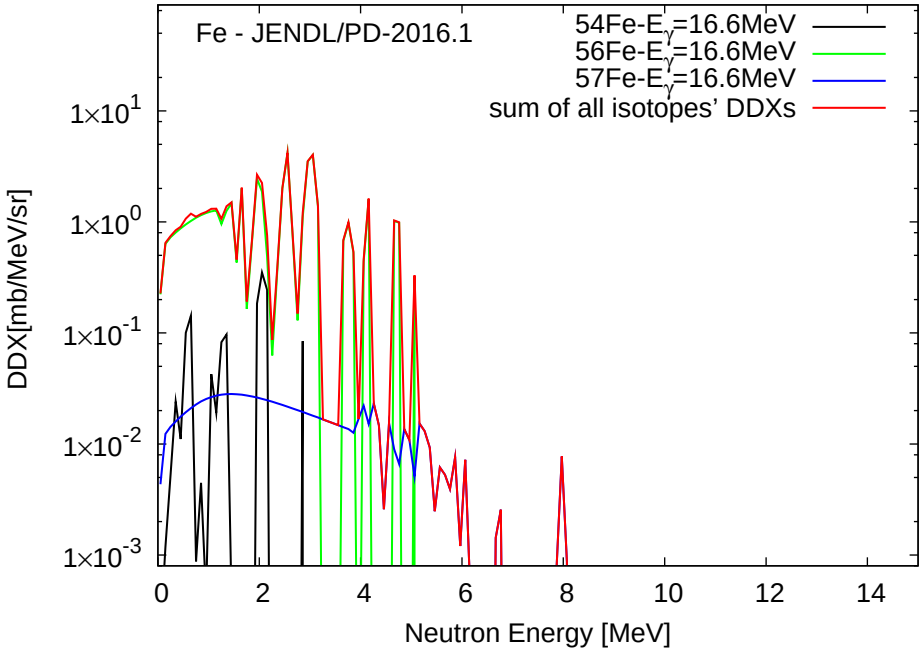

Figure 4.36: JENDL/PD-2016.1 DDX data normalized with the abundance of isotopes in a Fe target using 16.6 MeV photon.

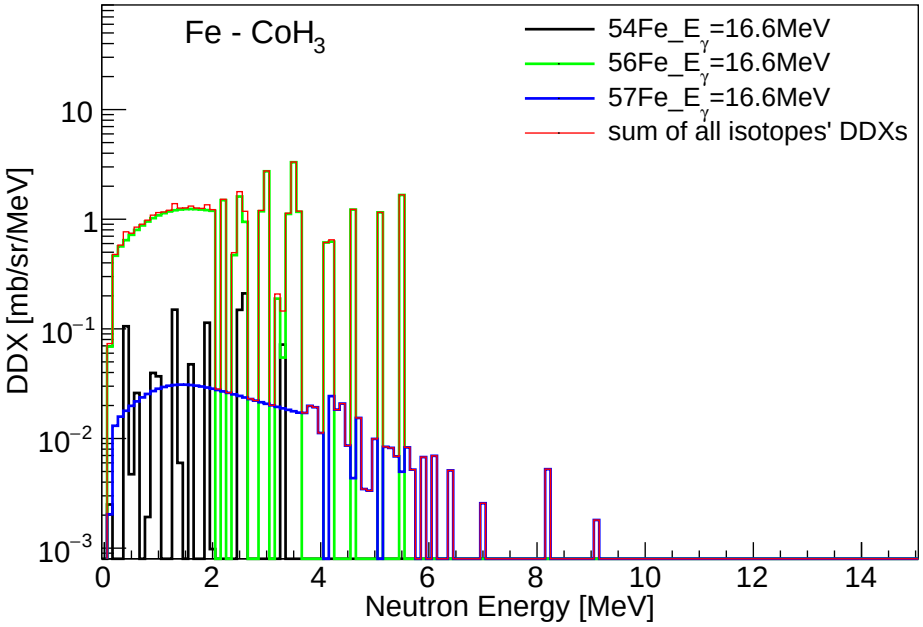

Figure 4.37: CoH_3 DDX data normalized with the abundance of isotopes in a Fe target using 16.6 MeV photon.

The cases of Ti are similar to the cases of Fe. The dominant isotope is ^{48}Ti; thus, it significantly contributes to the DDX data of the Ti target. The maximum energy of the neutron spectrum was determined by the data of ^{49}Ti because of its Q-value, 8.14 MeV. The residual isotope ^{48}Ti after neutron emission from ^{49}Ti has 62 discrete levels. Its excited energy is up to 5.0630 MeV. For instance, Figures 4.38 and 4.39 indicate that the fluctuation point ranges from 3.397 MeV up to 8.46 MeV.

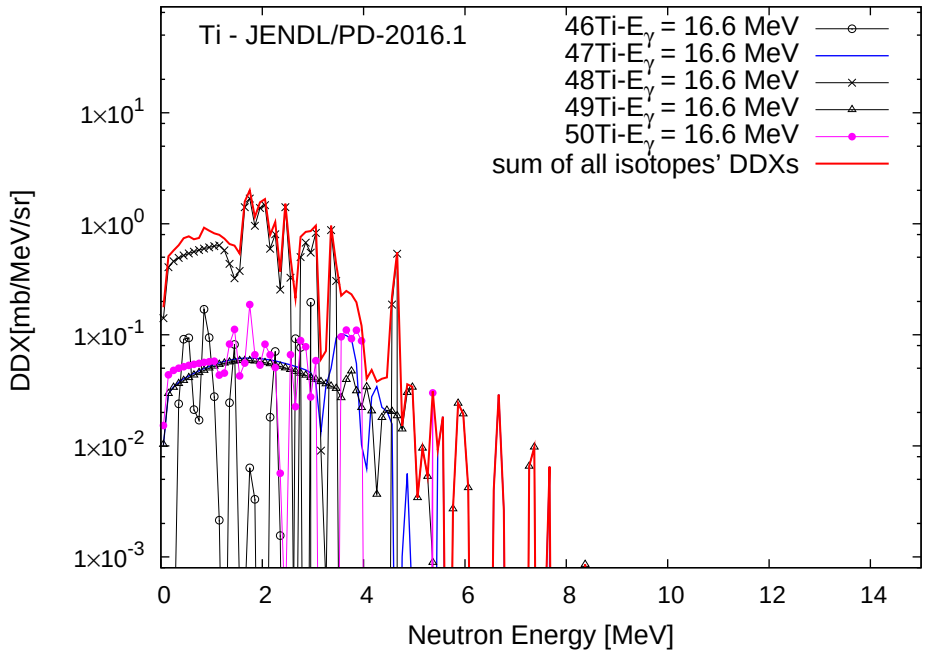

Figure 4.38: JENDL/PD-2016.1 DDX data normalized with the abundance of isotopes in a Ti target using 16.6 MeV photon.

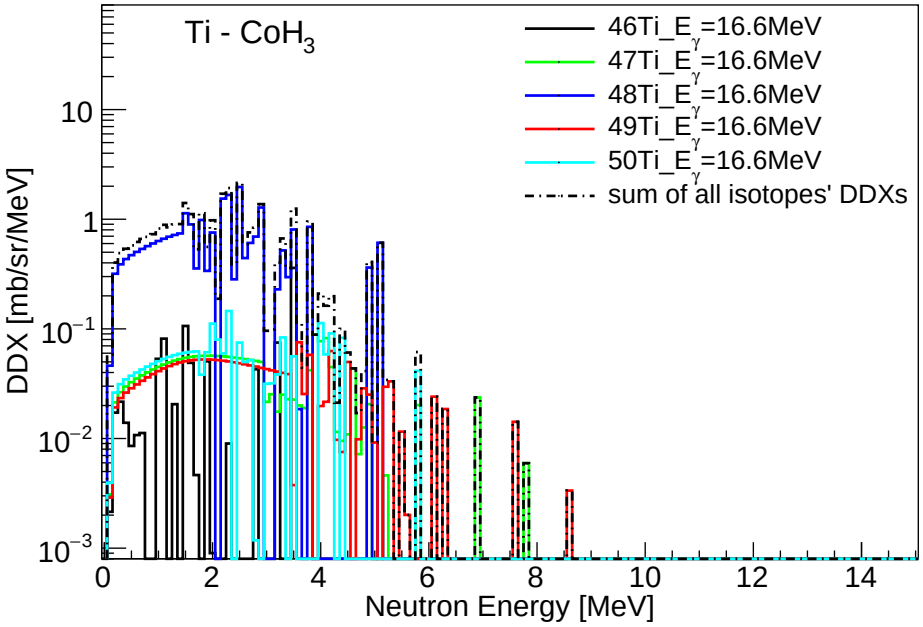

Figure 4.39: CoH_3 DDX data normalized with the abundance of isotopes in a Ti target using 16.6 MeV photon.

4.6 Photon energy width

In order to take the photon width effect into account, the DDX data were calculated with the photon energy varying from 14.7 MeV to 17 MeV under the distribution shown in Figure 4.40. The DDX data calculated with each photon energy in the range 14.7 – 17 MeV were normalized according to the photon spectrum distribution shown in Figure 4.40, which was presented in Reference [37]. Figure 4.41 to

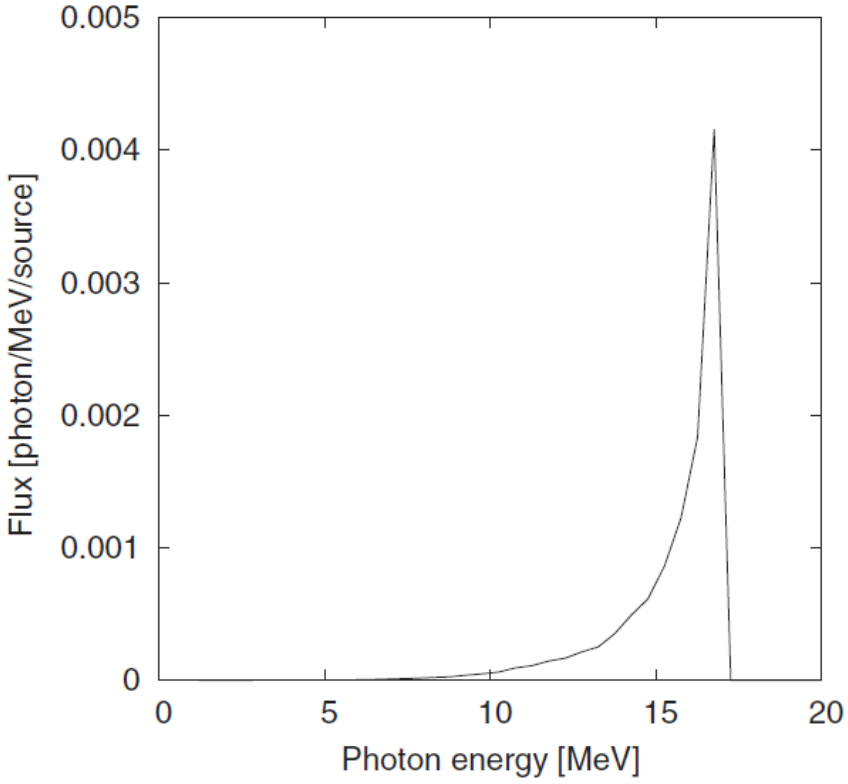

Figure 4.40: LCS photon spectrum obtained from simulation.

Figure 4.55 show the DDX from JENDL-2004, JENDL/PD-2016, and CoH_3, respectively, after considering the photon width for Pb, Au, Sn, Cu, Fe, and Ti targets.

For Pb, Au, and Sn, the Q-value of the (γ,2n) reaction is lower than the photon energy of 17 MeV; thus, two-neutron emission is possible. Consequently, the neutron spectrum shapes reproduced with the photon energies in the range of 14.7 MeV – 15 MeV were different from those for other energies, as can be seen clearly in Figures 4.42 and 4.47 for Pb and Sn, respectively.

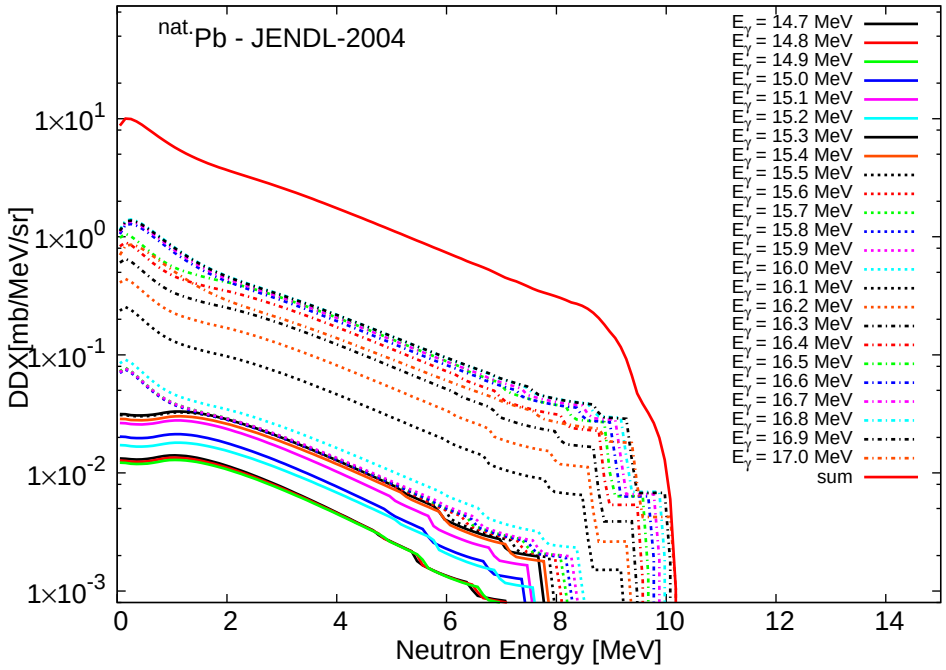

Figure 4.41: JENDL-2004 DDX data of Pb normalized with the photon energy width.

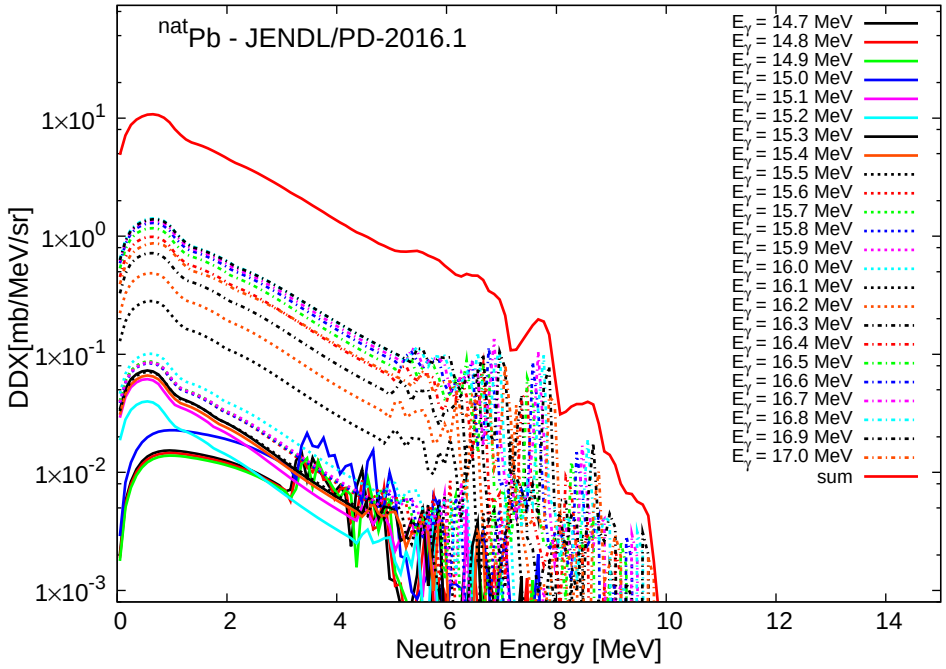

Figure 4.42: JENDL/PD-2016.1 DDX data of Pb normalized with the photon energy width.

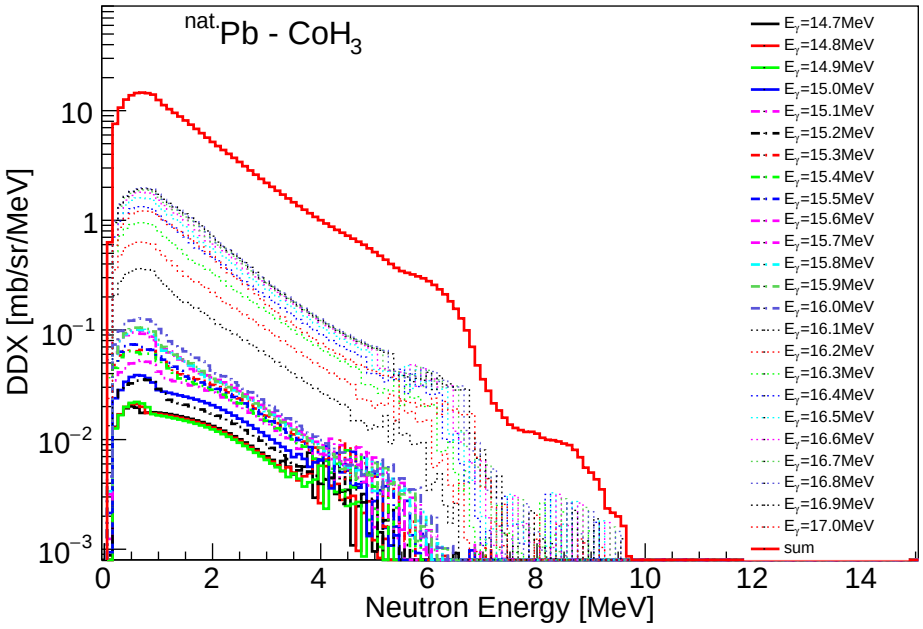

Figure 4.43: CoH_3 DDX data of Pb normalized with the photon energy width.

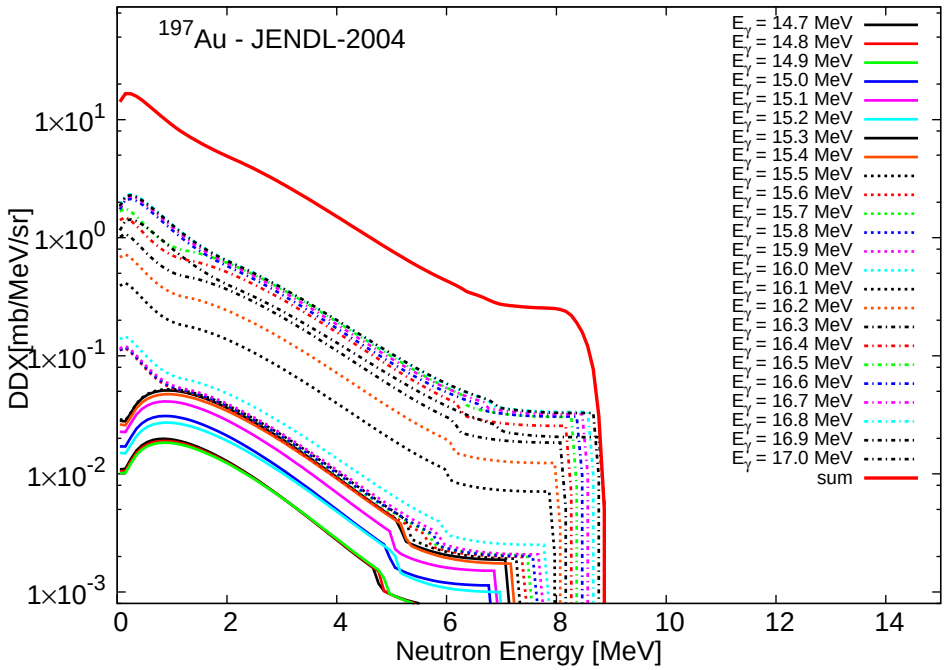

Figure 4.44: JENDL-2004 DDX data of Au normalized with the photon energy width.

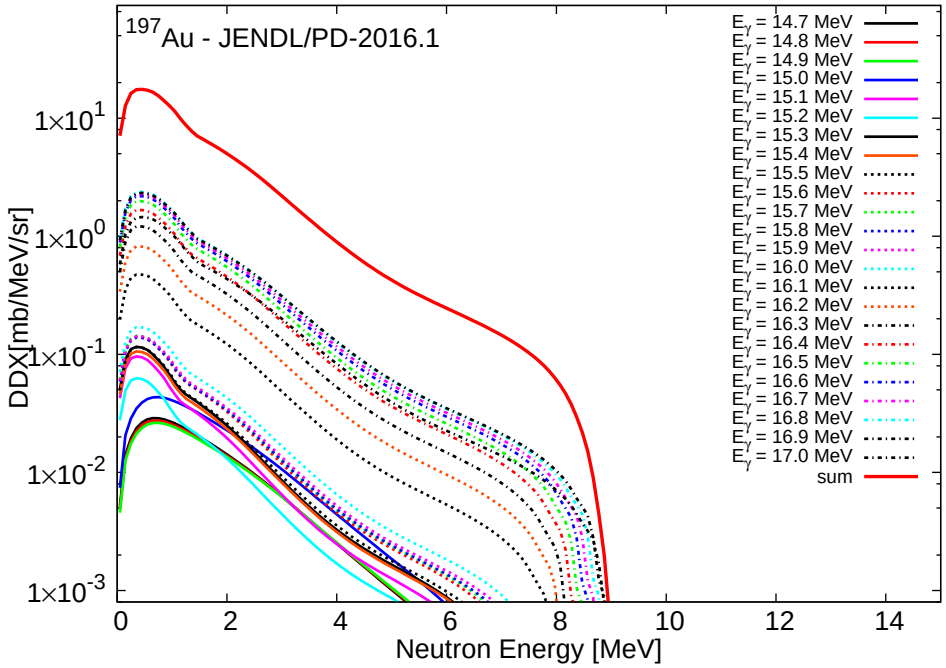

Figure 4.45: JENDL/PD-2016.1 DDX data of Au normalized with the photon energy width.

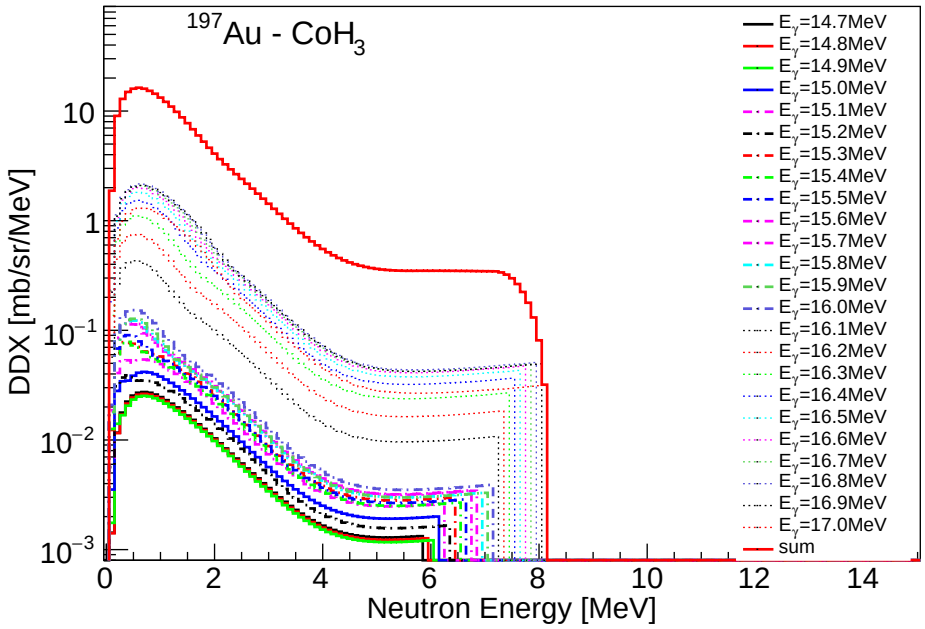

Figure 4.46: CoH_3 DDX data of Au normalized with the photon energy width.

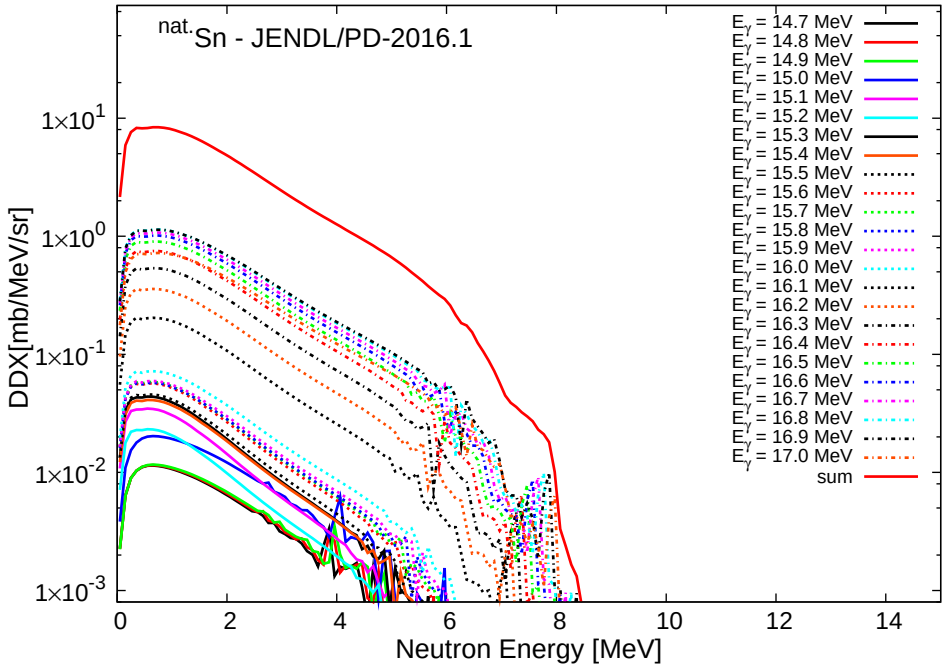

Figure 4.47: JENDL/PD-2016.1 DDX data of Sn normalized with the photon energy width.

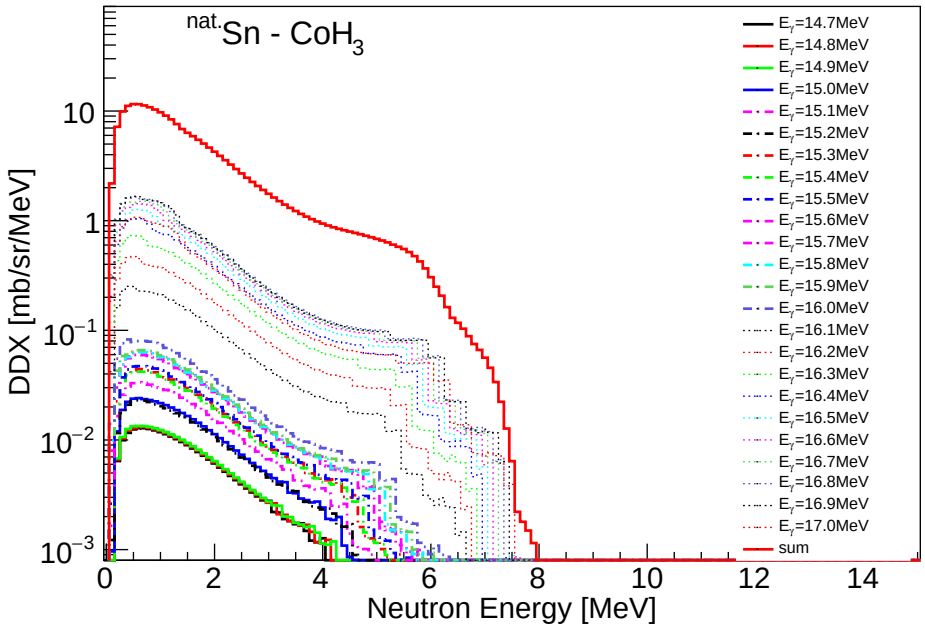

Figure 4.48: CoH_3 DDX data of Sn normalized with the photon energy width.

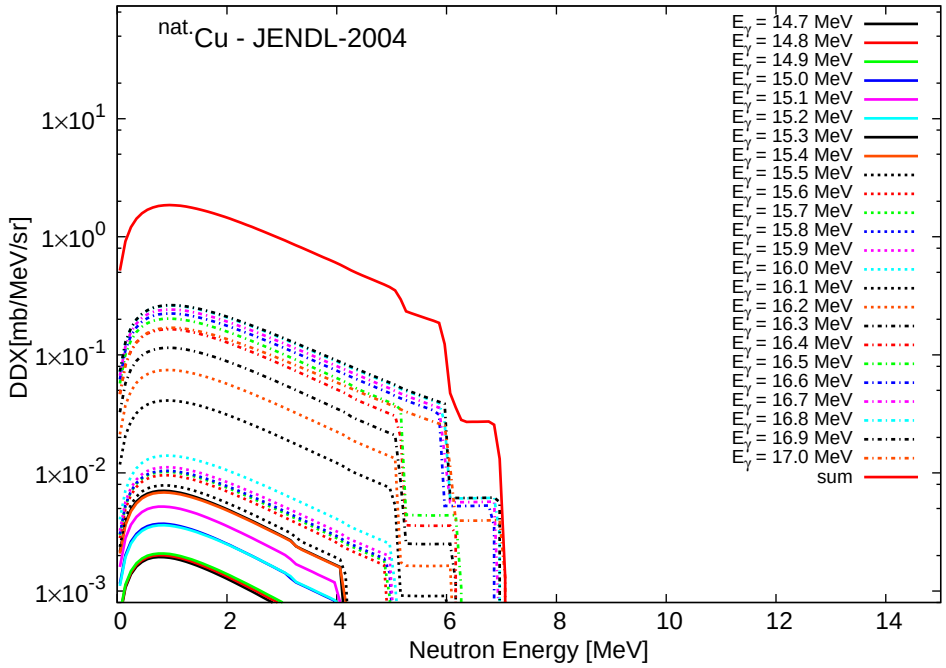

Figure 4.49: JENDL-2004 DDX data of Cu normalized with the photon energy width.

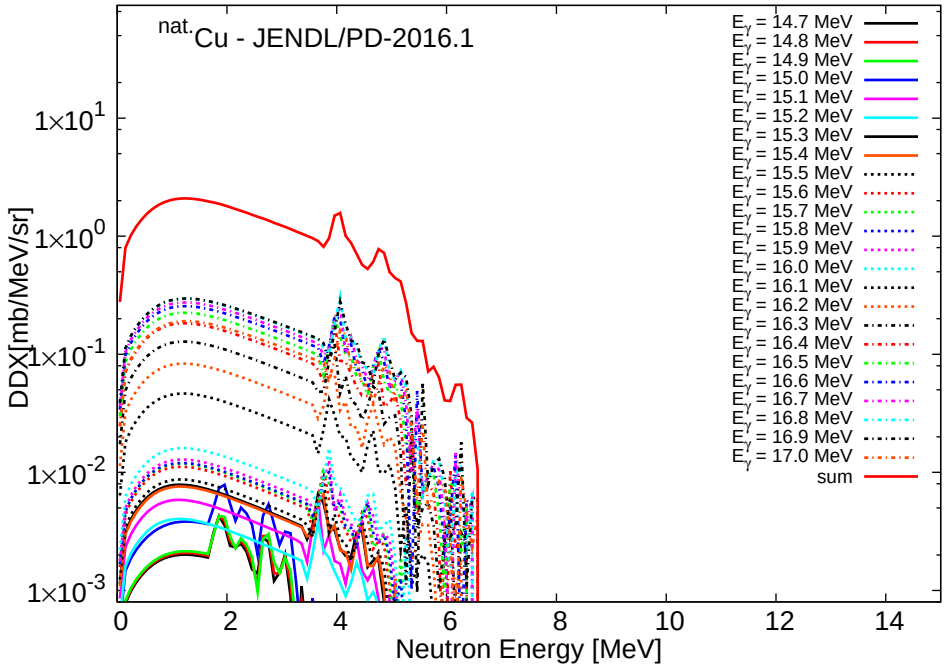

Figure 4.50: JENDL/PD-2016.1 DDX data of Cu normalized with the photon energy width.

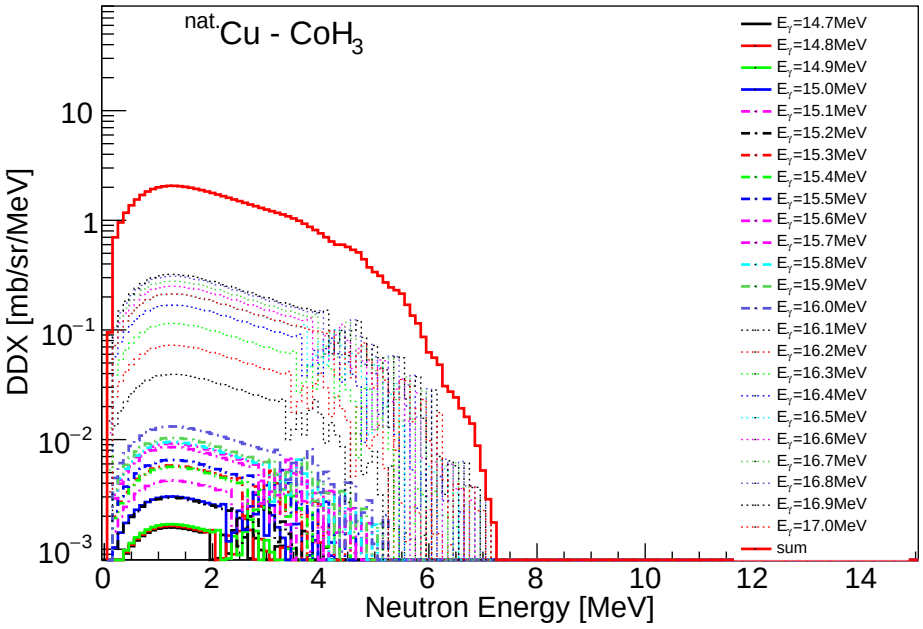

Figure 4.51: CoH_3 DDX data of Cu normalized with the photon energy width.

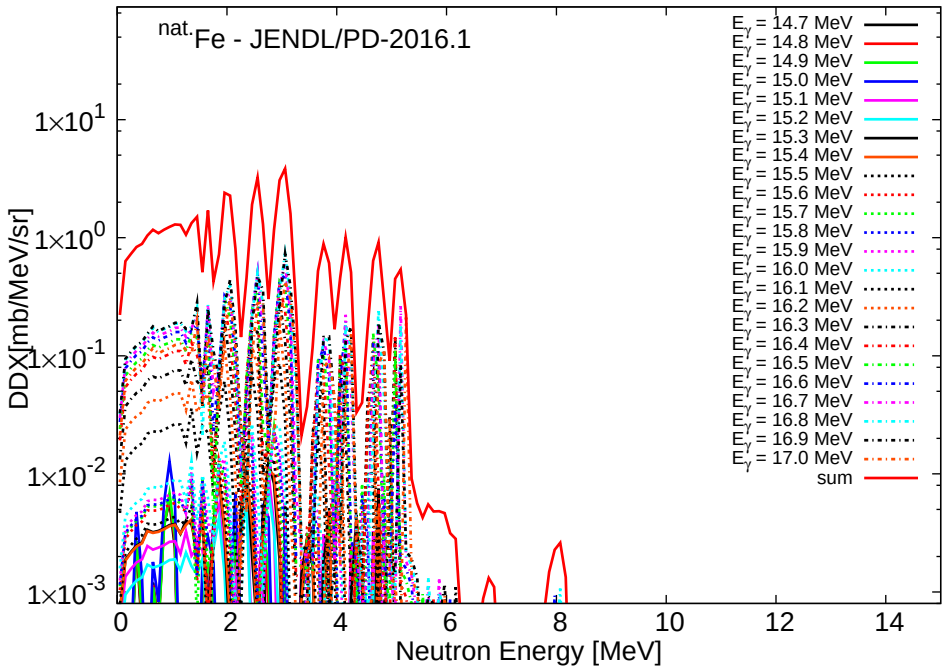

Figure 4.52: JENDL/PD-2016.1 DDX data of Fe normalized with the photon energy width.

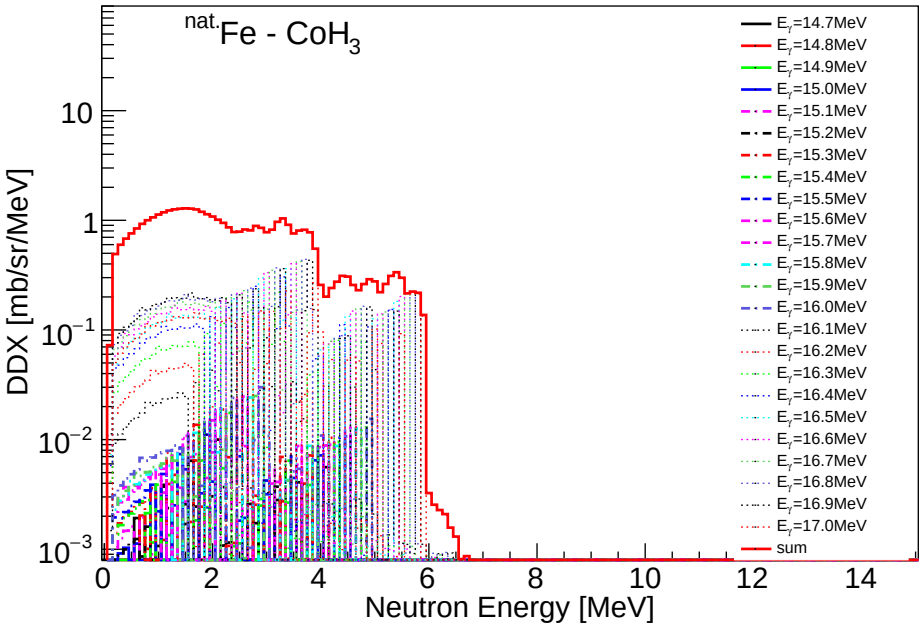

Figure 4.53: CoH_3 DDX data of Fe normalized with the photon energy width.

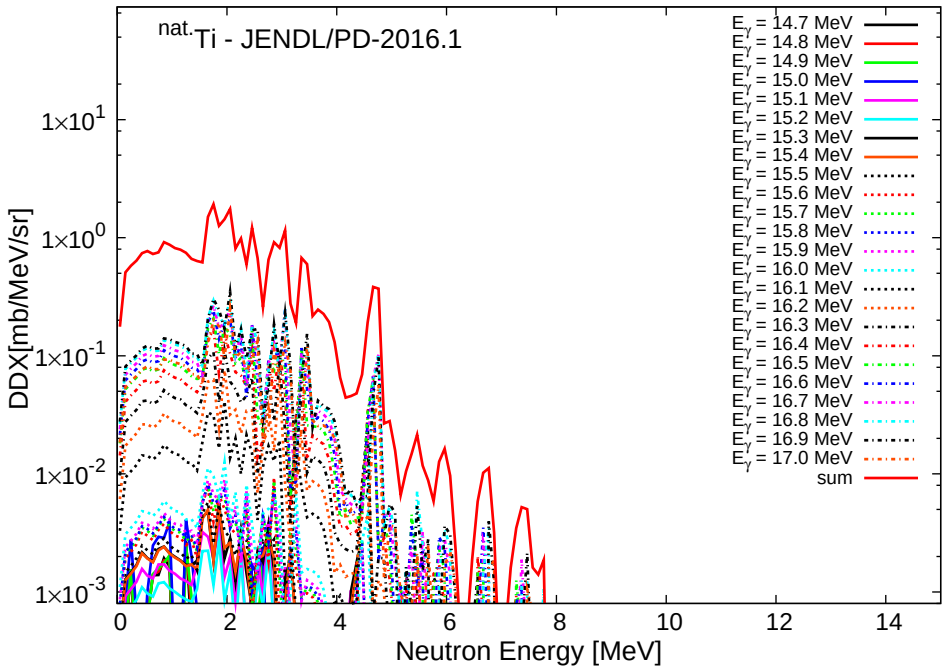

Figure 4.54: JENDL/PD-2016.1 DDX data of Ti normalized with the photon energy width.

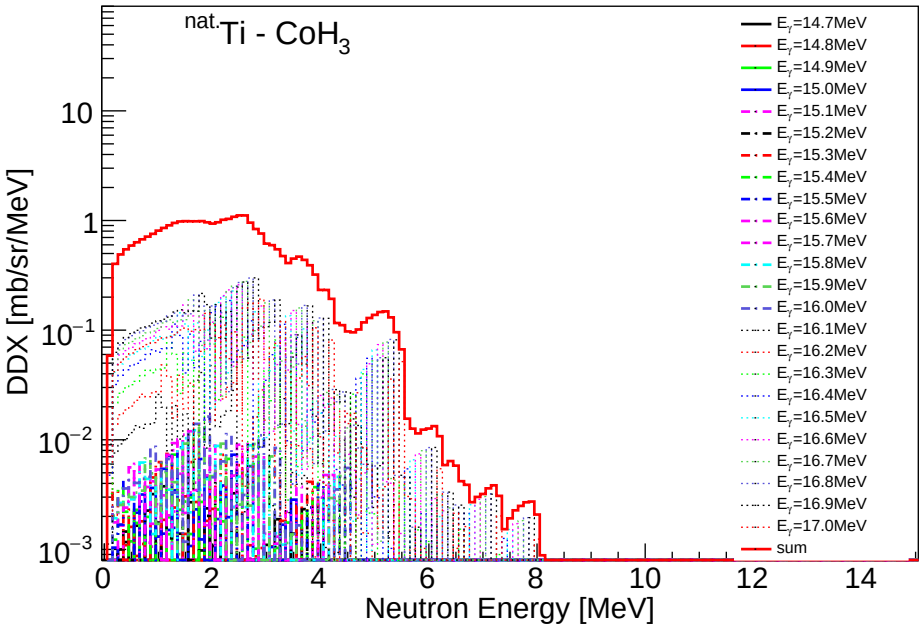

Figure 4.55: CoH_3 DDX data of Ti normalized with the photon energy width.

4.7 Neutron energy resolution

Finally, the neutron energy resolution in the DDX measurement was taken into account in the DDX data. The neutron energy resolution was calculated using Equation 3.8 and is shown in Figure 3.5. A function of the energy resolution was parameterized by fitting to the numerical values of the resolution by using Equation 4.2. Result of the fitting is shown in Figure 4.56, and the fitting function is as follows:

$$\Delta E = 0.131257 \cdot E \cdot \sqrt{0.092594 \cdot E + 1.85957} + 0.010433. \tag{4.2}$$

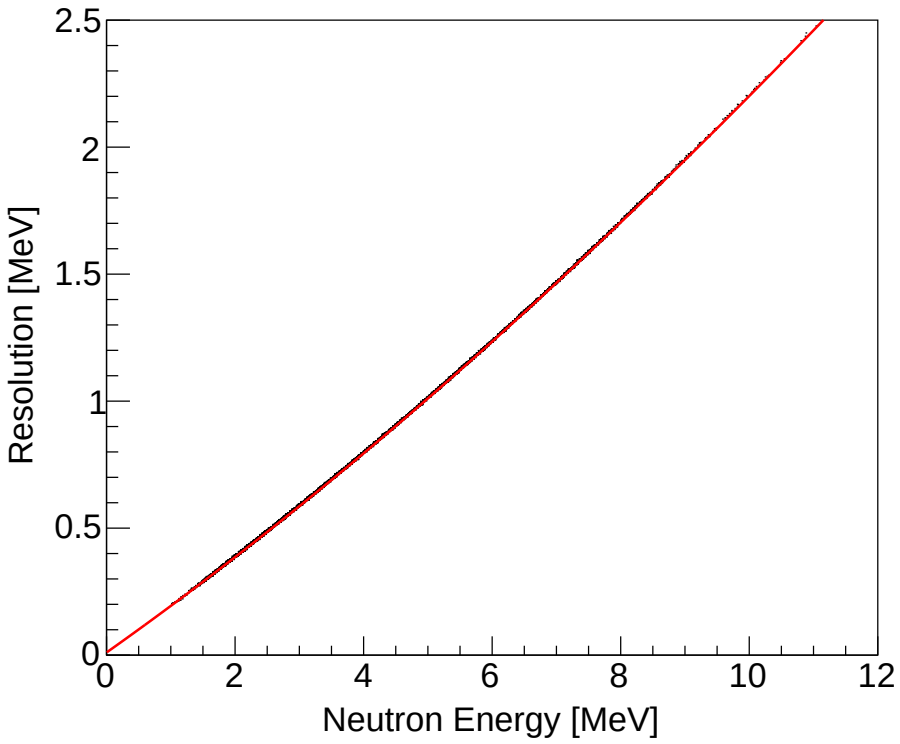

Figure 4.56: Energy resolution of neutron detector at H90 and its fitting function.

The energy resolution was taken into account in the calculated DDX data by using ROOT code. In this code, the resolution calculated from Equation 4.2 was applied to each energy bin of the neutron energy spectrum. Adding the energy

resolution in the calculated DDXs causes the peak structure to disappear and the maximum neutron energy on the calculated spectrum to be increased. Figure 4.57 to Figure 4.77 show the results of the DDX data considering the neutron energy resolution and their comparison with the original data.

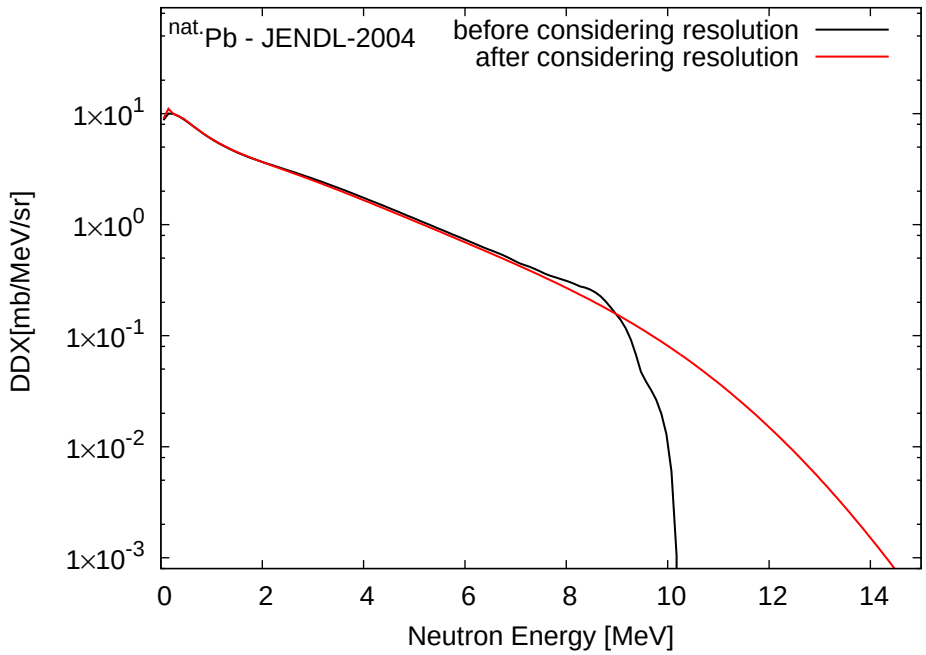

Figure 4.57: JENDL-2004 DDX data of Pb normalized with the neutron energy width.

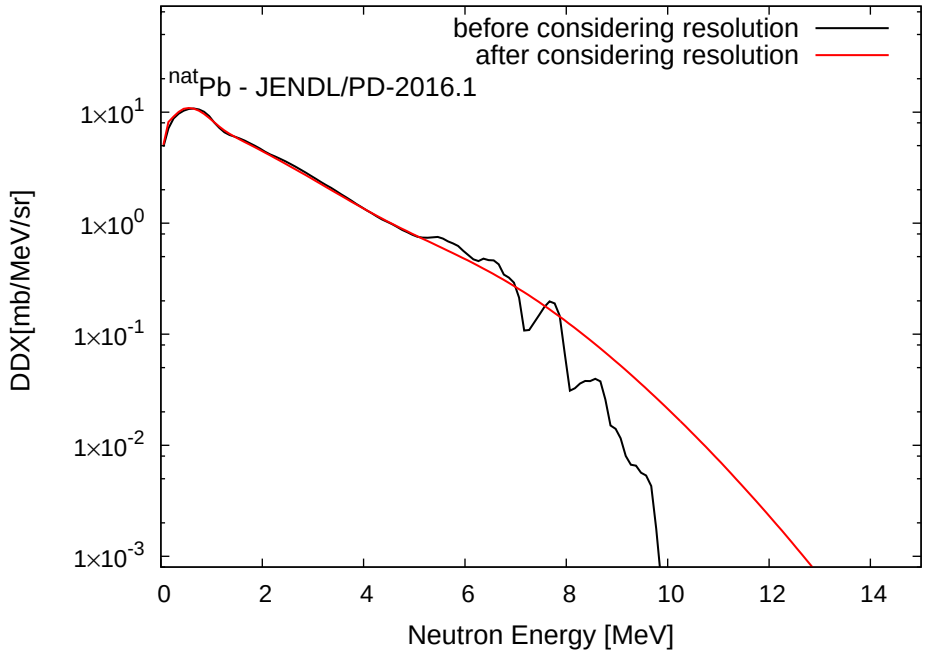

Figure 4.58: JENDL/PD-2016.1 DDX data of Pb normalized with the neutron energy width.

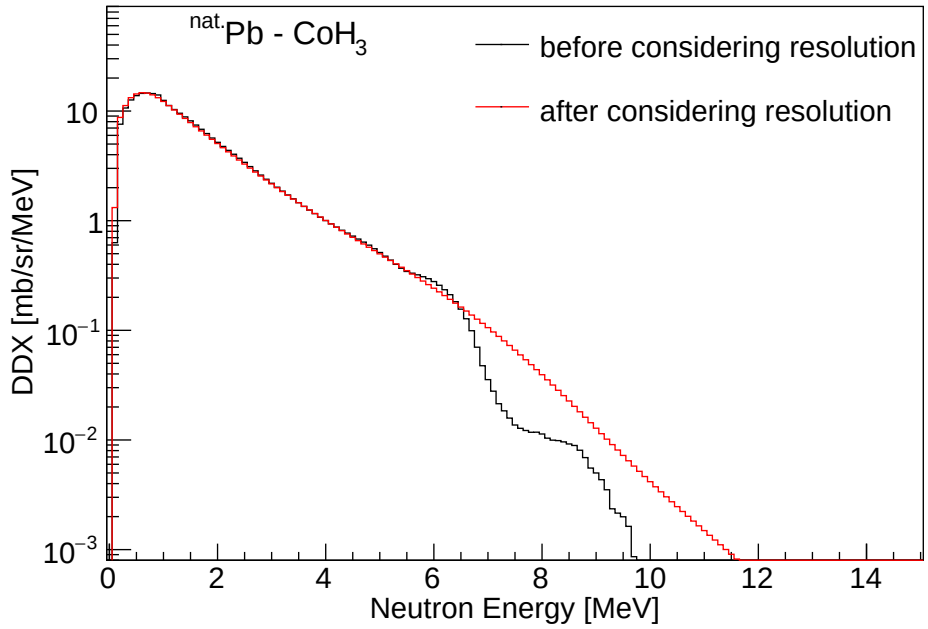

Figure 4.59: CoH_3 DDX data of Pb normalized with the neutron energy width.

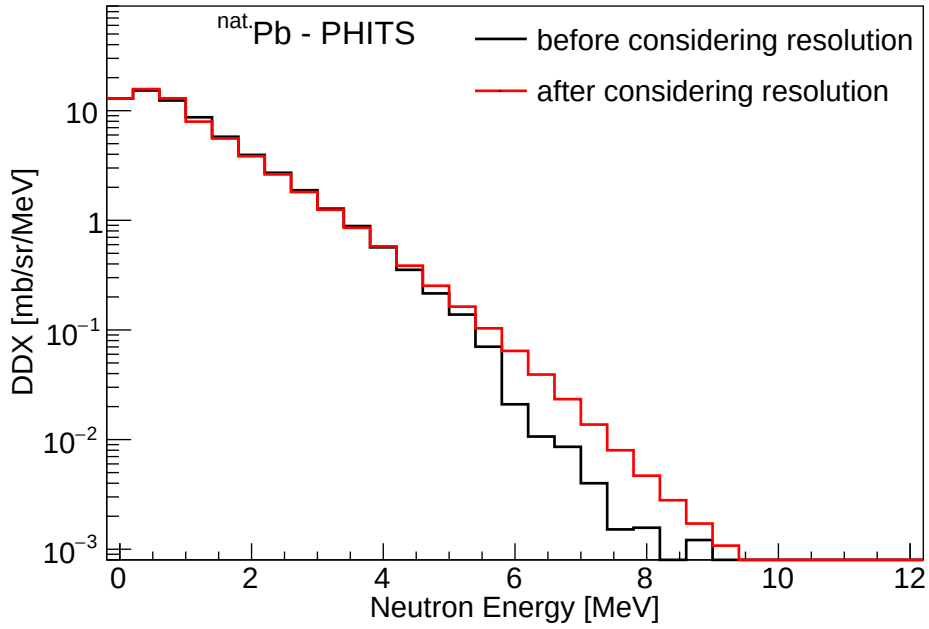

Figure 4.60: PHITS DDX data of Pb normalized with the neutron energy width.

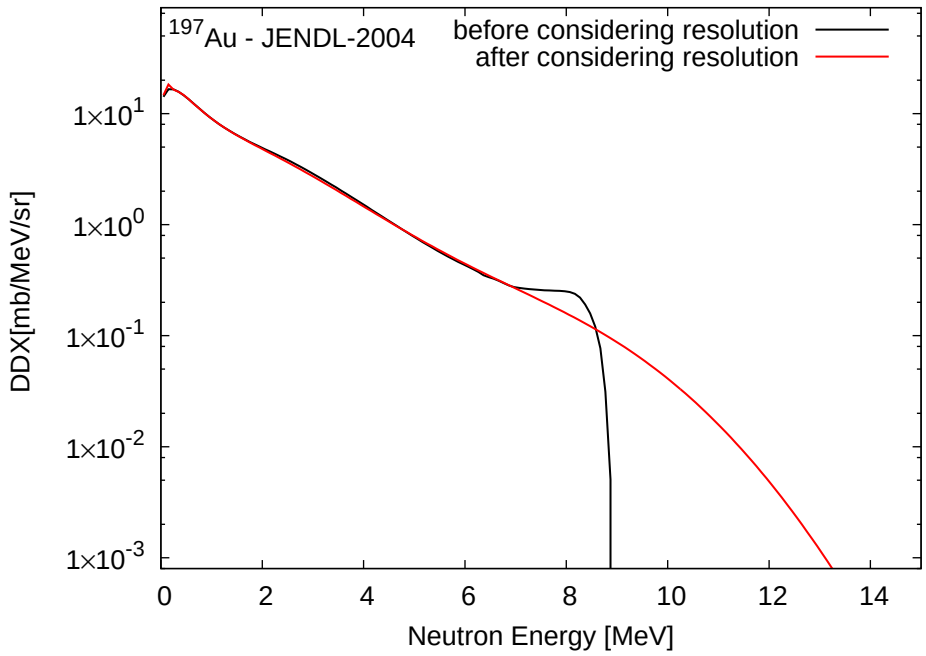

Figure 4.61: JENDL-2004 DDX data of Au normalized with the neutron energy width.

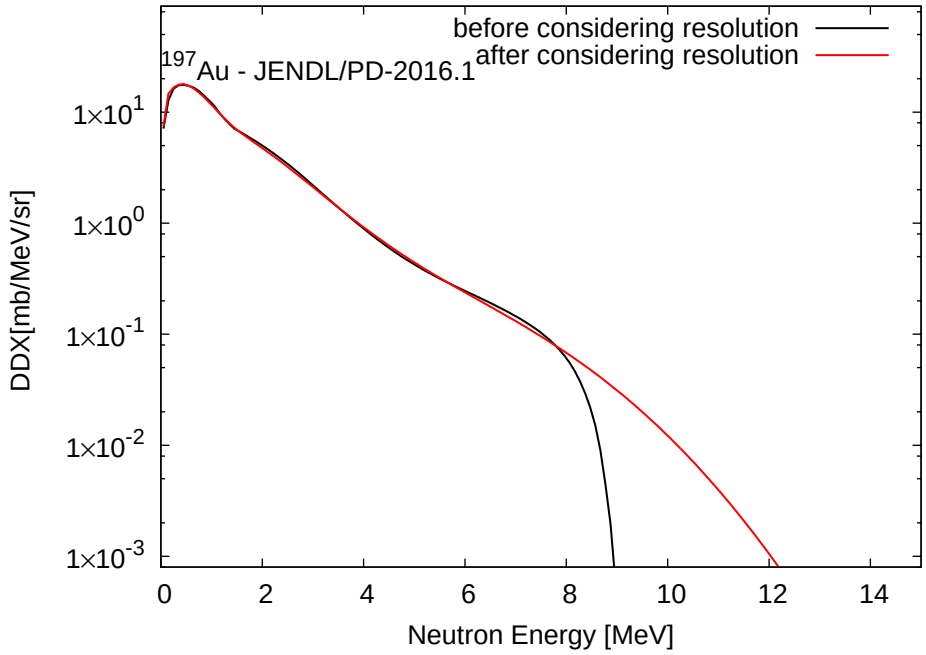

Figure 4.62: JENDL/PD-2016.1 DDX data of Au normalized with the neutron energy width.

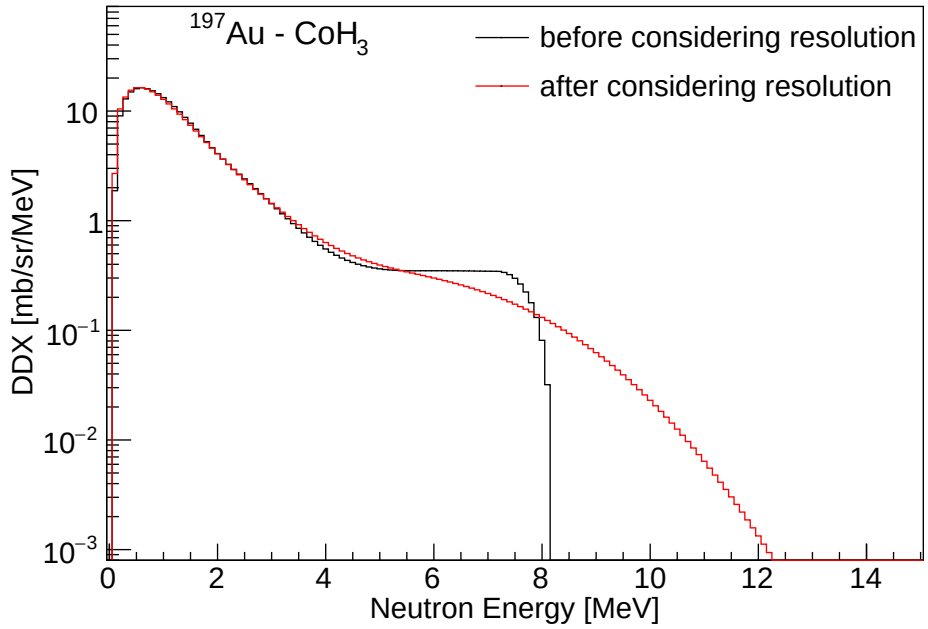

Figure 4.63: CoH_3 DDX data of Au normalized with the neutron energy width.

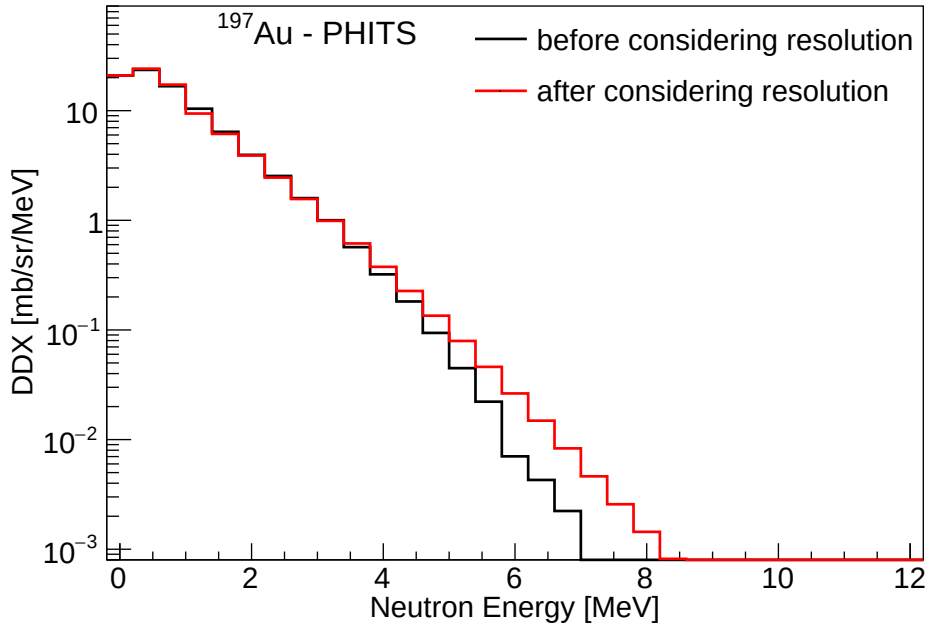

Figure 4.64: PHITS DDX data of Au normalized with the neutron energy width.

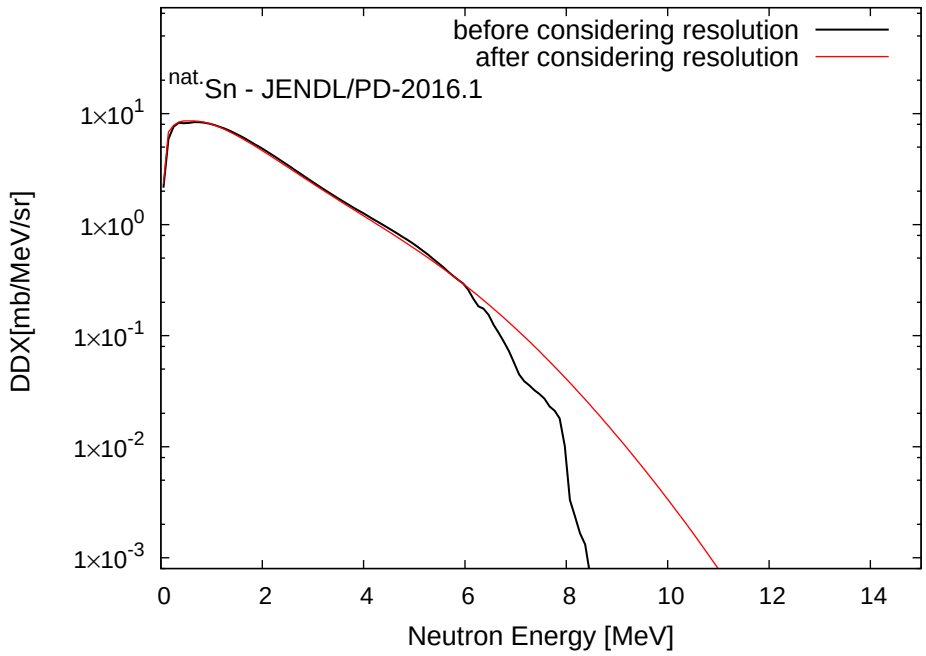

Figure 4.65: JENDL/PD-2016.1 DDX data of Sn normalized with the neutron energy width.

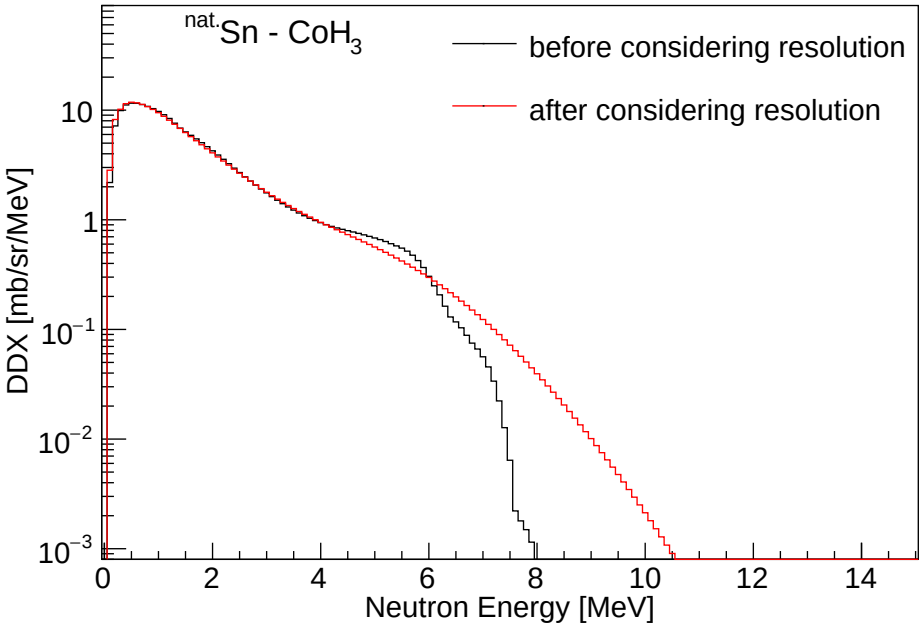

Figure 4.66: CoH_3 DDX data of Sn normalized with the neutron energy width.

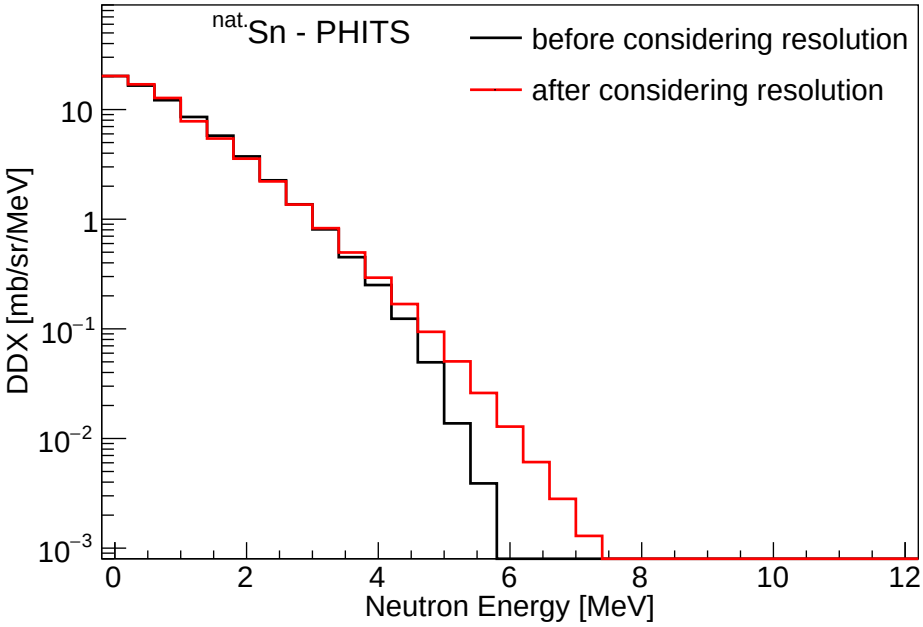

Figure 4.67: PHITS DDX data of Sn normalized with the neutron energy width.

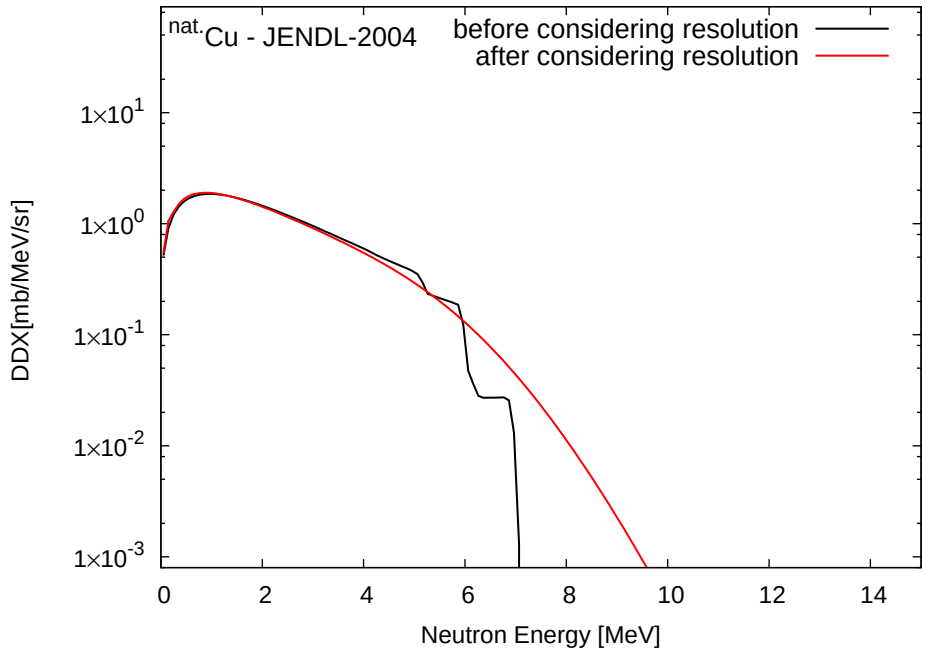

Figure 4.68: JENDL-2004 DDX data of Cu normalized with the neutron energy width.

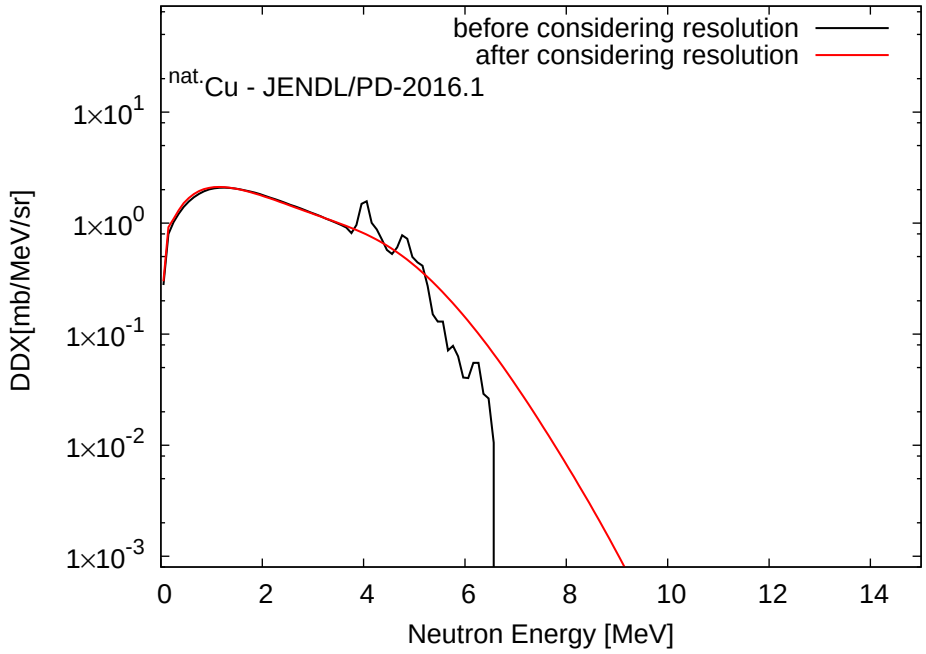

Figure 4.69: JENDL/PD-2016.1 DDX data of Cu normalized with the neutron energy width.

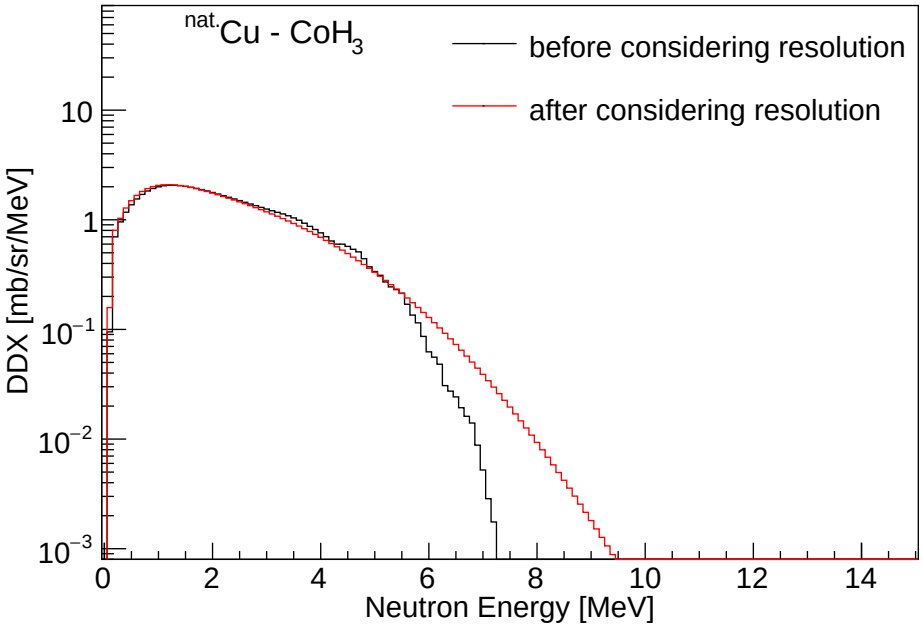

Figure 4.70: CoH_3 DDX data of Cu normalized with the neutron energy width.

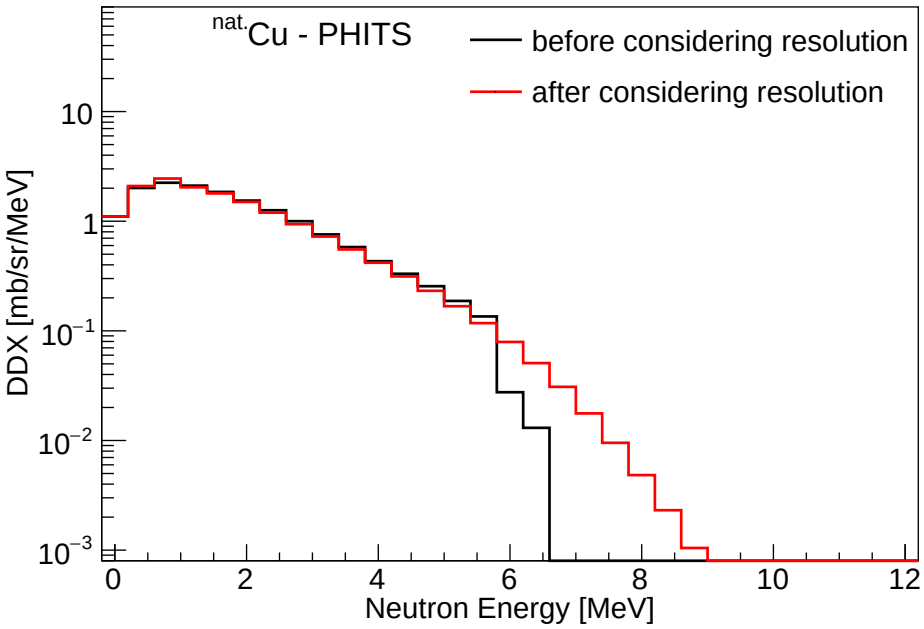

Figure 4.71: PHITS DDX data of Cu normalized with the neutron energy width.

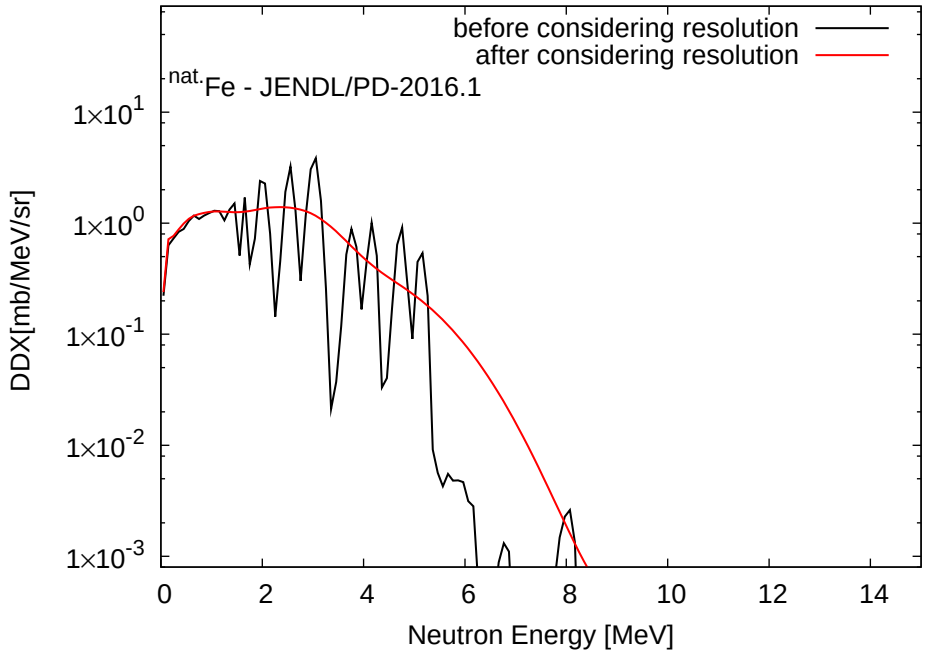

Figure 4.72: JENDL/PD-2016.1 DDX data of Fe normalized with the neutron energy width.

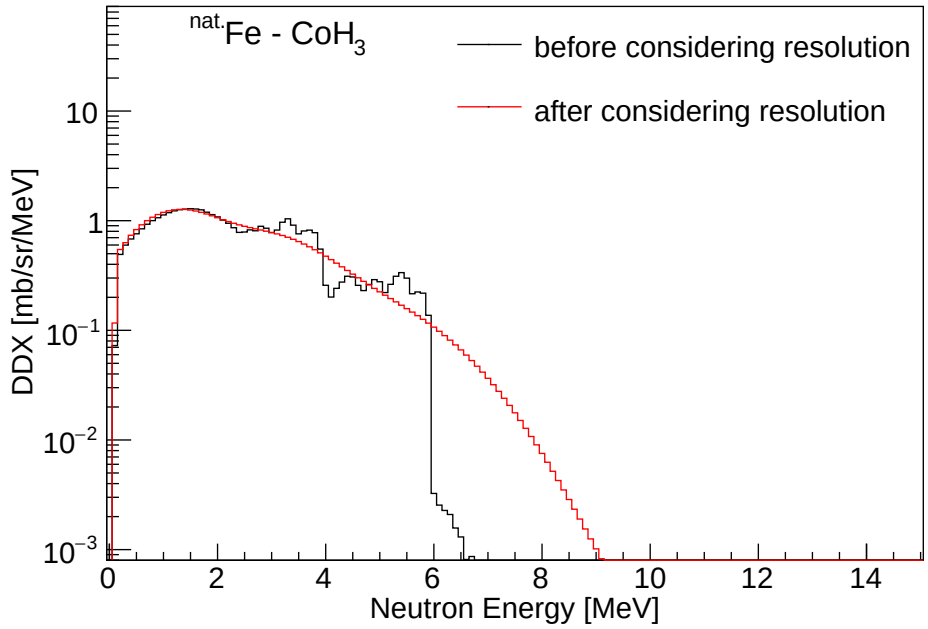

Figure 4.73: CoH_3 DDX data of Fe normalized with the neutron energy width.

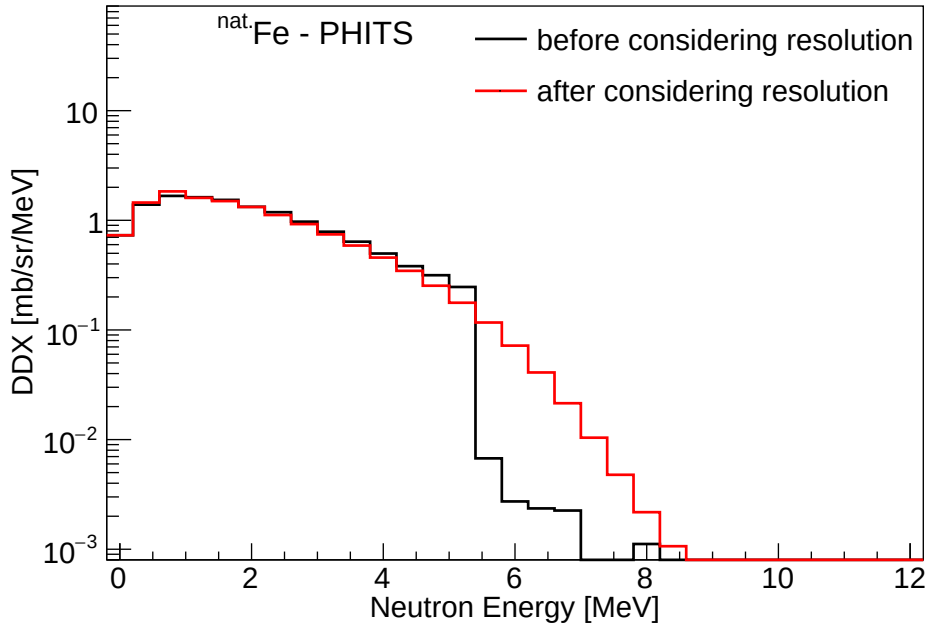

Figure 4.74: PHITS DDX data of Fe normalized with the neutron energy width.

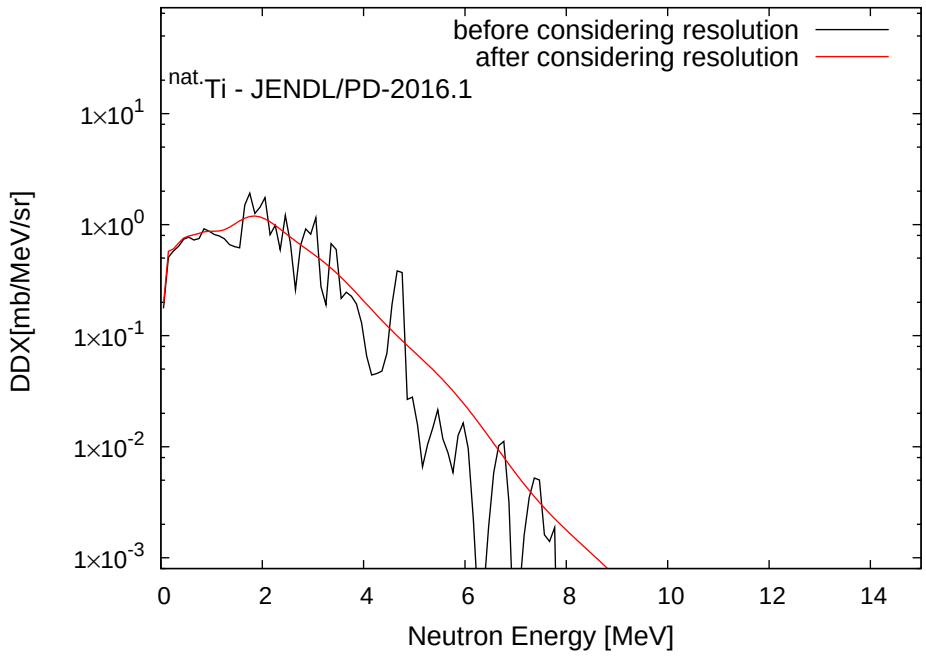

Figure 4.75: JENDL/PD-2016.1 DDX data of Ti normalized with the neutron energy width.

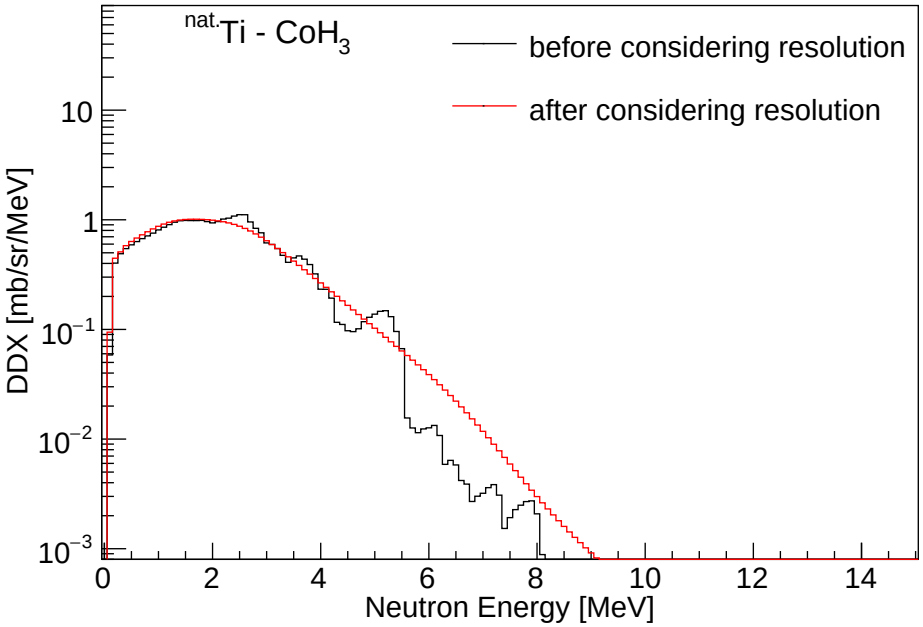

Figure 4.76: CoH_3 DDX data of Ti normalized with the neutron energy width.

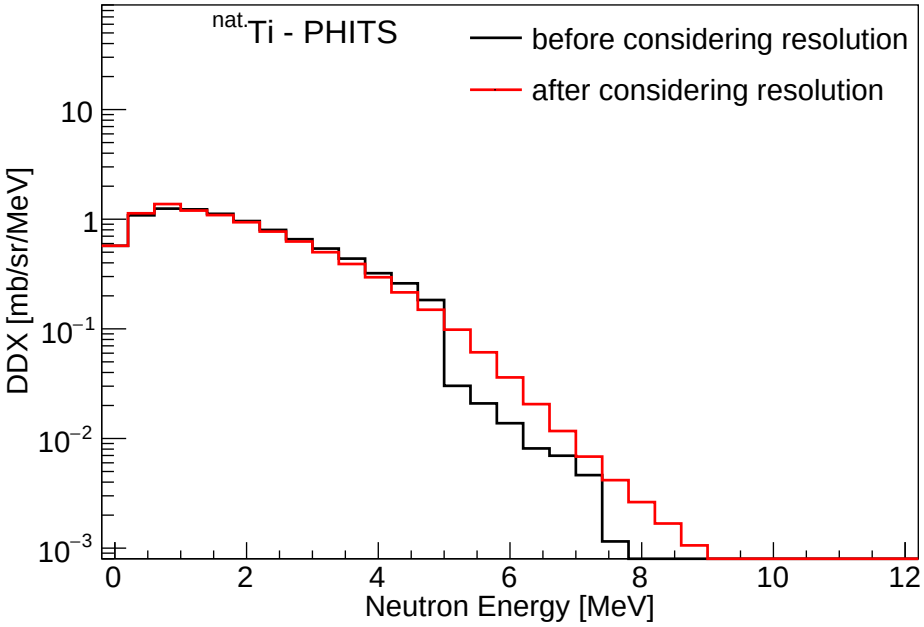

Figure 4.77: PHITS DDX data of Ti normalized with the neutron energy width.

4.8 Comparison of DDXs the theoretical calculation and nuclear data

In this section, the theoretical DDX spectra obtained using PHITS, JENDL/PD-2004, JENDL/PD-2016.1, and CoH_3 are compared. Figures 4.78 - 4.80 show the calculated DDX spectra of photoneutrons emitted from Pb, Au, Sn, Cu, Fe, and Ti. The black, magenta, red, and blue solid lines indicate the calculated DDX spectra produced by PHITS, JENDL/PD-2004, JENDL/PD-2016.1, and CoH_3, respectively.

To compare with experimental data, the calculations were performed with the consideration of the natural abundance of isotopes, the energy distributions of photons, and the energy resolution of neutron detectors for each target.

In general, the DDX spectra produced by these calculations of Pb, Au, or Sn are significantly different above 4 MeV owing to the consideration of pre-equilibrium processes in JENDL and CoH_3 but not PHITS; however, the calculated DDX spectra of Cu, Fe, and Ti are comparable.

In addition to the shapes of the DDX spectra, the maximum energies (E_{max}) of photoneutrons are also different. In JENDL/PD-2016.1 and CoH_3, the discrete nuclear energy levels are considered when calculating the photoneutron production. The discrepancy between the spectra from the nuclear data library (JENDL/PD-2016.1) and theoretical model (CoH_3) is due to the difference in calculation codes and initial states. The discrete energy levels considered in JENDL/PD-2016.1 lead to the fluctuation of DDX spectra obtained in Pb, Fe, and Ti even after smearing. Owing to the discrepancy among PHITS, JENDL, and CoH_3, an experimental data set is needed to confirm and develop a theoretical calculation model. The calculations in PHITS, JENDL/PD-2004, JENDL/PD-2016.1, and CoH_3 were conducted in different ways. In PHITS, GEM was used; therefore, the DDX spectrum contained only the isotropic evaporation component of the neutron spectrum. On the other hand, in JENDL/PD-2004, JENDL/PD-2016.1, and CoH_3, the photoneutron

production was calculated with the consideration of evaporation and pre-equilibrium processes; consequently, in the neutron energy range above 4 MeV, the DDX of either JENDL or CoH_3 was higher than the DDX of PHITS. However, considering the abundance of isotopes, the photon width effect reduced the fluctuating shape for Pb, Au, Sn, and Cu targets, while it did not for Fe and Ti. For Fe and Ti targets, the fluctuations of the spectra were huge because the discrete levels in the residual isotopes are quite significant.

Table 4.2 lists the angular differential cross sections (ADXs) reproduced by PHITS, JENDL/PD-2004, JENDL/PD-2016.1, and CoH_3 for all targets. The ADX values were computed by integrating the DDX values for the entire spectrum. Although these photoneutron distributions reproduced by the theoretical model, nuclear data library, and simulation code are different, the ADX values are comparable.

Table 4.2: ADX values in mbarn/sr calculated by PHITS, JENDL/PD-2004, JENDL/PD-2016.1, and CoH_3 for all targets in this study.

Target	PHITS [mb/sr]	JENDL/PD-2004 [mb/sr]	JENDL/PD-2016.1 [mb/sr]	CoH_3 [mb/sr]
^{nat}Pb	21.69	21.67	23.00	25.51
Au	26.97	28.32	28.29	25.23
^{nat}Sn	20.85		20.62	21.27
^{nat}Cu	5.89	5.82	6.92	6.51
^{nat}Fe	5.03		4.94	4.09
^{nat}Ti	3.57		3.11	3.11

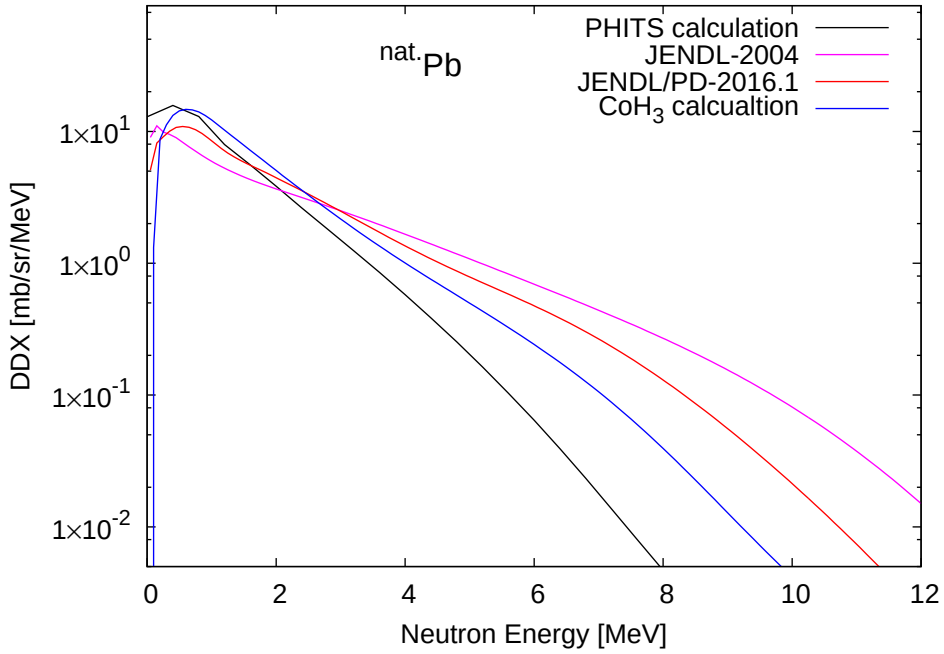

(a) Pb

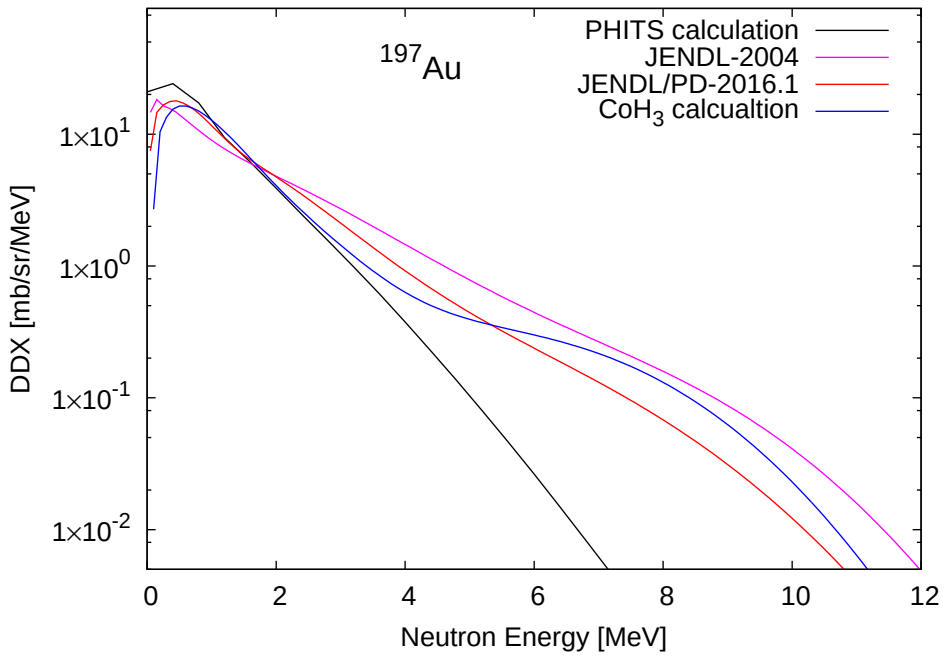

(b) Au

Figure 4.78: Comparison of the DDX calculation results for Pb and Au.

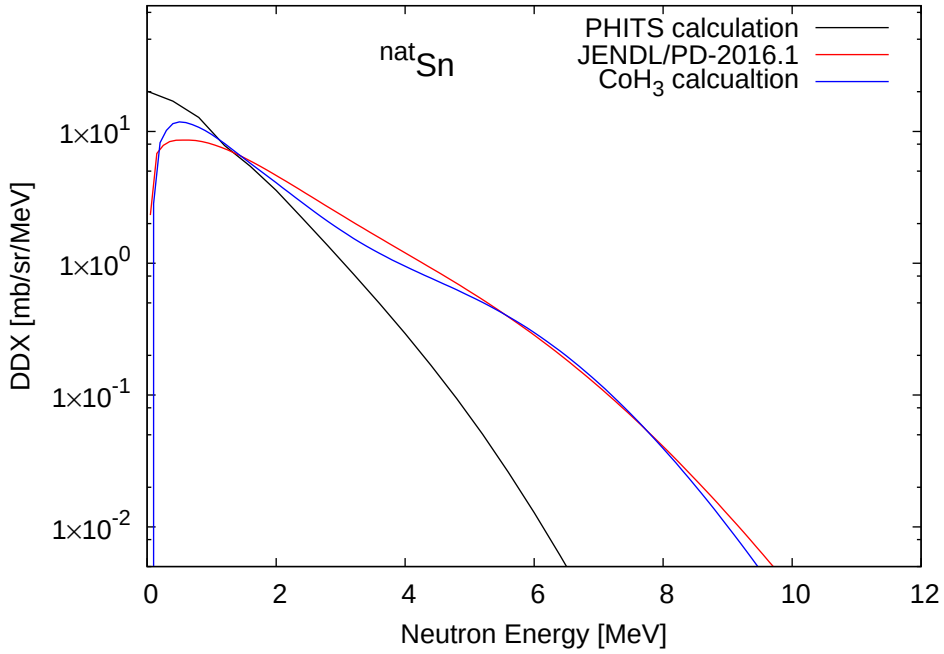

(a) Sn

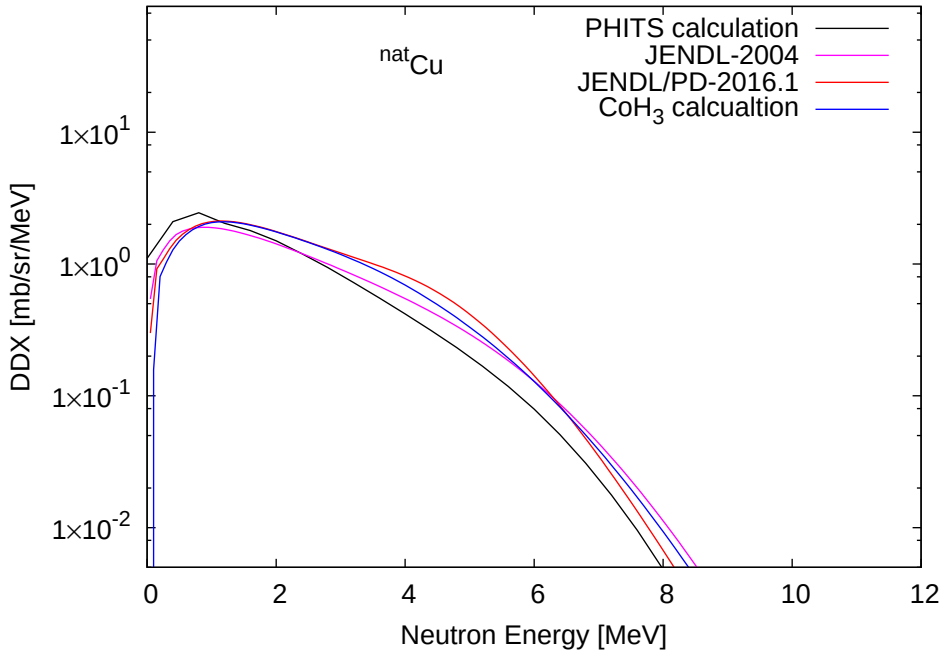

(b) Cu

Figure 4.79: Comparison of the DDX calculation results for Sn and Cu.

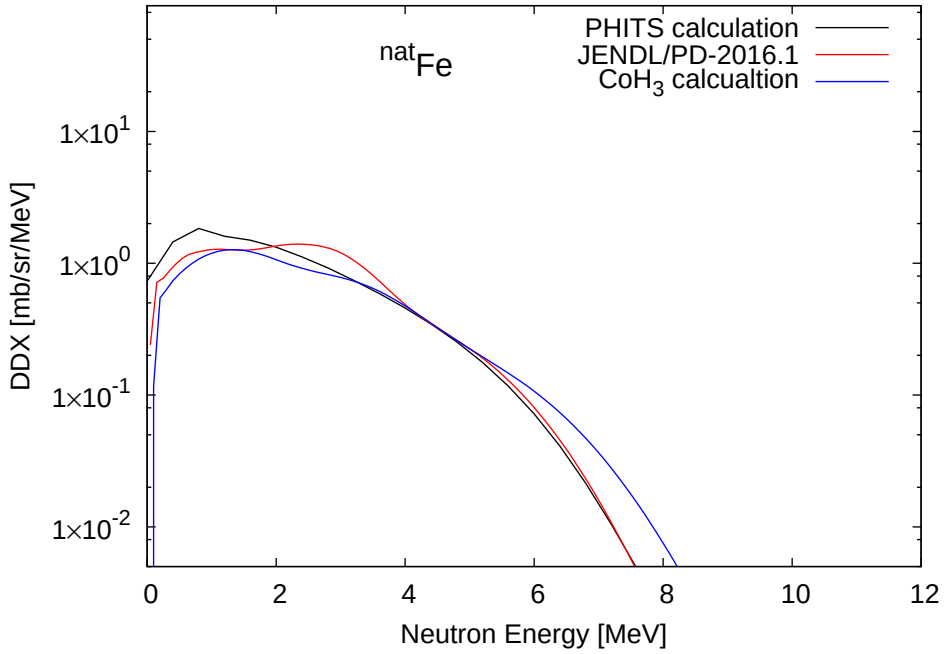

(a) Fe

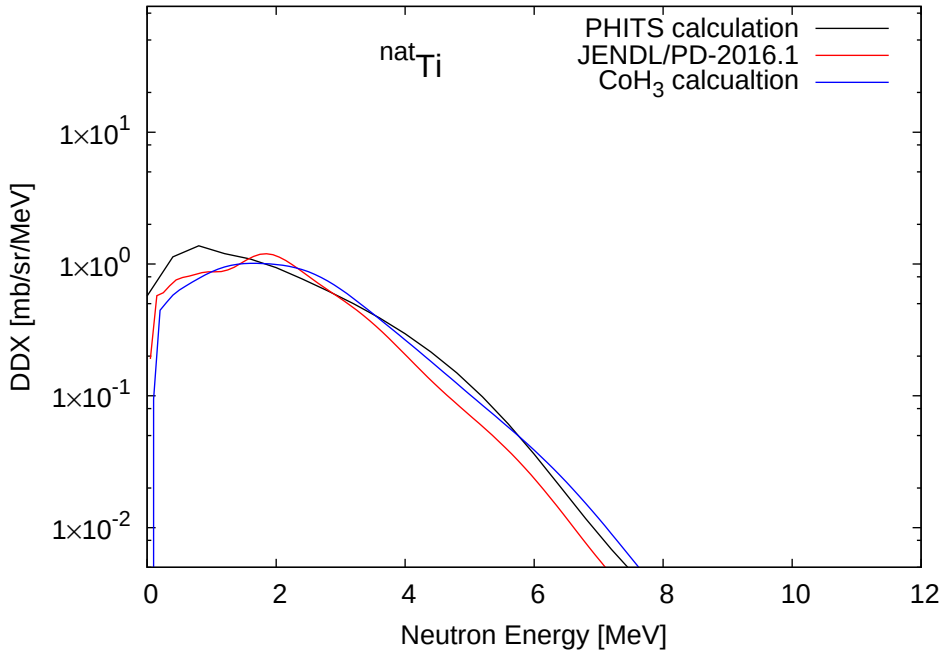

(b) Ti

Figure 4.80: Comparison of the DDX calculation results for Fe and Ti.

Chapter 5

Results and discussion

The DDXs of the photoneutrons were measured using polarized photons at New-SUBARU, as discussed in Chapter 2. After data acquisition, the data sets were analyzed to determine the DDXs, as described in Chapter 3. In this chapter, using the DDX data with 17 MeV photons, the energy and angular distributions of the photoneutrons are discussed. The target mass dependence and photon energy dependence of the photoneutrons are also discussed. Finally, to understand the current status of photoneutron production in particle transport simulation, the calculated DDXs and experimental data are compared.

5.1 Double-differential cross section of photoneutron production

The DDX values of (γ,xn) reactions on six targets ($^{nat.}$Pb, ^{197}Au, $^{nat.}$Sn, $^{nat.}$Cu, $^{nat.}$Fe, and $^{nat.}$Ti) at six angles (horizontal 30°, 60°, 90°, 120°, 150°, and vertical 90°) were obtained from experiments using a 17 MeV polarized photon beam, as shown in Figure 5.1. Six neutron detectors were labeled with H30, H60, H90, H120, H150, and V90, respectively. The minimum neutron energies of all data points were 2 MeV, and the maximum neutron energies ($E^{max}_{exp.}$) were slightly higher than the theoretical energies (E^{max}_{theory}) in Table 5.1 because the energy resolutions broaden the DDX distributions. The energy resolutions were discussed in section 3.3.2 and Figure 3.5.

In this study, the maximum energies of the neutrons (E^{max}_{theory}) produced from the photonuclear reactions in each target were calculated by subtracting the Q-values of the reaction from the energy of the incident photon. All the target material isotopes in this study had their natural abundances. The Q-values of neutron emission reactions are different. In Table 5.1, only the minimum Q-values of neutron emission reactions from isotopes with abundance greater than 10% are listed as E^{max}_{theory}. The Q-values of different isotopes were given in Reference [31].

Table 5.1: Maximum theoretical neutron energy for different targets.

Target	Maximum neutron energy, E^{max}_{theory} [MeV]
^{nat}Pb	9.9
^{197}Au	8.5
^{nat}Sn	7.5
^{nat}Cu	6.7
^{nat}Fe	5.4
^{nat}Ti	5.0

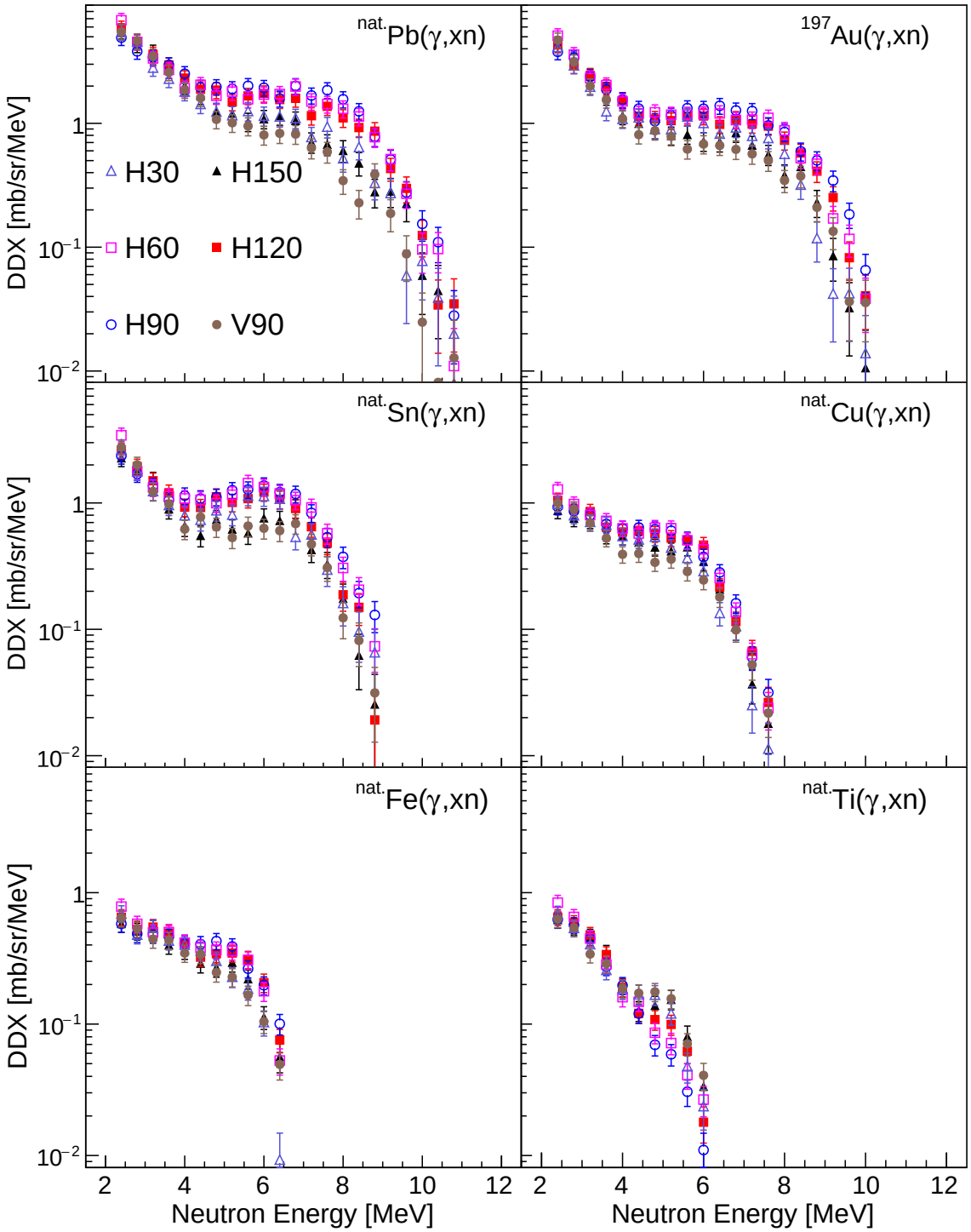

Figure 5.1: Experimental results of the DDXs of the (γ, xn) reaction for 17 MeV horizontally polarized photons on Pb, Au, Sn, Cu, Fe, and Ti targets.

In Figure 5.1, two components were observed in the DDX; one component mainly occupied the energy range of 2–4 MeV of the DDX, and the other component mainly occupied the energy range from 4 MeV to $E_{exp.}^{max}$. For energy lower than 4 MeV, shape of the energy distribution was similar to the tail of the Maxwell distrbution; thus, the energy distribution below 4 MeV was called the Maxwellian-shaped component. The photoneutrons in the Maxwellian-shaped component were expectedly independent of the neutron emission angle because the photoneutrons were produced by the evaporation process [27]. The variations in the Maxwellian-shaped component of DDX for different angles were caused by the uncertainties mentioned in Table 2.2.

The component with energy higher than 4 MeV was named the non-Maxwellian-shaped component. The neutrons in the non-Maxwellian-shaped component of DDX are known to be produced by direct, pre-equilibrium processes and the polarization effect of the polarized photons, according to previous studies [30, 37, 54, 55]. The experimental data obtained in the ^{197}Au(γ,xn) measurement were consistent with the results of neutron energy spectra reported by Kirihara et al. [37]. For targets except Ti, the minimum and maximum DDX values were obtained at the horizontal and vertical 90°, respectively. On the other hand, for Ti, the relationship is the opposite; the minimum and maximum DDX values were obtained at the horizontal 90° and vertical 90°, respectively. For further analysis, the Maxwellian-shaped and non-Maxwellian-shaped components must be separated. To determine the energy for separation of these two components, the Maxwellian-shaped component was fitted with a Maxwellian-shaped distribution, which can well explain the evaporation process; subsequently, the difference between the experimental data and fitting is identified. The Maxwellian fitting was performed for the data points in the energy range of 2–4 MeV.

In Figure 5.2 – Figure 5.7, the Maxwellian fitting function is plotted as a solid red line and shown together with the experimental data obtained in the measurement for each target.

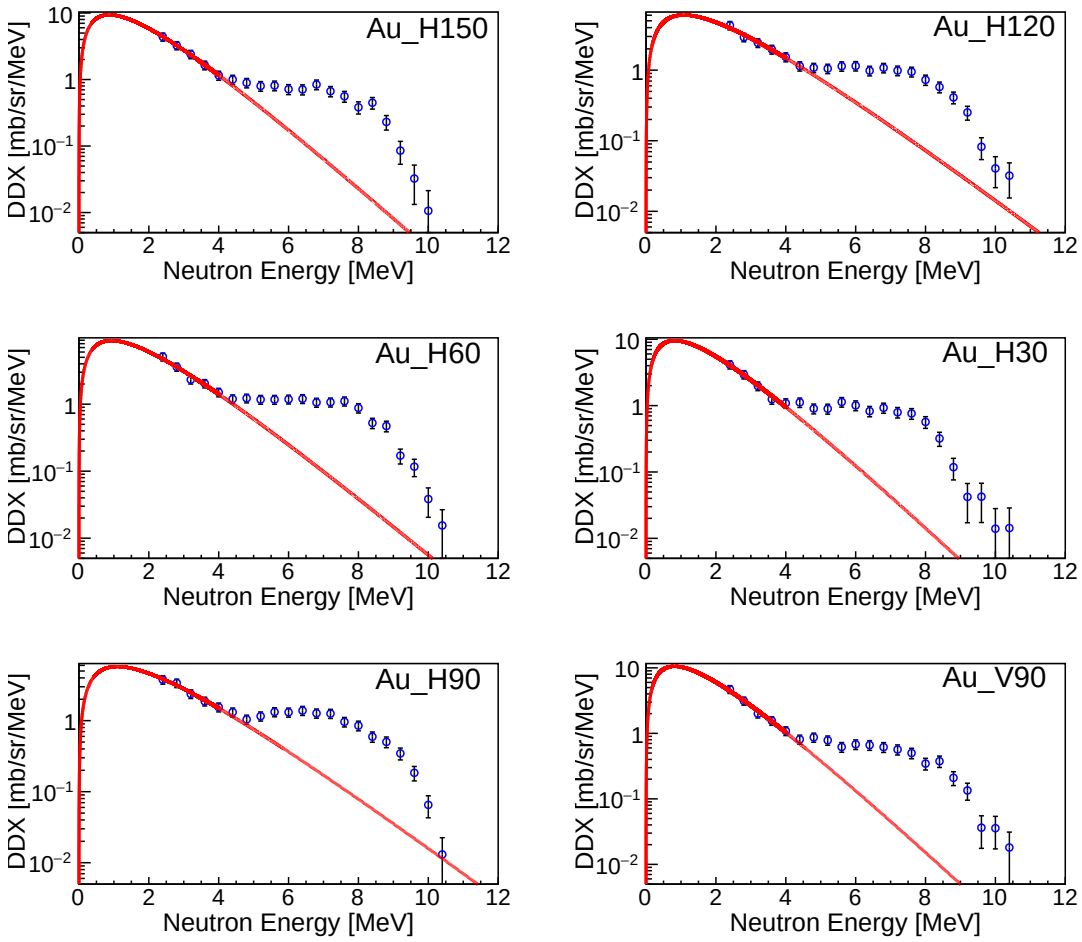

Figure 5.2: Fitting of a Maxwell distribution for the data obtained with an Au target.

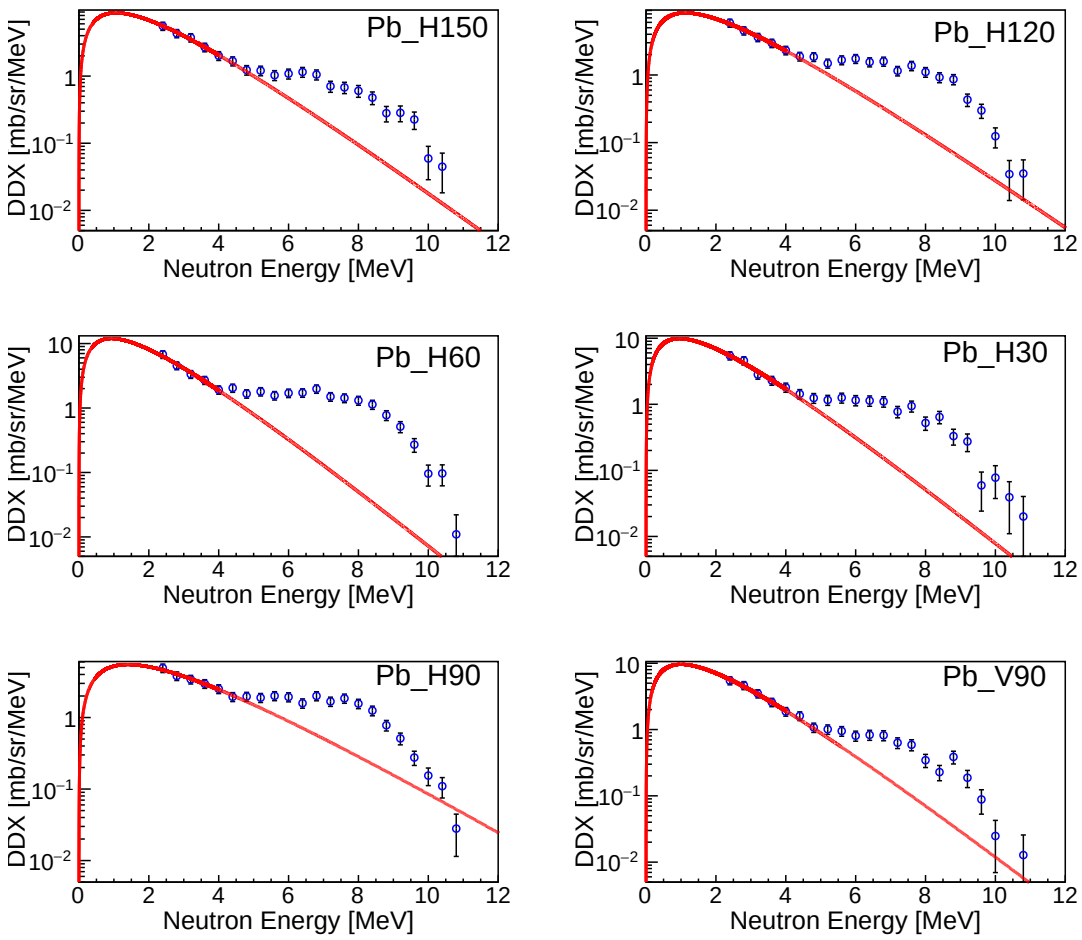

Figure 5.3: Fitting of a Maxwell distribution for the data obtained with an Pb target.

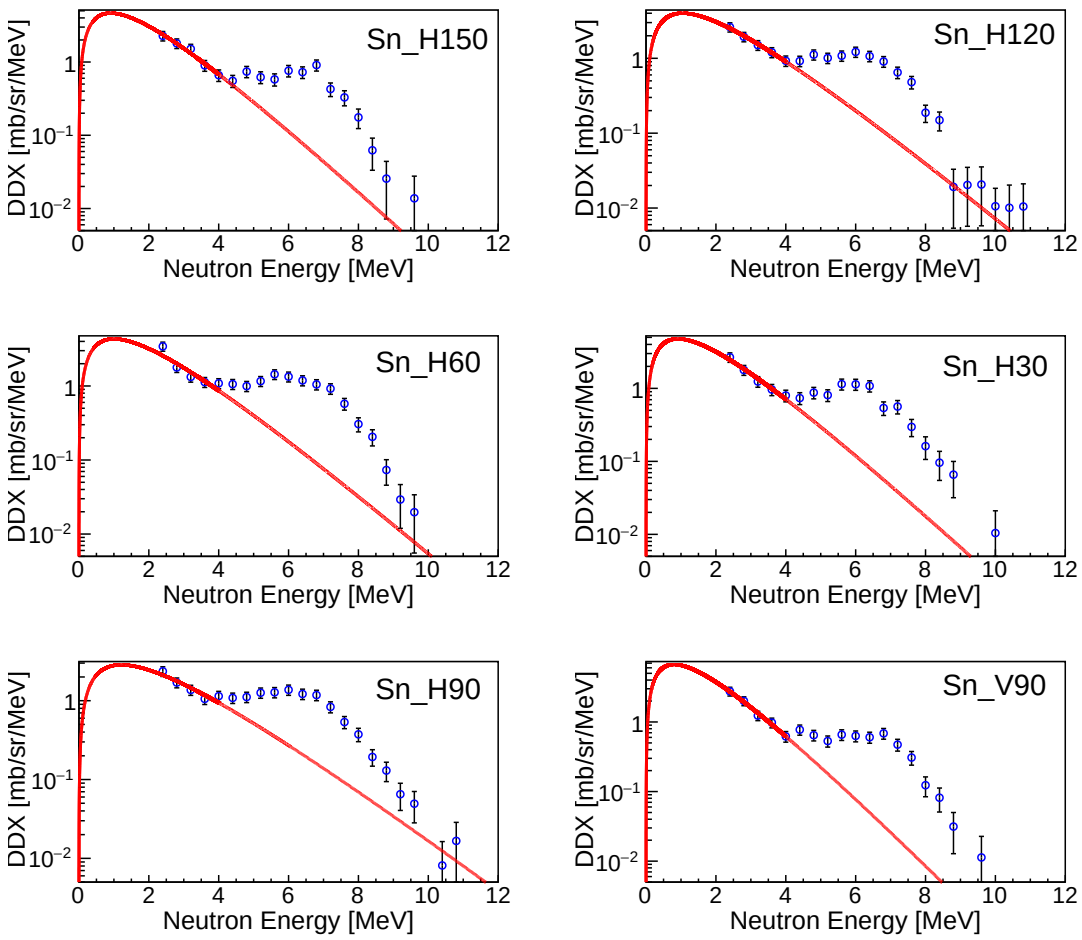

Figure 5.4: Fitting of a Maxwell distribution for the data obtained with an Sn target.

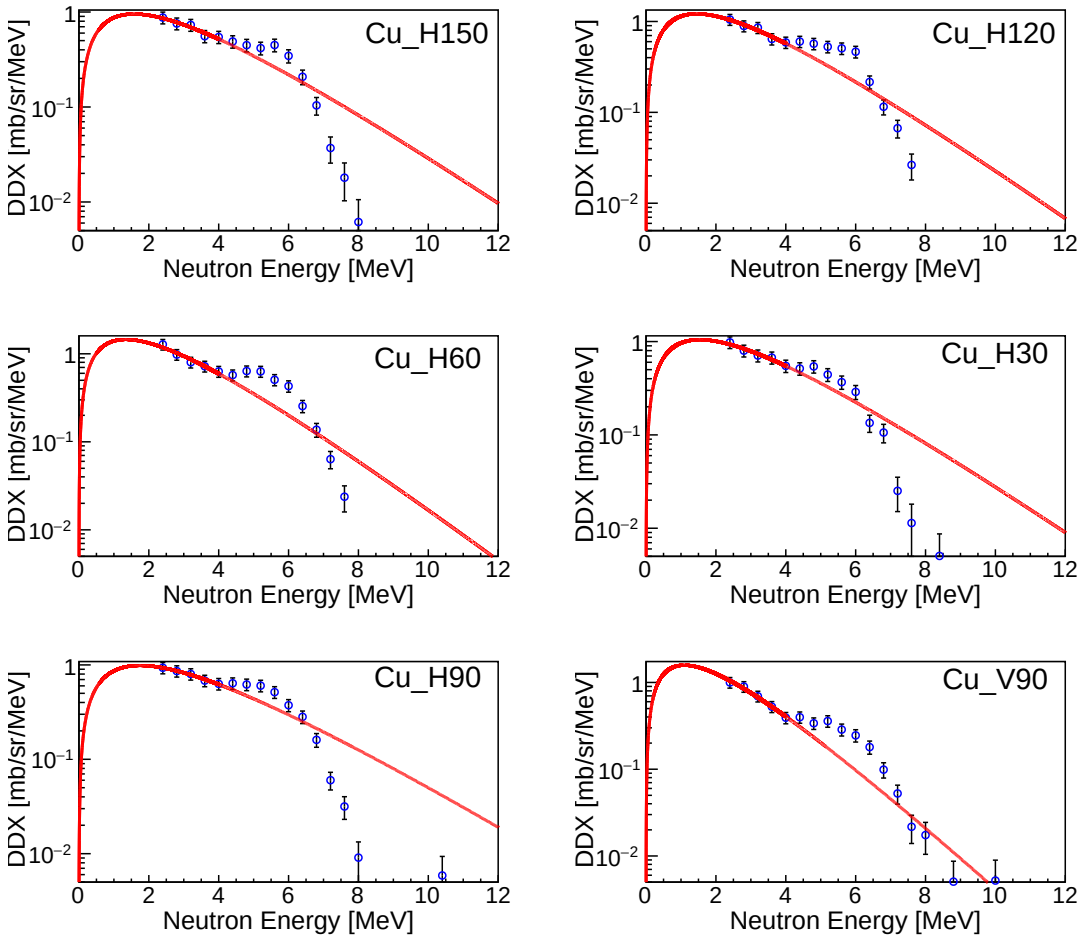

Figure 5.5: Fitting of a Maxwell distribution for the data obtained with an Cu target.

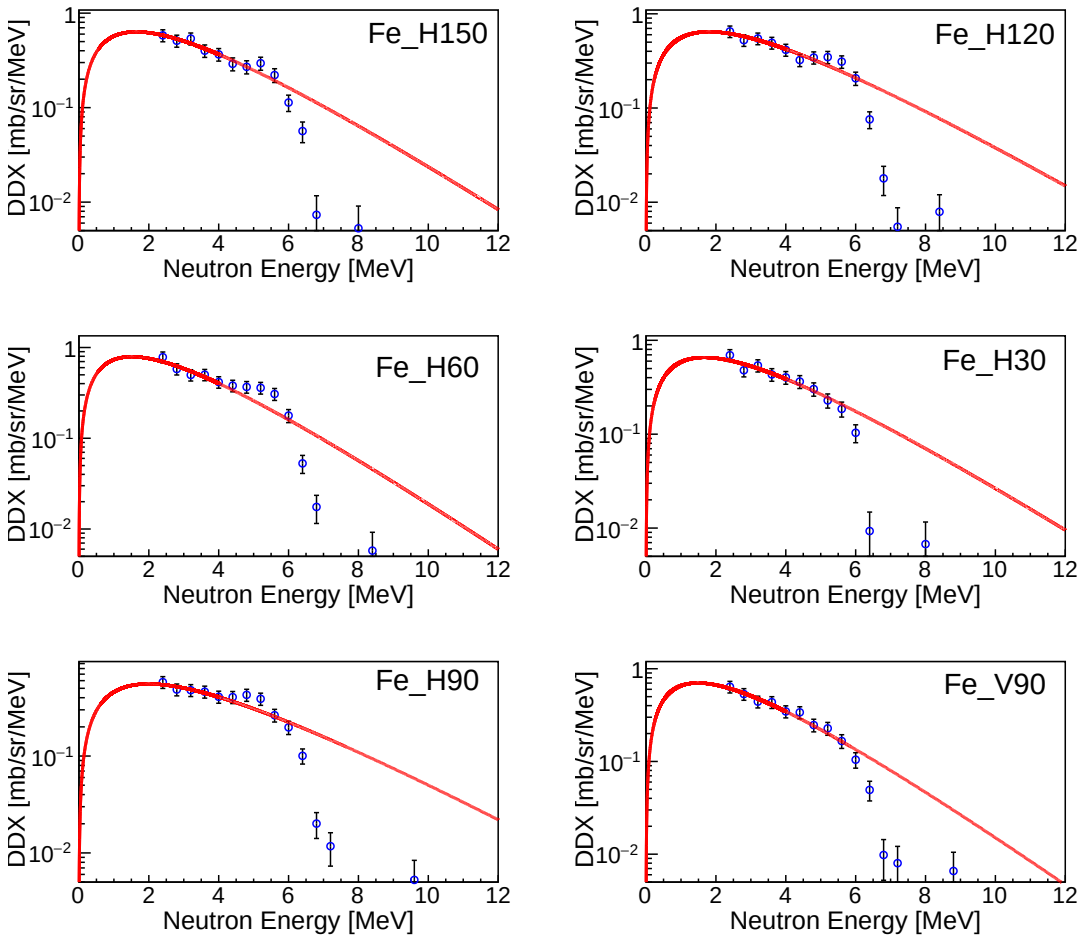

Figure 5.6: Fitting of a Maxwell distribution for the data obtained with an Fe target.

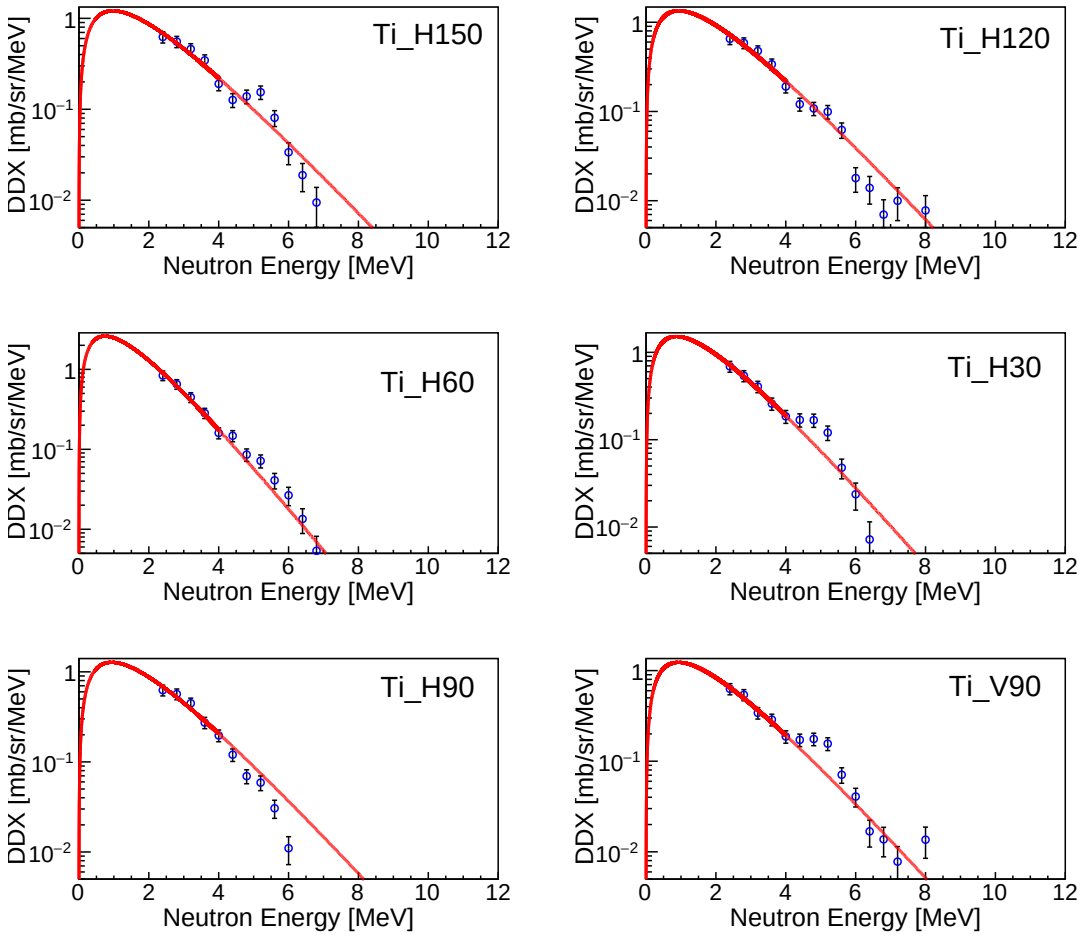

Figure 5.7: Fitting of a Maxwell distribution for the data obtained with an Ti target.

Table 5.2 lists the temperature parameters of the Maxwell distribution for the targets at different detection angles. The temperature parameters at different angles in the same target are inconsistent because the energy points below 2 MeV are missing in the experiment.

Table 5.2: Temperature parameters of Maxwell fitting for the targets.

Target	Temperature [MeV]					
	H30	H60	H90	H120	H150	V90
^{nat}Pb	0.95±0.11	0.92±0.10	1.4±0.22	1.12±0.14	1.05±0.12	1.00±0.10
^{197}Au	0.81±0.08	0.93±0.10	1.0±0.13	0.86±0.08	1.09±0.13	0.81±0.08
^{nat}Sn	0.91±0.12	1.00±0.15	1.2±0.19	1.04±0.13	0.90±0.10	0.80±0.08
^{nat}Cu	1.53±0.28	1.33±0.21	1.74±0.33	1.44±0.23	1.57±0.28	1.09±0.13
^{nat}Fe	1.66±0.35	1.5±0.27	1.99±0.45	1.80±0.36	1.63±0.31	1.48±0.26
^{nat}Ti	0.86±0.08	0.74±0.05	0.93±0.09	0.93±0.08	0.97±0.09	0.92±0.09

To identify the difference, the ratio of experimental data to the Maxwellain fitting data was taken at every energy. Figure 5.8 shows these ratios of the DDX data obtained at horizontal 60° in six targets. These ratios at neutron energies below 4.2 MeV, which is the upper boundary of the energy bin, ranged from 0.8 to 1.1 for all six targets. For energies higher than 4.2 MeV, the ratios quite different; they increase up to 1.2 and then decrease to approximately 0.2. The ratios obtained at other angles show the same trends. Therefore, the separation energy to separate the Maxwellian-shaped and non-Maxwellian-shaped component for all targets was set at 4.2 MeV. It is interesting that the same energy was applied to separate Maxwellian-shaped and non-Maxwellian-shaped components obtained from (γ,xn) on different nuclei with different excitation energies.

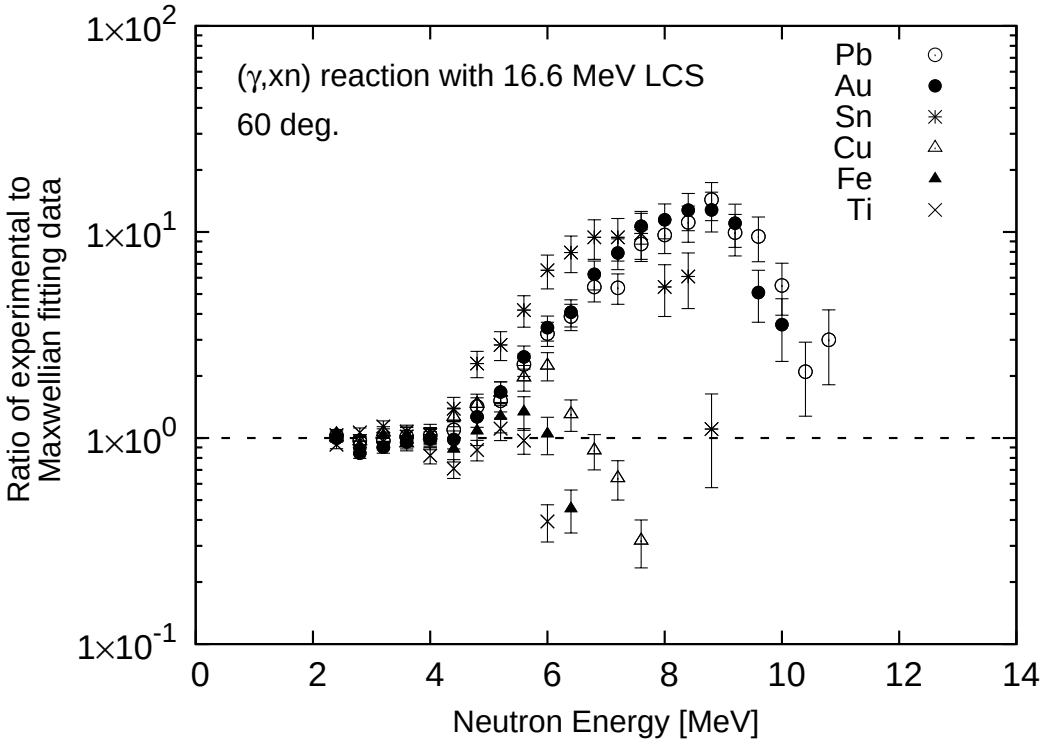

Figure 5.8: Ratio of experimental data to the Maxwellian fitting function for all targets.

5.2 Angular dependence of photoneutron production

5.2.1 Angular distribution of neutrons

This section discusses on the angular distribution of the Maxwellian-shaped and non-Maxwellian-shaped components discussed in section 5.1. To do that, it is necessary to consider the ADXs and the angles of incident photons and emitted neutrons. The ADXs for the Maxwellian-shaped and non-Maxwellian-shaped components were calculated by integrating the DDXs in the energy range from 2 MeV to 4.2 MeV, which were determined in section 5.1, and those in the range from 4.2 MeV to E_{exp}^{max},

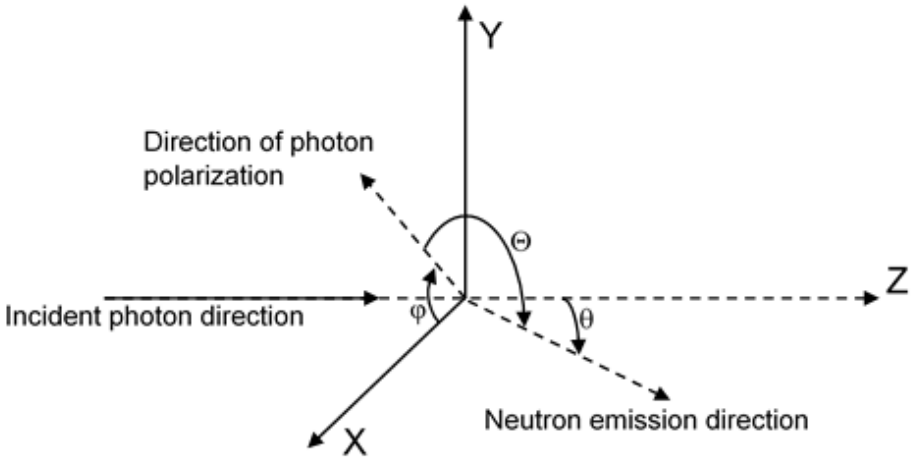

(a) Relationships among the φ, θ, and Θ angles.

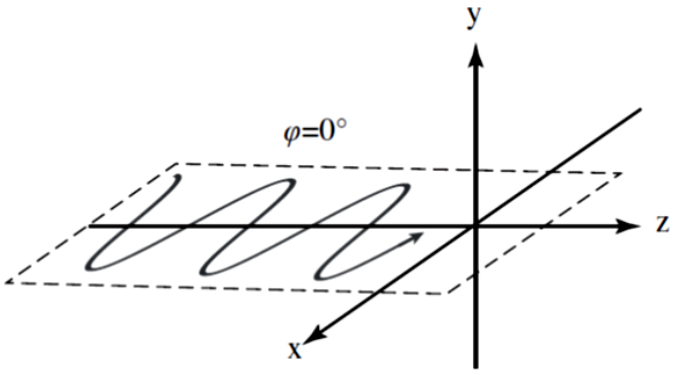

(b) Polarization angle of the LCS photons in this study

Figure 5.9: Relationship between the photon direction and neutron emission direction.

respectively.

Figure 5.9 shows the angles used in the discussion on the ADXs of photoneutrons. The incident photon direction is exactly on the Z axis. The XZ plane is defined by the horizontal NE213 detectors and the photon beam axis. These angles include the angle φ formed by the directions of photon polarization and the XZ plane, the angle Θ formed by the directions of photon polarization and emitted neutrons, and the angle θ formed by the directions of incident photons and emitted neutrons. Because φ is chosen to be parallel to the XZ plane, this angle is equal to 0° and 90° for horizontal and vertical detectors, respectively. The angle Θ is the main angle used in ADX. One can express the relationship among these angles as follows:

$$\cos(\Theta) = \sin(\theta) \cdot \cos(\varphi). \tag{5.1}$$

Using Equation 5.1, values of Θ from 0° to 90° were obtained as listed in Table 5.3.

Table 5.3: Values of Θ determined using Equation 5.1.

Detector	θ[°]	φ[°]	Θ[°]
H30	30	0	60
H60	60	0	30
H90	90	0	0
H120	120	0	30
H150	150	0	60
V90	90	90	90

As mentioned at the beginning of this section, the ADX values were calculated by taking the integral of the Maxwellian-shaped and non-Maxwellian-shaped DDXs for each target. The ADXs are shown in Figure 5.10 as a function of Θ of Maxwellian-shaped and non-Maxwellian-shaped neutrons for the six targets, with the values of Θ mentioned in Table 5.3. The function used for fitting ADX in Figure 5.10 as follows:

$$\mathrm{ADX}(\Theta) = \mathrm{a} + \mathrm{bcos}(2\Theta), \tag{5.2}$$

where a and b are fitting parameters.

Table 5.4 lists the obtained fitting parameters a and b for the Maxwellian-shaped and non-Maxwellian-shaped components in each target.

The ADX of the Maxwellian-shaped components in Figure 5.10 has a flatter an-

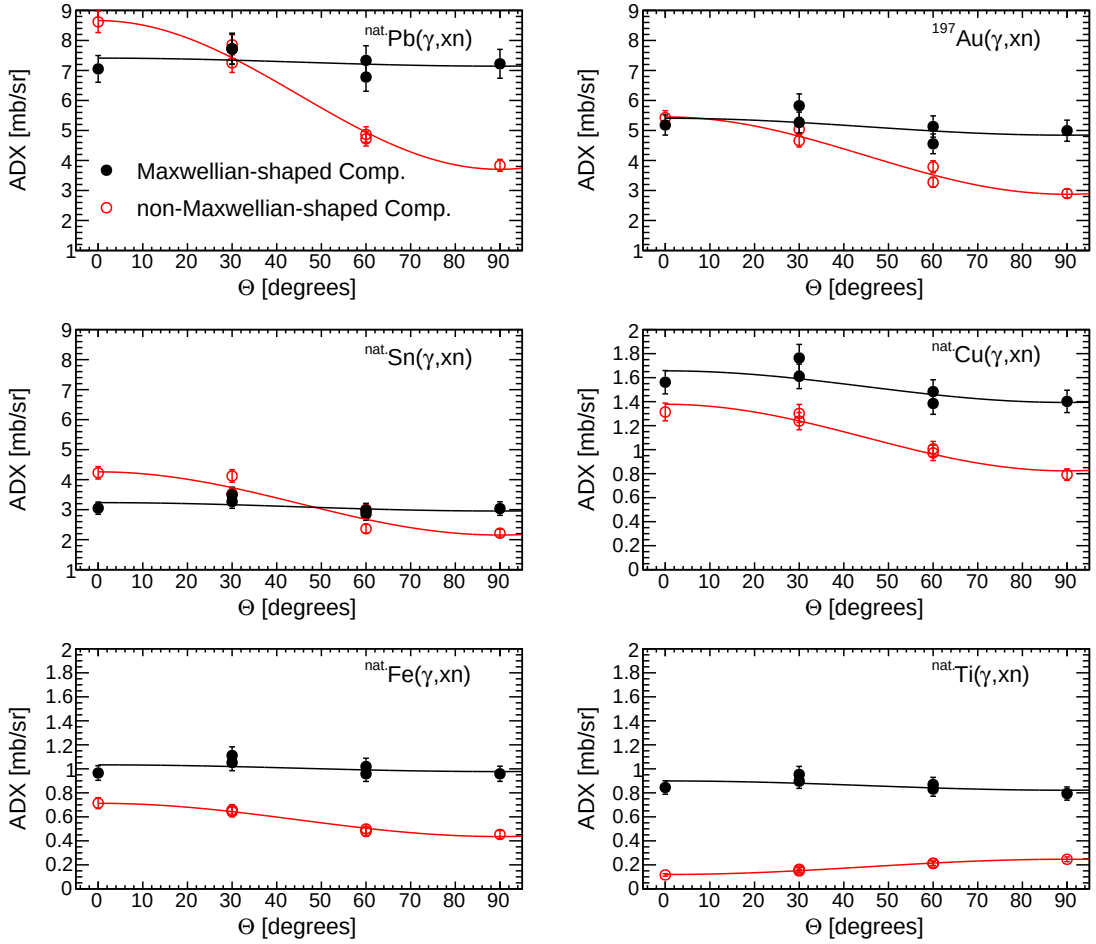

Figure 5.10: ADX as a function of the angle between the polarization and detector directions for the Maxwellian-shaped and non-Maxwellian-shaped components.

Table 5.4: Summary of the fitting parameters for Maxwellian-shaped and non-Maxwellian-shaped components.

Target	Maxwellian-shaped component			non-Maxwellian-shaped component		
	a_{Max}	b_{Max}	b_{Max}/a_{Max}	$a_{non-Max}$	$b_{non-Max}$	$b_{non-Max}/a_{non-Max}$
^{nat}Pb	7.28±0.20	0.13±0.27	0.02±0.04	6.18±0.12	2.48±0.16	0.40±0.03
^{197}Au	5.13±0.14	0.28±0.20	0.06±0.04	4.16±0.08	1.29±0.11	0.31±0.03
^{nat}Sn	3.09±0.09	0.14±0.13	0.05±0.04	3.21±0.07	1.05±0.10	0.33±0.03
^{nat}Cu	1.53±0.04	0.13±0.06	0.09±0.04	1.11±0.03	0.28±0.04	0.25±0.03
^{nat}Fe	1.01±0.03	0.03±0.04	0.03±0.04	0.57±0.02	0.14±0.02	0.24±0.04
^{nat}Ti	0.86±0.02	0.04±0.03	0.04±0.04	0.18±0.01	-0.06±0.01	-0.35±0.05

gular distribution than the non-Maxwellian-shaped ADX. a_{Max} increases with the target Z. The Maxwellian-shaped component neutrons in this research could not be measured at energies less than 2 MeV. This energy threshold causes an underestimation of the total amount of Maxwellian neutrons. Therefore, the tendency of a_{Max} must be confirmed using experimental data measured with a lower energy threshold. For light nuclei, because of the large negative reaction Q-value, the maximum neutron energy is relatively low; thus, it is important to measure the DDX data below 2 MeV to estimate the ADX values.

The values of b_{Max} and b_{Max}/a_{Max} reported in Table 5.4 are used to discuss the angular dependence of ADXs in different targets. The magnitude of angular dependence for the Maxwellian neutrons (b_{Max}) is smaller than that for the non-Maxwellian neutrons ($b_{non-Max}$). The ratios b_{Max}/a_{Max} and $b_{non-Max}/a_{non-Max}$ indicate the amplitude fluctuation of the angular dependence of Maxwellian and non-Maxwellian components, respectively. For the neutrons with energies less than 4.2 MeV, the ratio b_{Max}/a_{Max} is less than one tenth of the total Maxwellian component for all targets.

On the other hand, the angular dependence of the neutrons in the non-Maxwellian component, as shown in Figure 5.10, can be well explained by the fitting function in Equation 5.2. The maximum ADXs measured with Pb, Au, Sn, Cu, and Fe targets are observed at $\Theta = 0°$. However, at this angle $\Theta = 0°$, the minimum ADX value is obtained for the Ti target.

With a higher target Z, the total amount of neutrons in non-Maxwellian component and the $b_{non-Max}$ value both increase. The $b_{non-Max}/a_{non-Max}$ values indicating the anisotropy of non-Maxwellian neutrons are higher than 0.24 for all targets, except for Ti. This value implies that a significant number of emitted neutrons are sensitive to the photon polarization direction. For the Ti target, the obtained $b_{non-Max}$ is small (-0.06), but the ratio $b_{non-Max}/a_{non-Max}$ of this target is -0.35, implying that a significant number of neutrons exhibit an opposite angular distribution compared

to that of other targets.

The ratio b_{Max}/a_{Max} measured with Au in the present study (0.31 ± 0.03) is consistent with the ratio reported in a previous study [37] (0.35 ± 0.04). To make this comparison, the b_{Max}/a_{Max} ratio of Au in Reference [37] was calculated using the fitting parameters reported in that paper, and the uncertainty of this ratio was calculated by using a_2. The $b_{non-Max}$ of Au is 1.9 times smaller than that of Pb, although the difference in atomic number is not significant. The non-Maxwellian neutrons have a dependence on the Z of the target, and this dependence, together with the comparison with data from measurements using bremsstrahlung photons, will be discussed below.

The obtained cross section of the (γ, xn) reactions can be determined by integrating the ADX over the 4π solid angle range. It corresponds to $4\pi(a_{Max} + a_{non-Max})$, where a_{Max} and $a_{non-Max}$ are fitting results. Because the neutrons with energies below 2 MeV could not be measured in the present experiment, the obtained cross section, for example 169.06 mb for Pb, is different from the value of approximately 200 mb reported in a previous study of Varlamov et al. [31, 56]. This is motivation to perform a similar experiment with a lower energy threshold for neutrons in the near future, which will help in checking the consistency of the DDX data with the previously reported cross section of the (γ,xn) reactions.

5.2.2 Anisotropy parameter of the non-Maxwellian component

The angular distributions of the Maxwellian-shaped and non-Maxwellian-shaped components, which were the results of evaporation and pre-equilibrium processes, respectively, were measured with bremsstrahlung photons, which are unpolarized, in previous studies. The angular distribution of anisotropic neutrons can be expressed as a Legendre polynomial expansion [28]:

$$W(\theta) = a_{\circ} \sum_{n=1}^{\infty} (1 + a_n P_n(\cos(\theta))). \tag{5.3}$$

With n = 2, the parameter a_2 in the above equation implies the dipole component of the interaction. $P_2(\cos\theta)$ of Equation 5.2.2 can be written as

$$P_2(\cos\theta) = \frac{1}{2}(3\cos^2\theta - 1). \tag{5.4}$$

Thus, the expression inside parentheses can be written as follows:

$$1 + a_2 P_2(\cos\theta) = \left(1 - \frac{a_2}{2}\right)\left[1 + \frac{\frac{3}{2}a_2\cos^2\theta}{1 - \frac{a_2}{2}}\right]. \tag{5.5}$$

On the other hand, from Equation 5.1

$$a + b\cos(2\Theta) = a + b(2\cos^2\varphi\sin^2\theta - 1). \tag{5.6}$$

To compare the experimental data obtained in the present study with bremsstrahlung data, the average squared cosine value of the polarization angle φ (defined in Figure 5.9) from 0° to 90° was estimated as follows:

$$\cos^2\varphi = \int_0^{\pi/2} \cos^2\varphi d\varphi = \frac{1}{2}. \tag{5.7}$$

From Equation 5.6 and Equation 5.7, it is expressed as follows:

$$a + b\cos(2\Theta) = a - b\cos^2\theta. \tag{5.8}$$

If $k = \frac{b}{a}$, Equation 5.8 was written as follows:

$$a(1 - k\cos^2\theta). \tag{5.9}$$

Combining Equation 5.5 and Equation 5.9, formula of a_2 is expressed as follows:

$$a_2 = \frac{-2k}{3 - k}. \tag{5.10}$$

Therefore, the parameter a_2, which expresses angular dependence of neutron emission for unpolarized photons can be obtained from the ratio of parameters, a and b, that are obtained from polarized photon data. The numerical data in Table 5.4 were used to compare a_2 with previous angular dependence data obtained in the 1950s and 1960s.

5.2.3 Comparison of anisotropy parameters between the present results and previous data

The numerical values of a_2 for the non-Maxwellian-shaped component obtained in the present study are listed in Table 5.5 together with the data obtained from previous studies for comparison. In this table, the a_2 values are presented with different measurement conditions, including the energy of the incident photon beam (E_γ), how the photon source is produced, the energy threshold of neutrons, the measurement method, and the corresponding references. The referenced data are sourced from systematic data acquisition for the angular distribution of photoneutrons emitted from various materials by Mutchler [25], Price [26], Tagliabue [27], Baker [28], Horikawa [36], and Kirihara [37].

Table 5.5: Summary of numerical values of a_2 for the (γ, xn) reaction with 17 MeV polarized photons for the non-Maxwellian-shaped component in comparison with previous experiments with different photon sources and experimental techniques.

Target	-a_2	E_γ [MeV]	Photon source	E_n^{min} [MeV]	Method	References
^{82}Pb	0.31±0.02	17	LCS	4.2	TOF	This work
	0.42±0.03	22	Bremsstrahlung	6	^{28}Si(n,p)	Baker
	0.41±0.09	22	Bremsstrahlung	6	^{28}Si(n,p)	Tagliabue
^{79}Au	0.23±0.02	17	LCS	4.2	TOF	This work
	0.26±0.04	17	LCS	4	TOF	Kirihara
	0.38±0.03	13	Breamsstrahlung	6	TOF	Mutchler
	0.30±0.05	22	Breamsstrahlung	6	^{28}Si(n,p)	Tagliabue
	0.27±0.01	16.7	LCS	2	TOF	Horikawa
^{53}I	0.13±0.02	16.7	LCS	2	TOF	Horikawa
	0.04±0.05	22	Breamsstrahlung	6	^{28}Si(n,p)	Tagliabue
^{50}Sn	0.25±0.03	17	LCS	4.2	TOF	This work
^{29}Cu	0.18±0.03	17	LCS	4.2	TOF	This work
	0.19±0.04	22	Bremsstrahlung	4	^{27}Al(n,p)	Price
	0.29±0.04	22	Bremsstrahlung	6	^{28}Si(n,p)	Baker
	0.08±0.17	22	Bremsstrahlung	6	^{28}Si(n,p)	Tagliabue
	0.03±0.02	16.7	LCS	2	TOF	Horikawa
^{26}Fe	0.17±0.03	17	LCS	4.2	TOF	This work
	0.17±0.05	22	Bremsstrahlung	6	^{28}Si(n,p)	Baker
^{25}Mn	0.00±0.00	22	Bremsstrahlung	6	^{28}Si(n,p)	Tagliabue
^{23}V	-0.05±0.07	22	Bremsstrahlung	4	^{27}Al(n,p)	Price
^{22}Ti	-0.21±0.03	17	LCS	4.2	TOF	This work

The experiments of Price [26], Tagliabue [27], and Baker [28] were performed using a bremsstrahlung photon source, which provided a continuous photon energy

distribution. Their results, hence, were obtained for photoneutrons produced in the entire GDR. In other words, their a_2 results are "averaged" values for the energy range from the reaction threshold to the photon energies, considering weighting factors of the reaction cross section at different photon energies. It is clear that the dependence on the incident photon energy of a_2 was not studied, even if it existed. On the other hand, the LCS technique used by Horikawa [36], Kirihara [37], and the present study, provides a mono-energetic photon beam that is suitable for studying the photon energy dependence of a_2.

Mutchler measured the data using quasi-monoenergetic photons [25] to avoid the "photon energy average" by using two sets of data obtained with bremsstrahlung photons at different maximum energies. This method provided data for photons with a small energy width.

As for the detection techniques, Price, Tagliabue, and Baker obtained the photoneutrons by using activation detectors based on the (n,p) reactions on either ^{28}Si or ^{27}Al. These results were distorted by the excitation function of the reaction; however, the present TOF data are not distorted, because the energy dependency of the detection efficiency was considered. There are other sets of data not mentioned in this thesis, because they were obtained using detectors that are sensitive to neutron energy below 2 MeV. The Maxwellian-shaped neutrons do not have a significant angular distribution and mask the angular distribution of the non-Maxwellian-shaped neutrons because of their large yield.

The a_2 values of Cu and Fe reported herein are consistent with those obtained in previous studies [28], but the a_2 values of other targets are different. The a_2 values of Au reported by of Mutchler [25], for example, are 1.6 times higher than the value obtained in the present study. The two data sets were obtained from experiments with monoenergetic photons but with different energies. Therefore, the dependence on the incident photon energy of a_2 should be further investigated using monoenergetic LCS photons with different energies. The present Cu data are

2.25 times larger than those obtained with Tagliabue's data [27]. This is because the neutrons with energy above 6 MeV exhibit less angular dependence for Cu, as shown in Figure 5.1. Therefore, the ^{28}Si(n,p)^{28}Al reaction detector that was used in the previous study with an energy threshold of 6 MeV was not suitable for a measurement of photoneutrons from Cu.

The a_2 data of Sn and Ti nuclei were not available from previous experiments; data for nuclei with close Z values are presented in Table 5.5 for comparison. The present a_2 data for Sn are greater than those for I, but their Z values are close to each other. The a_2 for I in Reference [26] was obtained using a bremsstrahlung photon source; however, the data obtained with the same LCS photons [36] are half of the present result owing to the difference in detector response and the minimum energy of integration. The present a_2 data for Ti can be compared with those of V. Because the ADX of Ti exhibits opposite angular dependence, the sign of the present a_2 data is opposite to that of the others. The a_2 data of V also have an opposite sign; thus, the opposite angular dependence could be obtained for light nuclei.

The numerical values of a_2 used to deduce the ADXs are summarized in Table 5.6 for further discussion on the detector threshold effect with different minimum neutron energies. As shown by the polynomial formula in Equation 5.2.2, a_2 can be affected by a_0 parameter. Therefore, a_2 has a dependence on the minimum energy and energy response of the neutron detector. Considering the uncertainty caused by these factors, the present study provides data that are in good agreement with those of previous studies.

Table 5.6: Minimum energy dependence of a_2 for Pb, Au, Sn, Cu, Fe, and Ti.

Target	-a_2		
	$E_n \geq$2MeV	$E_n \geq$4MeV	$E_n \geq$6MeV
^{nat}Pb	0.14 ± 0.02	0.31 ± 0.02	0.40 ± 0.03
^{197}Au	0.12 ± 0.02	0.23 ± 0.02	0.29 ± 0.03
^{nat}Sn	0.14 ± 0.02	0.25 ± 0.03	0.24 ± 0.04
^{nat}Cu	0.11 ± 0.02	0.18 ± 0.03	0.18 ± 0.05
^{nat}Fe	0.07 ± 0.02	0.17 ± 0.03	
^{nat}Ti	-0.02 ± 0.02	-0.21 ± 0.03	

5.3 Target mass dependence of photoneutron spectrum

Figure 5.11 shows the photoneutron spectra of the (γ,xn) reaction on Pb, Au, Sn, Cu, Fe, and Ti targets at H90 with 17 MeV photons. The spectra were obtained from 2 MeV to the maximum energy. The two components, the Maxwellian-shaped component and the non-Maxwellian-shaped component, were observed on the photoneutron spectrum. The Maxwellian-shaped component was mainly observed in the energy range from 2 MeV to the separation energy (as mentioned in section 5.1), which is 4.2 MeV, and the non-Maxwellian-shaped component was mainly observed in the energy range from 4.2 MeV to the maximum energy of each spectrum. This phenomenon is the same for the data at H150, H120, H60, H30, and V90, as shown in Figure 5.1.

As shown in Figure 5.11, the magnitude of the spectrum and maximum energy decrease with decreasing target mass number. The decrease in the magnitude is reasonable because of the total reaction cross section. Using 17 MeV excitation photons, the number of emitted photoneutrons of Cu, Fe, and Ti nuclei is smaller than that of Pb, Au, and Sn nuclei.

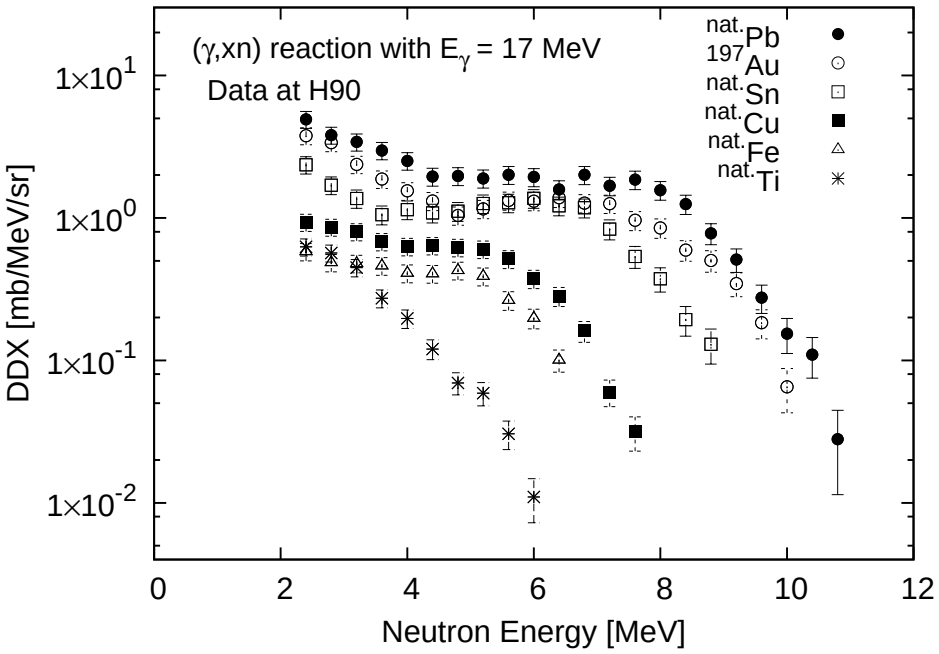

Figure 5.11: Photoneutron spectra of the (γ,xn) reaction at H90 with 17 MeV photons for medium-heavy targets.

The cross section for the Maxwellian-shaped component ($\sigma_{\mathrm{Max.}}$), the non-Maxwellian-shaped component ($\sigma_{\mathrm{non-Max.}}$), and the sum of these two components (σ_{sum}) can be calculated by integrating over the entire solid angle, as Equation 5.11, Equation 5.12, and Equation 5.13, respectively:

$$\sigma_{\mathrm{Max.}} = 4\pi \cdot \mathrm{a}_{\mathrm{Max.}}, \tag{5.11}$$

$$\sigma_{\mathrm{non-Max.}} = 4\pi \cdot \mathrm{a}_{\mathrm{non-Max.}}, \tag{5.12}$$

$$\sigma_{\mathrm{sum}} = 4\pi \cdot (\mathrm{a}_{\mathrm{Max.}} + \mathrm{a}_{\mathrm{non-Max.}}), \tag{5.13}$$

$$\mathrm{ratio}_{\mathrm{Max.}} = \frac{\sigma_{\mathrm{Max.}}}{\sigma_{\mathrm{sum}}}, \tag{5.14}$$

$$\mathrm{ratio}_{\mathrm{non-Max.}} = \frac{\sigma_{\mathrm{non-Max.}}}{\sigma_{\mathrm{sum}}}, \tag{5.15}$$

where the values of $\mathrm{a}_{\mathrm{Max.}}$ and $\mathrm{a}_{\mathrm{non-Max.}}$ are reported in Table 5.4.

Table 5.7 lists the obtained cross sections ($\sigma_{\mathrm{Max.}}$, $\sigma_{\mathrm{non-Max.}}$, and σ_{sum}) and ratios of the obtained cross sections ($\mathrm{ratio}_{\mathrm{Max.}}$, and $\mathrm{ratio}_{\mathrm{non-Max.}}$) for all the targets and their uncertainties. These ratios were calculated using Equation 5.14 and Equation 5.15, respectively.

The values of $\sigma_{\mathrm{Max.}}$, $\sigma_{\mathrm{non-Max.}}$, and σ_{sum} are plotted in Figure 5.12. According to the Ramsuer model [57], the total cross section can be expressed as:

$$\sigma_{\mathrm{T}} = 2\pi \left(\mathrm{R} + \lambda\right)^2 (1 - \alpha\cos\beta), \tag{5.16}$$

where

σ_{T} is the total cross section including absorption and scattering,

Table 5.7: Values of $\sigma_{\mathrm{Max.}}$, $\sigma_{\mathrm{non-Max.}}$, $\mathrm{ratio}_{\mathrm{non-Max.}}$, and $\mathrm{ratio}_{\mathrm{Max.}}$ for the Maxwellian-shaped component and the non-Maxwellian-shaped component.

Target	$\sigma_{\mathrm{Max.}}$ [mb]	$\sigma_{\mathrm{non-Max.}}$ [mb]	$\mathrm{ratio}_{\mathrm{Max.}}$	$\mathrm{ratio}_{\mathrm{non-Max.}}$
$^{\mathrm{nat}}$Pb	91.40 ± 2.47	77.30 ± 1.48	0.54 ± 0.02	0.46 ± 0.02
^{197}Au	64.37 ± 1.79	52.27 ± 1.01	0.55 ± 0.02	0.45 ± 0.02
$^{\mathrm{nat}}$Sn	38.87 ± 1.14	40.49 ± 0.91	0.49 ± 0.02	0.51 ± 0.02
$^{\mathrm{nat}}$Cu	19.15 ± 0.50	13.89 ± 0.33	0.58 ± 0.02	0.42 ± 0.02
$^{\mathrm{nat}}$Fe	12.62 ± 0.33	7.38 ± 0.20	0.63 ± 0.02	0.37 ± 0.02
$^{\mathrm{nat}}$Ti	10.80 ± 0.30	2.48 ± 0.08	0.81 ± 0.04	0.19 ± 0.01

$\mathrm{R} = \mathrm{r_0 A^{1/3}}$ is the nuclear radius with r_0 being the fundamental nuclear radius and A being the atomic mass number,

λ is the de Broglie wavelength,

α is a parameter related to absorbtion, and

β is the phase change between the transmitted and outside waves.

Because α is small, in the range 0.11–0.13 [58], the total cross section is approximated as follows:

$$\sigma_{\mathrm{T}} = 2\pi\,(\mathrm{R} + \lambda)^2, \tag{5.17}$$

which can be written as

$$\sqrt{\frac{\sigma_{\mathrm{T}}}{2\pi}} = \mathrm{r_0 A^{1/3}} + \lambda. \tag{5.18}$$

The cross sections in Figure 5.12 are fitted with Equation 5.18. σ_{sum} linearly increases with increasing target mass number. The values of $\sigma_{\mathrm{Max.}}$ and $\sigma_{\mathrm{non-Max.}}$ also increase with increasing target mass number.

The values of $\mathrm{ratio}_{\mathrm{Max.}}$ and $\mathrm{ratio}_{\mathrm{non-Max.}}$ for all targets with 17 MeV photons are plotted in Figure 5.13. The value of $\mathrm{ratio}_{\mathrm{non-Max.}}$ increases up to 0.5 with increasing target mass number, while the value of $\mathrm{ratio}_{\mathrm{Max.}}$ decreases from 0.81 down to 0.49. The increase and decrease of these ratios reach approximately 0.5 and then seem to remain constant with further increase in the target mass number. This implies that increasing the target mass number leads to a decrease in the contribution of the evap-

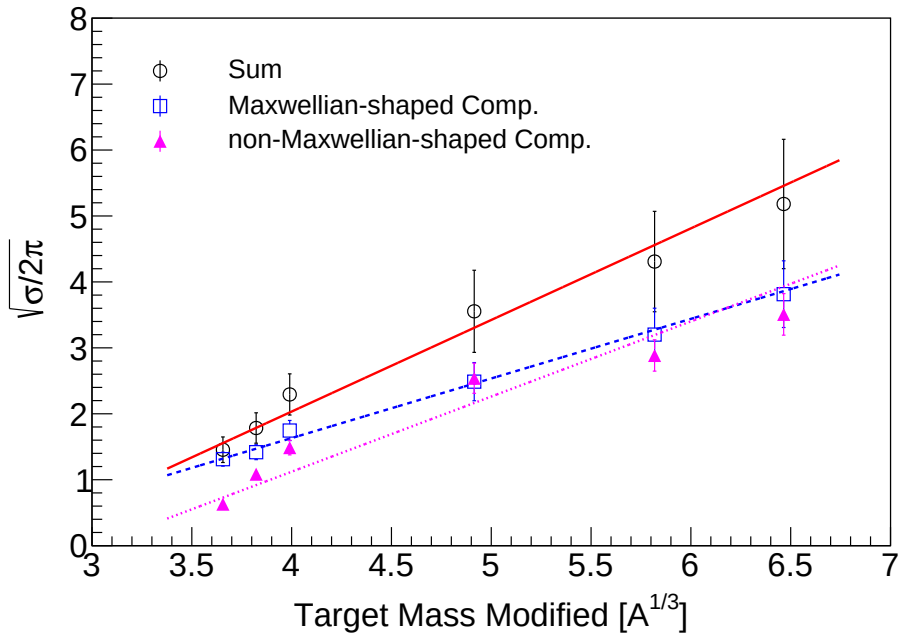

Figure 5.12: Fitting and values of the obtained cross section for the Maxwellian-shaped component, non-Maxwellian-shaped component, and sum of both components for Pb, Au, Sn, Cu, Fe, and Ti targets with 17 MeV photons. Red, blue, and magenta lines show fitting curves for the values of σ_{sum}, σ_{Max}, and $\sigma_{\mathrm{non-Max}}$.

oration process to the photoneutron spectrum but an increase in the contribution of the pre-equilibrium and direct processes. These contributions continue decreasing or increasing until the ratios become constant. However, the non-Maxwellian-shaped component still includes some amount of the Maxwllian-shaped component. It would be interesting to study this on the full data set (0 – maximum energy) for various photon energies.

As shown in Figure 5.13, for the medium-mass nuclei (Cu, Fe, and Ti), there is a significant contribution from the Maxwellian-shaped component, in which the photoneutrons were mainly generated from the evaporation process. On the other hand, the non-Maxwellian-shaped component, in which the photoneutrons were emitted by pre-equilibrium and direct processes, contribute modestly to the photoneutron spectrum for medium-mass nuclei with of 17 MeV excitation photons.

In cases of the heavy nuclei (Pb, Au, and Sn), the contributions of the two com-

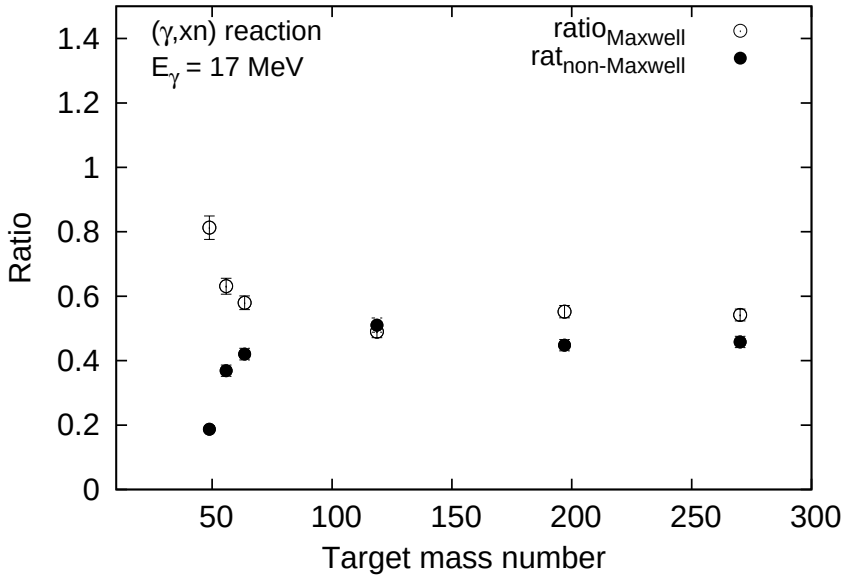

Figure 5.13: Values of ratio$_{\mathrm{Max.}}$ and ratio$_{\mathrm{non-Max.}}$ for Pb, Au, Sn, Cu, Fe, and Ti targets.

ponents to the photoneutron spectrum seem comparable. However, we can observe an impact of the tail of the Maxwellian fitting shape on the non-Maxwellian-shaped component in Figure 5.2, which indicates that the amount of photoneutrons emitted by the evaporation process (in the Maxwellian-shaped component) was included in $\sigma_{\mathrm{non-Max.}}$. The impact of the tail of the Maxwellian distribution on $\sigma_{\mathrm{non-Max.}}$ was 33.18 %. This value was estimated by taking the ratio of the Maxwellian fitting data to the experimental data for Au at H90. This ratio was calculated for the non-Maxwellian-shaped component corresponding to the energy range from 4.2 MeV to $\mathrm{E}_{\mathrm{exp}}^{\mathrm{max}}$. The data set for neutron energy lower than 2 MeV is necessary to accurately determine the Maxwellian fitting shape. This is useful to account for the non-Maxwellian-shaped component accurately by subtracting the Maxwellian-shaped component from the entire photoneutron spectrum. Although this data set is not perfect, the cases of Pb, Au, and Sn indicate that increasing the target mass number results in comparable contributions of the Maxwellian-shaped and non-Maxwellian-shaped components to the photoneutron spectrum, at approximately 50 %, each.

Figure 5.13 also provides useful information to choose the target material for the radiation shielding of electron accelerators. Using the medium-mass targets (Cu, Fe, Ti), the emission of the Maxwellian neutrons (the Maxwellian-shaped component) could be larger than that of the non-Maxwellian neutrons (the non-Maxwellian-shaped component); thus, the shielding of the Maxwellian neutrons is easier than that of the non-Maxwellian neutrons.

5.4 Photon energy dependence of photoneutron spectrum

5.4.1 Photoneutron spectrum for three photon energies

The photon energy dependence of the photoneutron spectrum is discussed in this section using the data from the second experiment. In this experiment, the photoneutrons were measured with 14 MeV, 17 MeV, and 20 MeV photons on Au, Cu, and Ti targets. Before starting the discussion, I checked the consistency between the data from the first and second experiments for Au with 17 MeV photons, as presented in section 3.9.

Figure 5.14, Figure 5.15, and Figure 5.16 present the experimental DDXs of the (γ,xn) reaction using 14 MeV, 17 MeV and 20 MeV photons on Au, Cu, and Ti at three different laboratory angles, horizontally 60°, 90°, and vertically 90°, named with H60, H90 and V90, respectively. Energy spectra were determined from 2 MeV to maximum energy, E_{exp}^{max}, which was obtained from the photon energy and Q-value.

Here, two components are observed in the energy distribution of DDX for all the three photon energies: one component is observed in the energy range 2–4.2 MeV, and the other component is observed in the range from 4.2 MeV to E_{exp}^{max}. The energy distribution of the component in the range 2–4.2 MeV, which is produced by the evaporation process, is comparable to the tail of the Maxwellian distribution; thus, this component is named the Maxwellian-shaped component. The other component in energy range above 4.2 MeV is called the non-Maxwellian-shaped component because, in this range, the photoneutrons does not follow the Maxwellian distribution. This phenomenon of the energy distribution is identical to that in the data obtained in the first experiment, as explained in section 5.1.

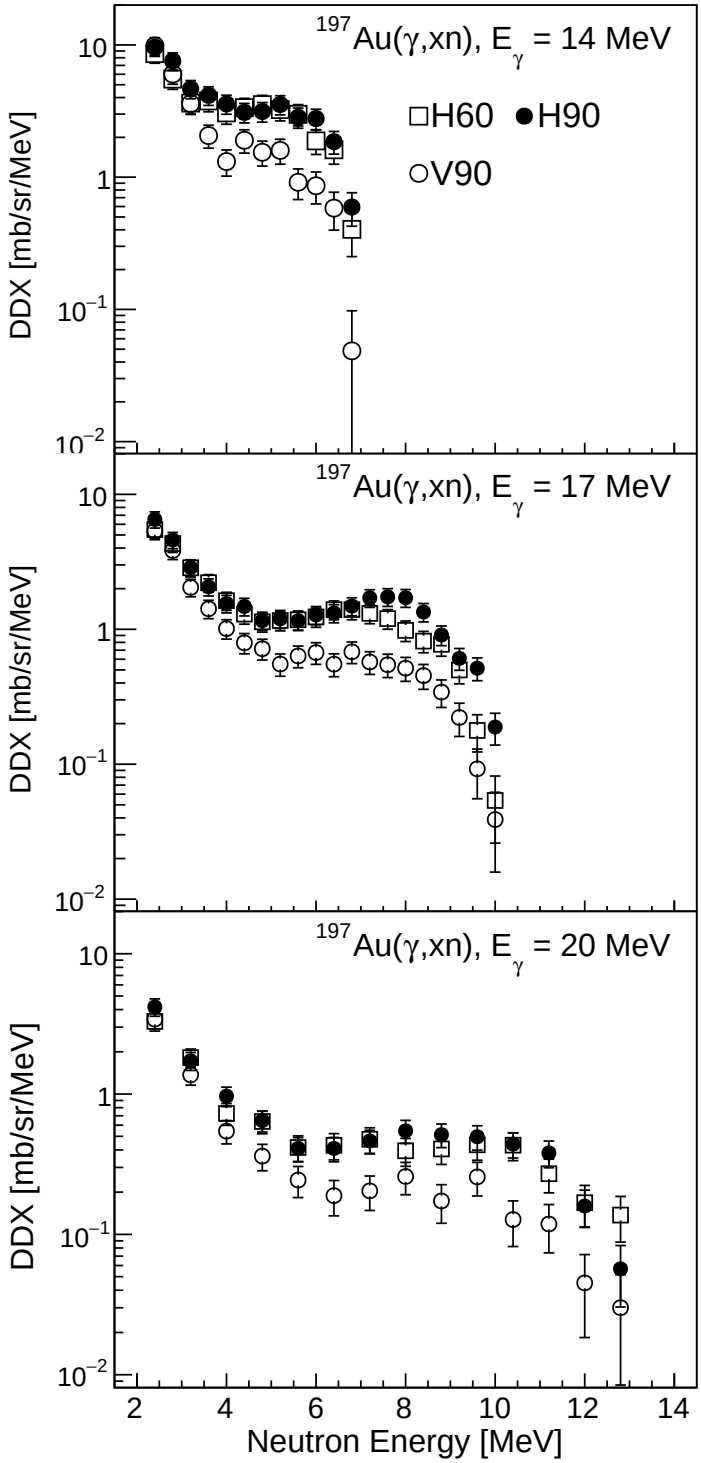

Figure 5.14: Neutron spectra from the (γ,xn) reaction for Au at H60, H90, and V90 with different photon energies.

Figure 5.14 and Figure 5.15 indicate that the DDX for the horizontal 90° is the highest. The DDX for the vertical 90° is the lowest. These phenomena are the same as for the data of Au and Cu targets, which were obtained with 14 MeV, 17 MeV, and 20 MeV photons.

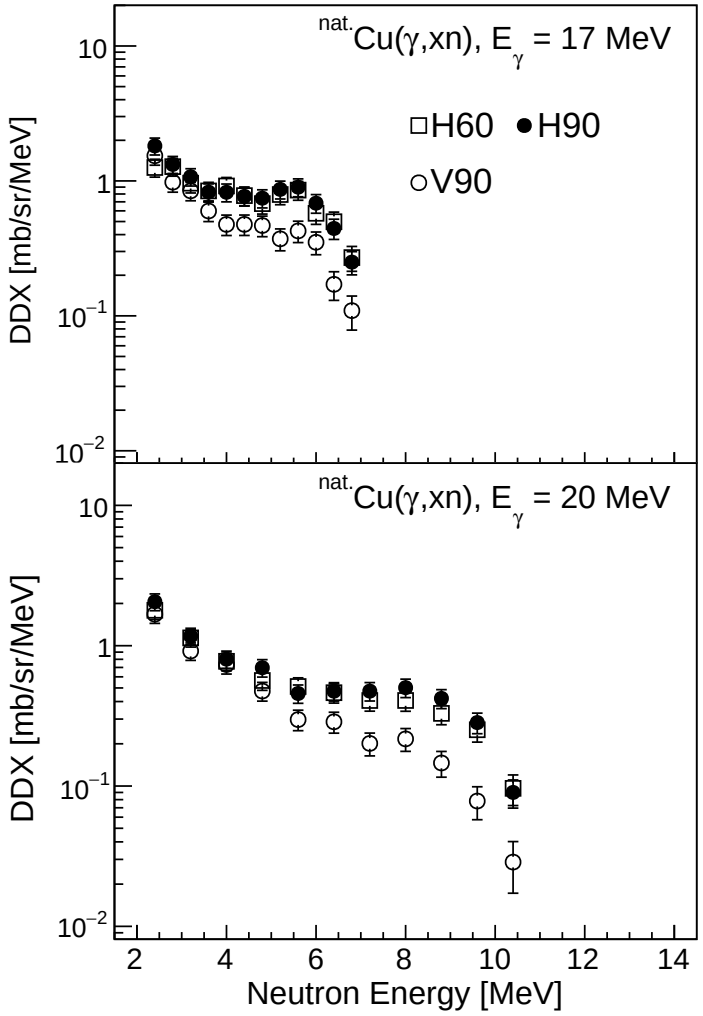

Figure 5.15: Neutron spectra from the (γ,xn) reaction for Cu at H60, H90, and V90 with different photon energies.

Figure 5.16 shows the data of the Ti target for 17 MeV photons; the highest DDX is at V90, and the lowest DDX is at H90. However, this relationship is opposite to that for 20 MeV photons; the highest and lowest DDXs are at H90 and V90, respectively.

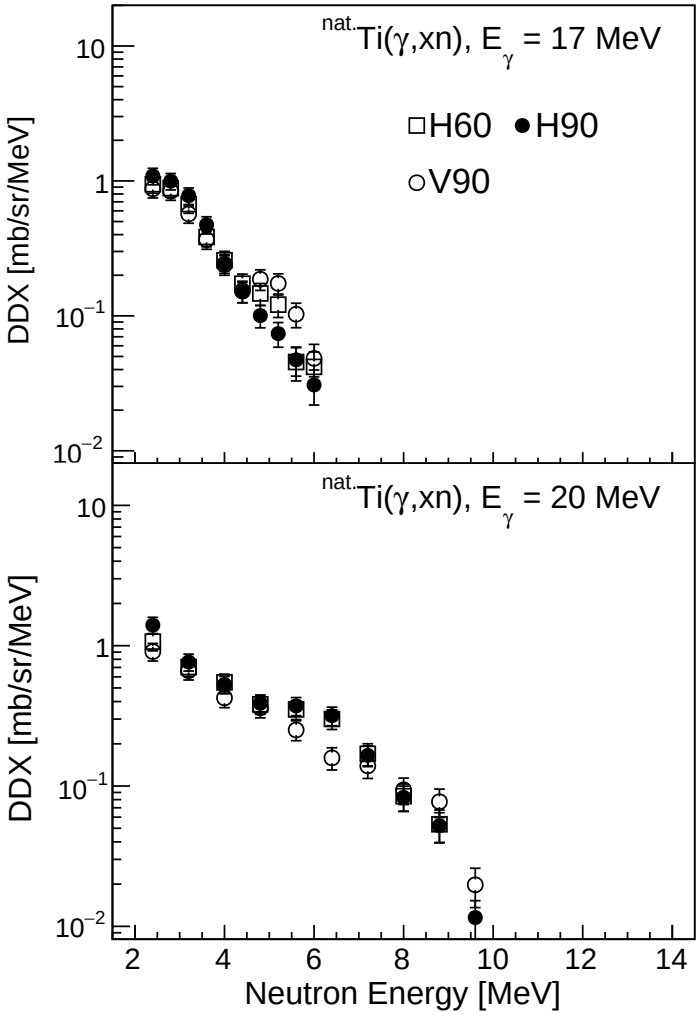

Figure 5.16: Neutron spectra from the (γ,xn) reaction for Ti at H60, H90, and V90 with different photon energies.

For the data of Au shown in Figure 5.14, the photoneutron spectra were observed using 14 MeV, 17 MeV, and 20 MeV photons. The obtained maximum energies (E_{exp}^{max}) are 6.8 MeV, 10 MeV, and 12.8 MeV, respectively. The magnitude of the photoneutron spectrum tends to decrease as the photon energy increases from 14 MeV to 20 MeV. This is consistent with the total cross section of the Au(γ,xn) reaction, which is the highest with 14 MeV photons and decreases with increasing photon energy, as shown in Figure 5.17.

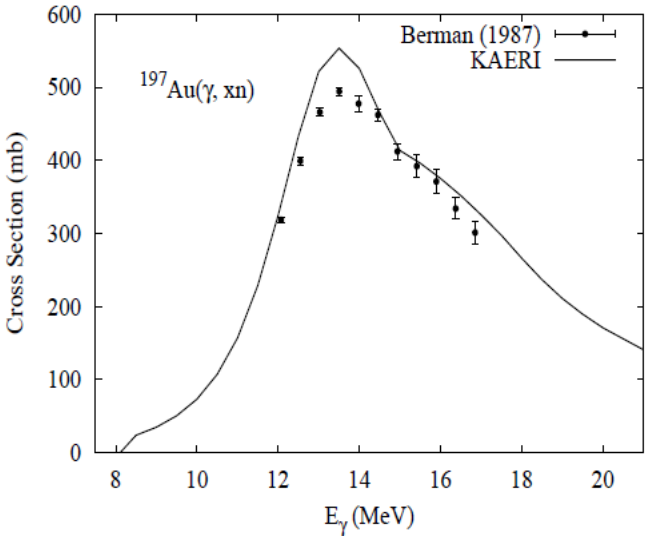

Figure 5.17: Cross section of the ^{197}Au(γ,xn) reaction [31].

In the case of the Cu target, the energy spectra of the photoneutron were measured with 17 MeV and 20 MeV photons, the E_{exp}^{max} for which were 6.8 MeV and 10.4 MeV, respectively (as shown in Figure 5.15). For the natural Cu target, containing ^{63}Cu (69.17 %) and ^{65}Cu (30.83 %), total cross section of the Cu(γ,xn) reaction is 67.09 mbarn at 17 MeV photon and 54.87 mbarn at 20 MeV; these values were calculated based on Figure 5.18. However, the number of photoneutrons obtained at 20 MeV is slightly higher than that obtained at 17 MeV.

Correspondingly, the energy spectra of the Ti target were also observed with these photon energies. The E_{exp}^{max} was 6 MeV and 9.6 MeV for 17 MeV and 20 MeV photons, as demonstrated in Figure 5.16. The number of obtained photoneutrons decreases with increasing photon energy. This can be explained by the fact that

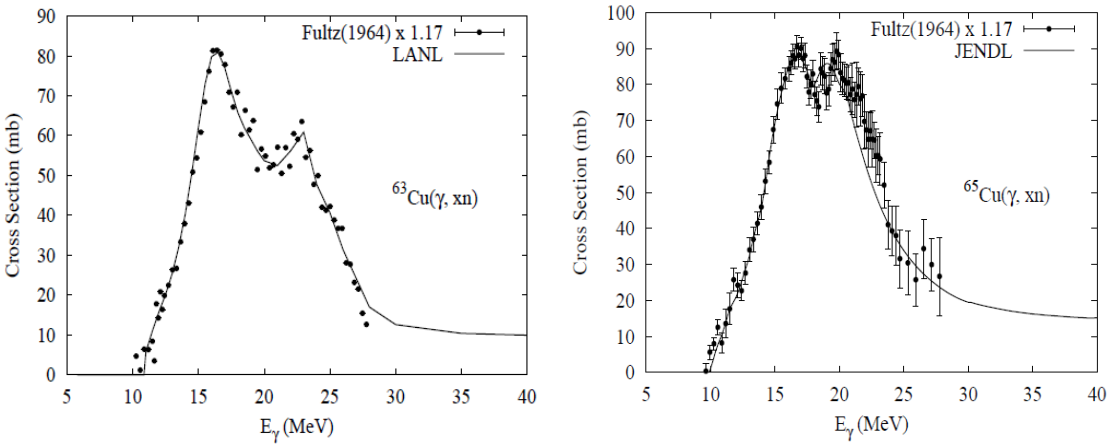

(a) ^{63}Cu **(b)** ^{65}Cu

Figure 5.18: Cross section of the ^{63}Cu(γ,xn) reaction [56].

the total cross section at 20 MeV is at the third among the GDR peaks, which are illustrated in Figure 5.19, while that at 17 MeV is closer to the bottom of the first peak.

Additionally, it is noted that the angular distribution of photoneutrons also changes with increasing photon energy. The angular distribution observed with 17 MeV photons is opposite to that observed with 20 MeV photons, as shown in Figure 5.16.

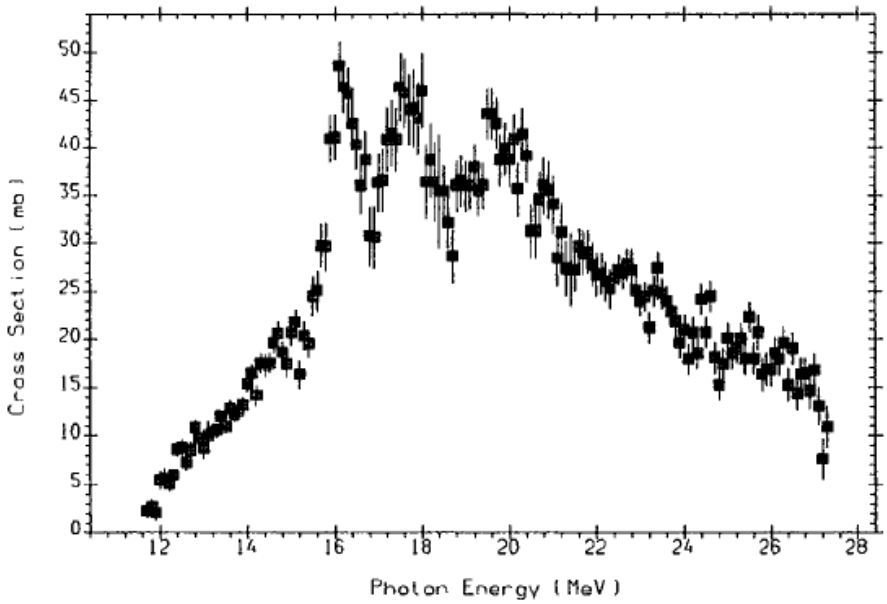

Figure 5.19: Cross section of the ^{48}Ti(γ,xn) reaction [31].

5.4.2 Separation energy of DDXs for three photon energies

To determine the separation energy, the DDX data were fit using a Maxwellian distribution. Figure 5.20, Figure 5.21, Figure 5.22, and Figure 5.23 show the fitting for the DDX data obtained at H60, H90, and V90 using the 14 MeV and 20 MeV photons for Au, Cu, and Ti targets. The red lines in these figures are the Maxwellian fitting curves, and the circular points are the experimental DDX data. For the data obtained with 17 MeV photons, the fitting was described in section 5.1.

Table 5.8 lists the numerical values of temperature parameters for fitting the Maxwellian distribution to the DDX data. For the fitting for same target and same photon energy, the temperature parameters at different angles are not identical. In addition, when increasing the photon energy, the temperature changed. These phenomena should be deeply studied with a data set including neutron energy lower than 2 MeV because such data play an important role in the fitting of the Maxwellian distribution.

Table 5.8: Temperature parameters of Maxwellian distribution fitting for the photoneutron spectra of Au, Cu, and Ti targets with 14 MeV, 17 MeV, and 20 MeV photons.

Temperature [MeV]			
Target	H60	H90	V90
	E_γ = 14 MeV		
^{197}Au	1.05±0.18	1.02±0.14	0.62±0.05
	E_γ = 17 MeV		
^{197}Au	0.93±0.1	1.0±0.13	0.81±0.08
^{nat}Cu	1.33±0.21	1.74±0.33	1.09±0.13
^{nat}Ti	0.74±0.05	0.93±0.09	0.93±0.08
	E_γ = 20 MeV		
^{197}Au	0.79±0.08	0.80±0.09	0.67±0.06
^{nat}Cu	1.18±0.18	1.09 ± 0.15	1.19±0.20
^{nat}Ti	1.35±0.24	1.07±0.15	1.25±0.20

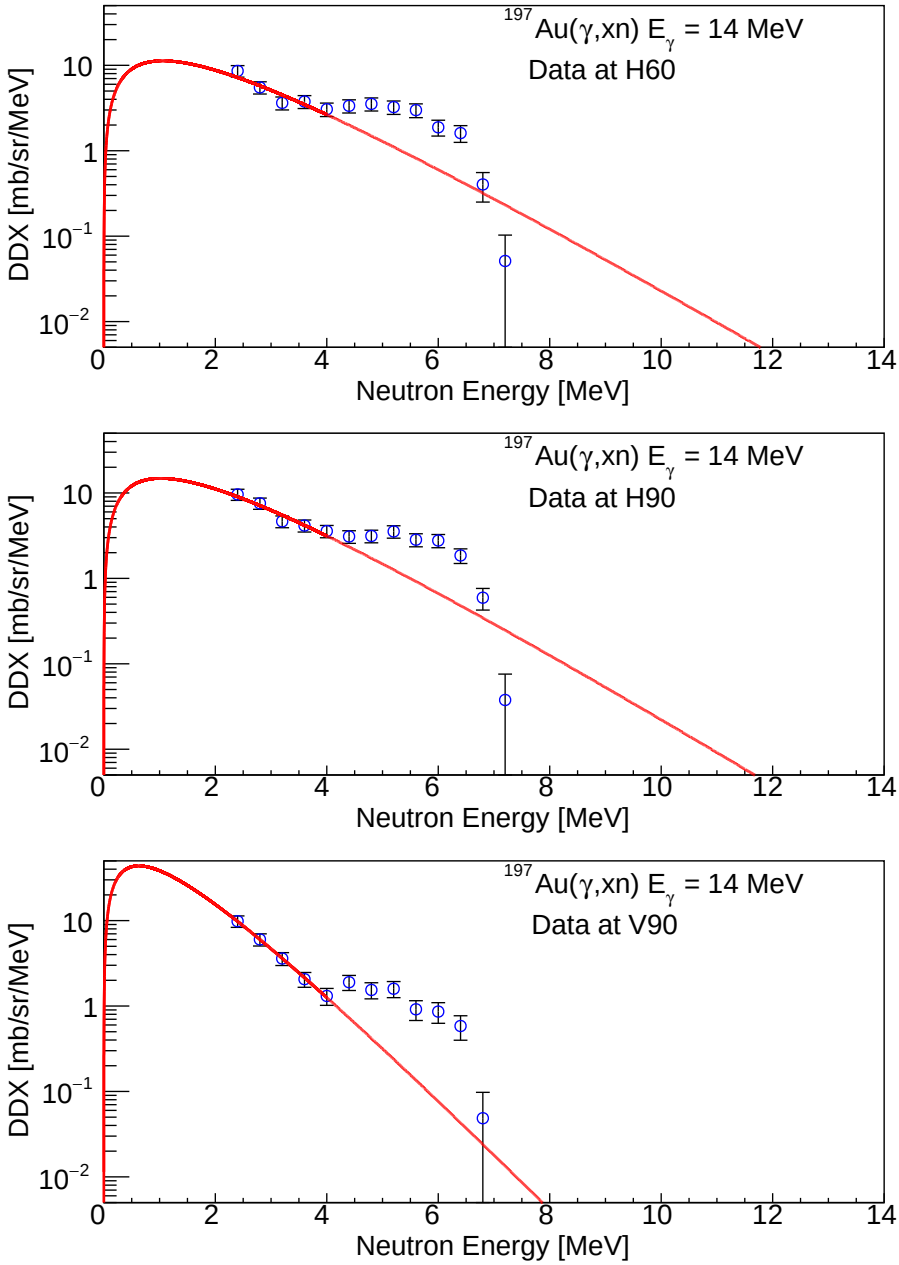

Figure 5.20: Photoneutron spectra and Maxwell fitting for the data of an Au target with 14 MeV photons.

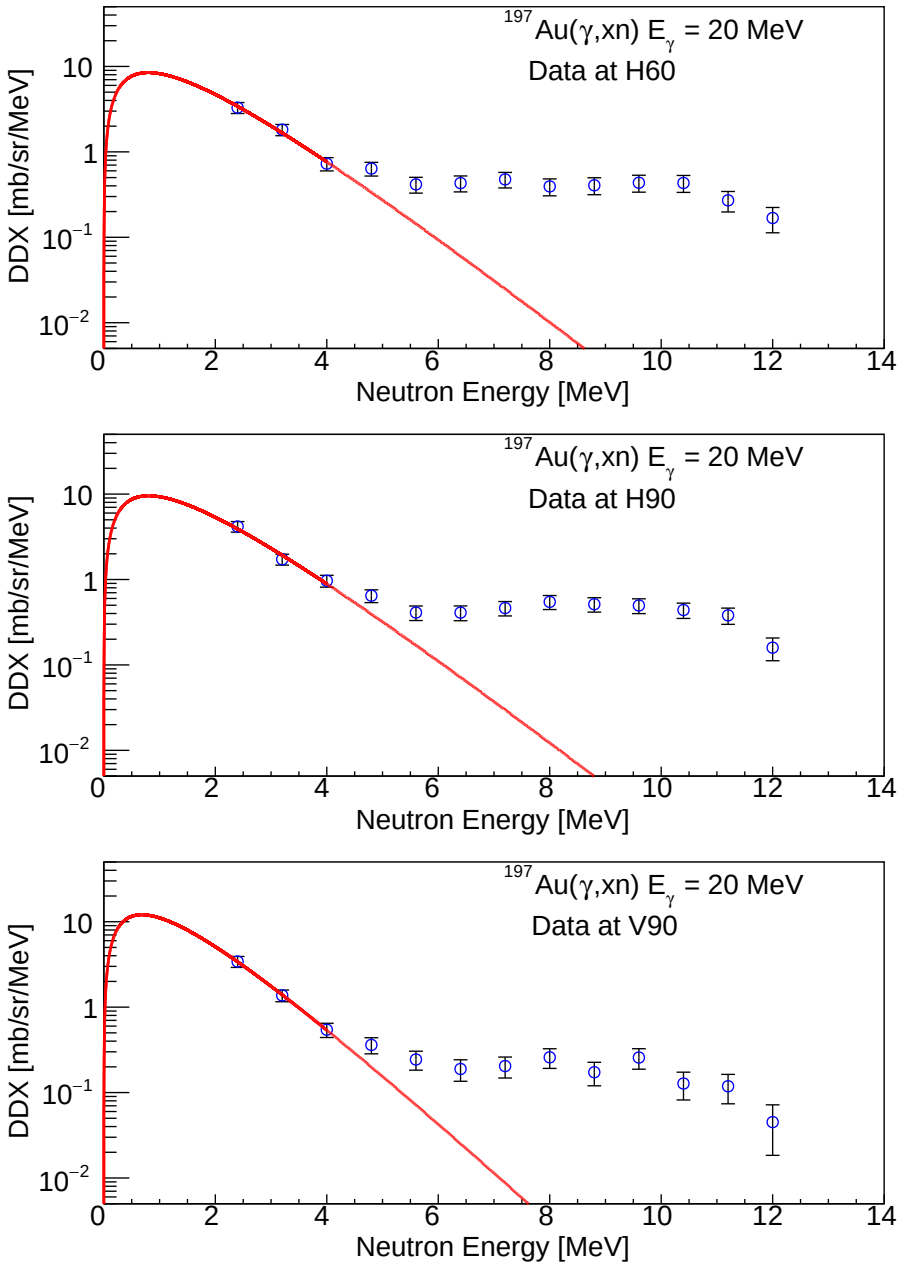

Figure 5.21: Photoneutron spectra and Maxwellian fitting for the data of an Au target with 20 MeV photons.

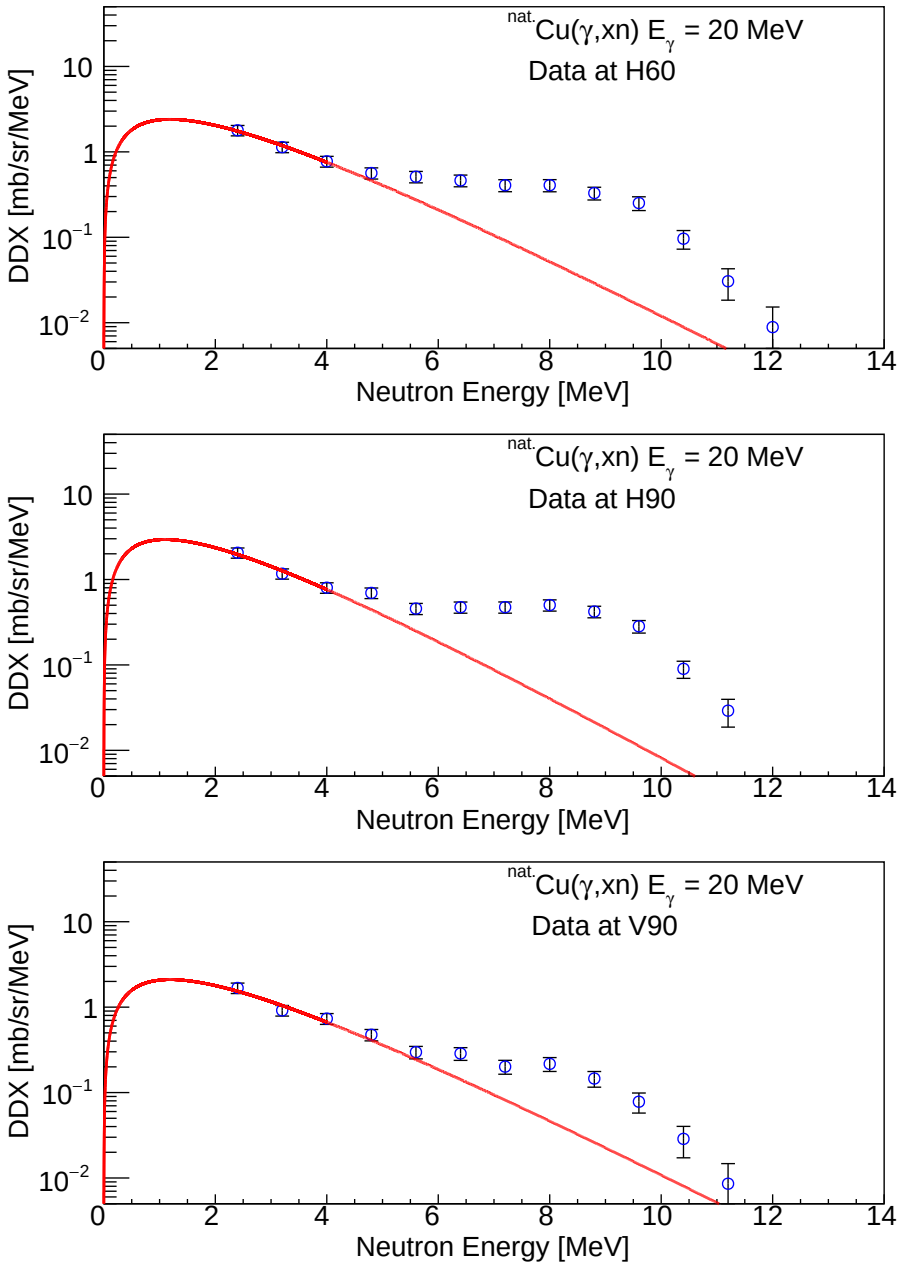

Figure 5.22: Photoneutron spectra and Maxwellian fitting for the data of an Cu target with 20 MeV photons.

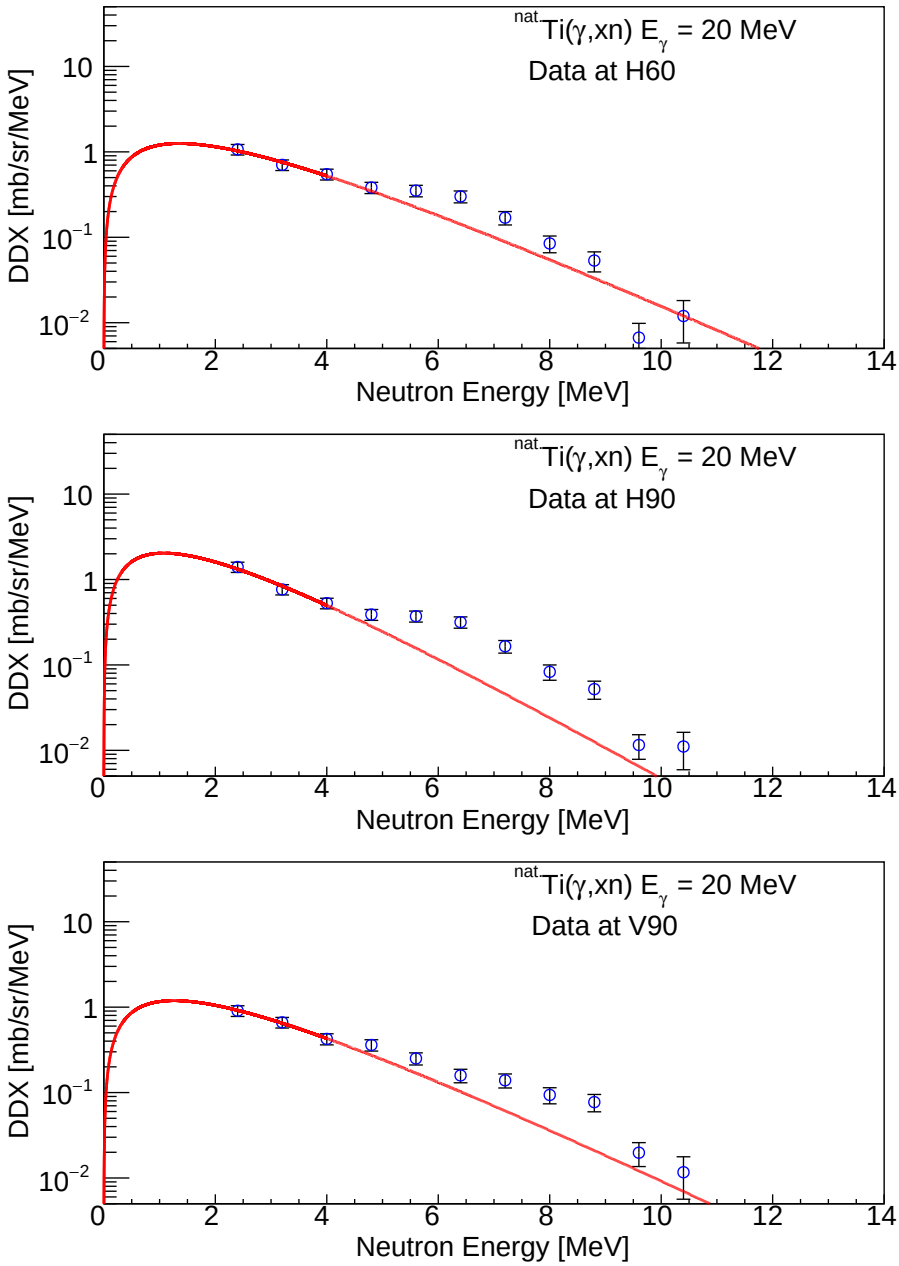

Figure 5.23: Photoneutron spectra and Maxwellian fitting for the data of an Ti target with 20 MeV photons.

The separation energy was determined using data obtained by dividing the experimental data with the Maxwellian fitting data. Figure 5.24 and Figure 5.25 display the ratio of experimental data to Maxwellian fitting data. The ratio was approximately equal to 1 with for data points below 4.2 MeV for all the photon energies. Thus, the separation energy is set to 4.2 MeV to separate the two components.

In Figure 5.24, for the data on an Au target obtained with 14 MeV and 20 MeV photons, the ratio at V90 is the highest in the energy range above 4.2 MeV. This is because the Maxwellian fitting curve for the data at V90 is significantly different from the fitting curves for the data at H90 and H60. Furthermore, the temperature parameter of fitting at V90 is quite small in comparison with the parameters at H90 and H60, as reported in Table 5.8. The difference is illustrated in Figure 5.20 and Figure 5.21.

The separation energy is the same for distinguishing the Maxwellian-shaped component and the non-Maxwellian-shaped component observed from the (γ,xn) reaction on different nuclei with 14 MeV, 17 MeV, and 20 MeV incident photons. The experimental data in this study were fit using a Maxwellian distribution in the energy range 2 MeV – 4 MeV because of the lack of data points below 2 MeV.

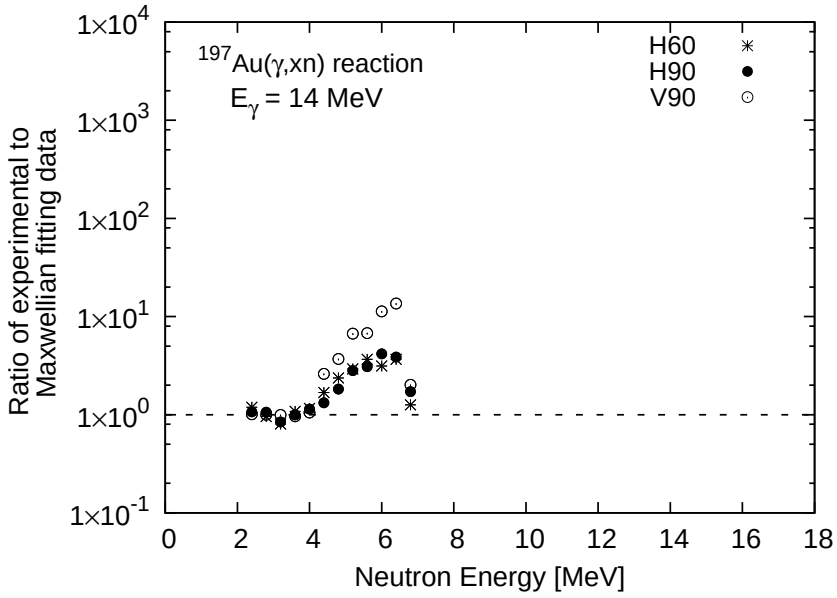

(a) 14 MeV photons

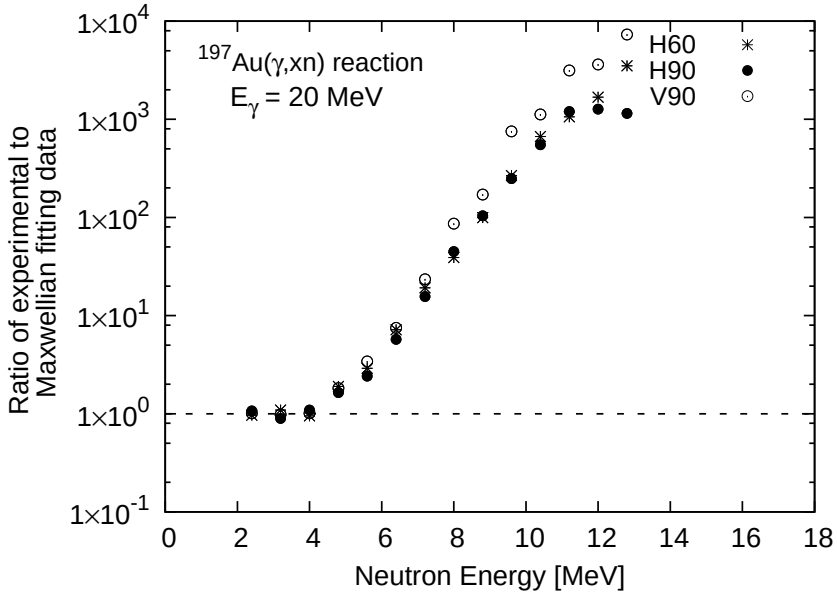

(b) 20 MeV photons

Figure 5.24: Ratio of the experimental data to the Maxwellian fitting function for Au with 14 MeV and 20 MeV photons.

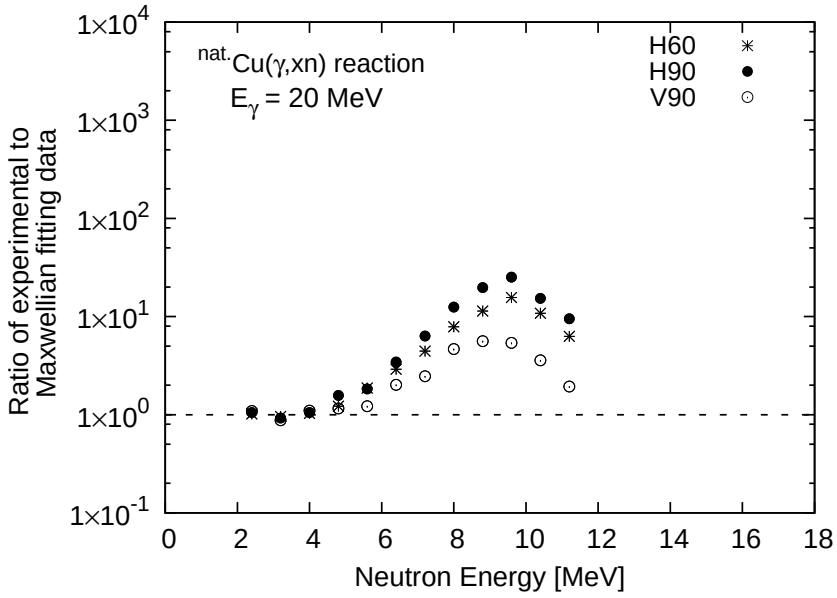

(a) Cu target

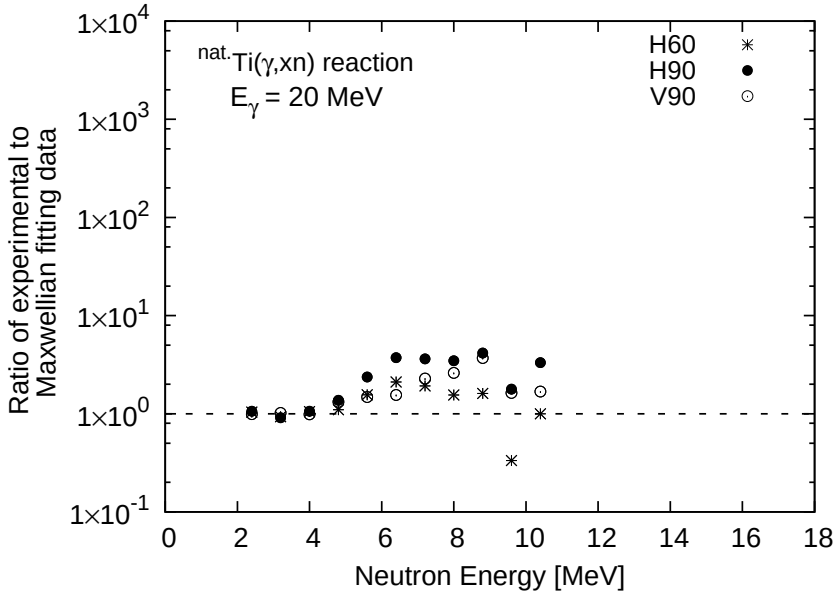

(b) Ti target

Figure 5.25: Ratio of the experimental data to the Maxwellian fitting function for Cu and Ti with 20 MeV photons.

5.4.3 Angular differential cross section

The ADXs of the Maxwellian-shaped component ($ADX_{Max.}$) and the non-Maxwellian-shaped component ($ADX_{non-Max.}$) were calculated by integrating the DDXs from 2 MeV to the separation energy, 4.2 MeV, and from 4.2 MeV to E_{max}^{exp}, respectively. Table 5.9 lists the numerical values of the ADXs for the Maxwellian-shaped and non-Maxwellian-shaped components at H60, H90, and V90 for Au, Cu, and Ti with the three photon energies.

Table 5.9: Numerical values of the ADXs for the Maxwellian-shaped component and the non-Maxwellian-shaped component for Au, Cu, and Ti with different photon energies.

		$ADX_{Max.}$ [mb/sr]			$ADX_{non-Max.}$ [mb/sr]		
Target	E_γ [MeV]	H60	H90	V90	H60	H90	V90
^{197}Au	14	9.82±0.76	11.82±0.86	9.13±0.78	6.80±0.51	7.13±0.49	2.97±0.28
	17	6.60±0.45	7.03±0.49	5.46±0.40	5.84±0.27	7.11±0.30	2.95±0.15
	20	4.67±0.45	5.49±0.52	4.26±0.44	3.36±0.23	3.61±0.22	1.60±0.14
^{nat}Cu	17	2.10±0.14	2.34±0.16	1.77±0.13	1.77±0.11	1.86±0.11	0.94±0.07
	20	2.95±0.25	3.22±0.27	2.66±0.23	2.42±0.14	2.71±0.15	1.38±0.09
^{nat}Ti	17	1.25±0.08	1.43±0.09	1.15±0.08	0.21±0.02	0.16±0.01	0.26±0.02
	20	1.85±0.15	2.15±0.18	1.59±0.13	1.07±0.08	1.11±0.07	0.88±0.06

As the Maxwellian-shaped component with the same photon energy is isotropic neutron emission, the $ADX_{Max.}$ at H90, V90, and H60 are expected to be comparable. Here, these $ADX_{Max.}$ values are different. This difference has not been explained in this study.

The difference is clearly discussed by plotting the values of $ADX_{Max.}$ and $ADX_{non-Max.}$ (reported in Table 5.9) in Figures 5.26, 5.28, and 5.30 for Au, Cu, and Ti targets, respectively. The horizontal axis in these figures represents the angle between the directions of photon polarization and neutron emission, Θ. The Θ is 0°, 30°, and 90° corresponding to H90, H60 and V90. Relationship of the Θ and the angle between directions of the incident photon and neutron emission was explained in Figure 5.9 and Equation 5.1.

Figure 5.26 shows values of the $ADX_{Max.}$ and $ADX_{non-Max.}$ of the Au(γ,xn) with the 14 MeV, 17 MeV for two experiments and 20 MeV photons. Red points in

Figure 5.26 show the data of 17 MeV obtained in the first experiment. A difference of two ADX data at 17 MeV is due to inconsistency of the photoneutron spectrum that is shown in section 3.9. The ADX of the both components decrease with a higher photon energy. A difference of the ADX values obtained with different photon energy is calculated as ratio of the ADX at 14 MeV to 17 MeV, ratio of the ADX at 14 MeV to 20 MeV and ratio of ADX at 17 MeV to 20 MeV, for the both components. These ratio are expressed in Figure 5.27 for the Maxwellian-shaped component and the non-Maxwellian-shaped component.

For the Maxwellian-shaped component, ratio of ADX_{14}/ADX_{17} is 1.6 while this ratio of the non-Maxwellian-shaped component is 1.0. This means the contribution of the non-Maxwellian-shaped component of 14 MeV data is comparable with that of 17 MeV data while the GDR peat at 14 MeV. Thus, at GDR peak, 14 MeV, besides the evaporation process, the photoneutrons which were produced through pre-equilibrium process still contribute to the obtained photoneutron spectrum. In addition, the angular distribution of the non-Maxwellian-shaped component change when increasing the photon energy. The angular distribution of the data at 14 MeV and 17 MeV starting from difference ADX values at $\Theta = 0^\circ$ but stopping at $\Theta = 90^\circ$ with the same ADX values.

In comparison of the ADX obtained by 17 MeV and 20 MeV, ratio of ADX_{17}/ADX_{20} of the Maxwellian-shaped component is approximate to 1.2 and it is about 1.9 for the non-Maxwellian-shaped component. On the order hand, the ratio of ADX_{14}/ADX_{20} of the both components are approximate to 2.0. At 20 MeV, the pre-equilibrium process could be more dominant than the evaporation process. However, from this observation, the photoneutron produced by the evaporation process can be observed on the obtained photoneutron spectrum at 20 MeV.

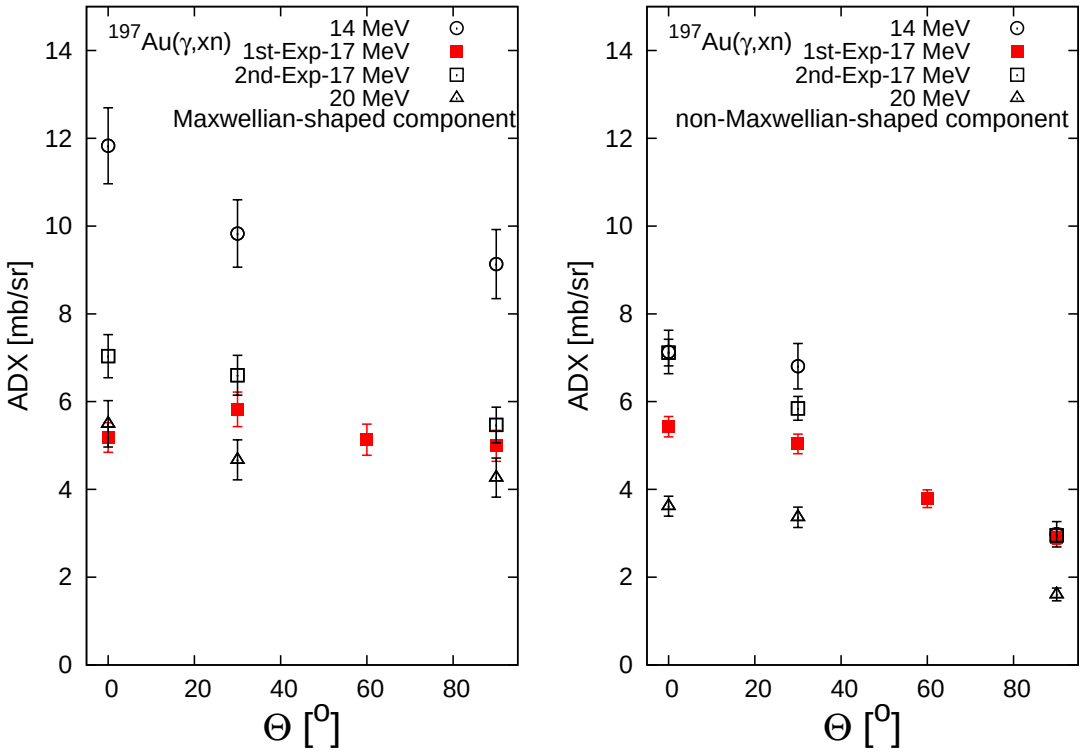

Figure 5.26: ADX values of the Maxwellian-shaped component and non-Maxwellian-shaped component for Au target.

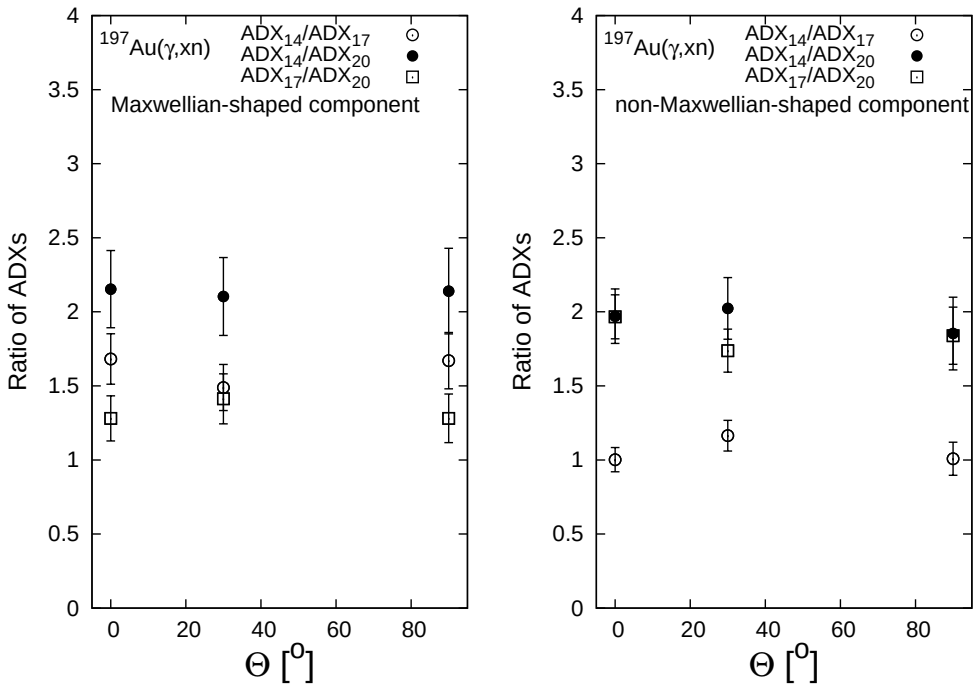

Figure 5.27: Ratio of ADX values obtained with various photon energies on Au target for the Maxwellian-shaped component and non-Maxwellian-shaped component.

Figure 5.28 indecate the values of $ADX_{Max.}$ and $ADX_{non-Max.}$ obtained by the 20 MeV photon are greater than those obtained with the 17 MeV photon for the Cu target. Number of the photoneutrons in the two components increase with increasing the photon energy while the reaction cross of the (γ,xn) section decreases.

The ratio of ADX_{17}/ADX_{20} of the two components are expressed in Figure 5.29. These ratio are comparable with is their uncertainties, about 0.7, while the ratio of the total cross section obtained 17 MeV photon to that of 20 MeV photon is 1.22. Because the photoneutron data in this study do not include the data points lower than 2 MeV, difference of the ratio of ADX values and the ratio of cross section is not explained in detail in this study. However, from Figure 5.29, it is indicated that the angular distribution of Cu data does not change with increasing the photon energy while the data of Au does not.

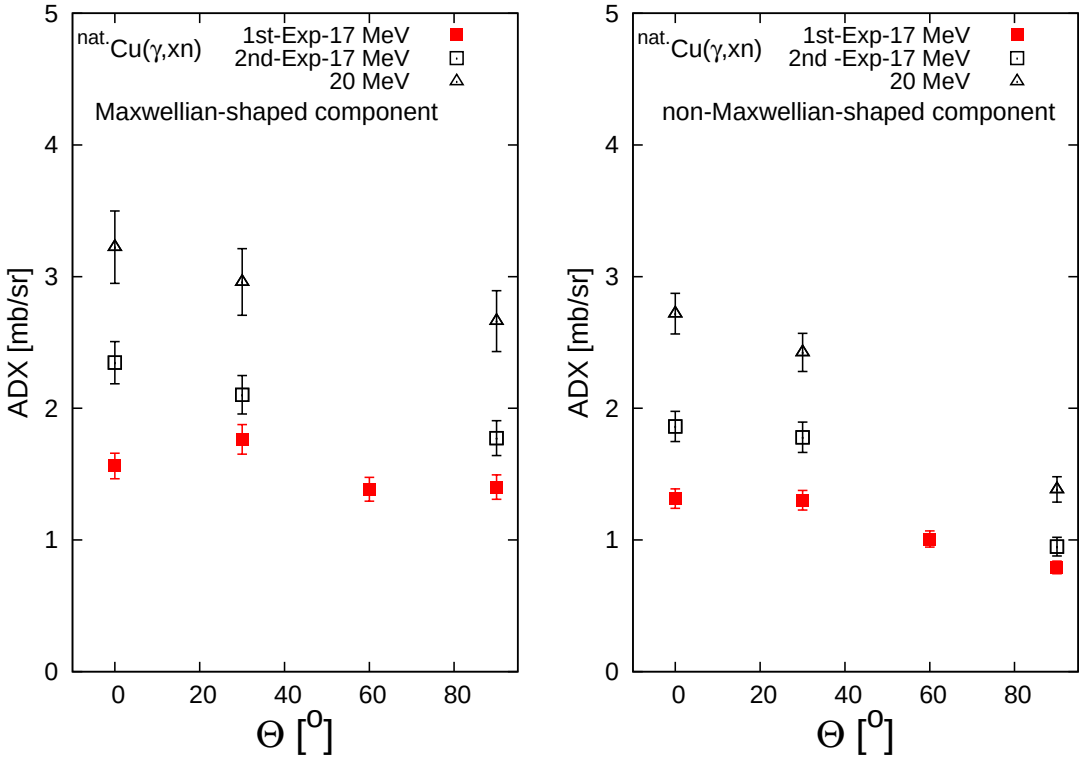

Figure 5.28: ADX values of the Maxwellian-shaped component and non-Maxwellian-shaped component for Cu target.

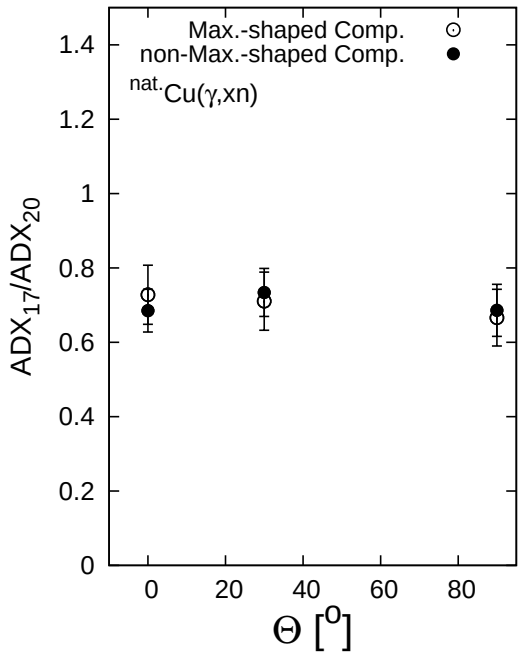

Figure 5.29: Ratio of ADX values obtained with 17 MeV and 20 MeV on Cu target for the Maxwellian-shaped component and non-Maxwellian-shaped component.

In case of Ti target, values of the $ADX_{Max.}$ and $ADX_{non-Max.}$ also increases with increasing the photon energy, as shown in Figure 5.30. For the non-Maxwellian-shaped component, the ADX data obtained at 17 MeV in both experiments are comparable. In addition, the angular dependence of the distribution of the photoneutron obtained at 20 MeV is opposite to that of the 17 MeV data. It means the angular distribution of the non-Maxwellian-shaped component show the dependence on incident photon energy.

In Figure 5.31 indicate value of ratio of ADX_{20}/ADX_{17} for two components. Values of the $ADX_{Max.}$ increase approximately 1.4 times with their uncertainties when the photon energy increase from 17 MeV to 20 MeV with keeping it distribution. On the order hand, values of the ratio for the non-Maxwellian-shaped component are 6.9, 5.11 and 3.31 corresponding to data at $\Theta = 0°$, $30°$, $90°$. It also means the angular distribution of the photoneutron of ^{nat}Ti(,xn) are significantly changed when increasing the excitation photon energy. The $ADX_{non-Max}$ obtained by 20 MeV photon strongly increase than data of 17 MeV.

The number of the photoneutrons produced through pre-equilibrium process are strongly increased with increasing the photon energy from 17 MeV to 20 MeV while the Maxwellian-shaped component slight increase. This can be imagined that with low Q-value of Ti, increasing the photon energy leads to increasing the remaining energy in excited nuclei. It results in probability of photoneutron emission through pre-equilibrium is in proportion to the remaining energy.

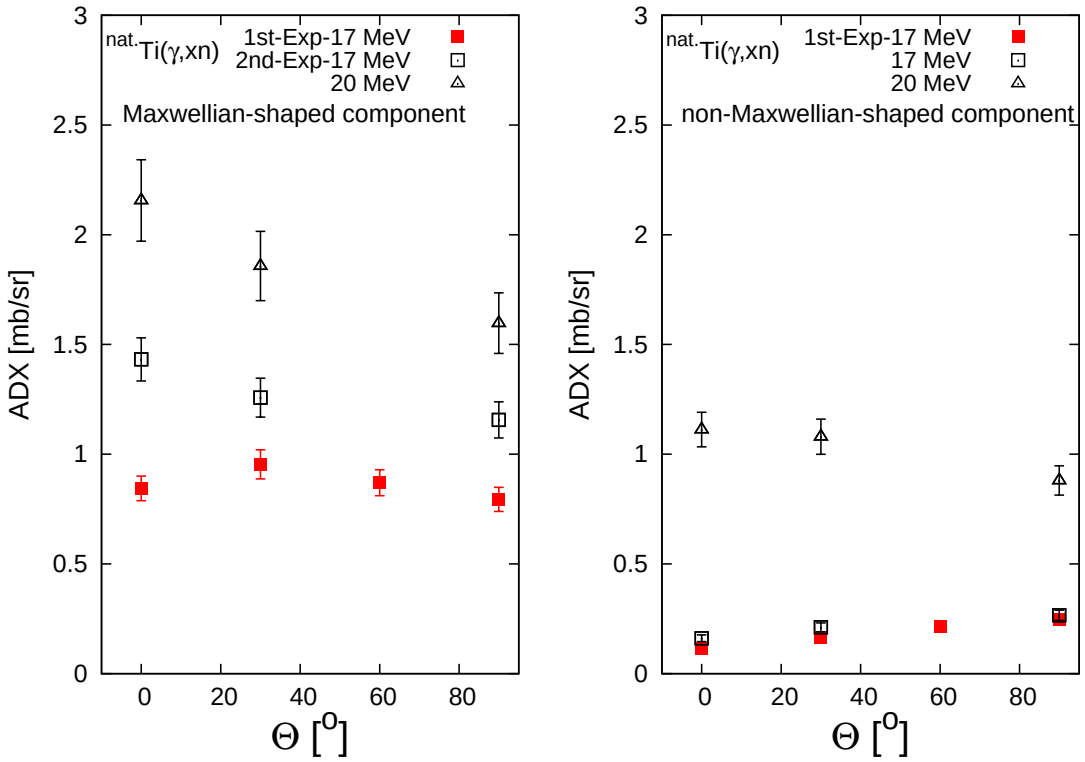

Figure 5.30: ADX values of the Maxwellian-shaped component and non-Maxwellian-shaped component for Ti target.

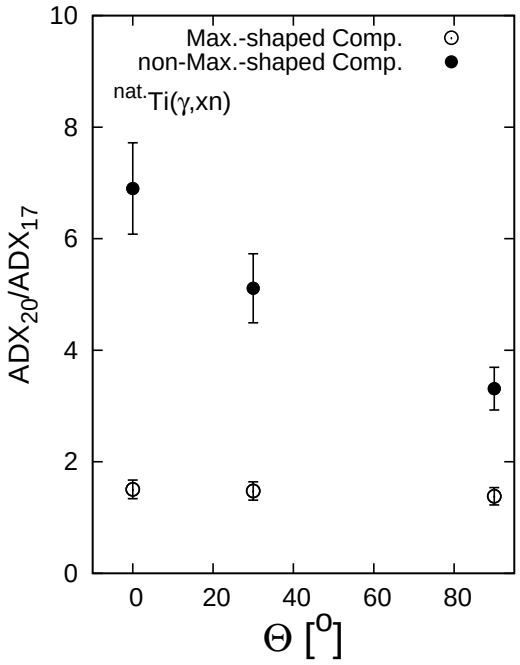

Figure 5.31: Ratio of ADX values obtained with 17 MeV and 20 MeV on Ti target for the Maxwellian-shaped component and non-Maxwellian-shaped component.

5.5 Comparison of DDXs between calculation and experiment

This section presents and discusses the inconsistency between the experimental DDX data obtained in this study and the DDX data calculated using PHITS simulation, JENDL/PD-2004, JENDL/PD-2016.1, and CoH_3. For every target used in this study, the DDX spectra obtained from the measurements at the V90 and H90 detectors were compared with simulation and calculation at the same photon energy of 17 MeV. The experimental and calculated DDX spectra of ^{nat}Pb, ^{197}Au, ^{nat}Sn, ^{nat}Cu, ^{nat}Fe, and ^{nat}Ti are plotted in Figures 5.32, 5.33, and 5.34. In these figures, the black and red data points are, respectively, the experimental data obtained at the H90 and V90 detectors, where the highest and lowest polarization photon effect, respectively, were obtained. The black, magenta, red, and blue solid lines show the DDX spectra calculated using PHITS, JENDL/PD-2004, JENDL/PD-2016.1, and CoH_3. The DDX values for ^{nat}Sn, ^{nat}Fe, and ^{nat}Ti were not available in JENDL/PD-2004.

For Pb (Figure 5.32a), Au (Figure 5.32b), and Sn (Figure 5.33a), the experimental DDX data at neutron energy higher than 4 MeV (the anisotropic region) are higher than the DDX values obtained from the PHITS simulation and other calculations.

The energy of emitted photoneutrons strongly depend on the nuclear energy levels, which were considered in CoH_3 and JENDL/PD-2016.1. The DDX spectra produced by two versions of JENDL contain both isotropic components, but the photoneutron production was not calculated with the consideration of the dependence on the polarization of incident photons.

For Pb, Au, and Sn targets, the DDX spectra obtained from JENDL and CoH_3 were different from the DDX calculated using PHITS (Figures 5.32a, 5.32b, and 5.33a). For Pb, Au, and Sn, the Q-value for the (γ,xn) reactions is approximately 8 MeV,

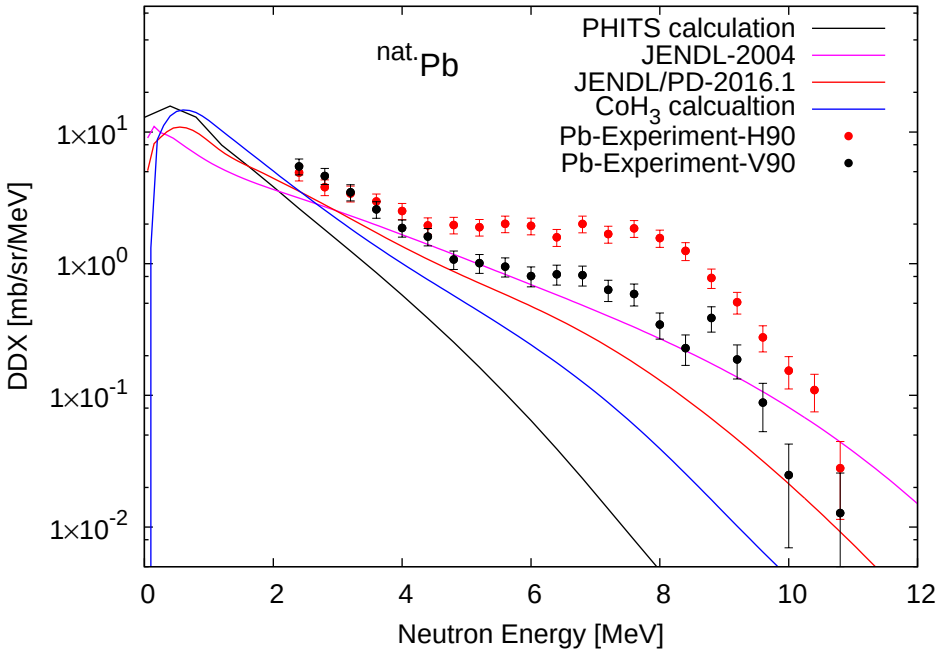

(a) Pb

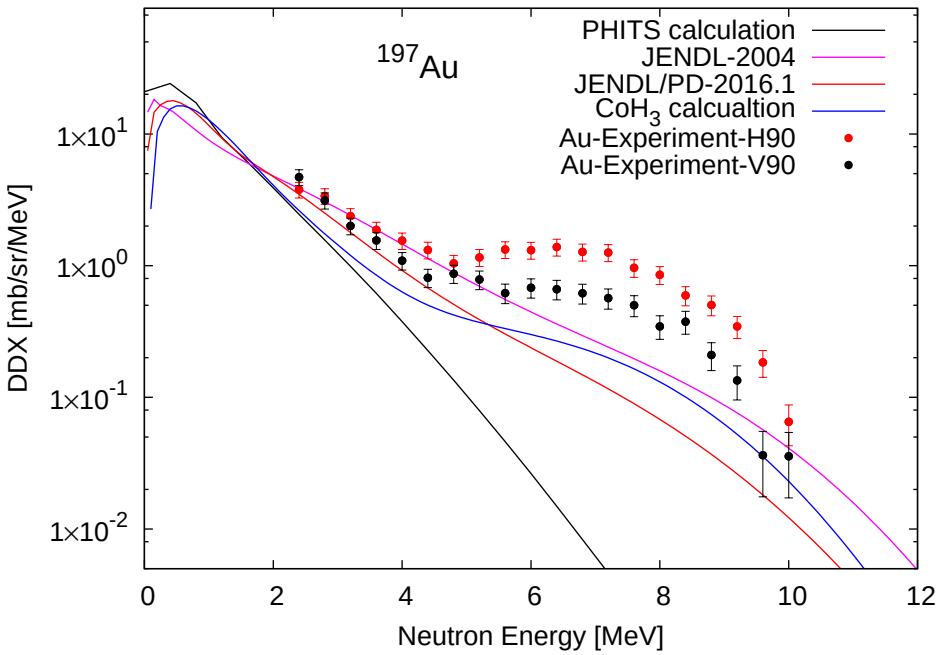

(b) Au

Figure 5.32: Calculated and experimental DDXs of Pb and Au.

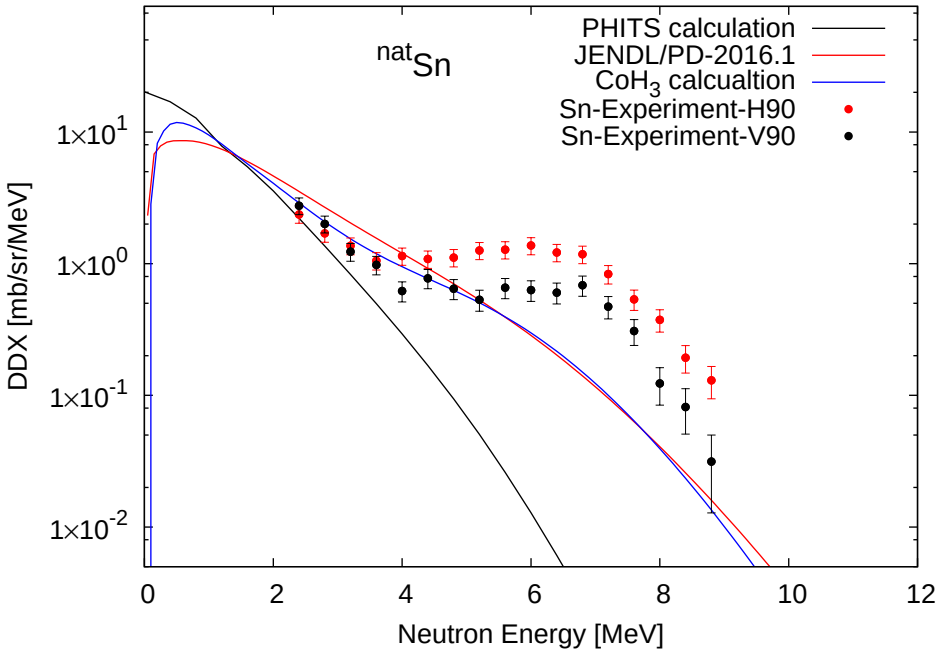

(a) Sn

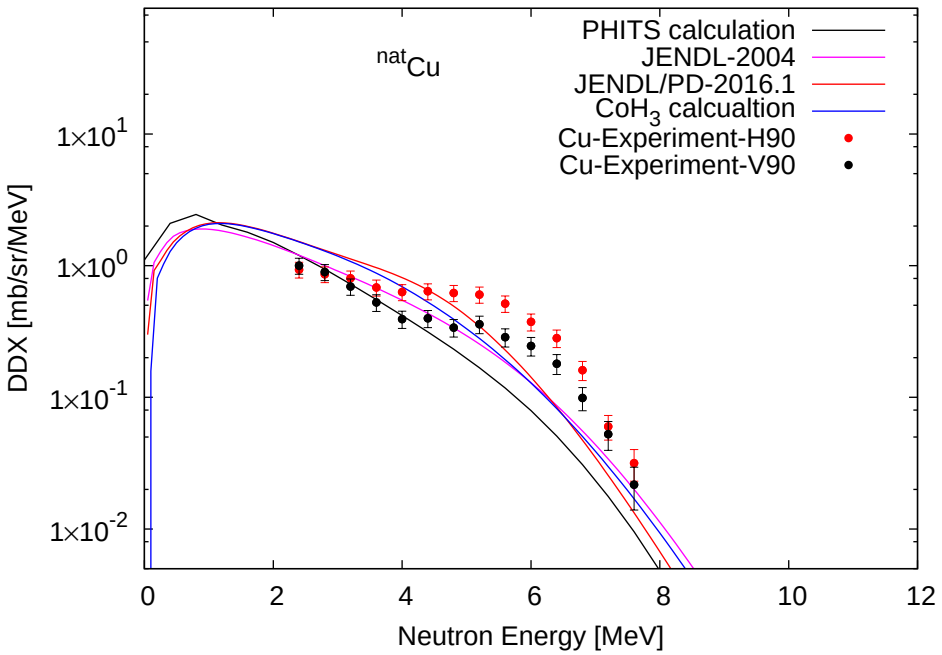

(b) Cu

Figure 5.33: Calculated and experimental DDXs of Sn and Cu.

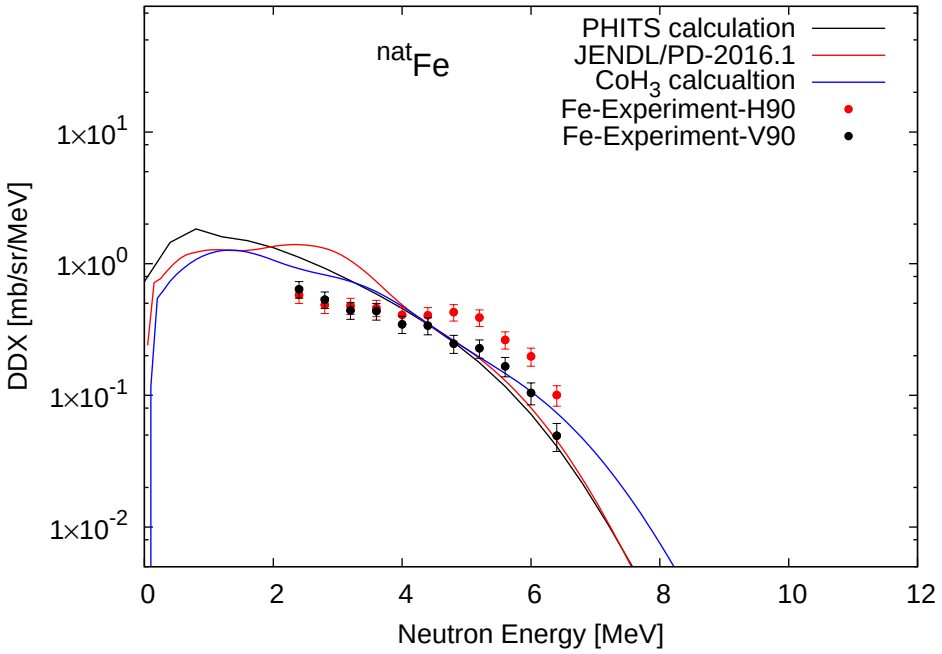

(a) Fe

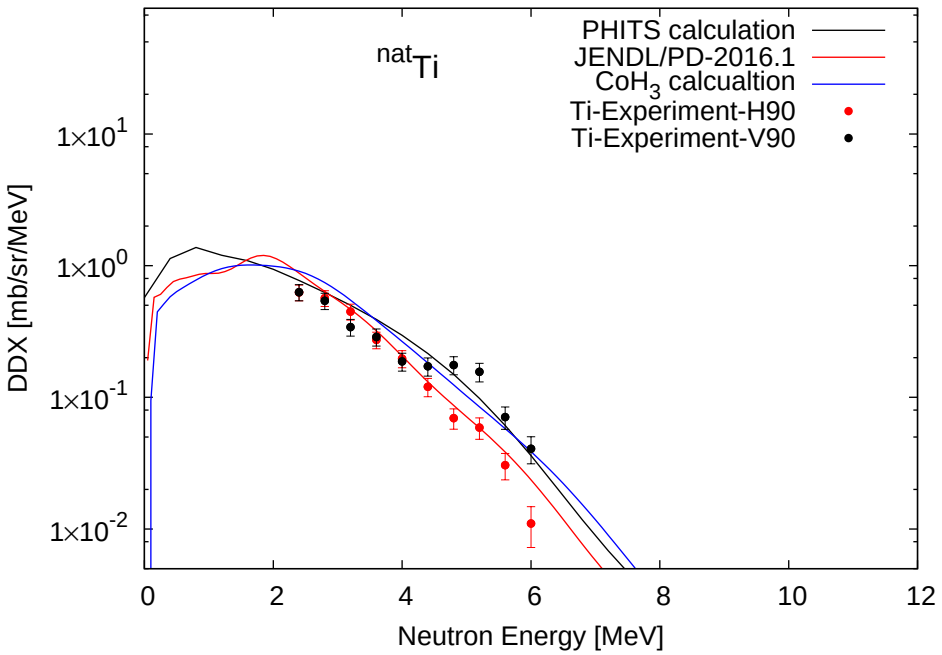

(b) Ti

Figure 5.34: Calculated and experimental DDXs of Fe and Ti.

as described in Table 4.1. Hence, with the photon energy of 17 MeV, the kinetic energy of neutrons can be up to 9 MeV, which is visible in the non-Maxwellian-shaped component. On the other hand, for the Cu, Fe, and Ti targets, the DDXs produced by theoretical calculations were quite consistent (Figures 5.33b, 5.34a, and 5.34b). For Cu, Fe, and Ti, the Q-value for the (γ,xn) reactions is 10.9 MeV, 11.2 MeV, and 11.6 MeV, respectively. Hence, the kinetic energy of neutrons can be up to 7 MeV, which is hardly visible on the non-Maxwellian-shaped component because the Maxwellian-shaped component is more dominant.

For Cu target (Figure 5.33b), the DDX obtained from PHITS, JENDL, and CoH_3 within the energy region below 4 MeV (or the isotropic component) are quite consistent with each other. For the energy region above 4 MeV, the DDX data obtained from the experiment are larger than the values obtained from PHITS, JENDL, and CoH_3.

For Fe and Ti (Figure 5.34a, 5.34b), the experimental DDX data are quite consistent with the calculated values. The experimental DDX values can be well explained by the DDX data obtained from JENDL/PD-2016.1 within 2.4 – 5 MeV.

To compare quantitatively, the ADX of photoneutrons obtained from the measurement at the H90 and V90 detectors, JENDL/PD-2004, JENDL/PD-2016.1, PHITS, and CoH_3 for neutron energy above 2 MeV were computed by taking the integral of the DDX data. Figure 5.35 shows these values of the ADX (as expressed in section 5.2.1) as a function of the atomic number of the target. Black, red, green, blue, magenta, and cyan, respectively, represent the ADXs of DDX obtained from PHITS, CoH_3, JENDL/PD-2016.1, JENDL/PD-2004, the measurement at H90, and the measurement at V90. Typically, the ADX values increase with increasing atomic number. For medium atomic number (Ti, Fe, and Cu), the experimental ADX values are quite consistent with the calculated ADX values. For high atomic number (Sn, Au, and Pb), the experimental ADX values are higher than the calculated ADX values.

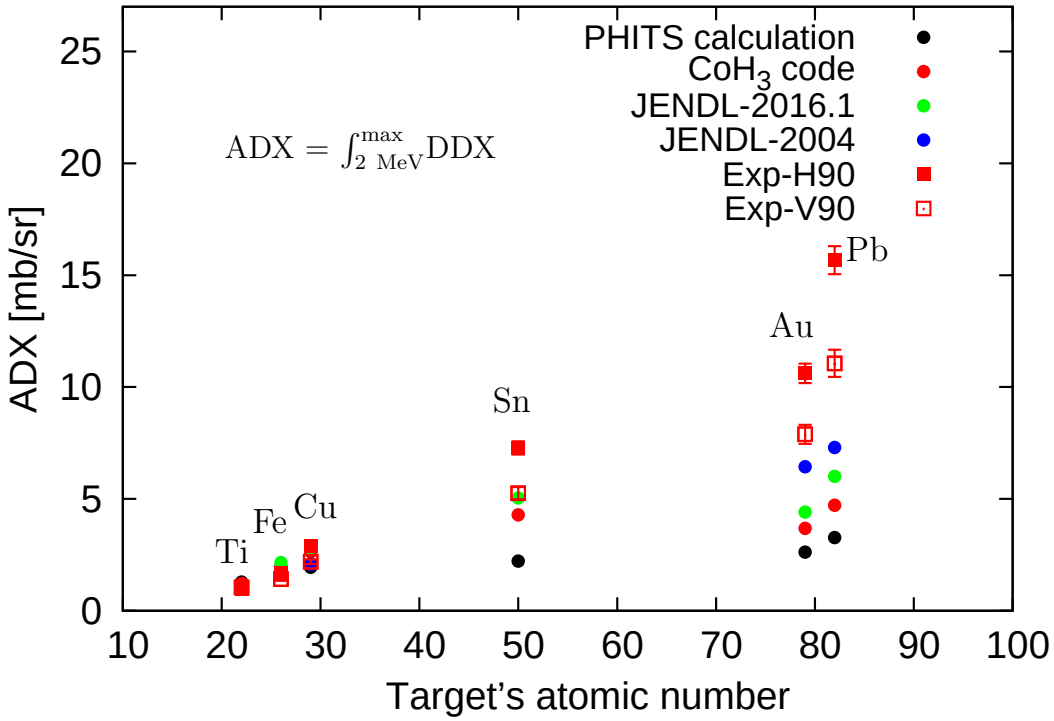

Figure 5.35: Comparison of ADX between experimental and calculated data.

To compare the differences quantitatively, the ratios of the ADX of PHITS, JENDL/PD-2004, and JENDL/PD-2016.1 to the ADX of the measurement at V90 are listed in Table 5.10. For the Ti target, the ratio is approximately 1.0, which indicates that the ADXs reproduced from the PHITS and JENDL/PD-2016.1 are quite consistent with the experimental data at V90.

The ratio of PHITS/V90 for Pb, Au, Sn, and Cu ranges from 0.26 to 0.78 because PHITS generates photoneutrons by the equilibrium process only. Thus, the non-Maxwellian-shaped component found in the experiment is not expressed in PHITS. In the case of the Pb, Au, and Sn targets, both JENDL and CoH_3 reproduce photoneutrons not only based on the equilibrium process but also the pre-equilibrium process. The non-Maxwellian-shaped component was reproduced by JENDL and CoH_3, but the DDXs are still lower than the experimental data at V90. The ratios of JENDL/PD-2016.1/V90 and CoH_3/V90 for Cu and Fe are

greater than 1.0, implying that the DDXs reproduced by JENDL/PD and CoH_3 are higher the V90 experimental data.

Table 5.10: Ratio of the ADX data of PHITS, JENDL/PD-2004, JENDL/PD-2016.1, and CoH_3 to the experimental ADX data.

Target	PHITS/V90	JENDL/PD − 2004/V90	JENDL/PD − 2016.1/V90	CoH_3/V90
^{nat}Pb	0.30	0.66	0.54	0.43
^{197}Au	0.33	0.82	0.56	0.47
^{nat}Sn	0.42		0.96	0.82
^{nat}Cu	0.89	0.95	1.28	1.20
^{nat}Fe	1.38		1.52	1.26
^{nat}Ti	1.23		0.93	1.17

Chapter 6

Impact on shielding calculation

The DDXs of the (γ,xn) reactions were measured for medium-heavy targets using polarized photons in the GDR energy region. The Maxwellian-shaped component and non-Maxwellian-shaped component were identified in the experimental neutron spectra for all targets, but the non-Maxwellian-shaped component of relatively heavy targets was underestimated by the calculation codes, as described in section 5.5.

In this chapter, the effect of the photoneutron spectrum on shielding calculation was studied considering the leakage dose. Below, the calculation is described in detail. Data for a Pb target, which is commonly used for stopping electron beams, were chosen as the source neutron spectrum. In addition, the number of obtained neutrons was the highest for Pb. The experimental neutron energy distribution was employed for the calculation of the leakage dose for a simple shielding structure, that is, concrete shielding with various thicknesses.

6.1 Geometry for the shielding calculation

Figure 6.1 shows the geometry for the concrete shielding calculation using PHITS. A sphere geometry was used for this calculation. The neutron source was a point source placed at the center of the sphere, 100 cm away from the inner surface of the concrete. The shield thickness in the calculations ranged from 0 to 180 cm. The other parts were considered to be vacuum.

In this calculation, the cut-off energy of neutrons was 10^{-10} MeV. The density and chemical composition of concrete are listed in Table 6.1. The scoring plane was a spherical surface, 350 cm away from the neutron source. The particle fluence in units of [counts/cm^2/source] is determined from the scored neutrons on the plane and the number of incident sources. The physics models were set with the default values. The input file in the calculation of dose for the Maxwellian-shaped component, which was discussed in chapter 5, is shown in Appendix B. The computation of the

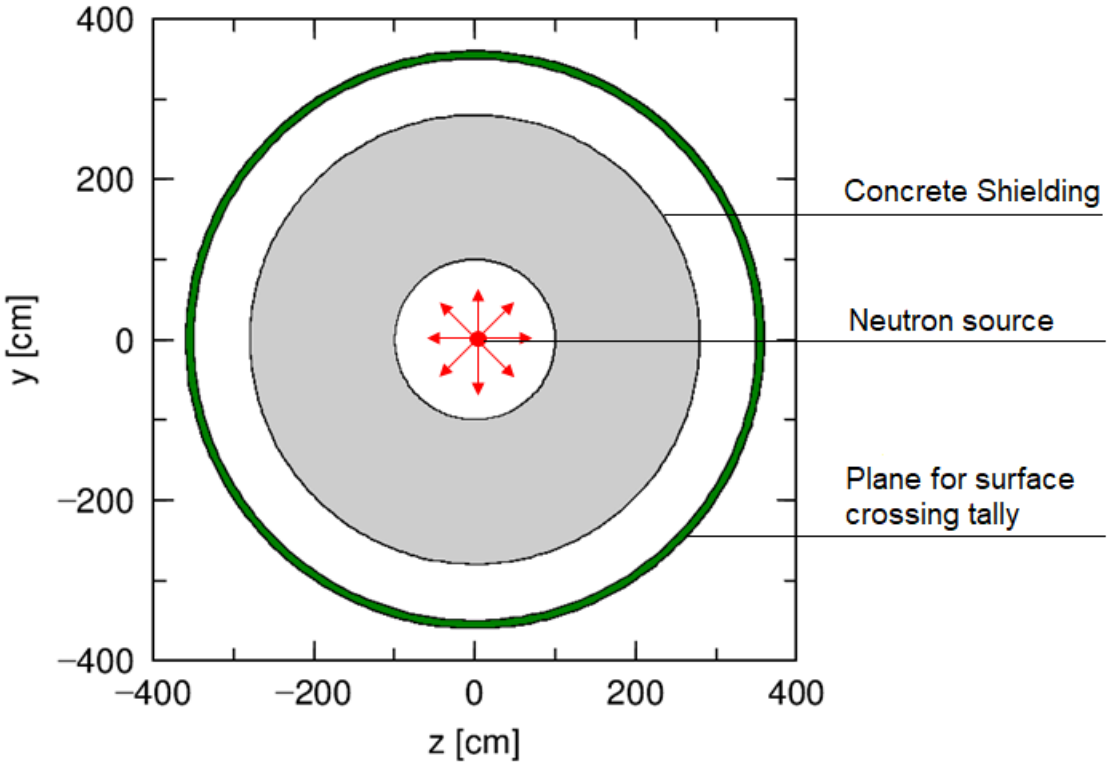

Figure 6.1: Calculation result of the spatial distribution of neutron flux with the geometry for shielding calculation.

dose of the total component including the Maxwellian-shaped component and the non-Maxwellian-shaped component (as discussed in chapter 5) is similar to that of the Maxwellian-shaped component, except the parameters in the [Source] section of the input file. They were changed as described in section 6.2.

Table 6.1: Chemical composition and density of concrete.

Concrete	Density: 2.302 g/cm^3
Element	Weight fraction
H	2.30E-02
C	2.30E-03
O	1.22
Na	3.68E-02
Mg	5.00E-03
Al	7.80E-02
Si	7.75E-01
K	2.99E-02
Ca	1.0E-01
Fe	3.2E-02

Neutrons from the source were attenuated when passing through the shielding material. After passing through the material, the number of neutrons as a function of energy was scored on the outer surface of the material. The number of neutrons was converted to a neutron dose by multiplying with the dose conversion coefficient of an effective dose for the anteroposterior (AP) geometry, given in ICRP publication 116 [59]. In the input file, the [Multiplier] section was used for dose estimation using the dose conversion factor. In the dose calculation, the neutron energy region between 10^{-9} MeV and 10 MeV was divided into 25 steps.

6.2 Source neutron spectrum

The neutron spectra of the evaporation component (Maxwellian shape) and total component were applied for shielding calculations. The spectrum of the total component was generated by combining the experimental photoneutron data at H90, which were measured on a Pb target with the 17 MeV photons and fit using a Maxwellian distribution. The data at H90 were chosen in this calculation because the maximum DDX was obtained at H90, as shown in Figure 5.1.

To define the evaporation component in the shielding calculation, the Maxwellian fitting was performed to determine the fitting parameters of the Maxwell function. Figure 6.2 shows the Maxwell fitting curve for the H90 data of Pb, which were measured with 17 MeV photons. Using the fitting result, the Maxwell function is obtained as Equation 6.1 with E, that is the neutron energy in MeV.

$$\mathrm{DDX(E)} = 14.95 \times \frac{\mathrm{E}}{1.402} \times \exp\left(-\frac{\mathrm{E}}{1.402}\right). \tag{6.1}$$

The evaporation component was modeled by using Equation 6.1. Figure 6.3 shows the neutron source spectra for the calculation. Red points show the data of both the evaporation component and non-Maxwellian-shaped component, called the total component in this calculation. Black points are the data of the Maxwellian-shaped component. Below 2 MeV, the data points of the total component were obtained from the fitting equation, Equation 6.1, because there were no experimental data for this energy range.

In the input file, the [Source] section is used to initialize the parameters of the source. e-type = 22 was set to produce an energy distribution of the total component for the source, and the direction of source emission was 4π (dir = all). The energy distributions of the source correspond to the energy distributions shown in Figure 6.3 for the both the components.

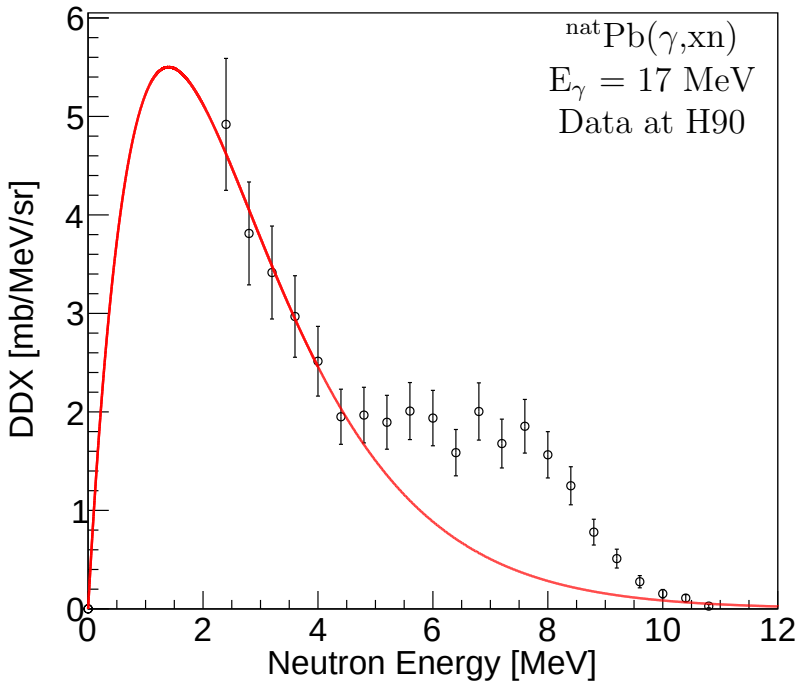

Figure 6.2: Fitting off the H90 data of a Pb target obtained with 17 MeV photons. The red line is the fitting curve, and the open circle points are the experimental data.

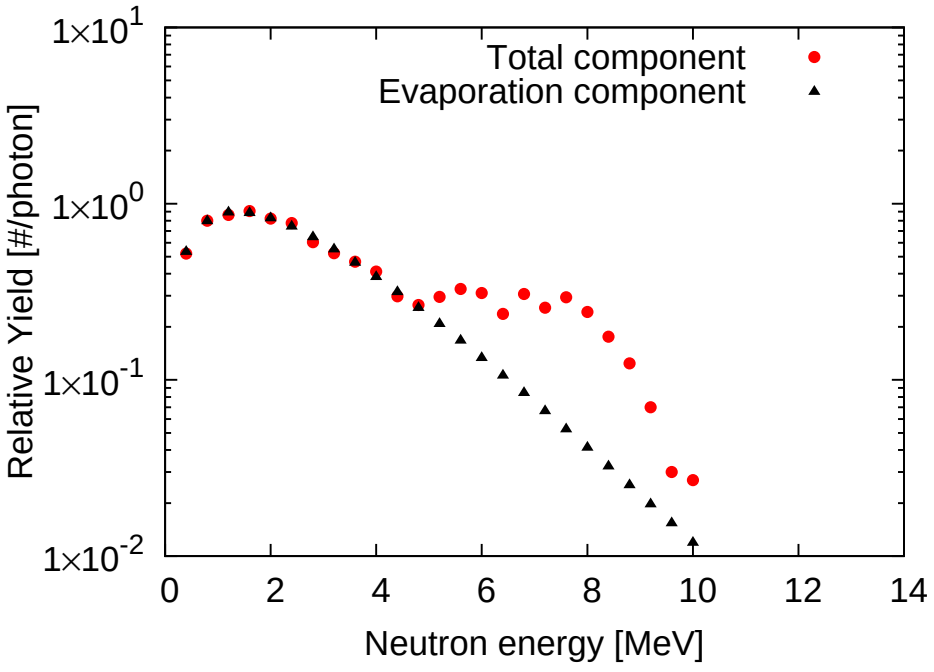

Figure 6.3: Neutron energy distributions determined by fitting the experimental data for shielding calculations.

6.3 Results and discussions

6.3.1 Neutron spectrum

Figure 6.4 shows the calculation results for the neutron spectra with the different shielding thicknesses for the evaporation component (black points) and the total component (red points).

When the thickness of the concrete shield was increased, the flux was reduced owing to the attenuation of neutrons in the shield. In Figure 6.4, the neutrons in the non-Maxwellian-shaped component region lose their energy and create differences in the lower energy part with increasing the shielding thickness. Finally, the spectral shape became quite similar for thicknesses of 120 cm or higher. In this condition, the spectral shape was in equilibrium, and only the magnitude was different. This difference is shown in Figure 6.5. This figure indicates the ratio of flux of the total spectrum to that of the evaporation spectrum with different shielding thicknesses. For energy higher than 6 MeV, the ratios of different thicknesses are comparable, while the ratios increase from approximately 1 to 2 approximately for energy lower than 6 MeV.

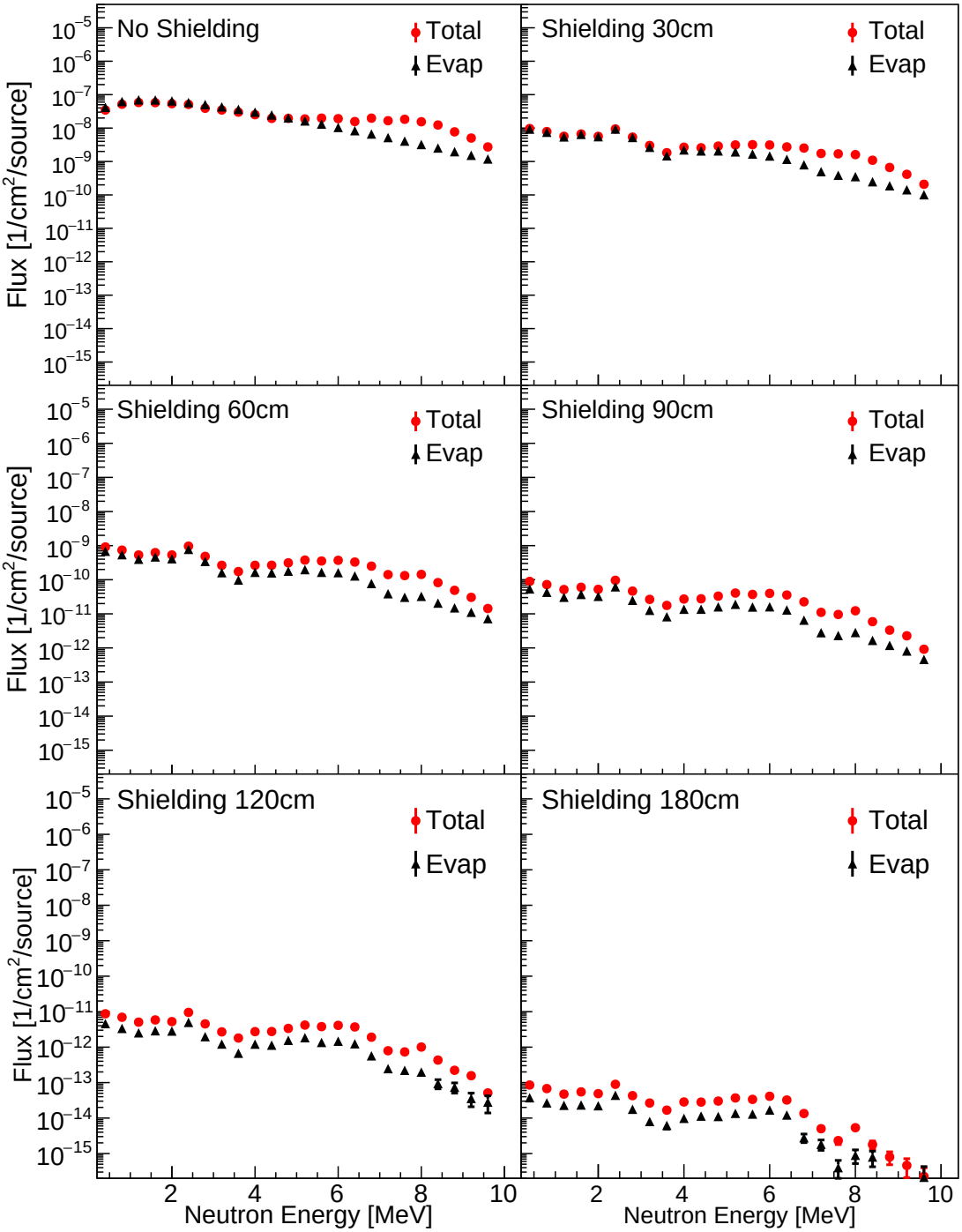

Figure 6.4: Neutron energy spectrum after neutrons passed through different shielding thicknesses.

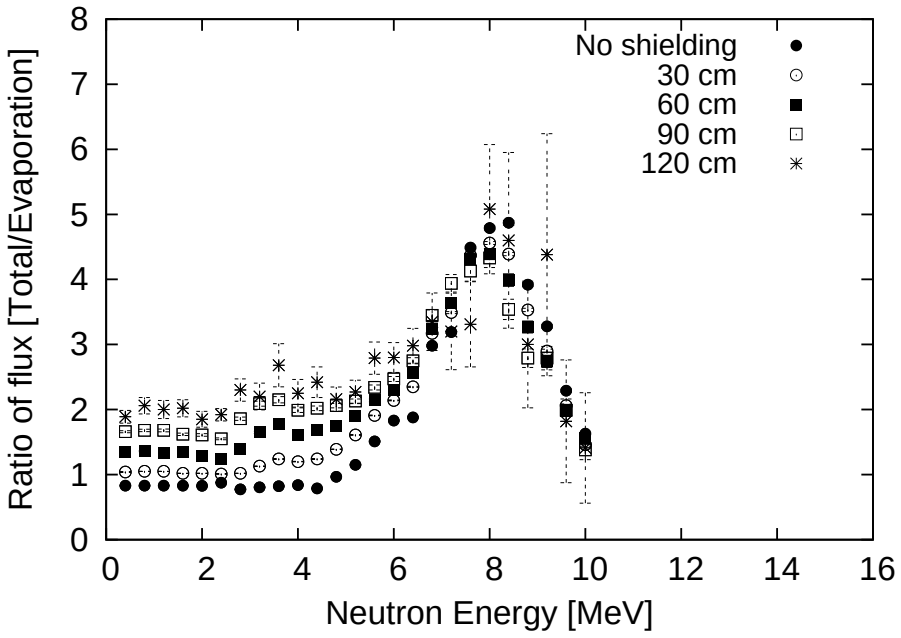

Figure 6.5: Ratio of flux of the total spectrum to that of the evaporation spectrum with different thicknesses.

6.3.2 Attenuation of dose

Figure 6.6 shows the ratio of dose between for the total component and the Maxwellian-shaped component. The contribution from the non-Maxwellian-shaped component, which was obtained by subtracting the Maxwellian-shaped component from the total component, became significant with increasing shielding thickness. According to this calculation, as the thickness was increased from 0 to 180 cm, the dose ratio of the total component to the Maxwellian-shaped component increased from 1.26 to 2.47 and then saturated. This fact implies that the dose could be underestimated by a factor of almost 2.5 with increasing shielding thickness if we use a simple Maxwellian-shaped spectrum for shielding calculation.

It should be noted that the ratio was obtained for the worst-case scenario because the non-Maxwellian-shaped component decreased with variation on the direction of polarization, and bremsstrahlung photons have a broad energy distribution that changes the ratio of the non-Maxwellian-shaped to the Maxwellian-shaped components. In this work, we used horizontally polarized photons, for which the non-Maxwellian-shaped component was the highest. In the shielding design, bremsstrahlung photons were generated, and the ratio can be reduced by 70% by using these unpolarized photons. This value was estimated from the ratio $b_{non-Max.}/a_{non-Max.}$ for the Pb target in Table 5.4 and Equation 5.2. According to Equation 5.2, $ADX_{max} = a + b$ and $ADX_{min} = a - b$ with $\Theta = 0$ and $\pi/2$, respectively. For bremsstrahlung photons, which are unpolarized photon, the ADX is the average of ADX_{max} and ADX_{min}, $ADX_{aver} = a$. In this study, $b_{non-Max.}/a_{non-Max.} = 0.4$; thus, $ADX_{max} = a + 0.4a$. It is estimated that the ratio of the effective dose may be reduced approximately $ADX_{aver}/ADX_{max} = 1/1.4 = 0.7$ (70%).

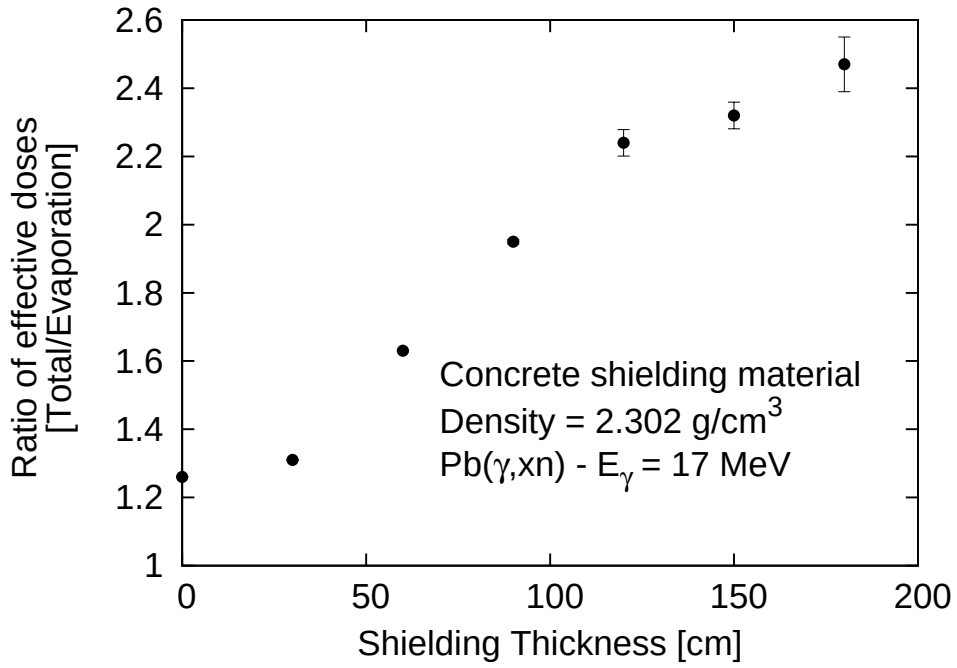

Figure 6.6: Ratio of the dose calculated from the total component to that calculated from the evaporation component.

Chapter 7

Conclusion

In this thesis, I studied neutron anisotropic emission from photonuclear reactions in GDR energy region. Two experiments were performed at NewSUBARU, BL01 with monoenergetic polarized photons. The first experiment aimed to clarify target mass dependence of the photoneutron spectrum; thus, the DDX was obtained for Pb, Au, Sn, Cu, Fe, and Ti targets with 17 MeV polaried photons. In addition, a second experiment was performed to discuss the photon energy dependence of the photoneutron spectrum. The DDX data were measured for Au (14 MeV, 17 MeV, and 20 MeV), Cu (17 MeV and 20 MeV), and Ti (17 MeV and 20 MeV).

In both the experiments, the photoneutrons were detected by NE213 detectors placed at six laboratory angles. PSD and ToF techniques were employed to select neutron events and determine the neutron energy. The raw data sets were analyzed event by event. The neutron yield was normalized with the number of photons, the photon attenuation and the neutron attenuation, target atom, detection efficiency, and solid angle for the DDX.

The DDX of the photoneutron production reaction was obtained for all targets with polarized photon energies of 14 MeV, 17 MeV, and 20 MeV. The data spanned the energy range from 2 MeV to the maximum energy. Data for energies less than 2 MeV were not recorded, owing to insufficient detection efficiency. Maxwellian-

shaped and non-Maxwellian-shaped components were found on the neutron spectrum for all targets with all three energies. The separation energy to distinguish the two components, 4.2 MeV, was the same for all the targets and photon energies. The DDXs facilitate the development and validation of photonuclear reaction models used in particle transport simulations, which have been used for the design and operation of electron accelerator facilities. It is desirable to obtain DDXs for energies lower than 2 MeV, which were not obtained in this study, because the data are necessary to determine the total Maxwellian-shaped component.

The angular distribution was discussed for 17 MeV photons. The angular distribution of photoneutrons exhibits the highest value at horizontal 90° for Pb, Au, Sn, Cu, and Fe; however, it exhibits the lowest value at this angle for Ti. This indicates that the angular distribution for Ti is opposite to that for the other targets. The angular distribution was parameterized using the fitting function a + b $\cos(2\Theta)$. The parameters a and b were obtained for each target and component.

A coefficient of the second-order Legendre polynomial, a_2, which describes the component of angular dependence from photonuclear reactions with bremsstrahlung photons, was deduced from the DDXs. The numerical values of a_2 for Ti and Sn targets were measured for the first time in this study. The a_2 values in Cu and Fe were consistent with the results obtained in previous studies, while the a_2 values of Pb and Au were smaller than the results reported in previous studies.

The target mass dependence of the photoneutron spectrum was discussed in relation to the DDX of Pb, Au, Sn, Cu, Fe, and Ti targets obtained with 17 MeV photons. The number of the obtained photoneutrons of Cu, Fe and Ti nuclei is smaller than that of Pb, Au, and Sn nuclei. In medium-mass nuclei (Ti, Fe, and Cu), the contribution of the Maxwell-shaped component was larger than that of the non-Maxwellian-shaped component; this was revealed through analysis of the obtained cross section (σ). On the order hand, for Sn, Au, and Pb, the contributions of the two components were comparable, approximately 50%, on the photoneutron

spectrum. The obtained cross section was fitted using a linear function of $A^{1/3}$.

For the photon energy dependence of the photoneutron spectrum, the DDX data at H60, H90, and V90 were used to discuss the photon energy dependence. Typically, the magnitude of the photoneutron spectrum increases with increasing photon energy. For Au and Cu, the maximum DDX value was at H90, while the minimum DDX was at V90; this was the same for all three photon energies. For data of Ti obtained with 20 MeV photons, the maximum DDX value was at H90, and the minimum DDX was at V90, this was opposite to that obtained with 17 MeV photons. For Au, at the GDR peak, 14 MeV, in addition to the evaporation process, photoneutrons produced through pre-equilibrium processes still contribute to the obtained photoneutron spectrum. From the observation in this study, the photoneutrons emitted through the evaporation process can still be observed at 20 MeV, which is close to the bottom of the GDR peak. For Cu, the ADX of both components increased with increasing the photon energy, while the total cross section of the (γ,xn) reaction decreased. For Ti, the ADX values strongly increased with increasing photon energy, especially for the non-Maxwellian-shaped component. The angular distribution was discussed based on the ADX at $\Theta = 0°$, 30°, and 90°. The angular distribution of the photoneutrons in the non-Maxwellian-shaped component changed with increasing photon energy, except for the Cu target. The shape of the angular distribution of the neutron data obtained at 17 MeV was opposite to that of 20 MeV data.

The DDXs were also calculated using PHITS code and extracted from nuclear data files for comparison with the experimental data. Using PHITS version 3.20, the DDXs were calculated with a geometry similar to the experiment setup, where the target had a cylindrical shape 5 μm in diameter and thickness. The effects of the photon width, abundance of isotopes in the target, and neutron energy resolution were considered in the extracted DDXs. These calculations indicate that the Maxwellian-shaped component, which was attributed to the evaporation process,

was reproduced by PHITS and theoretical models, while the non-Maxwellian-shaped component was not reproduced by the PHITS calculation. The agreement between nuclear data files (JEND-2004, JENDL/PD-2016.1, CoH_3) and experimental data was markedly better than the agreement between PHITS and the experimental data. Improvement in the physical models could be studied to generate a neutron spectrum consistent with the experimental data.

As the calculated photoneutron spectrum was inconsistent with the experimental spectrum, neutrons can be underestimated when designing radiation shielding for electron accelerators. In the present study, the effect of the photoneutron spectrum on shielding design was investigated based on the experimental data of the Pb(γ,xn) reaction with 17 MeV polarized photons. The Maxwellian-shaped and non-Maxwellian-shaped components were observed in the experimental photoneutron spectrum. Based on the spectral data, neutron spectra for the Maxwellian-shaped component alone and the total component were determined for the shielding calculation. The neutron dose was calculated using these two neutron spectra. The ratio of doses for the total component to the Maxwellian-shaped component alone increased with shielding thickness and reached 2.5 for a concrete thickness of 180 cm. This result implies the requirement of either a nuclear reaction model or database to reproduce a photoneutron spectrum including the non-Maxwellian-shaped component for the shielding calculation of an electron accelerator facility.

Bibliography

[1] A. Bohr, A. and B.R. Mottelson, *Nuclear Structure. 2nd Edition*, (World Scientific: Singapore, 1998).

[2] M. Pisharody, E. Semones, and P.K. Job, *Dose measurements of Bremsstrahlung-produced neutrons at the advanced photon source*, ANL/APS/LS-269, Argonne National Laboratory, the University of Chicago (1998).

[3] Evans Hayward, Reviews of Modern Physics **35**, 324 (1963).

[4] M.B. Chadwick, P. Oblozinsky, P.E. Hodgson, and G. Reffo, Physical Review C. **44**, 814 (1991).

[5] M.C. White, *Development and Implementation of Photonuclear Cross-Section Data for Mutually Coupled Neutron-Photon Transport Calculations in the Monte Carlo N-Particle (MCNP) Radiation Transport Code*, Dr. thesis, University of Florida (2000).

[6] J.R. Wu, and C.C. Chang, Physical Review C. **16**, 1812 (1977).

[7] M. Blann, B.L. Berman, and T.T. Komoto, Physical Review C. **28**, 2286 (1983).

[8] M.B. Chadwick, P.G. Young, and S. Chibas, Journal of Nuclear Science and Technology. **32**, 1154 (1995).

[9] T. Kawano, Y. S. Cho, P. Dimitriou, D. Filipescu, N. Iwamoto, V. Plujko, X. Tao, H. Utsunomiya, V. Varlamov, R. Xu, R. Capote, I. Gheorghe, O.

Gorbachenko, Y.L. Jin, T. Renstrøm, K. Stopani, Y. Tian, G. M. Tveten, J.M. Wang, T. Belgya, R. Firestone, S. Goriely, J. Kopecky, M. Krtička, R. Schwengner, S. Siem, and M. Wiedeking, arXiv:1908.00471v1.

[10] K. Masumoto, Hiroshi Matsumura, Kazuaki Kosako, Kotaro Bessho, and Akihiro Toyoda, J. Radiat. Prot. Res. **41**, 286 (2016).

[11] I. Gudowska, A. Brahme, P. Andreo, W. Gudowski, and J. Kierkegaard, Phys. Med. Biol., **44**, 2099 (1999).

[12] O. Sato, N. Yoshizawa, S. Iwai, T. Uehara, Y. Sakamoto, and S. Tanaka, J. Nucl. Sci. Technol., **37:sup1**, 861 (2000)

[13] William P. Swanson, *Radiological safety aspects of the operation of electron linear accelerators, Technical reports series No. 188*, (International Atomic Energy Agency, 1979)

[14] A. Boudard, J. Cugnon, J.-C. David, S. Leray, and D. Mancusi, Phys. Rev. C, **87**, 014606 (2013).

[15] S. Furihata, Nucl. Inst. Meth. B, **171**, 251 (2000).

[16] N. Kishida, T. Murata, T. Asami, K. Kosako, K. Maki, H. Harada, Y.-O. Lee, J. Chang, S. Chiba, and T. Fukahori, AIP Conference Proceedings, **769**, 199 (2005).

[17] S. Noda, S. Hashimoto, T. Sato, T. Fukahori, S. Chiba, and K. Niita, Journal of Nuclear Science and Technology **52**, 57 (2015).

[18] M. Chadwick, P. Young, R. MacFarlane, M. White, and R. Little, Nuclear Science and Engineering **144**, 157 (2003).

[19] M. White, R. Little, M. Chadwick, P. Young, and R. MacFarlane, Nuclear Science and Engineering **144**, 174 (2003).

[20] W. Hauser, H. Feshbach, Phys. Rev. **87**, 366 (1952).

[21] N. Iwamoto, K. Kosako, and T. Murata, Proc. Symp. Nucl. Data, 2015, pp. 53 (2016).

[22] O. Iwamoto, N. Iwamoto, S. Kunieda, F. Minato, and K. Shibata, Nuclear Data Sheets, **131**, pp. 259 (2016).

[23] M. Herman, R. Capote, M. Sin, A. Trkov, B.V. Carlson, P. Oblozinsky, C.M. Mattoon, H. Wienke, S. Hoblit, Young-Sik Cho, G.P.A. Nobre, V.A. Plujko, V. Zerkin, INDC(NDS)-0603, International Atomic Energy Agency (2013).

[24] T. Kawano, Proc. of the 6th Int. Workshop on Compound-Nuclear Reactions and Related Topics CNR*18, 2019, p. 27.

[25] G.S. Mutchler, Cambridge, Massachusetts Institute of Technology; 1966.

[26] G.A. Price, Phys. Rev. Vol., **93**, 1279 (1954).

[27] F. Tagliabue, and J.Goldemberg, Nucl. Phys., **23**, 144 (1961).

[28] R.G. Baker, and K. G. McNeill, Canadian J. Phys., **39**, 1158 (1961).

[29] G.C. Reinhard, W D. Whitehead, Nucl. Phys., **30**, 201 (1962).

[30] D.B. Gayther, et al., J. Nucl. Ener., **21**, 733 (1967).

[31] A.V. Varlamov and V.V. Varlamov and D.S. Rudenko and M.E. Stepanov, *Atlas of Giant Dipole Resonances: Parameters and Graphs of Photonuclear Reaction Cross Sections, Work Performed under the Coordinated Research Project on Compilation and Evaluation of Photonuclear Data for Applications* (IAEA Tech Rep. INDC(NDS)-394. IAEA; 1999).

[32] L.M. Bollinger and G. E. Thomas, Review of Scientific Instruments, **32**, 1044 (1961).

[33] A. Agodi, Nuovo Cimento, **5**, 21 (1957).

[34] S. Miyamoto, Y. Asano, S. Amano, D. Li, K. Imasaki, H. Kinugasa, Y. Shoji, T. Takagi, and T. Mochizuki, Radiat. Meas., **41**, S179 (2007).

[35] Y. Asano, S. Miyamoto, and LEPS-II collaboration, Prog. Nucl. Sci. Tech., **4**, 252 (2014).

[36] K. Horikawa, S. Miyamoto, T. Mochizuki, S. Amano, D. Li, K. Imasaki, Y. Izawa, K. Ogata, S. Chiba, and T. Hayakawa, Phys. Lett. B, **737**, 109 (2014).

[37] Y. Kirihara, H. Nakashima, T. Sanami, Y. Namito, T. Itoga, S. Miyamoto, A. Takemoto, M. Yamaguchi, and Y. Asano, Journal of Nuclear Science and Technology, **57**, 444 (2020).

[38] H. Zen, Y. Taira, T. Konomi, T. Hayakawa, T. Shizuma, J. Yamazaki, T. Kii, H. Toyokawa, M. Katoh, H. Ohgaki, Energy Procedia, **89**, 335 (2016).

[39] V.V. Verbinski, W.R. Burrus, T.A. Love, W. Zobel, N.W. Hill, R. Textor, Nucl. Instr. Meth., **65**, 8 (1968).

[40] G. Dietze and H. Klien, Nucl. Instr. Meth, **193**, 549 (1982).

[41] W. Braunschweig, E. K. onigs, W. Sturm, W. Wallraff, Nucl. Instr. and Meth. **134**, 261 (1976).

[42] T. Kobayashi, T. Sugitate, Nucl. Instr. and Meth. A, **287**, 389 (1990).

[43] D.A. Gedcke, W.J. McDonald, Nucl. Instr. and Meth. **58**, 253 (1968).

[44] M.R. Maier, P. Sperr, Nucl. Instr. and Meth. **87**, 13 (1970).

[45] L. Heilbronn, Y. Iwata, H. Iwase, Nucl. Inst. Meth. Phys. Res. A **522**, 495 (2004).

[46] N. Tsoulfanidis, and S. Landsberger, *Measurement and Detection of Radiation, 4th Edition* (CRC Press; 2015).

[47] N. Nakao, *Experimental study of shielding for high energy proton accelerator*, Dr. thesis, Tohoku University (1998).

[48] H. Hirayama, Y. Namito, A.F. Bielajew, S.J. Wilderman, and W.R. Nelson, SLAC-R-730 and KEK-REPORT-2005-8 (2005).

[49] T. Sato, K. Niita, N. Matsuda, S. Hashimoto, Y. Iwamoto, S. Noda, T. Ogawa, H. Iwase, H. Nakashima, T. Fukahori, K. Okumura, T. Kai, S. Chiba, T. Furuta, L. Sihver, Journal of Nuclear Science and Technology, **50**, 913 (2013).

[50] D. Satoh, S. Kunieda, Y. Iwamoto, N. Shigyo, and K. Ishibashi, Journal of Nuclear Science and Technology, **39:sup2**, 657 (2002).

[51] T. Win, *Experimental Studies on Fast Neutron-Induced Fission Spectra for* ^{237}*Np and* ^{233}*U*, Ph.D. thesis of Tohoku University, Sendai, Japan, March 1999.

[52] T. Sato, K. Niita, N. Matsuda, S. Hashimoto, Y. Iwamoto, T. Furuta, S. Noda, T. Ogawa, H. Iwase, H. Nakashima, T. Fukahori, K. Okumura, T. Kai, S. Chiba, and L. Sihver, Annals of Nuclear Energy, **82**, 110 (2015).

[53] Y. Sakaki, *Note on Evaluated Nuclear Data Library and a new tool "endf6_reader"*, KEK, 2020.

[54] E.D. Courant, Phys. Rev., **81**, 703 (1951).

[55] N. N. Kaushal, E. J. Winhold, P. F. Yergin, H. A. Medicus, and R. H. Augustson, Phys. Rev., **175**, 1330 (1968).

[56] A.I. Blokhin, M.B. Chadwick, T. Fukahori, Y. Han, Y.-O. Lee, M.N. Martins, S.F. Mughabghab, P. Oblozinskv, V.V. Varlamov, B. Yu, and J. Zhang, *IAEA-TECDOC-1178.* (IAEA-VIENNA, 2000).

[57] J. D. Lawson, Phil. Mag., **44**, 102 (1953).

[58] R.W. Bauer, J. D. Anderson, S. M. Grimes, and V. A. Madsen, Proc. of International Conference on Nuclear Data for Science and Technology, 1997.

[59] C.H. Clement and et al., ICRP publication 116, Ann. ICRP **40** (2-5).

[60] K. Strauch, Annual Review of Nuclear Science, **2**, 105 (1953).

[61] J.S. Levinger, Annual Review of Nuclear Science, **4**, 13 (1954).

[62] M. Danos and E.G. Fuller, Annual Review of Nuclear Science, **15**, 29 (1965).

[63] C. Segebade and A. Berger, Encyclopedia of Analytical Chemistry (eds R.A. Meyers and R.A. Meyers), DOI: https://doi.org/10.1002/9780470027318.a6211.pub2

[64] M.S. Johnson, J. M. Hall, D. P. McNabb, J. L. McFarland, E. B. Norman, W. Bertozzi, S. E. Korbly, R. J. Ledoux, and W. H. Park, J. Korean Phy. Soc., **59**, 1414 (2011).

[65] C. Jin-Gen, X. Wang, W. Hong-Wei, G. Wei, M. Yu-Gang, C. Xiang-Zhou, L. Guang-Cheng, X. Yi, P. Qiang-Yan, and Y. Ren-Yong, Chinese Physics C, **32**, 677 (2008).

[66] E.G. Fuller and H.Gerstenberg, *Photonuclear data - abstract sheets 1955-1982, Report of the US National Bureau of Standards, NBSIR 83-2742, vol. I-XV (1983-1986)*, (National Institute for Standards and Technology, Gaithersburg, MD.)

[67] B.L. Berman, *Atlas of photoneutron cross-section obtained with monoenergetic photons*, Atomic Data and Nuclear Data Tables, **15**, 319 (1975).

[68] B.S. Ishkhanova, and S.Yu.Troschiev, Moscow University Physics Bulletin, **65**, 39 (2010).

[69] A. Veyssiere, H. Beil, R.Bergere, P.Carlos, J.Fagot, A.Lepretre, and J.Ahrens, Nucl. Inst. Meth., **165**, 417 (1979).

[70] K. Hirose, M. Chiba, M. Inoue, H. Kanda, R. Kimura, K. Kino, Y. Kobayashi, O. Konno, K. Maeda, H. Miyase, A. Miyamoto, T. Ohtsuki, A. Saito, T. Suda, K. Takahashi, T. Tamae, Y. Terasaki, T. Terasawa, H. Tsubota, T. Tsuruta, M. Utoyama, H. Yuuki, Y. Yamaguchi, and H. Yamazaki, Nucl. Ins. Meth. A, **564**, 100 (2006).

[71] O.V. Bogdankevich, and F.A.Nikolaev, *Methods in Bremsstrahlung Research*, (USA: Academic Press, New York, 1966).

[72] A.S. Penfold, and J. E. Leiss, Phys. Rev., **114**, 1332 (1959).

[73] E. Bramanis, T. K. Deague, R. Hicks, R. S. Hughes, E. G. Muirhead, R. H. Sambell, and R. J. J. Stewart, Nucl. Inst. Meth., **100**, 59 (1972).

[74] S.S. Belyshev, D. M. Filipescu, I. Gheoghe, B. S. Ishkhanov, V. V. Khankin, A. S. Kurilik, A. A. Kuznetsov, V. N. Orlin, N. N. Peskov, K. A. Stopani, O. Tesileanu, and V. V. Varlamov, Eur. Phys. J. A, **51**, 67 (2015).

[75] H. Naik, G. Kim, K. Kim, M. Zaman, A. Goswami, M.W. Lee, S.-C. Yang, Y.-O. Lee, S.-G. Shin, and M.-H. Cho, Nucl. Phys. A, **948**, 28 (2016).

[76] B.L. Berman, J. T. Caldwell, R. R. Harvey, M. A. Kelly, R. L. Bramblett, and S. C. Fultz, Phys. Rev., **162**, 1098 (1965).

[77] E. Wolynec, and M.N. Martins, Discrepancies between Saclay and Livermore photoneutron cross sections, Re- vista Brasileira de Fisica, **17**, 56 (1987).

[78] H. Utsunomiya, I. Gheorghe, D.M. Filipescu, T. Glodariu, S. Belyshev, K. Stopani, V. Varlamov, B. Ishkhanov, S. Katayama, D. Takenaka, T. Ari-izumi, S. Amano, and S. Miyamoto, Nucl. Inst. Meth. A, **871**, 135 (2017).

[79] A.B. Smith, P. R. Fields, and J. H. Roberts, Phys. Rev. Vol. **108**, 411 (1957).

Appendix A

Comparison of DDX data for Cu and Ti from two experiments

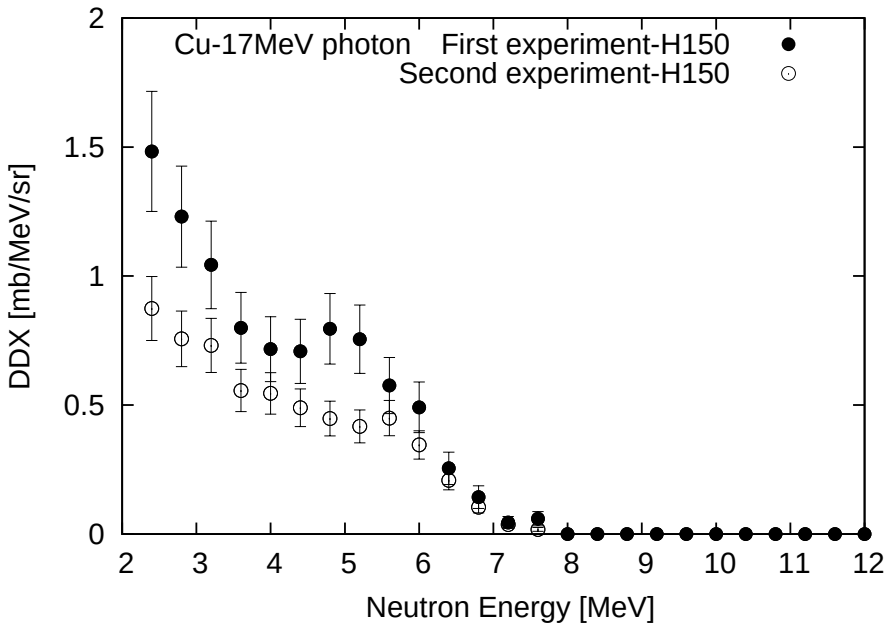

Figure A.1: DDX results of Cu at H150 obtained in both experiments.

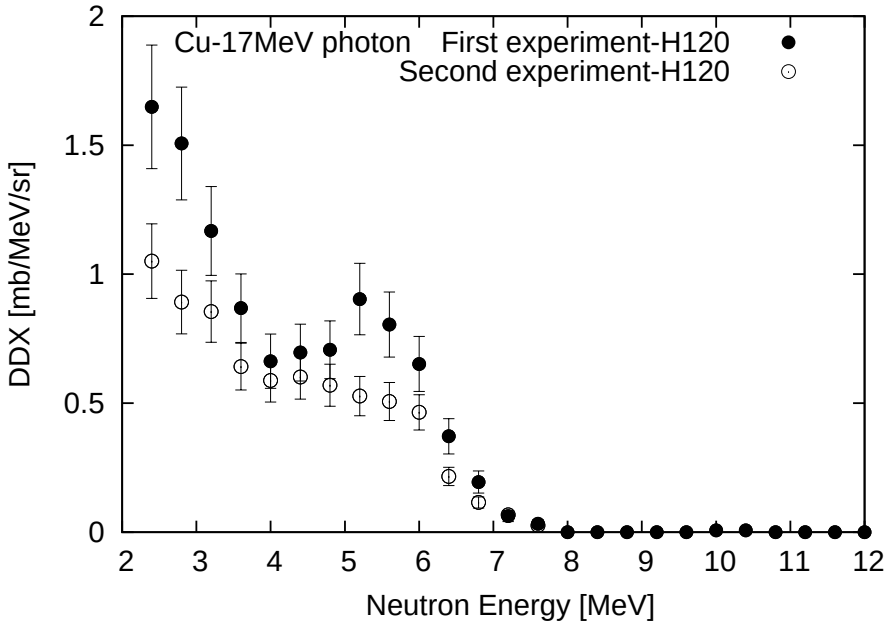

Figure A.2: DDX results of Cu at H120 obtained in both experiments.

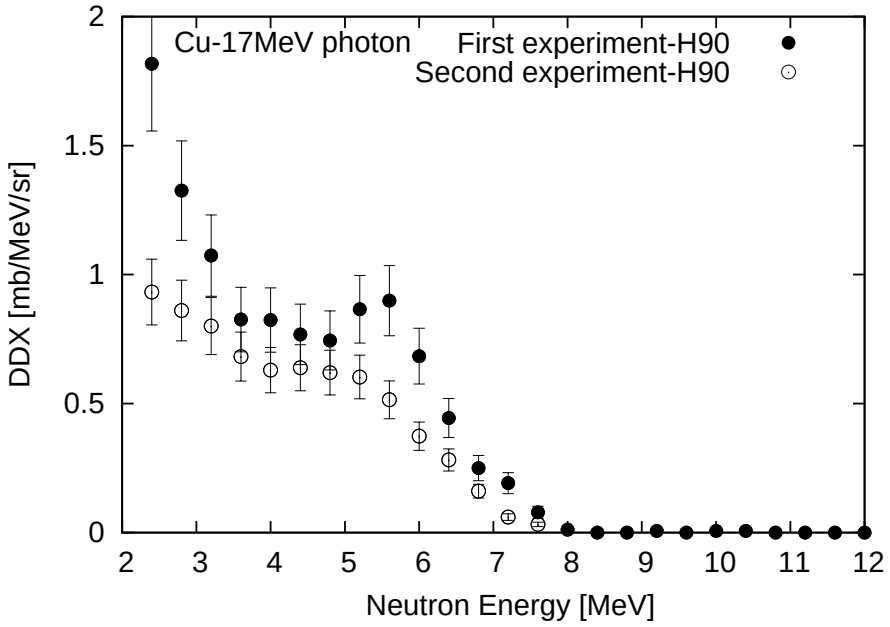

Figure A.3: DDX results of Cu at H90 obtained in both experiments.

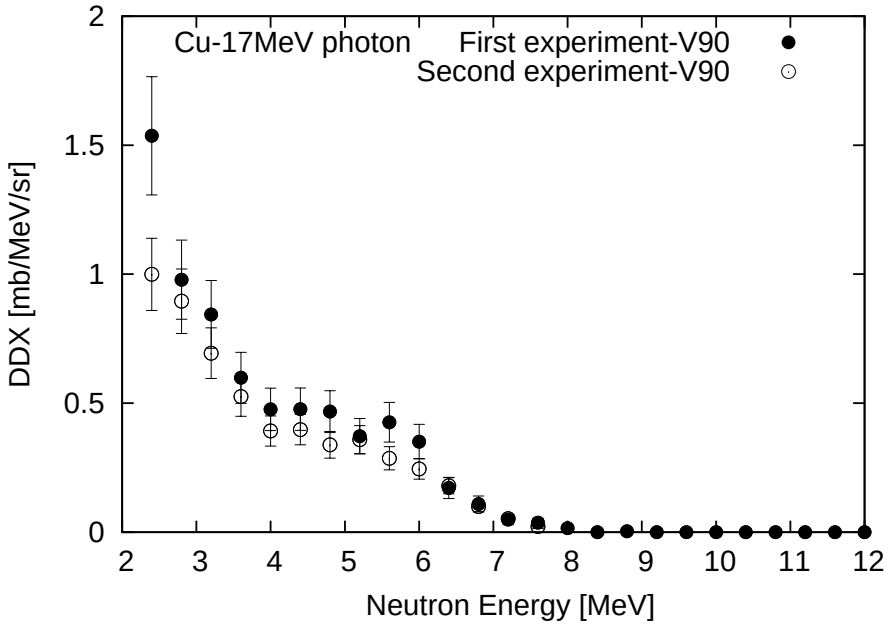

Figure A.4: DDX results of Cu at V90 obtained in both experiments.

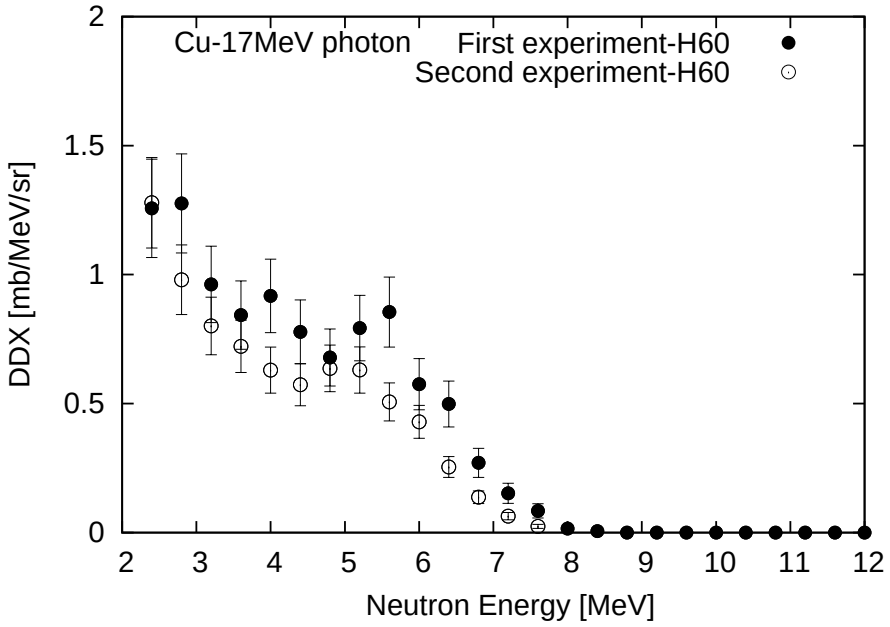

Figure A.5: DDX results of Cu at H60 obtained in both experiments.

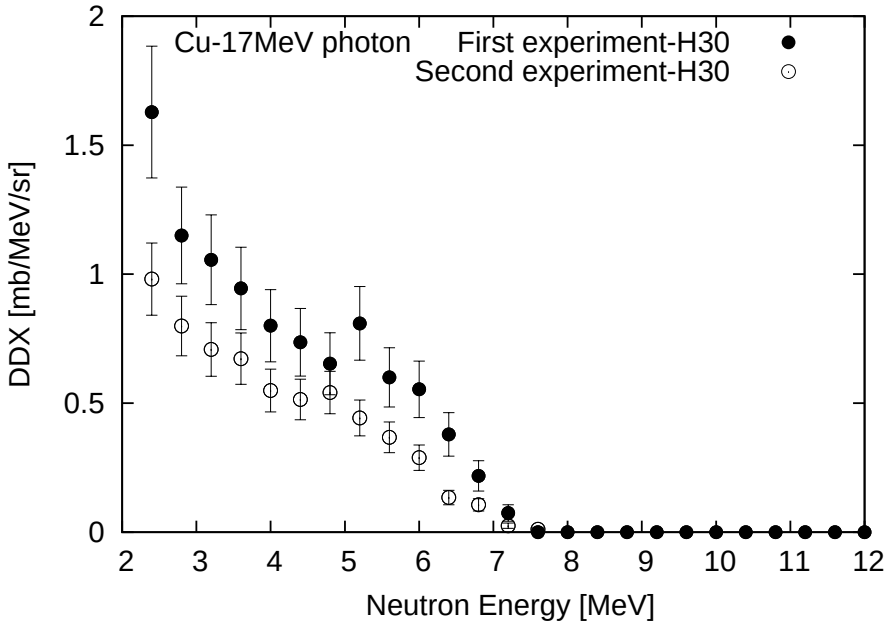

Figure A.6: DDX results of Cu at H30 obtained in both experiments.

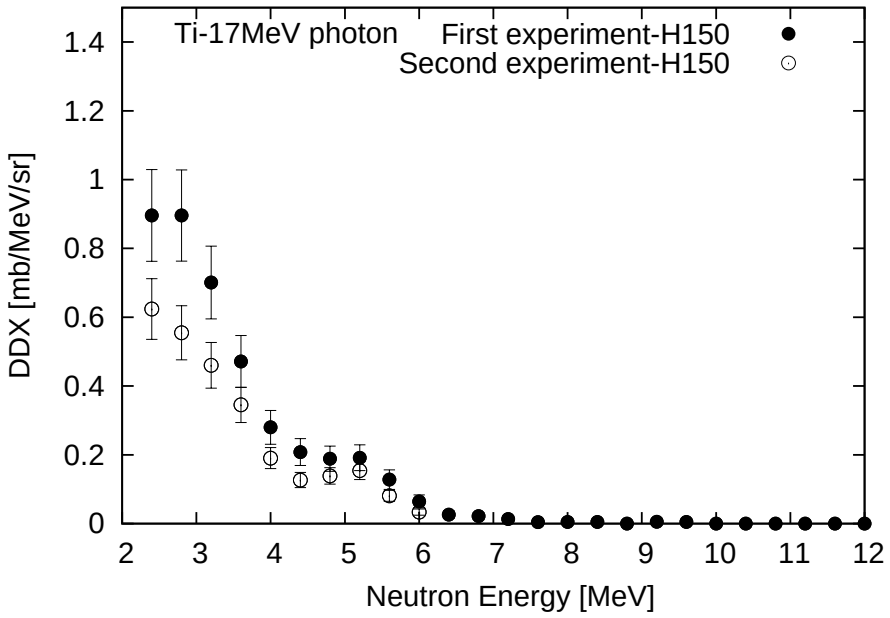

Figure A.7: DDX results of Ti at H150 obtained in both experiments.

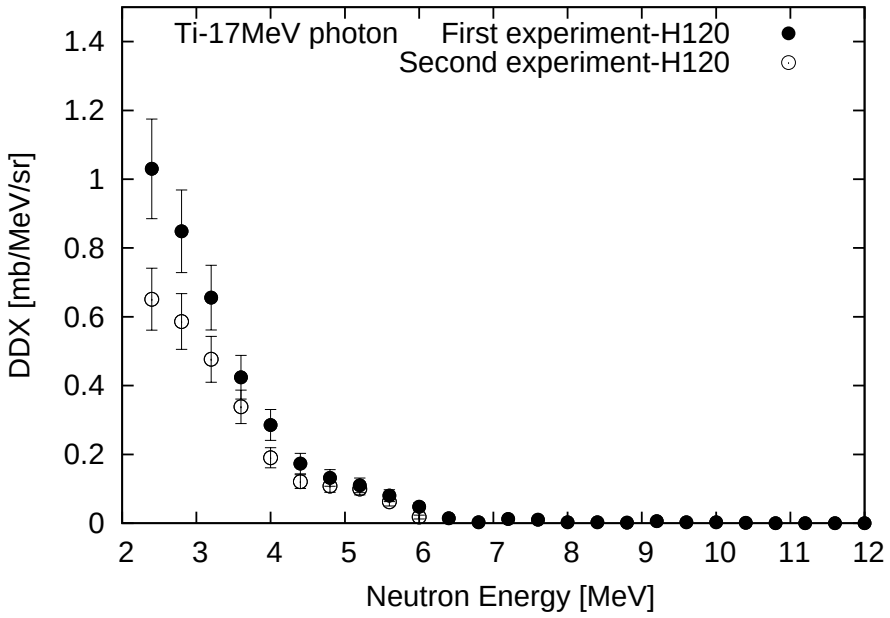

Figure A.8: DDX results of Ti at H120 obtained in both experiments.

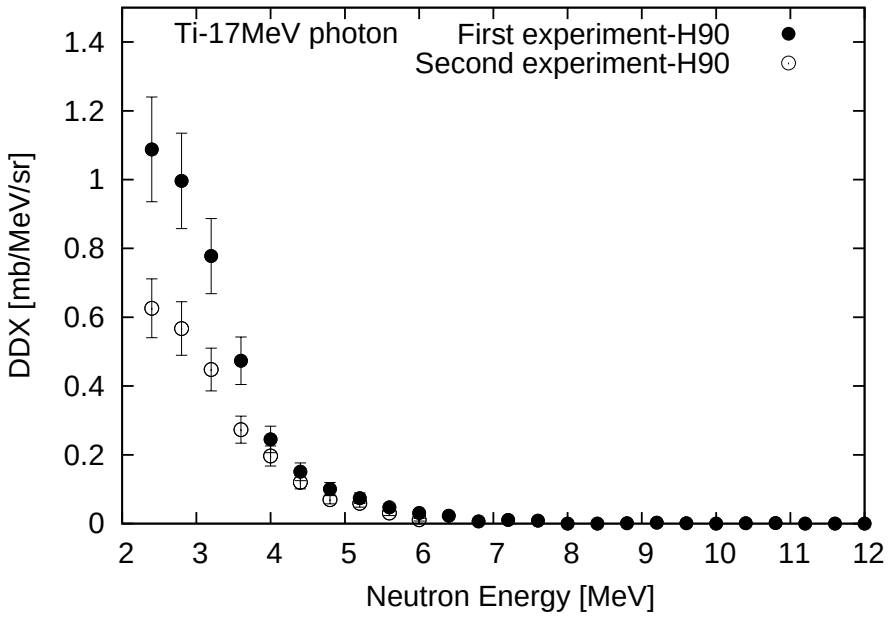

Figure A.9: DDX results of Ti at H90 obtained in both experiments.

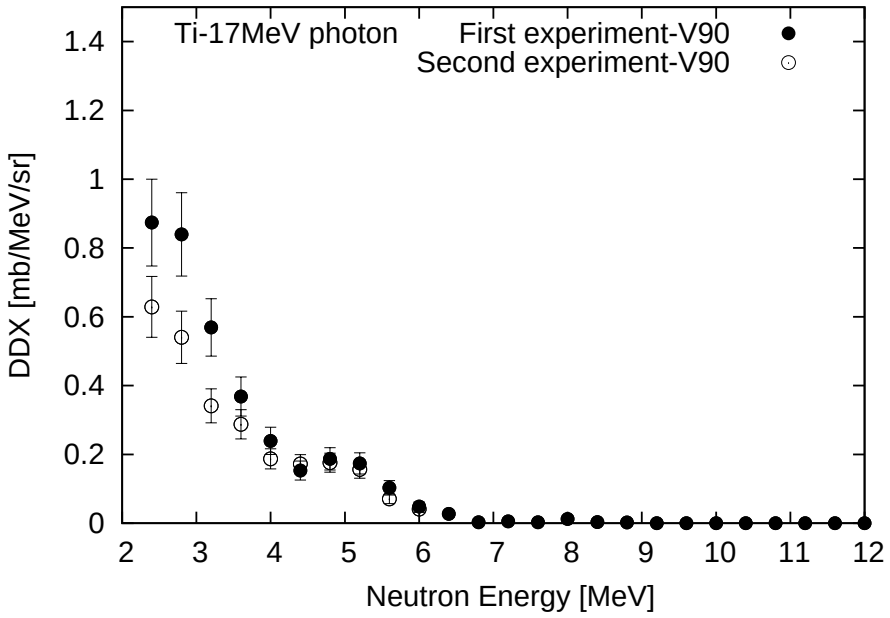

Figure A.10: DDX results of Ti at V90 obtained in both experiments.

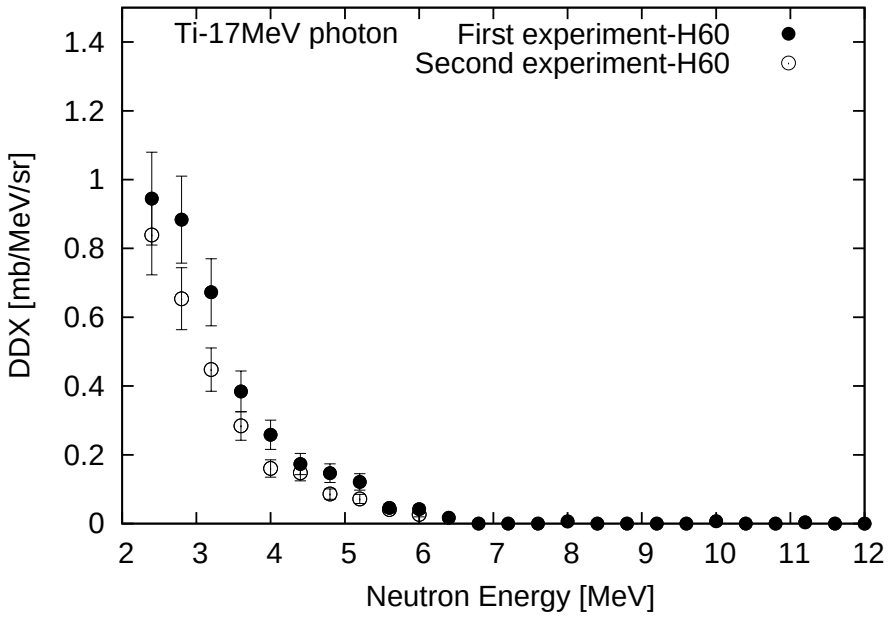

Figure A.11: DDX results of Ti at H60 obtained in both experiments.

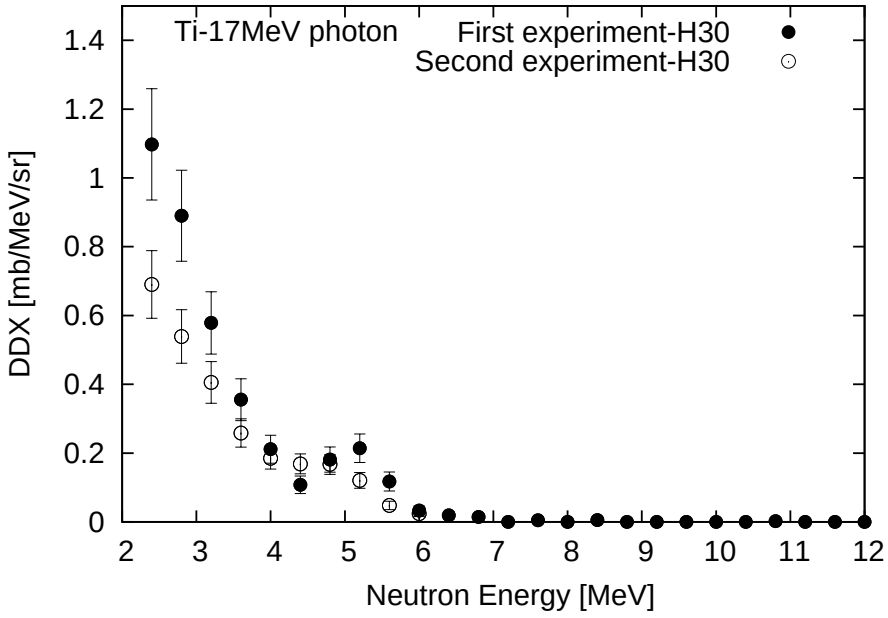

Figure A.12: DDX results of Ti at H30 obtained in both experiments.

Appendix B

Input file in dose calculation using PHITS

[T i t l e]

Shielding Calculation [Experimental photoneutron data of Pb material, Maxwellian-shaped Component, thickness = 30cm]

[P a r a m e t e r s]

icntl = 0 $ (D=0) 3:ECH 5:NOR 6:SRC 7,8:GSH 11:DSH 12:DUMP

itall = 1 $ (D=0) 0:no tally at batch, 1:same, 2:different

maxcas = 1e6 $ (D=10) number of particles per one batch

maxbch = 50 $ (D=10) number of batches

rseed = 1111111

file(6) = phits.out $ (D=phits.out) general output file name

file(7) = /phits/data/xsdir.jnd

file(14) = /phits/data/trxcrd.dat

file(20) = /phits/XS/egs

inclg = 1 $ (D=1) 0: no, 1:INCL for p,n,pi,d,t,3He,alpha, 2:p,n,pi only

icrhi = 1 $ (D=1) 0: Shen, 1: NASA, 2: KUROTAMA

icxsni = 0 $ (D=0) 0: Pearlstein-Niita, 1: KUROTAMA, 2: Sato

ipnint = 1 $ (D=0) photonuclear GDR, 1:analog, -1:implicit

e-mode = 0 $ (D=0) 0: Normal, 1: Event generator mode

emin(2) = 1e-10 $ cut-off neutron [MeV]

emin(14) = 3 $ cut-off gamma [MeV]

infout = 8

[S o u r c e]

totfact = 1.0 $ (D=1.0) global factor

s-type = 1 $ mono-energetic axial source

proj = neutron $ kind of incident particle

e-type = 22

ne = 30

$Energy lower	$ Energy upper	$Weight
0.2	0.6	6.45E-01
0.6	1.0	9.63E-01
1.0	1.4	1.08E+00
1.4	1.8	1.07E+00
1.8	2.2	1.00E+00
2.2	2.6	8.97E-01
2.6	3.0	7.81E-01
3.0	3.4	6.66E-01
3.4	3.8	5.60E-01
3.8	4.2	4.64E-01
4.2	4.6	3.81E-01
4.6	5.0	3.10E-01
5.0	5.4	2.51E-01
5.4	5.8	2.02E-01

5.8	6.2	1.61E-01
6.2	6.6	1.28E-01
6.6	7.0	1.02E-01
7.0	7.4	8.05E-02
7.4	7.8	6.35E-02
7.8	8.2	4.99E-02
8.2	8.6	3.91E-02
8.6	9.0	3.06E-02
9.0	9.4	2.38E-02
9.4	9.8	1.86E-02
9.8	10.2	1.44E-02
10.2	10.6	1.12E-02
10.6	11.0	8.69E-03
11.0	11.4	6.73E-03
11.4	11.8	5.20E-03
11.8	12.2	4.02E-03

r0 = 0.0 $ radius [cm]

x0 = 0.0000 $ (D=0.0) center position of x-axis [cm]

y0 = 0.0000 $ (D=0.0) center position of y-axis [cm]

z0 = 0.000 $ minimum position of z-axis [cm]

dir = all $ z-direction of beam [cosine]

[M a t e r i a l]

$ Concrete

m1

H	-0.023
C	-0.0023
O	-1.22

Na -0.0368

Mg -0.005

Al -0.078

Si -0.775

K -0.0299

Ca -0.1

Fe -0.032

set: c1[200.0] $ diameter of shielding

set: c3[30.0] $ thickness of shielding

set: c5[10.0] $ thickness of monitor [cm]

set: c6[700]

set: c20[4*pi*(c6/2)*(c6/2)]

[Surface]

1 so 800

$ Shielding

2 so c1/2

3 so [c1/2+c3]

$ Monitor

4 so [c6/2]

5 so [c6/2+c5]

6 so [c1/2+c3]

7 so [c6/2]

[Cell]

100 0 -1 #101 #102 #103

101 1 -2.302 2 -3 $ shielding

102 0 4 -5 $ monitor

103 0 6 -7 $ vacuum

999 -1 1

[M u l t i p l i e r] $ Dose conversion coefficient for neutron ICRP116

number = -201

interpolation = log

ne = 43

1.0E-9 3.09

1.0E-8 3.55

2.5E-8 4.00

1.0E-7 5.20

2.0E-7 5.87

5.0E-7 6.59

1.0E-6 7.03

2.0E-6 7.39

5.0E-6 7.71

1.0E-5 7.82

2.0E-5 7.84

5.0E-5 7.82

1.0E-4 7.79

2.0E-4 7.73

5.0E-4 7.54

0.001 7.54

0.002 7.61

0.005 7.97

0.01 9.11

0.02 12.2

0.03 15.7

0.05 23.0

0.07 30.6

0.1 41.9

0.15 60.6

0.2 78.8

0.3 114

0.5 177

0.7 232

0.9 279

1.0 301

1.2 330

1.5 365

2.0 407

3.0 458

4.0 483

5.0 494

6.0 498

7.0 499

8.0 499

9.0 500

10.0 500

12.0 499

[T-Track]

title = [t-track] in xyz mesh

mesh = xyz

y-type = 2

ymin = -400.00000

ymax = 400.00000

ny = 800

x-type = 1

nx = 1

-1.00000E+01 1.00000E+01

z-type = 2

zmin = -400.00000

zmax = 400.00000

nz = 800

e-type = 2

emin = 0.000000

emax = 10000.00

ne = 1

unit = 1

material = all

2D-type = 3

axis = yz

file = yz.out

part = neutron photon

gshow=3

epsout = 1

[T - C r o s s]

title = Energy spectrum of neutron crossing surface

mesh = reg $ mesh type is region-wise

reg = 1 $ number of crossing regions

r-from r-to area

103 102 c20

```
part = neutron
e-type = 4 $ e-mesh is log given by emin, emax and edel
edel = 0.4
emin = 1.e-9
emax =1.0e+1
axis = eng $ axis of output
unit = 1 $ unit is [1/cm2/source]
output = flux $ surface crossing flux
file = dose.out $ file name of output for the above axis
epsout = 1 $ (D=0) generate eps file by ANGEL
y-txt = Effective dose [Sv/h]
multiplier = all $ number of material group
part = neutron
emax = 1000.0
mat mset1
all (1.0 -201)
angel = ymin(1.0e-8) ymax(1.0e2)

    [ T - C r o s s ]
title = Energy spectrum of neutron crossing surface
mesh = reg $ mesh type is region-wise
reg = 1 $ number of crossing regions
r-from r-to area
103 102 c20
part = neutron
e-type = 4 $ e-mesh is log given by emin, emax and edel
edel = 0.4 $ width of e-mesh points
emin = 0.2 $ minimum value of e-mesh points
```

emax = 10.2 $ maximum value of e-mesh points

axis = eng $ axis of output

unit = 1 $ unit is [1/cm2/source]

output = flux $ surface crossing flux

file = flux.out $ file name of output for the above axis

epsout = 1 $ (D=0) generate eps file by ANGEL